

9-1-2022

Applications of Temperature Transient Analysis for Reservoir Surveillance

Refaat Galal Aboelfotoh Hashish
Louisiana State University and Agricultural and Mechanical College

Follow this and additional works at: https://repository.lsu.edu/gradschool_dissertations



Part of the [Geological Engineering Commons](#), and the [Other Engineering Commons](#)

Recommended Citation

Hashish, Refaat Galal Aboelfotoh, "Applications of Temperature Transient Analysis for Reservoir Surveillance" (2022). *LSU Doctoral Dissertations*. 5961.
https://repository.lsu.edu/gradschool_dissertations/5961

This Dissertation is brought to you for free and open access by the Graduate School at LSU Scholarly Repository. It has been accepted for inclusion in LSU Doctoral Dissertations by an authorized graduate school editor of LSU Scholarly Repository. For more information, please contact gradetd@lsu.edu.

APPLICATIONS OF TEMPERATURE TRANSIENT ANALYSIS FOR RESERVOIR SURVEILLANCE

A Dissertation

Submitted to the Graduate Faculty of the
Louisiana State University and
Agricultural and Mechanical College
in partial fulfillment of the
requirements for the degree of
Doctor of Philosophy

in

The Craft and Hawkins Department of Petroleum Engineering

by

Refaat Galal Aboelfotoh Hashish
B.S., Cairo University, 2013
M.S., Cairo University, 2016
December 2022

Table of Contents

List of Tables	v
List of Figures	vi
Abstract	xii
Chapter 1. Introduction	1
1.1. Background and Research Motivations.....	1
1.2. Problem Statement	3
1.3. Modeling Approaches	4
1.4. Overview of Chapters.....	5
Chapter 2. Literature Review	8
2.1. Advances in Downhole Temperature Monitoring Tools.....	8
2.2. Temperature Warmback Analysis Applications for Conventional Reservoirs	9
2.3. Temperature Warmback Analysis Applications for Unconventional Reservoirs ..	12
2.4. Monitoring CO ₂ Plume Migration during Geologic CO ₂ Storage Using Temperature Data.....	14
Chapter 3. Temperature Warmback Analysis for Estimating Injection Profile in Vertical Injection Wells	23
3.1. Temperature Warmback Analysis During Injection via Vertical Injection Well...	23
3.2. Warmback Analysis Application for Conventional Reservoirs - Considering Heat Exchange Between Injection Zones	34
Chapter 4. Application of Temperature Warmback Analysis under Variable Injection Rate and Variable Injection Temperature	48
4.1. Injection under Variable Rate and Variable Temperature.....	48
4.2. Injection under Variable Rate and Variable Temperature for Advection- dominant Heat Transfer.....	51
4.3. Accounting for the Wellbore System	53
4.4. Forward Modeling.....	56
4.5. Inverse Modeling.....	57
4.6. Validation with Numerical Results	59
4.7. Inversion Procedure Application.....	64
Chapter 5. Applications of Temperature Warmback Analysis for Injection Profile in Horizontal Wells	67
5.1. Problem Description.....	67
5.2. Inversion Procedure.....	72
5.3. Validation Results	74
5.4. Inversion Procedure Application.....	77
Chapter 6. Warmback Analysis Application for Hydraulic Fracture Characterization	80
6.1. Problem Description.....	80

6.2. Inversion Procedure.....	86
6.3. Validation Results	88
6.4. Inversion procedure for fracture geometry.....	93
Chapter 7. Application of Temperature Warmback Analysis for Allocating CO ₂ Injection Rate and Plume Extent Evaluation using Temperature Warmback Analysis.....	96
7.1. Forward Modeling.....	96
7.2. Inverse Modeling.....	104
7.3. Solution Validation.....	105
7.4. Inverse Modeling Application.....	108
Chapter 8. Application of In-well and Formation Heat Pulse Testing for CO ₂ Plume Monitoring.....	111
8.1. In-well Heat Pulse Testing	111
8.2. Formation Heat Pulse Testing	125
Chapter 9. Application of Passive Temperature Monitoring for Tracking CO ₂ Migration	139
9.1. Monitoring CO ₂ Migration in Storage Aquifer	139
9.2. Monitoring CO ₂ Migration Through Improperly Abandoned Wells.....	153
Chapter 10. Conclusions and Recommendations.....	163
10.1. Temperature Warmback Analysis for Estimating Injection Profile in Vertical Injection Wells.....	163
10.2. Application of Temperature Warmback Analysis under Variable Injection Rate and Variable Injection Temperature	163
10.3. Applications of Temperature Warmback Analysis for Injection Profile in Horizontal Wells.....	164
10.4. Application of Temperature Warmback Analysis for Hydraulic Fracture Characterization.....	165
10.5. Application of Temperature Warmback Analysis for Allocating CO ₂ Injection Rate and Plume Extent Evaluation using Temperature Warmback Analysis	165
10.6. Application of In-well and Formation Heat Pulse Testing for CO ₂ Plume Monitoring.....	166
10.7. Application of Passive Temperature Monitoring for Tracking CO ₂ Migration ...	167
10.8. Recommendations for Future Work	169
Appendix A. Numerical Investigation of Wellbore Temperature Behavior During Non- Isothermal Fluid Injection	170
Appendix B. Derivation of the Semi-analytical Temperature Solution During the Injection Period under Variable Rate – Variable Temperature	173
Appendix C. Derivation of the Temperature Solution During the Warmback Period Following Injection under Variable Rate - Variable Temperature.....	177

Appendix D. Derivation of the Temperature Solution During the Injection under Variable Rate - Variable Temperature Considering Advection-Dominant Heat Transfer	178
Appendix E. Derivation of the Temperature Solution During the Injection Period for Constant Rate – Variable Temperature	182
Appendix F. Analytical Solution for the Temperature During and Shortly after Non-isothermal Fluid Injection via Horizontal Injection Well	184
Appendix G. Solution for the Temperature and Saturation Evolutions During CO2 Injection in Deep Saline Aquifers	188
References.....	191
Vita.....	202

List of Tables

3. 1. Input data for the synthetic case.....	28
3. 2. Inversion results obtained using the graphical techniques.....	31
3. 3. Reservoir properties for the synthetic case.	44
3. 4. Results of the inversion procedures.	47
4. 1. Summary of the closed-form analytical solutions and the corresponding asymptotic forms.....	53
4. 2. Input data for the validation cases (empty cells indicate identical properties to the left column).	60
4. 3. Inversion results for Cases 1 and 2.	65
5. 1. Input data for the synthetic case.....	75
5. 2. Inversion results for the synthetic case.	79
6. 1. Input data for the validation cases.....	90
6. 2. Inversion results for the validation cases.	94
7. 1. Input data for the synthetic case.....	106
7. 2. Inversion results obtained using the graphical technique	109
8. 1. Input data for the synthetic case.....	116
8. 2. Input data for the synthetic case (before and after CO2 arrival).	132
8. 3. Inversion results obtained using the graphical interpretation methods	138
9. 1. 2D radial model properties.....	141
9. 2. Reservoir properties of the simulation study.	154
9. 3. Well properties of the simulation study.	155
A. 1. Input data for the numerical investigation study.	171

List of Figures

2. 1. Backscattered light spectrum generated from a typical fiber optic DTS tool.....	9
2. 2. (a) Waterfall chart displaying temperature evolution during injection and warmback periods (b) temperature profiles during shut-in period (shown on solid lines) approaching geothermal temperature gradient (shown on green dashed line) (modified after Sadigov et al. (2021)).....	11
2. 3. CO2 leakage pathways from a geological storage reservoir (Gaurina-Međimurec and Mavar 2017).....	16
2. 4. CO2 saturation and temperature profiles in an aquifer during an isothermal CO2 injection.....	17
2. 5. Schematic illustration of the different types of a typical thermal tracer test. Right-hand side plots show the temperature signature to be observed in each test (Bense et al. 2016).	20
3. 1. Schematic illustration of the model for a single-layer reservoir.....	23
3. 2. Temperature profiles after a shut-in time of 1 day.	29
3. 3. Temperature profiles after a shut-in time of 2 days.....	29
3. 4. Analytically and numerically calculated sandface temperature during the warmback period.	29
3. 5. Application of the graphical techniques for: (a) layer 1, (b) layer 5, and (c) layer 9.	30
3. 6. Graphical illustration of the injection rate distribution among the injection layers.	31
3. 7. Bottomhole flow rate during the shut-in period at different wellbore storage coefficients.....	32
3. 8. (a) Analytically and numerically calculated sandface temperature during the warmback period considering fluid after-flow, (b) application of the graphical technique to the observed sandface temperature data.....	33
3. 9. (a) Reservoir thermal conductivity range, (b) estimated injection rate, and (c) estimation errors.....	33
3. 10. Effect of injection rate and injection zone thickness on temperature recovery with/without considering heat gain from the surrounding strata.	35
3. 11. Temperature profile during the injection period ($t = 0.5$ days) considering different heat transfer mechanisms (heat conduction, heat advection, and heat gain from the surrounding strata) (Case 1).....	35

3. 12. Schematic illustration of the conceptual model for a single-layer reservoir.	36
3. 13. Schematic illustration of the conceptual model for a multilayer reservoir.	39
3. 14. The temperature profiles in the reservoir during the warmback period after: (a) 2 days, (b) 3 days.	45
3. 15. Analytically and numerically calculated sandface temperature during the shut-in period.	46
3. 16. Application of the first graphical technique to the numerical results.	46
3. 17. Application of the second graphical technique to the numerical results.	47
4.1. Rate and temperature history during the injection and shut-in periods.	49
4. 2. Flow chart of the solution procedure using the semi-analytical solution for injection under variable-rate and variable-temperature and the subsequent warmback period.	57
4. 3. Injection rate and injection temperature history during the injection period (Case 1).	60
4. 4. Temperature profile during the injection period (a and b) and the shut-in period (c and d) for the uppermost layer and lowermost layer, respectively (Case 1).	61
4. 5. Sandface temperature recovery during the warmback period at the injection layers (Case 1).	62
4. 6. Injection rate and injection temperature history during the injection period (Case 2).	62
4. 7. Temperature profile during the injection period (a and b) and the shut-in period (c and d) for the uppermost layer and lowermost layer, respectively (Case 2).	63
4. 8. Sandface temperature recovery during the warmback period at the injection zones (Case 2).	64
4. 9. Application of the graphical technique to the observed sandface temperature data of (a) Case 1, and (b) Case 2.	65
4. 10. Regression analysis results for Case 2: (a) Injection profile estimation (b) solution progress during the regression analysis.	65
5. 1. Schematic illustration of the conceptual model showing a horizontal injection well completed through an injection zone which is sandwiched between an impermeable cap and bed strata.	68
5. 2. Type curves for sandface temperature solution at $t_{Dinj} = 0.01$	74

5. 3. Temperature profile during the injection period for (a) 1st interval, (b) 3rd interval, and (c) 5th interval.	76
5. 4. Visual illustration of thermal fronts propagation at end of the injection period.....	77
5. 5. Sandface temperature recovery during the shut-in period.	77
5. 6. Visual illustration of temperature warmback along the lateral of the horizontal well.....	77
5. 7. Application of the inversion procedure on 1st interval.....	78
5. 8. Application of the inversion procedure on 5th interval.	78
6. 1. Schematic illustration of a horizontal with multiple transverse fractures.....	80
6. 2. Schematic illustration of the problem showing the study domain (one quarter of the transverse fracture).....	82
6. 3. Type curves of sandface temperature during the warmback period.	85
6. 4. Temperature profile in (a) the fracture plane and (b) the surrounding matrix during the warmback period (Case 1).	90
6. 5. Analytically and numerically calculated temperature at the perforation during the warmback period (Case 1).	91
6. 6. 3D map showing a spatiotemporal temperature evolution in (a) the fracture plane and (b) the surrounding matrix during the warmback period (Case 1).....	91
6. 7. Temperature profile in (a) the fracture plane and (b) the surrounding matrix during the warmback period (Case 2).	92
6. 8. Analytically and numerically calculated sandface temperature at perforations during the warmback period (Case 2).	92
6. 9. 3D map of a spatiotemporal temperature evolution in (a) the fracture plane and (b) the surrounding matrix during the warmback period (Case 2).	93
6. 10. Solution fitness progress during the optimization process: (a) Case 1 (b) Case 2.....	94
6. 11. Type-curve matching of sandface temperature results: (a) Case 1, (b) Case 2.....	95
6. 12. Application of late-time graphical interpretation technique: (a) Case 1, (b) Case 2.	95
7. 1. Schematic illustration of the physical model for a single-layer reservoir.	97
7. 2. Schematic illustration of the three-region model showing the temperature and saturation profiles at the end of the injection period as obtained from Bratvold and Horne (1989)'s solution.	101

7. 3. (a) fg-Sg plots with the characteristic curves (b) slopes of the fractional flow curves along with the saturation solution in terms of the similarity variable defined by Eq. G.9.....	106
7. 4. (a) Transient temperature profile at the end of the injection period (b) transient temperature profile during the warmback period obtained using TOUGH3 and the three-region analytical solution (layer 1).....	107
7. 5. Transient sandface temperature during the warmback period obtained using TOUGH3 and the three-region analytical solution.....	108
7. 6. Application of the graphical technique for the numerical sandface temperature data.....	109
8. 1. Schematic illustration of the downhole electrical heater: (a) In the first scenario, the heater constitutes a thermal coil that is shielded in a conductive housing (b) in the second scenario, the thermal coil is wrapped around a deployed tubing. In both scenarios, the fiber optic cable is wrapped around the heater/tubing to increase the resolution of temperature measurements.	112
8. 2. Temperature (left) and velocity (right) evolutions in the flow stream around the heating source for the single-phase CO ₂ case described in the Application section.....	114
8. 3. (a) Brine and CO ₂ mass flow rate and (b) pressure and CO ₂ saturation at the monitoring well during CO ₂ injection in deep saline aquifer.....	116
8. 4. Schematic illustration of the numerical model in COMSOL Multiphysics platform showing: (a) grid discretization (b) boundary conditions.....	117
8. 5. Temperature results of the downhole heater using COMSOL Multiphysics simulation tool and Churchill and Bernstein (1977)'s correlation at external fluid velocity of 20 -140 $\mu\text{m/s}$ for a single-phase brine scenario (shown in black color) and a single-phase CO ₂ scenario (shown in red color).....	118
8. 6. (a) Average surface temperature versus electrical power for 10 different heat pulses (b) estimated fluid velocity obtained using Churchill and Bernstein (1977)'s correlation compared with those obtained numerically for 10 different heat pulses for single-phase brine and single-phase CO ₂ scenarios.	119
8. 7. Heater temperature for flowing fluid velocity = 80 $\mu\text{m/s}$ during CO ₂ arrival at different CO ₂ saturations.....	120
8. 8. Velocity evolution in the borehole and the surrounding formation (single-phase brine).....	122
8. 9. Transient evolution of downhole heater temperature after the heater is switched on at different: (a) fluid velocity, and (b) heater diameter (single-phase brine).....	123

8. 10. (a) Stabilized temperature and (b) estimated velocity versus flow inclination for single-phase brine and single-phase CO ₂ cases.....	124
8. 11. Description of the problem: (a) Schematic illustrating a CO ₂ plume, injection well, and monitoring well (b) schematic cross section showing the A-DTS cable as a heating source with indication of fluid flow across the cable and (c) schematic cross-section showing the scenario in which the heating source is deployed inside the monitoring well. In this case, the heating source constitutes a deployed tubing over which a heating cable is wrapped, and the monitoring DTS cable is cemented behind the casing at the cement/formation interface.	126
8. 12. Schematic illustration of the numerical model showing: (a) storage aquifer and the high permeability streak with indication of the injection well and the A-DTS cable (b) grid discretization.	133
8. 13. Relative permeability curves constructed using Corey's model (Corey 1954) and CO ₂ fractional flow curve.	133
8. 14. Total velocity, CO ₂ velocity, CO ₂ saturation, and temperature evolutions during the heat pulse tests.	135
8. 15. Temperature buildup during the heat pulse test (before CO ₂ arrival).....	136
8. 16. Temperature buildup during the heat pulse test (before and after CO ₂ arrival).....	138
9. 1. (a) Schematic diagram of the 2D radial model showing the locations of the injection and observation wells (b) logarithmic discretization of the 2D symmetric radial model.....	140
9. 2. (a) Pressure and temperature (b) mutual solubility (c) CO ₂ saturation profiles in the aquifer after 5 year of CO ₂ injection for a closed reservoir at different sizes ($r_e = 5 - 100$ km) and an open reservoir model at $z = 5$ m.	144
9. 3. Pressure and temperature measurements at the observation wells for an infinite-acting (left) and a closed reservoir case ($r_e = 5$ km) (right) at $z = 5$ m (solid line represents pressure and dashed line represents temperature).	146
9. 4. Multilevel CO ₂ saturation and temperature results for an infinite-acting (left) and a closed reservoir ($r_e = 5$ km) (right) model at OW1 (a - b), OW2 (c - d), and OW3 (e - f) (solid line represents CO ₂ saturation and dashed line represents temperature) (OW = Observation well).....	147
9. 5. CO ₂ saturation evolution during CO ₂ propagation in the reservoir (an infinite-acting reservoir).....	148
9. 6. Evolution of relative permeability to gas phase during CO ₂ injection (an infinite-acting reservoir).	149

9. 7. CO ₂ injection rate, pressure, and temperature at OW3 (r = 100 m) and z = 5 m for a closed reservoir (a and b) and an infinite-acting reservoir (c and d) case.	150
9. 8. Temperature and saturation results obtained at OW1 at different levels inside the wellbore (solid lines) and behind the casing (dash lines) using an infinite-acting reservoir model (OW = Observation well).	151
9. 9. Temperature and saturation results obtained at OW1 at z = 5 m in an infinite-acting reservoir with different formation porosity. Temperature results are shown in solid lines, while the saturation results are shown in dashed lines (OW = Observation well).	152
9. 10. Schematic illustration of the conceptual model showing the locations of injection and abandoned wells.	154
9. 11. CO ₂ plume propagation in the storage aquifer at t = 1, 5, 10, and 15 days.	156
9. 12. Pressure evolution in the storage aquifer at t = 1, 5, 10, and 15 days.	156
9. 13. Gas mass flow rate, liquid mass flow rate, gas velocity, and liquid velocity in the abandoned wellbore at different depths (open wellbore case).	157
9. 14. (a) Pressure (MPa), (b) temperature (oC), (c) CO ₂ saturation (fraction), and (d) CO ₂ solubility in brine (mass fraction) in the wellbore for total simulation time of 28 days at different depths (open wellbore).	158
9. 15. CO ₂ and brine mass flow rate in the abandoned well showing a counter flow at the CO ₂ arrival time (closed wellbore case).	160
9. 16. (a) Pressure (MPa), (b) temperature (oC), (c) CO ₂ saturation (fraction), and (d) CO ₂ solubility in brine (mass fraction) in the abandoned well at different depths (closed wellbore).	161
9. 17. Pressure evolution inside the wellbore during CO ₂ migration in a closed abandoned well.	162
A. 1. Bottomhole temperature behavior during a short-term injection at different injection rates (q = 2000, 1000, 500, and 250 bbl/day).	171
A. 2. Bottomhole flow rate during/following a short-term injection for different wellbore storage coefficients: (a) injection period (b) shut in period.	172
A. 3. Bottomhole temperature shortly after a short-term injection with/without considering the thermal wellbore storage.	172

Abstract

Reservoir monitoring is a key factor in the management of oil and gas resources. With the recent developments of permanent downhole temperature monitoring tools such as Fiber-Optic Distributed Temperature Sensing (FO-DTS), temperature transient analysis has evolved as a new alternative for reservoir monitoring. In this work, different techniques of temperature data analysis are presented for monitoring and characterization of hydrocarbon and geologic carbon storage (GCS) reservoirs. The objective of this study is to present new approaches that enable monitoring injection profile through vertical and horizontal injection wells using temperature warmback analysis. Application of temperature warmback analysis is also extended for diagnosis of hydraulic fracture treatments in unconventional reservoirs. In the context of GCS, the applications of passive and active temperature monitoring to track CO₂ migration through storage aquifers and improperly abandoned wells are presented.

To achieve the objectives of this study, novel analytical models are presented to describe the temperature evolution during and shortly after non-isothermal fluid injection operations. The analytical models are developed through solving heat and mass conservation equations in the reservoir after making relevant assumptions using different mathematical techniques. Inversion procedures are presented accordingly to enable estimating injection flow profile through injection wells using graphical techniques and regression analysis. The validity of the analytical solutions and the inversion techniques is demonstrated through validating the analytical results with those obtained from commercial simulation tools during forward and inverse modeling. Different scenarios are presented that cover the possible operating conditions, different injection well types, and different injection applications.

To monitor CO₂ migration in storage aquifers, two approaches are presented using passive and active temperature monitoring. Passive temperature monitoring is implemented to track CO₂ plume migration in the subsurface and CO₂ migration to the surface via improperly abandoned wells. Active temperature monitoring is implemented through in-well and formation heat pulse testing at monitoring wells to track CO₂ migration in a storage aquifer. New graphical interpretation techniques are presented for estimating individual phase velocity, CO₂ saturation, subsurface thermal properties, and detecting CO₂ arrival through analyzing the transient temperature signal obtained over the monitoring interval during the heat pulse testing.

Chapter 1. Introduction

1.1. Background and Research Motivations

Reservoir monitoring is one of the key factors in the management of oil and gas resources. It provides industry experts with the information required to maximize oil recovery in applications such as Improved oil recovery (IOR) and Enhanced Oil Recovery (EOR). Reservoir monitoring can be used to record changes in fluid saturation, measure the location of the injected fluid in the reservoir, and subsequently predict future distribution of the injected fluids. Besides, monitoring the conformance of the injected fluid is crucial to assess and predict the effectiveness of the injection method. Maintaining a uniform injection profile over the injection zones is required during injection operations to improve the displacement efficiency, enhance the ultimate oil recovery, and avoid premature breakthrough.

Reservoir monitoring is not only restricted to the oil and gas industry, but it is also important to dictate the success of other applications such as Geological CO₂ Storage (GCS). Recently, GCS has become a prominent proposal for mitigating global warming by injecting anthropogenic CO₂ into geologic storage reservoirs, thus achieving long-term isolation from the atmosphere. Monitoring CO₂ plume in the target reservoir is important to track CO₂ migration in the subsurface and identify CO₂ leakage to the surface. Different techniques are available to monitor fluid flow dynamics through reservoirs, such as geophysical logging, seismic monitoring, geochemistry monitoring, and pressure testing. Each method has its own advantages and disadvantages. Some of them are tailored for specific applications, while others can be used for general monitoring purposes. Monitoring fluid dynamics through injection wells is doable using logging methods such as injection logging tools (ILTs). However, the limitations for their deployment, especially for deep and inclined wells, and the limited range of the flow rates that they can measure make them inefficient in specific applications. Additionally, they are relatively expensive and pose a deferment to injection activity.

Until recently, temperature monitoring has been used for limited monitoring applications such as identifying entry and exit points through production and injection wells, respectively and identifying the potential for wellbore leakage. It was recently, when temperature monitoring evolved as a promising technique for reservoir monitoring and characterization. The recent advances in permanent downhole monitoring tools such as fiber optic Distributed Temperature Sensing, make real-time temperature measurements along the wellbore available with high accuracy and resolution. Additionally, DTS tools have the flexibility to be installed in wells, permanently, semi-permanently, or retrievably and, they can be deployed via tubing inside the wellbore or cemented behind the casing.

Given the capabilities of the new evolved temperature monitoring techniques, different temperature interpretation methods have been developed to qualitatively/quantitatively allocate injection flow rate along injection wells during water flooding and/or EOR processes. Those techniques include thermal wave front analysis, storage analysis, and warmback analysis. Temperature warmback analysis is widely used to quantify injection profile using temperature data obtained shortly after injection stops. The rate of temperature recovery over the injection interval during the shut-in period reveals important information about the injection profile and the effectiveness of the completion design. Layers that accept most of the injected fluid exhibit a lag in temperature recovery compared with those which admit a smaller amount of the injected

fluid. Besides, the established temperature signal provides a reliable indication for the effectiveness of the isolation between the completed zones and each other. Compared with the other techniques, warmback analysis has the potential to isolate the intervention effects of fluid flow inside the wellbore because it is performed during the shut-in period. Throughout this dissertation, we will investigate the feasibility of analyzing temperature data obtained during the warmback period using novel graphical interpretation techniques to allocate flow rate through injection zones. Different scenarios will be studied including different injection well types (vertical versus horizontal), complex operating conditions, and different injection applications.

Applications of temperature transient analysis (TTA) have been extended to unconventional reservoirs which are subjected to stimulation by hydraulic fracturing. Multi-stage fractured horizontal wells have widely been used to develop complex oil and gas resources such as shale gas and shale oil. Monitoring temperature along multi-stage fractured horizontal wells is used to identify fractures' locations, infer injection rate distribution among the fractures, investigate the degree of stages isolation, and identify the geometry and propagation of the created fractures. Temperature warmback analysis can effectively be used to diagnose fracture treatments. Perforated regions exhibit lag in temperature recovery compared with cased intervals. Consequently, the established temperature contrast along the lateral of the horizontal well during the warmback period provides reliable indication for the locations of fracture initiation and size of created fracture clusters. Additionally, rate of temperature buildup during the shut-in period that follows the stimulation treatment can reveal important information about fracture dimensions, fracture propagation, and thermal properties of the adjacent matrix. As such, we will investigate the possibility of analyzing the temperature data obtained along the lateral of MFHWs during the warmback period to obtain characteristic information about the created transverse fractures.

In the context of geologic carbon storage, temperature monitoring has been used as a means to monitor CO₂ plume migration in underground storage reservoirs. For static field applications, temperature profile along observation wells can be used to locate CO₂ storage intervals. Reduction of thermal conductivity of the storage reservoir due to CO₂ content of porous medium implies a thermal blanket effect for the formations located at the bottom of the storage reservoir. This results in higher temperature in the storage reservoir compared with the original geothermal temperature. For dynamic field applications, CO₂ injection in saline aquifers results in a warming front that moves contemporaneously with the CO₂ plume. The warming front is generated exclusively due to the exothermic dissolution of CO₂ into the in-situ brine at the plume front. Accordingly, CO₂ plume migration in storage aquifers can be tracked through monitoring the warming front at observation wells. Additionally, temperature monitoring has recently been studied to detect CO₂ migration from the storage reservoir to shallower formations. The hydrothermal processes associated with CO₂ migration such as Joule-Thomson expansion and endothermic exsolution of CO₂ from the flowing brine can result in a significant temperature change which can be monitored to infer CO₂ migration. This motivated our research to investigate the application of temperature monitoring to infer CO₂ migration in the subsurface and through improperly abandoned wells.

In all the studies devoted to showing the applications of temperature monitoring in GCS projects, temperature data was obtained using DTS tools deployed in passive mode. Recently, DTS tools have been deployed in active mode in which the DTS cable can be used as a heating and monitoring tool in applications such as heat pulse testing. Heat pulse testing has been used

widely in hydrology in which heat is introduced to the formation using a distributed heating source, and the corresponding temperature signal is tracked/analyzed to estimate formation fluid flow, in-well fluid flow, and subsurface thermal properties. Heat pulse testing can be used in GCS applications for monitoring CO₂ plume migration in the subsurface given the sensitivity of thermal properties of the porous medium to CO₂ content. In this study, we will investigate the applications of this technique for CO₂ plume monitoring and the capabilities of that technique compared with the traditional monitoring techniques.

1.2. Problem Statement

The problems that will be addressed in this research are:

1. To develop novel forward models to describe temperature evolution in a reservoir during cold fluid injection via vertical and horizontal wells and during a pause of the injection activity. The forward models are developed by solving the energy balance equation in the reservoir during the injection and the subsequent shut-in periods. The methodology used to develop the models is through analytical modelling. Inversion procedures are provided for estimating the injection profile using the observed temperature recovery during the shut-in period. Inversion procedures are presented using graphical techniques such as log-log plot, semi-log plot, and type curves. To prove the validity of the developed solutions, numerical results obtained using a thermal simulation tool are compared with the analytical-based results. Next, the proposed solutions are extended to consider realistic operating conditions (variable bottomhole injection rate and injection temperature) and the implications of heat exchange between the injection zones.
2. Extend the application of temperature warmback analysis to evaluate CO₂ injection profile during CO₂ storage in a deep saline aquifer. In this application, two-phase fluid flow conditions (aqueous brine and gaseous CO₂) are considered while solving the energy and mass conservation equations in the reservoir. A forward model will be developed to describe the temperature evolution during a non-isothermal CO₂ injection and a pause in the injection operation. An inversion procedure is presented accordingly to evaluate the CO₂ injection profile and the extent of CO₂ plume along the injection interval using the temperature recovery obtained during the warmback period.
3. To develop a forward model to simulate temperature evolution during stimulation of unconventional reservoirs using multi-stage fractured horizontal well and the subsequent warmback period. The analytical model will be developed through solving the energy conservation equations for the fracture and the reservoir during the stimulation and post-stimulation periods. Inversion procedure will be introduced using graphical interpretation techniques to estimate the created fracture characteristics such as fracture half-length and fracture width using temperature recovery observed during the warmback period.
4. To study the feasibility of using passive temperature monitoring to track subsurface CO₂ migration in a storage aquifer during geologic CO₂ storage. A thermal compositional simulation tool will be used for the modeling study. A wellbore model will be added to the system to enable analysis of measurements out of the target zone. Besides, CO₂ migration through improperly abandoned wells will be studied using a coupled wellbore-reservoir model to investigate temperature and pressure evolutions during CO₂ migration through the wellbore. The objective of the study is to show the feasibility of monitoring

CO₂ migration through abandoned wells using surface pressure and temperature measurements.

5. To study the applications of in-well and formation heat pulse testing at a monitoring well to track CO₂ plume migration in a storage aquifer during geologic CO₂ storage. Analytical models are developed to model temperature evolution during heat pulse testing considering the two-phase flow conditions encountered during CO₂ storage in deep saline aquifers. Graphical interpretation techniques are developed accordingly to estimate subsurface fluid velocity, fluid saturation, and thermal properties of the host formation.

1.3. Modeling Approaches

Two modeling approaches are adopted to achieve the objectives of this study, which are analytical and numerical modeling. In this section, the mathematical tools and numerical models used in this study are introduced.

1.3.1. Analytical Model

Analytical modeling is the primary technique to be used in this work to solve heat and mass conservation equations during fluid flow in porous medium. The solution procedure implies using mathematical tools such as: integral transformation using Hankel transform, Laplace transform, double Laplace transform, and Fourier transform that enable simplifying initial-boundary value problems into simpler problems in the transformed domain. Analytical modeling is fast and relatively easy compared with numerical models that require spatial and temporal discretization of the governing equations, which in turn render that technique computationally expensive and time consuming. Analytical modeling also helps to gain better insight on the physics of the problem to be solved through explicitly relating the parameters affecting heat transport in porous medium with the established temperature signal. Additionally, analytical models can be casted into simple graphical techniques that provide an easy and stable inversion procedure compared with inverse modeling using numerical models, which can be time consuming and highly non-unique.

In some problems, a semi-analytical approach may be used which involves numerical discretization of a single independent parameter (e.g., time) to obtain a solution to the problem. In this case, regression analysis is adopted as an inversion technique which iterates on independent variables that reproduce the observed temperature signal.

1.3.2. Numerical Model

Numerical models are widely considered reliable methods to solve complex physical problems given the computation and memory storage capabilities of modern machines. In these models, governing equations (such as heat, mass, and momentum) are solved through spatial and temporal discretization of the system under consideration. Different discretization approaches are available, such as finite difference, finite element, and finite volume. This approach transformed the governing equations into a system of algebraic equations for the discretized regions of the given system. Next, algebraic solvers are used to solve the resulting system of equations for primary variables such as pressure, temperature, saturations of flowing phases, and

concentrations of chemical species. Numerical models are widely used because they can solve complicated physical problems with no restricted assumptions. On the other hand, their solution procedure may be computationally expensive and time consuming.

In this work, CMG-STARS (2020) is used while modeling heat transport through porous media for single-phase and two-phase flow problems. CMG-STARS (2020) solves coupled mass and energy conservation equations using finite difference method. This numerical model is used while solving the research problems 1, 3, and 5. While solving the research problems 2 and 4, TOUGH3/ECO2N is adopted, which is a numerical simulator capable of simulating nonisothermal multiphase and multicomponent fluid flow in porous medium (Jung et al. 2018). TOUGH3 solves the coupled energy and heat transport equations in the porous medium using finite element method. ECO2N is a fluid property module used in the TOUGH3, which evaluates the thermophysical properties of brine and CO₂ mixture for pressure up to 600 bar, temperature range from 10 °C to 300 °C, and salinity up to full halite saturation (Pruess 2005). The experimentally calibrated correlations implemented in ECO2N make TOUGH3 more efficient while modeling CO₂ flow through porous medium. T2Well/ECO2 simulation tool is used while modeling mass and heat transport through wellbore system. This tool extends the numerical reservoir simulator TOUGH2, to model fluid flow in both wellbore and reservoir (Pan et al. 2011). T2Well is used while solving problem 4. Finally, COMSOL (2018) which is a general purpose finite element simulation tool is used while modeling heat and fluid transport in wellbore during in-well heat pulse testing in research problem 5.

1.4. Overview of Chapters

In this section, an overview of the upcoming chapters in this dissertation is presented.

Chapter 2 introduces a comprehensive literature review on the research state of the topics addressed in the subsequent chapters. It includes the developments of downhole temperature monitoring tools and their capabilities compared with the traditional monitoring techniques. It also presents the contributions of the previous studies on the applications of temperature warmback analysis for estimating injection profile and diagnosing hydraulic fracture treatments and their shortcomings. Additionally, a literature review is presented on the applications of passive and active temperature monitoring for tracking CO₂ plume migration in the subsurface and detecting CO₂ leakage to the surface.

Chapter 3 introduces the development of novel forward models that describe temperature evolution in a reservoir during non-isothermal fluid injection via a vertical well and during a pause in the injection activity. The developed models allow predicting temperature recovery at injection well during the warmback period considering different mechanisms of heat transport in porous medium such as heat transfer by conduction, advection, and heat exchange with the surrounding strata. Novel graphical interpretation techniques are presented to estimate the injection profile using the observed temperature recovery.

Chapter 4 extends the previously developed forward model to consider complex operating conditions such as injection with constant injection rate - variable bottomhole injection temperature and variable injection rate - variable bottomhole injection temperature. Besides, the implications of deploying temperature monitoring tool within the wellbore are considered through considering heat transfer inside the wellbore system while developing the forward

models. Novel graphical interpretation techniques are presented accordingly to enable estimating the injection profile using the observed temperature recovery.

Chapter 5 shows the application of temperature warmback analysis for estimating injection profile through a horizontal well. In this chapter, novel forward models are presented to describe temperature evolution during non-isothermal fluid injection and during a pause of the injection operation. The analytical models solve heat transport equations assuming linear fluid and heat transport regimes in the reservoir. The developed solution is presented graphically in the form of appropriate type curves. A novel inversion procedure is introduced to estimate injection profile along the lateral of the horizontal well through type curve matching of observed temperature data.

Chapter 6 shows the application of temperature warmback analysis for allocating CO₂ injection rate and extent of CO₂ plume propagation along injection well during GCS application. In this work, the heat and mass conservation equations are solved simultaneously during the injection and shut-in periods considering two-phase (aqueous brine and gaseous CO₂) flow in the storage reservoir. The resulting heat transport equation is non-linear because of the dependency of coefficients (fractional flow of CO₂ and brine) on temperature. A novel forward model is presented to solve for temperature in which the aquifer is discretized into small regions and the corresponding energy balance equations are solved simultaneously considering appropriate boundary conditions at the interfaces. Inversion procedure is presented using graphical interpretation technique to estimate the injection profile and the extent of CO₂ plume propagation along the injection well.

Chapter 7 presents the application of temperature warmback analysis for characterizing hydraulic fracture treatments in unconventional hydrocarbon reservoirs. The analytical solutions are developed through solving heat transport in the fracture system and the surrounding impermeable matrix during the stimulation and post-stimulation. The late-time asymptotic solution of the developed solution is casted into a simple graphical technique that enables estimating fracture dimensions such as fracture width and fracture half-length using the observed temperature recovery.

Chapter 8 presents the application of in-well and formation heat pulse testing to monitor CO₂ plume migration in a storage aquifer. A new approach is presented to estimate subsurface fluid velocity and detect CO₂ arrival at a monitoring well during in-well heat pulse testing. In the formation heat pulse testing, new graphical interpretation techniques are presented that can provide spatial estimates of CO₂ saturation, individual phase velocity, and subsurface thermal properties along a monitoring well using temperature data obtained during the heating period.

Chapter 9 shows the feasibility of using passive temperature monitoring for tracking CO₂ plume migration through storage aquifers and CO₂ migration through improperly abandoned wells. Passive temperature monitoring implies monitoring temperature using DTS cable deployed as a monitoring tool at monitoring or abandoned wells. A sensitivity analysis is presented to investigate the potential effects of aquifer's outer boundary conditions, injection history, level, and location of the temperature monitoring tool on the established temperature signal. Additionally, a coupled wellbore-reservoir system is used to study CO₂ migration from a storage aquifer via an improperly abandoned well for two scenarios: open and closed wellbore at the surface. This study aims at investigating the feasibility of using surface pressure and temperature monitoring to detect CO₂ migration.

Finally, conclusions and recommendations for future work are presented in *Chapter 10*.

Chapter 2. Literature Review

2.1. Advances in Downhole Temperature Monitoring Tools

Temperature logging has long been used for different applications in the oil and gas industry, such as evaluating cement top, indicating wellbore leakage, and identifying exit and entry points in injection and production wells, respectively. Temperature logging was performed using a variety of sensors including temperature-sensitive resistors, thermistors, and diodes. Those instruments are deployed at discrete locations within injection and production wells. They are delicate instruments easily damaged by abuse and provide temperature measurements with poor accuracy and resolutions (Bateman 1985). Over the last decades, temperature monitoring tools have undergone significant technological improvements which have widened their applications. The recent advanced downhole temperature monitoring tools such as: fiber-optic Distributed Temperature Sensing and Fiber Bragg grating can provide real-time continuous measurements of temperature with high spatiotemporal resolution and decent accuracy. In addition, fiber optic cables are immune to electromagnetic noise, corrosion, and high pressure and temperature conditions (Edouard et al. 2022).

DTS instrumentation was first introduced in the 1980s, and they can provide temperature data with spatial resolution down to a few centimeters, temporal resolution as short as 1 s, and accuracy on the order of 0.01 °C (Bense et al. 2016). They can be deployed in wells up to several kilometers deep. Operation of DTS tool involves using a laser to launch short pulses of light into the fiber optic cable and monitoring the backscattered light. The scattered light involves three spectrums: Rayleigh, Raman, and Brillouin. Raman scattering is responsible for temperature measurements along the entire length of the fiber-optic cable. Raman backscattered light involves two bands based on the energy of the backscattered light, which are Stokes and anti-Stokes. Stokes scattering occurs when the material absorbs the energy of the incident light and as such the scattered light has lower energy (higher wavelength) compared with the incident light (see Fig. 2.1). On the other hand, anti-Stokes scattering occurs due to energy lost from the material and as such resulting in light with higher energy than the incident light. While Stokes Raman scattering is temperature independent, the intensity of the anti-Stokes Raman scattering increases with increasing temperature. Consequently, the ratio of the anti-Stokes to Stokes Raman light intensities is used to estimate the absolute temperature, while the location of the backscattering point is determinable from the two-way travel time of the incident and the backscattering signal (Edouard et al. 2022).

Given the capabilities of fiber-optic tools, they are recently used in many monitoring applications in the oil and gas industry, such as monitoring well integrity, flow profiling, fracture initiation and propagation, sand production, and enhanced oil recovery (Ranjan and McColpin 2013, Ashry et al. 2022). Compared with pressure monitoring, temperature measurements are independent of many reservoir parameters such as injection/production history, reservoir boundary conditions, and overall system properties. Consequently, temperature monitoring can effectively be used to estimate individual layers properties which may be challenging using pressure monitoring, allocating flow rate distribution through injection and production wells given the higher accuracy and longer coverage of temperature measurements compared with pressure measurements, and detecting fluid leakage and identifying the type of leaking fluids given the sensitivity of temperature signal to the type of leaking fluids. In the context of GCS,

temperature monitoring has been extensively studied as a promising technique for detecting CO₂ arrival at monitoring wells. Unlike pressure, temperature monitoring can effectively detect CO₂ arrival through identifying the temperature heating signal established at the CO₂ plume front that is generated by CO₂ dissolution into the in-situ brine. In the next section, a detailed literature review is presented showing the state of research on applications of temperature analysis for reservoir monitoring and characterization.

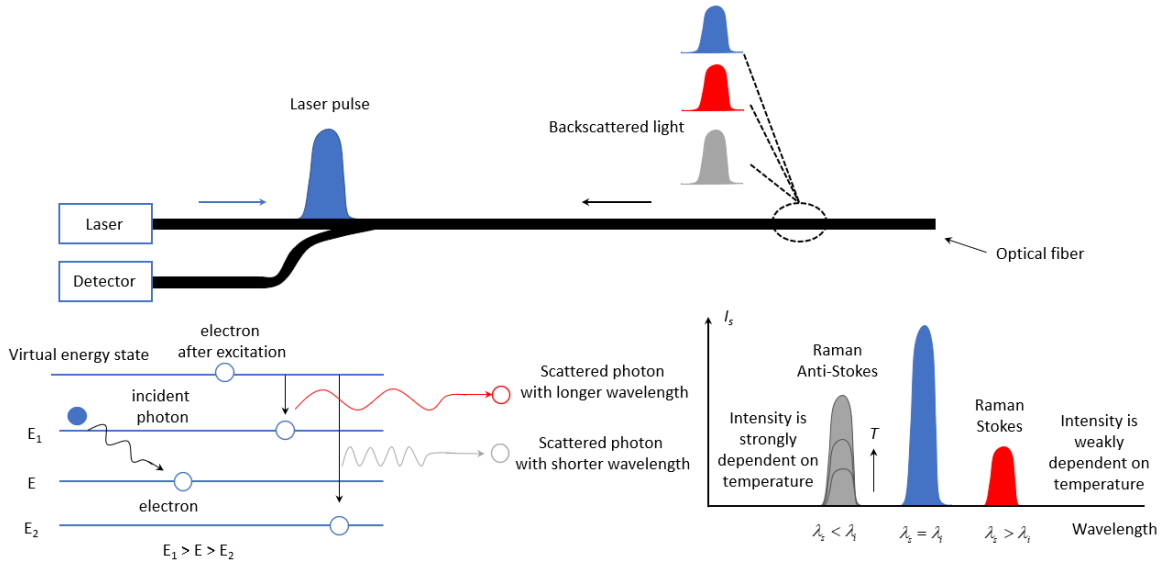


Figure 2. 1. Backscattered light spectrum generated from a typical fiber optic DTS tool.

2.2. Temperature Warmback Analysis Applications for Conventional Reservoirs

Fluid injection operations are encountered in many applications during reservoir lifetime, such as Improved Oil Recovery (IOR) and Enhanced Oil Recovery (EOR). To maximize oil recovery during IOR and EOR, the contact area between the injected fluid and reservoir fluids should be maximized. The degree of reservoir coverage by the injected fluid is known as sweep efficiency, and it depends on many factors, among of which is the injection profile (Smith and Cobb 1997). During fluid injection into stratified and heterogeneous reservoirs, injected fluid often moves into preferential flow paths such as high permeability streaks or thief zones and bypasses the remaining oil in the reservoir. Consequently, improper fluid displacement is established which results in premature breakthrough and lower oil recovery. To improve the sweep efficiency, the injection profile at the injection wells should be maintained uniform through the injection zones. Accordingly, monitoring injection profile is important to identify thief zones and to allow remedial actions to be taken either to plug the thief zones or to re-perforate plugged perforations.

Using temperature measurements to evaluate the flow profile in injection well is not new; it was first introduced by Nowak (1953). The feasibility of using temperature measurements to infer injection profile increased significantly due to the recent developments of fiber optic DTS tools. Different interpretation techniques are adopted in the industry to evaluate injection profile and assess the effectiveness of the injection method using temperature data obtained during the injection and warmback period (Brown et al. 2003, Bui and Jalali 2004, Foo et al. 2014, Brown

et al. 2004, Pimenov et al. 2005). Storage analysis is a temperature data interpretation technique in which the temperature data acquired during injection and shut-in periods are plotted in a space-time plot, called a “Waterfall” chart (Shirdel et al. 2019). During non-isothermal fluid injection (e.g., water flooding), the temperature of the swept region cools down due to the temperature contrast between the initial reservoir temperature and the injected fluid temperature. Although injected fluid heats up as it flows down the well, it is still significantly cooler than reservoir. When injection terminates, the temperature of the swept region warms back due to heat transfer from unswept regions (with undisturbed initial temperature) to swept regions of lower temperature. Rate of temperature recovery differs along wellbore depending on the relative amount of cold fluid injected per zone. Zones with high injectivity admit a higher percentage of the injected fluid and consequently exhibit slower warmback rates. Meanwhile, zones with low injectivity admit a lower percentage of the injected fluid and consequently exhibit higher warmback rates (see Fig. 2.2). Based on that, visual inspection of the temperature map can help to identify zones with cooler temperature, which have high injectivity and zones with higher temperature, which have lower injectivity (Foo et al. 2014). This technique provides qualitative indication of the injection profile over the injection interval. Besides it helps to assess the wellbore integrity.

Wavefront analysis is a temperature data interpretation technique in which a non-isothermal slug of fluid is injected inside the wellbore, and the temperature profile along the wellbore is monitored during the injection period. Temperature data are inspected to locate the non-isothermal slug given the pronounced contrast between the slug’s temperature and the ambient temperature. Tracking the thermal plume established by the injected slug helps to estimate the slug velocity and the established flow rate given the size of the injection tubing / casing (van der Horst 2015). To avoid the necessity of non-isothermal slug injection, injection may stop to allow wellbore fluid to warmback. Different temperature warmback rates over the injection zones create intervals with a pronounced temperature contrast which can be tracked to estimate the injection profile during the injection period. The shortcoming of this technique is attributed to the lack of tubing size details along the wellbore. Additionally, the established wavefront should be distinct (i.e., have a high-temperature contrast) and travel for a measurable distance (Foo et al. 2014).

Warmback analysis is a temperature interpretation technique which is adopted to quantify injection profile using temperature recovery data obtained during the shut-in period. In this technique, a regression analysis is used to iterate on the injection profile that reproduces the observed temperature recovery (Foo et al. 2014). Warmback analysis is commonly used because it provides quantitative evaluation of injection profile, and it does not require distinct temperature contrast along the wellbore compared with the wave front technique. Additionally, it has the potential to isolate the thermal effects associated with the fluid flow in wellbore because it is performed during the shut-in period. Different numerical and semi-analytical models are available in the literature which solve mass and energy balance equations in the reservoir to estimate injection profile using temperature data obtained during the warmback period.

Pimenov et al. (2005) developed a semi-analytical model to model the temperature evolution along a horizontal injection well during the injection and the subsequent warmback periods. Their inversion procedure involved iterations on the injection profile to match the observed temperature recovery along the lateral of the horizontal well. Brown et al. (2003) modeled the temperature warmback using a numerical model to infer the injection profile.

However, no details on their numerical model have been reported. Brown et al. (2004) also attempted to model the temperature warmback in order to assess the injection profile during water alternating gas (WAG) injection application through numerical modeling. Bui and Jalali (2004) proposed a semi-analytical technique to evaluate the injection profile along a horizontal well for a short-term injection operation (up to a few hours). The authors used regression analysis to iterate on the radius of the cooled front along the wellbore that reproduces the observed temperature recovery. The analytical solution developed by the authors considers heat propagation in a radial composite geometry around the wellbore and assumes a sharp temperature boundary between the cold and the warm regions. Glasbergen et al. (2009) developed a coupled wellbore-reservoir numerical model to evaluate injection profile along horizontal well during matrix-acid stimulation treatment. They validated their model's results with field data; however, no details on their numerical model were presented. Tabatabaei et al. (2013) developed a coupled wellbore-reservoir numerical model that models temperature evolution along a horizontal well during and shortly after acid stimulation treatment. Their model is developed through solving heat transport equations in the wellbore and the reservoir using a finite difference approach. The authors estimated the injection profile through iterating on the injected fluid distribution that reproduces the observed temperature recovery with the help of least-squares nonlinear regression solvers. Yoshida et al. (2020) presented a field study showing the application of temperature analysis to estimate injection profile through a deviated injection well. In their work, temperature data is acquired using a fiber optic DTS cable, which is deployed via coiled tubing in the deviated well. The authors utilized a numerical simulation tool to iterate on the injection profile that reproduces the observed temperature data at the end of the injection and shut-in periods.

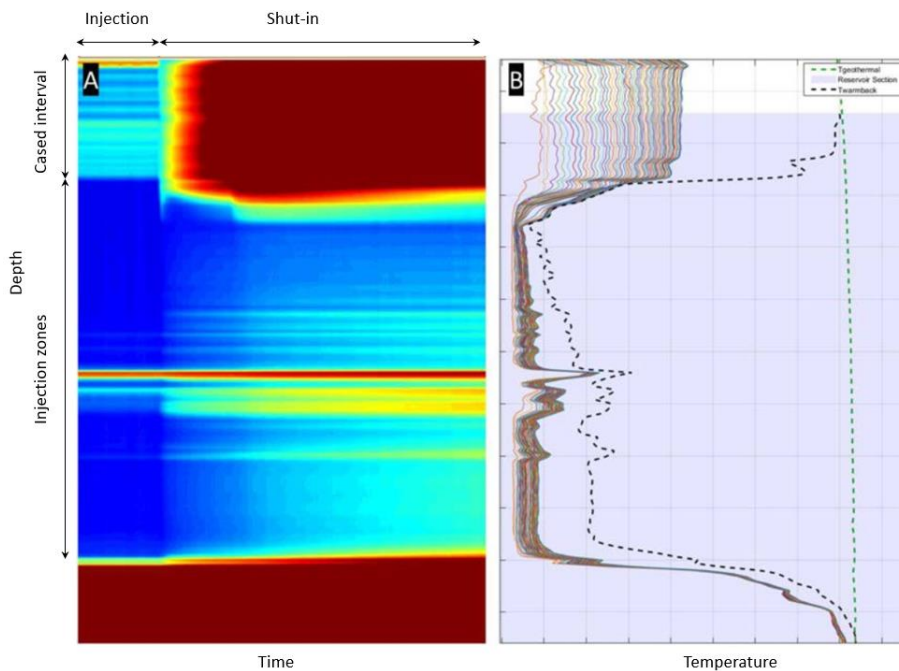


Figure 2. 2. (a) Waterfall chart displaying temperature evolution during injection and warmback periods (b) temperature profiles during shut-in period (shown on solid lines) approaching geothermal temperature gradient (shown on green dashed line) (modified after Sadigov et al. (2021)).

Seabrook et al. (2020) adopted the analytical-based graphical technique developed by Hashish and Zeidouni (2019) to analyze DTS data obtained during acidizing stimulation to investigate the effectiveness of the stimulation treatment. The acidizing treatment is performed on an extended reach horizontal well which is completed with a limited entry liner. The authors used the analytical-based graphical technique to estimate the injection profile along the lateral and estimate the distributed geotherm prior to the acidizing stimulation. The analytical-based graphical technique is shown to “fit very well and be robust to limited prior knowledge of the distributed geotherm”. Additionally, the authors indicated that “this technique should be broadly applicable to the analysis of mature injection wells”. Recently, Mawalkar et al. (2019) presented a field study showing the application of temperature warmback analysis to identify flow distribution over the injection interval during CO₂ injection in deep saline aquifers. The authors analyzed the field temperature data to infer the injection profile and assess the potential for CO₂ migration along the wellbore. Almost all the models that are developed in the previous studies utilized numerical modeling to predict temperature evolution during the injection and warmback periods. These models require complicated procedures during forward modeling, inverse modeling, or both. Their inversion techniques can be time-consuming and highly non-unique (Tabatabaei et al. 2013). Consequently, new forward analytical modeling is required to enable modeling temperature evolution during and shortly after injection operations. Besides, a simple inversion technique is required that can provide an easy and stable procedure for estimating injection profile using the observed temperature data.

2.3. Temperature Warmback Analysis Applications for Unconventional Reservoirs

Horizontal wells with multi-stage fractures have widely been used to develop complex oil and gas resources such as shale gas and shale oil. Monitoring and diagnosis of fracture treatments are essential to dictate the success of the fracture treatments. Diagnosis of the fracture treatment involves identifying fracture initiation along the lateral of horizontal well, evaluating injected fluid distribution among the fracture stages, assessing the degree of isolation between fracture stages, and characterizing the geometry of the created fractures (Li and Zhu 2018).

In unconventional reservoirs, temperature monitoring during hydraulic fracturing, during warmback period, and during flowback period are adopted to evaluate the effectiveness and the geometry of the created fractures. There are two categories of models that are developed to describe the transient temperature during reservoir stimulation by fracturing. The first category models are fully analytical that describe the transient temperature during fracture propagation (injection period) (Wheeler 1969, Whitsitt and Dysart 1970, Sinclair 1971, Biot et al. 1987, Meyer 1989). These solutions were mainly developed to describe temperature dependence of the rheological properties for the injected fluid and its effect on the fracture geometry as well as the effectiveness of the stimulation treatment. The second category is semi-analytical and numerical models, which are used to describe transient temperature behavior during fracture propagation (injection period) and the subsequent warmback period (Seth et al. 2010, Hoang et al. 2011, Li and Zhu 2018). Injection of cold stimulation fluid during fracture propagation cools down the fracture region and the surrounding matrix. After injection stops, temperature in the created fracture warms back due to heat flux from the surroundings. Temperature data observed during the injection period along the lateral can indicate the location of the fractures and the degree of communication between the fracture stages. On the other hand, temperature recovery observed

after injection termination helps to evaluate flow rate distribution among the created fractures and estimate fracture characteristics.

Biot et al. (1987) developed a semi-analytical model to describe the temperature evolution during fracture propagation with leak-off using the variations principle. The authors used 2D fracture propagation model to describe fracture dimensions and leak-off as a function of time. Solving the fracture propagation model along with the thermal model, the temperature distribution in the created fracture is predicted. Seth et al. (2010) introduced a numerical model to describe the temperature evolution during hydraulic fracturing of vertical well and the subsequent warmback period. Their model is established using a fracture propagation model, which is based on a volumetric balance of the injected volume, created fracture volume, and volume of leak-off. Heat transfer is controlled by convection and conduction during fracturing while it is governed by conduction only during the shut-in period. The fracture model coupled with a wellbore thermal model is used to predict temperature in the wellbore, fracture, and surrounding matrix. An inversion procedure is presented to evaluate injection profiling along wellbore using the observed temperature data by a regression technique.

Huckabee (2009) presented a field study showing the potential capabilities of temperature monitoring during injection and shut-in to evaluate the effectiveness of hydraulic fracturing stages. In his study, temperature monitoring is used to evaluate production profiling in stratified reservoirs depleted by commingled production well, estimate the effectiveness of fracturing stimulation in horizontal and vertical wells, and infer injection profile in disposal injectors stimulated by hydraulic fracturing. Ugueto et al. (2019) investigated the near wellbore complexities during hydraulic fracture stimulation, such as induced fractures, tortuosity, and complex fracturing networks using DTS and DAS. In their study, the authors divided the reservoir into three regions according to the distance from the wellbore: the wellbore region, the near wellbore region, and the far-field region. Their diagnosis helps to determine the dimensions of the fractured zone and optimizes the spacing between the perforation clusters. Post-stimulation warmback analysis was adopted in their work to give insight into the size of the fractured zone and the created fractures geometry (longitudinal versus transverse fractures). During the warmback, intervals that contain fractures exhibit warmback lag compared with non-fractured intervals and thereby fractured zone size can be identified. A double peak in the lagging portion of the warmback temperature profile indicates the occurrence of two transverse wings associated with the main longitudinal fracture.

Hoang et al. (2011) developed a numerical model to relate the temperature profile to the injection rate distribution during a multi-zone fracturing process. Their work includes a forward model that is developed by solving mass and energy conservation equations using a finite difference approach to model the temperature profile in the wellbore, created fracture, and the surrounding matrix. The forward model was then integrated with an inverse algorithm to estimate flow rate distribution along the wellbore using the observed temperature data. The authors recommended using the model to obtain the stage's injection rate and the corresponding fracture characteristics for limited entry completion. Li and Zhu (2018) introduced a numerical model that describes the temperature along the wellbore for a multi-stage fractured horizontal well using a fully implicit finite difference approach. The numerical model combines the reservoir, wellbore, and fractures during fracture propagation and shut-in period (warmback). The forward model is coupled with inverse algorithm to estimate the fracture half length, fluid

distribution, and evaluate the effectiveness of the zonal isolation using observed temperature data along the lateral.

Almost all applications of temperature analysis for hydraulic fracturing stimulation are devoted to diagnosing main fracture treatments. However, pre-fracture tests such as Diagnostic Fracture Injection Test (DFIT) can be subjected to temperature analysis to extract valuable information about reservoir and fracture characteristics (Barree et al. 2009, McClure* et al. 2019, Zanganeh et al. 2019). DFIT is a pre-fracture test that involves injection of water at a sufficient injection rate and pressure for a short injection period (few minutes) to create a fracture followed by a shut-in period that can extend from a few days to months. During the injection period, bottom hole pressure builds up quickly to formation breakdown pressure and a bi-wing fracture initiates and propagates throughout the reservoir. After injection stops, pressure inside the fracture decreases due to flow back and a fluid leakoff into the surrounding matrix and consequently the fracture width decreases to virtually zero or a residual fracture width. Almost all the models that analyze warmback temperature data are numerical models which require complex inversion techniques to characterize the created fracture. The available inversion procedures using optimization routines are time consuming and may be highly non-unique. Apart from this, new analytical forward modeling is required to describe temperature evolution in the hydraulic fracture and the surrounding matrix by solving the energy balance equation in the fracture-reservoir system. Inversion procedure using analytical-based graphical technique will be developed which can be simple and straightforward compared with the published techniques. The proposed forward and inverse models will be applied for characterizing hydraulic fractures during hydraulic fracture treatment and diagnostic fracture injection test.

2.4. Monitoring CO₂ Plume Migration during Geologic CO₂ Storage Using Temperature Data

Greenhouse gas emissions caused by human activities such as burning fossil fuels, are believed to be responsible for global warming and the severe consequences of climate change since the industrial revolution. Different solutions have been proposed to mitigate anthropogenic greenhouse gas emissions, such as increasing energy efficiency, switching to renewable energy, or using carbon capture and storage (CCS). Carbon capture and storage is considered the most effective solution for cutting carbon dioxide emissions on a large scale. CCS involves separating carbon dioxide from industrial or other point generation sources, transporting the captured CO₂ to specific sites via pipelines or trucks, and utilizing or storing the captured CO₂, thus achieving a long-term isolation of CO₂ from the atmosphere. The potential candidates for CO₂ storage include underground geological storage, deep ocean storage, and mineral carbonation. Geologic carbon dioxide storage (GCS) is the most viable storage candidate because of the economic aspects, site accessibility (compared with the case of ocean and mineralization storage), and associated concerns regarding the security of stored CO₂ and the negative impacts of mineralization and ocean storage. There are several potential geologic storage options for CO₂ that include saline aquifers, depleted oil and gas reservoirs, hydrate storage of CO₂, unmineable coal seams, basalt formation, enhanced oil recovery using CO₂, and CO₂-based enhanced geothermal systems. By far, geologic CO₂ storage in deep saline aquifers is considered the most feasible GCS storage option, partly because aquifers provide the largest storage capacity (in terms of pore volume). Additionally, they are widely available and they may not be suitable for other synergic and conflicting applications (Aminu et al. 2017). Numerous GCS

projects have been or are being established at different scales worldwide to demonstrate the feasibility and safety of the GCS technology (IEA 2008a, 2008b).

For successful implementation of GCS technology, CO₂ should be injected in supercritical state into deep saline aquifers (deeper than 800 m) that should provide sufficient pore volume for CO₂ storage, high injectivity to accommodate the industrial scale of CO₂ storage, and effective trapping mechanism to maintain the stored CO₂ for long time scale. One of the major risks associated with the implementation of this technology is the potential for CO₂ leakage from the storage reservoir. CO₂ can leak from the storage reservoir to shallower freshwater zones or even back to the atmosphere via different pathways such as transmissive faults or fractures that may be preserved in the cap strata, poorly sealed injection, production, and monitoring wells, and improperly abandoned wells (see Fig. 2.3). CO₂ leakage not only decreases the effectiveness of the GCS technology but also increases the human health risk associated with groundwater contamination.

To assure the containment of the injected CO₂ in the storage reservoir, monitoring is essential before, during, and after CO₂ injection. Pre-storage monitoring is required to evaluate the feasibility of the target reservoir for CO₂ storage, the integrity of the structural cap rock, and to establish a baseline for future monitoring. During- and after-storage monitoring is essential to track CO₂ plume migration and identify CO₂ leakage (if exists) (Zeidouni 2011). Different techniques are available for CO₂ monitoring in the GCS industry, such as pressure and temperature monitoring, surface and borehole seismic technologies, geophysical logging, and geochemistry monitoring. Previously, temperature monitoring was done using memory-style gauges which were placed inside the wellbore at discrete depths. They did not provide real-time data, nor provide the vertical spatial resolution required to assess conditions along the wellbore (Mawalkar et al. 2019). The recent advances in permanent downhole monitoring tools such as fiber optic DTS provide a new alternative for CO₂ plume monitoring in GCS applications.

Injecting CO₂ into an underground storage reservoir is associated with hydrothermal processes that perturb the prevailing thermal equilibrium in the reservoir. These processes include Joule-Thomson expansion effect, exothermic CO₂ dissolution, and endothermic water vaporization (Han et al. 2010, Zeidouni et al. 2014). As the injected CO₂ enters the formation, it experiences Joule-Thomson cooling upon expansion. Joule-Thomson expansion is an isoenthalpic expansion process in which there is no heat exchange with the surroundings and no external work is applied on the fluid upon expansion. Temperature changes associated with Joule-Thomson expansion can be estimated using Joule-Thomson coefficient, which is defined by (Oldenburg 2007, Mathias et al. 2010, Han et al. 2010):

$$\mu_{JT} = \lim_{\Delta p \rightarrow 0} \left(\frac{\Delta T}{\Delta p} \right)_H = \left(\frac{\partial T}{\partial p} \right)_H \quad (2.1)$$

During storage of CO₂ in depleted hydrocarbon reservoirs, the effect of Joule-Thomson expansion can be significant because Joule-Thomson coefficient of CO₂ increases as pressure decreases. As a result, excessive cooling can be obtained which may result in gas hydrate formation and damage to wellbore injectivity (Mathias et al. 2010). On the other hand, CO₂ storage in deep saline aquifers located at deep depths and high pressures result in minor temperature cooling.

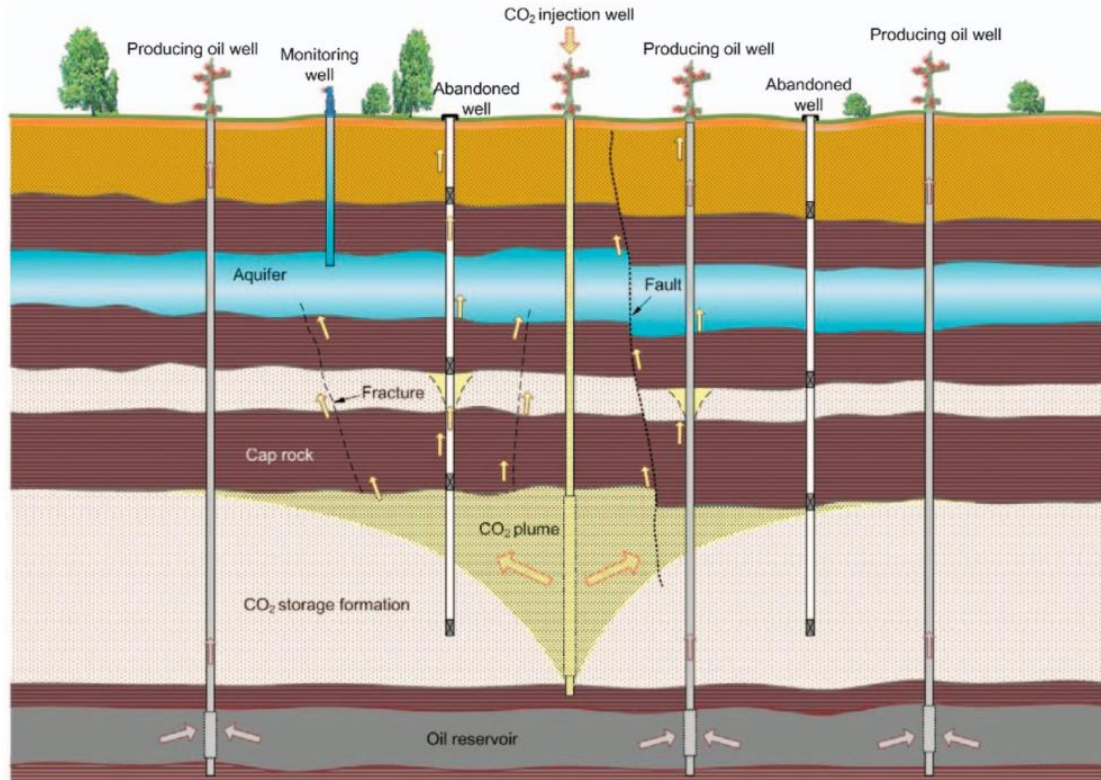


Figure 2. 3. CO₂ leakage pathways from a geological storage reservoir (Gaurina-Međimurec and Mavar 2017).

When injected CO₂ comes into contact with in-situ brine; water vaporizes into the flowing CO₂ stream while the dissolved salts deposit within the dry-out region. Due to water vaporization, a second front is established (i.e., a dry-out front) and follows the plume front during CO₂ injection in the storage reservoir. Within the two-phase region, mass exchange between the displacing fluid (CO₂) and the displaced fluid (brine) takes place, which is associated with different thermodynamic processes. At the trailing edge of the two-phase region, water vaporization dominates mass exchange between the interacting fluids, and excessive cooling is obtained due to endothermic water vaporization. On other hand, at the leading edge of the two-phase region, CO₂ dissolution into the in-situ brine dominates mass transfer processes, and temperature warming is obtained due to the exothermic reaction of CO₂ dissolution into the displaced brine (Han et al. 2010, Han et al. 2012).

Ahead of the two-phase region, a water bank is established in which a single phase of fresh brine is flowing. Due to the pressure gradient at the flooded front, the displaced brine undergoes Joule-Thomson expansion and consequently, the temperature of flowing brine increases. The obtained heating upon expansion is attributed to the negative value of Joule-Thomson coefficient for brine (Stauffer et al. 2014). The abovementioned thermodynamic processes result into a characteristic temperature profile in the storage reservoir which may change slightly according to the petrophysical properties of the storage formation (porosity and permeability) as illustrated in Fig. 2.4.

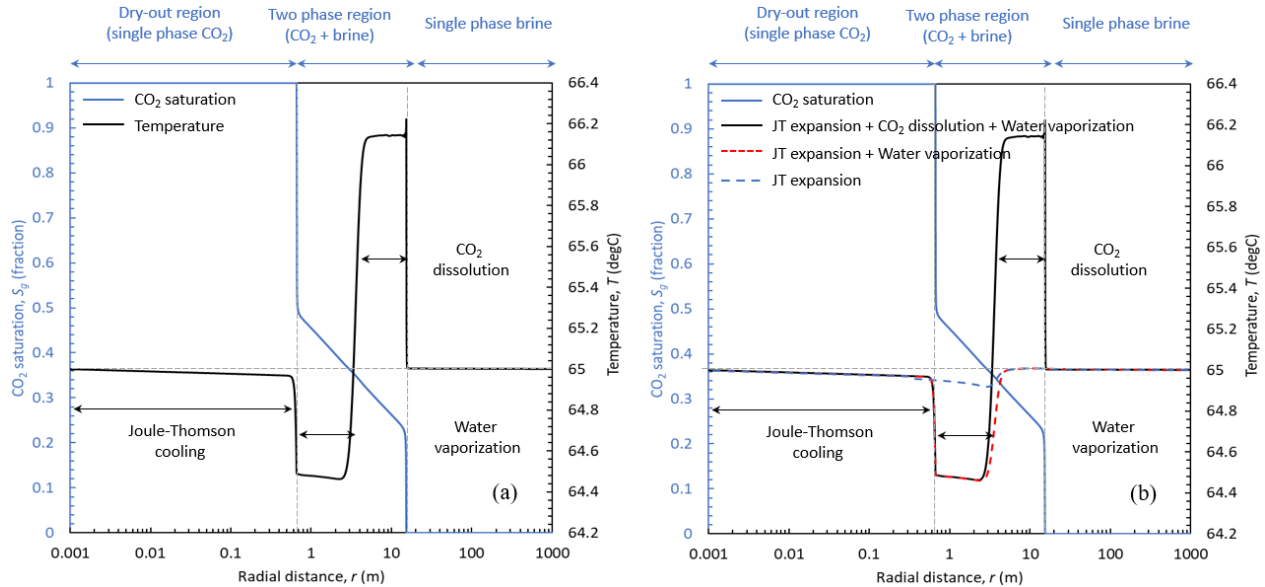


Figure 2. 4. CO₂ saturation and temperature profiles in an aquifer during an isothermal CO₂ injection.

Different studies were devoted to investigating the thermal effects associated with isothermal/non-isothermal CO₂ injection in deep saline aquifers and depleted hydrocarbon reservoirs in GCS projects. The purpose of these studies is to understand the causes of temperature perturbation in the reservoir, the factors that affect the temperature profile within the storage reservoir, and the potential of using temperature to monitor CO₂ plume migration. Bielinski et al. (2008) presented a numerical simulation study to investigate the effect of non-isothermal CO₂ injection on the temperature profile in the reservoir and the feasibility of using temperature monitoring to track CO₂ migration in the storage reservoir. During non-isothermal CO₂ injection, carbon dioxide transfers heat by advection to the in-situ brine. Accordingly, a distinct temperature is established at the flooded front, which can be detected using temperature sensors at monitoring wells. The magnitude of the temperature signal obtained depends on the injection temperature and the arrival time of the thermal front. Their study also shows the sensitivity of CO₂ plume configuration to reservoir permeability. Lower permeabilities result in a cylindrical CO₂ plume because capillary forces dominate buoyancy forces, while high permeabilities result in strong segregation of CO₂ and non-uniform propagation of the flooded front.

Han et al. (2010) studied the potential non-isothermal effects that evolve during CO₂ injection in the wellbore and the reservoir. The thermal effects that are responsible for temperature evolution during CO₂ flow in the wellbore are adiabatic compression of CO₂, heat exchange with the surrounding formation, and frictional energy loss. In their study, the surface injection temperature was not identical (higher) to the ambient temperature. Higher bottomhole injection temperature is obtained at higher injection rates due to the excessive adiabatic compression of flowing CO₂ in the wellbore as well as the decreased conductive heat loss to the surrounding formations. The authors also studied the thermal effects that perturb reservoir temperatures during CO₂ storage, such as Joule-Thomson cooling (JT) effect, heat of vaporization, and CO₂ dissolution into the in-situ brine. Based on their study, adiabatic

compression is the most dominating effect of temperature perturbation in the wellbore-reservoir system, then heat of vaporization (at the trailing edge of the two-phase region), and finally heat of dissolution (at the leading edge of the two-phase region) and JT expansion (in the dry-out region of the reservoir) are approximately of the same magnitude.

Zhao and Cheng (2015) used 2D numerical model to investigate the effect of injection temperature on CO₂ storage in deep saline aquifers while CO₂ is injected at a lower temperature than the reservoir temperature. The numerical results show the same characteristic temperature profile with a warming front (~ 1 °C) propagating ahead of the CO₂ front. Despite that a temperature response of 1 °C can be detected by temperature sensors at monitoring wells, the magnitude of the temperature rise decreases as CO₂ propagates deeper in the aquifer. Consequently, monitoring CO₂ using temperature monitoring is not feasible for long term injection, especially after injection terminates.

Mathias et al. (2010) studied the thermodynamic processes that evolve during CO₂ storage in depleted gas reservoirs. Their study revealed that Joule-Thomson expansion of injected CO₂ in the reservoir results in excessive cooling at the near wellbore region. To quantify temperature cooling, they developed an analytical solution to describe transient temperature profile established during CO₂ injection into a depleted gas reservoir. The analytical solution was developed assuming steady state flow conditions with constant thermodynamic fluid properties. According to the authors, excessive cooling can be obtained for depleted gas reservoirs, which can result in hydrate formation in the near wellbore region. Hydrate formation can plug the pore space and decreases well injectivity.

Jayne et al. (2019) conducted numerical modelling using 1D, 2D, and 3D models to investigate the temperature distribution during CO₂ injection into heterogeneous basalt reservoirs. Their study reveals that a warming front which is generated by heat of dissolution is established and migrates contemporaneously with a hydraulic flooded front. For heterogeneous reservoirs, the warming front can migrate ahead of the hydraulic front due to the high mobility of the displaced brine at the plume front, which results in advection heat transport, a head of the trailing CO₂. The authors recommended using temperature to monitor the warming front in order to track CO₂ plume migration.

Different numerical studies were also conducted to investigate the feasibility of using temperature measurements to monitor CO₂ leakage from saline aquifers. According to Zeidouni et al. (2014), CO₂ leakage from the storage reservoir (injection zone) undergoes hydrothermal processes which are slightly different from the hydrothermal processes associated with CO₂ migration within the reservoir. During CO₂ leakage, significant pressure drop may be observed associated with excessive cooling due to Joule-Thomson expansion effect. Unlike pressure signals, temperature signal monitored during leakage is sensitive to the leaking fluid. Before CO₂ arrival, only brine is leaking and accordingly warming signal is obtained in the above zone monitoring interval (AZMI) due to JT expansion of brine. When CO₂ reaches the leakage pathway (either leaky well or leaky fault), excessive cooling is obtained due to JT expansion of the leaking CO₂. Mao et al. (2017) investigated the sensitivity of the temperature signal generated by CO₂ leakage to the properties of the flow pathway and the nature of porous media (homogenous, dual porosity, dual-porosity-dual permeability). The sensitivity analysis was performed for two leakage scenarios: leaky well and leaky fault. The authors' results reveal that the temperature signal obtained is attributed to JT expansion of leaking fluid through the leakage

pathway (cooling effect) and adiabatic compression of leaking fluid in the AZMI (heating effect).

In the previous studies, several potential effects were disregarded while modeling temperature evolution in storage aquifers such as reservoir boundary conditions, injection history, level, and location of the temperature monitoring tool. An infinite-acting reservoir model has been adopted in the previous studies which excludes the effect of outer boundary conditions. In this study, we will investigate the characteristic temperature signal that establishes during the subsurface flow of CO₂ in a saline aquifer during boundary-dominated flow conditions. Besides the effect of the level and the location (inside wellbore versus behind the casing) of the monitoring tool on the observed temperature signal are investigated. CO₂ leakage from a storage aquifer via an improperly abandoned well will also be studied. We will investigate the evolutions of pressure, temperature, and fluid saturation during CO₂ migration through an improperly abandoned well to the surface. The objective of this study is to examine the potential for detecting CO₂ migration through abandoned wells using pressure and temperature measurements obtained at the surface.

Traditionally, temperature data were obtained using temperature monitoring tools operating in passive mode. In the last few decades, many hydrogeological studies were devoted to investigate the application of active temperature monitoring during heat pulse testing for evaluating subsurface hydraulic properties and monitoring groundwater flow (Ballard 1996, Diao et al. 2004, Leaf et al. 2012, Liu et al. 2013, Read et al. 2014, Read et al. 2015, Bakker et al. 2015, des Tombe et al. 2019, Simon et al. 2021, del Val et al. 2021). In these studies, heat is used as a tracer that is introduced to the formation using a distributed heating source, and the corresponding temperature signal is tracked/analyzed to estimate formation fluid flow, in-well fluid flow, and subsurface thermal properties. The advantage of using heat as a tracer over other geochemical tracers is that it is ubiquitous, economic, more diffusive than chemical solutes by several orders of magnitudes, and easy to be measured in-situ with high resolution (Bense et al. 2016). The thermal tracer tests presented in these studies can be categorized as thermal advection test, in-well heat pulse test, and formation heat pulse test (see Fig. 2.5).

Thermal advection test, also known as thermal plume tracking test, is deployed to allocate and quantify the magnitude of inflows and outflows over the monitoring interval. This test is designed for flowing (pumping or injecting) wells. It involves introducing a temperature anomaly in the wellbore at the bottom of the monitoring interval and tracking the thermal plume as it moves vertically inside the wellbore when pumping begins. The rate of advection of the established plume equates to the average fluid velocity inside the wellbore (see Fig. 2.5). Leaf et al. (2012) presented a field study showing the application of a thermal advection test for hydrostratigraphic characterization of a fractured reservoir. In their study, the thermal plume was established by introducing hot fluid inside the wellbore at the bottom of the monitoring interval using a small diameter tubing. When pumping starts, the established thermal plume is tracked with DTS to infer vertical fluid flow inside the wellbore. Their method was successfully used to quantify vertical flow in the wellbore as well as the changes in wellbore flow rate associated with fracture flow and porous medium flow. In some applications, a point heating source is deployed to warm up a packet of wellbore fluid at the bottom of the monitoring interval. Then, the movement of the warmed up packet is tracked as it moves vertically inside the wellbore when pumping starts. Sellwood et al. (2015) and Read et al. (2015) presented field studies showing the application of the advection test for estimating vertical borehole flow with DTS using a point

heating source. In their work, an electrical resistance heater is used to heat a slug of wellbore fluid at the bottom of the monitoring interval and track the heat migration using DTS to estimate the wellbore fluid flow. This technique is applicable for long monitoring intervals as long as thermal dilution due to inflows, dispersion, and cooling by conduction to the surroundings does not render the thermal plume undetectable with DTS (Read et al. 2015).

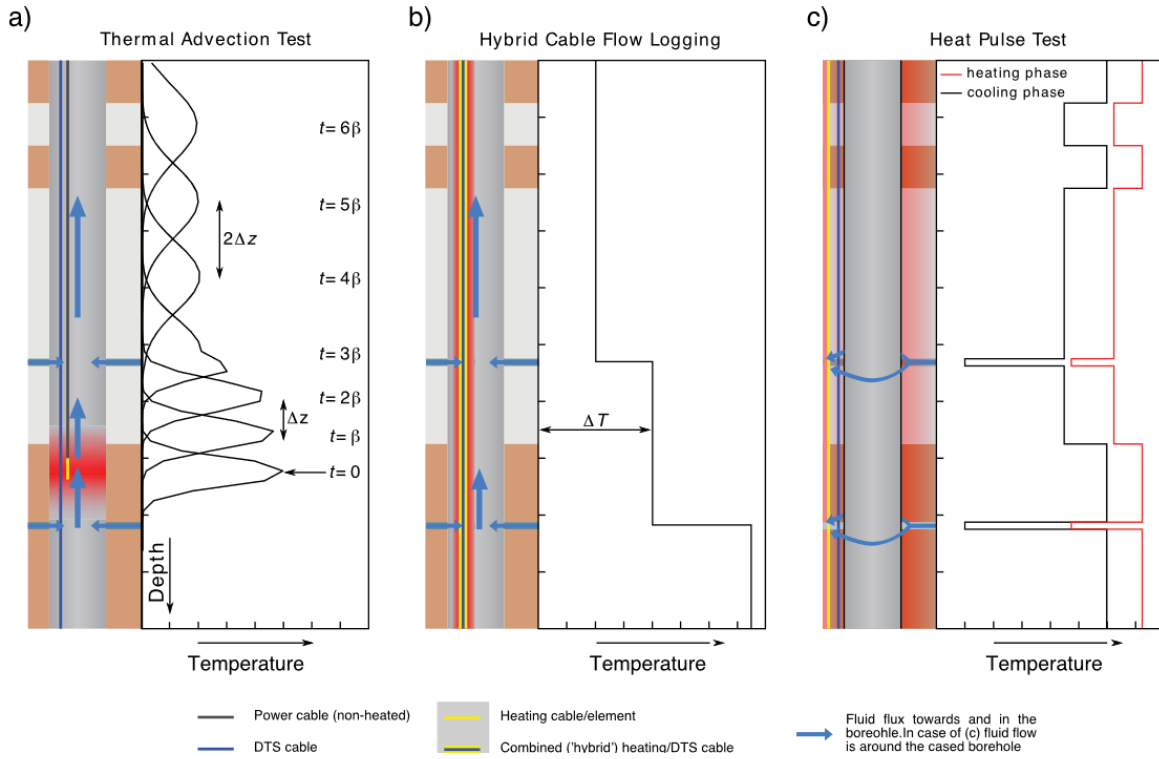


Figure 2. 5. Schematic illustration of the different types of a typical thermal tracer test. Right-hand side plots show the temperature signature to be observed in each test (Bense et al. 2016).

In-well vertical flow can also be monitored using an in-well heat pulse test, also called hybrid cable logging. In this test, thermal anomalies are induced by a distributed heating source along the depth range over which the velocities are to be determined. Higher fluid velocity effectively decreases the temperature of the heating source by decreasing the thermal boundary layer in the fluid surrounding the heating source (see Fig. 2.5). Also, the type of the flowing fluid can be inferred because fluid type (gaseous versus liquid) significantly affects the observed temperature signal obtained during the heating period (Hashish and Zeidouni 2022). Liu et al. (2013) presented a field study showing the application of an in-well heat pulse test to qualitatively provide high-resolution estimation of groundwater flux in a heterogeneous aquifer. In their work, the heating and the fiber optic cables are wrapped around a small diameter tubing which is deployed inside the wellbore. The authors showed that wrapping the cables around the deployed tubing can increase the spatial resolution of temperature measurements by two orders of magnitudes (from meter to centimeter).

Recently, fiber optic DTS cable has been used as a distributed heating source by deploying the cable in active mode i.e., active DTS (A-DTS). In this mode, heating occurs within the same cable as the optical fiber. The fiber optic cable has a steel armor to provide strength. That armor is used to heat the cable given its resistance to electrical conduction. When electricity

is supplied through the steel armor, heat is generated, and temperature is monitored with the fiber optic cable. Read et al. (2014) adopted this technique to develop a distributed borehole flowmeter in a pumping well, which is completed in a fractured rock aquifer. Vertical fluid flow in the pumping well is correlated with the observed temperature signal through convection heat transfer coefficient. Using this technique, the authors estimated flow rate distribution along the completed interval and identified the inflowing fractures which may be misidentified using the traditional flowmeters. One of the limitations of deploying the test using A-DTS is the cable installation inside the wellbore. The authors used centralizers to minimize the cable contact with the borehole wall and avoid the associated temperature artifacts. In those studies, temperature data obtained during in-well heat pulse testing were analyzed to qualitatively evaluate the subsurface heterogeneity of groundwater flux. New analysis methods are required to enable quantification of lateral fluid velocity across the wellbore. Besides, the application of in-well heat pulse testing will be extended in this study for monitoring CO₂ plume migration in storage aquifers. The implications of two-phase flow on the established temperature signal during the heating period will be analyzed to investigate the potential of in-well heat pulse testing for monitoring CO₂ arrival at monitoring wells.

In-well heat pulse testing was exclusively aimed at obtaining fluid flow inside the wellbore. This test has been extended so that the heat is dissipated within the geological formation rock of interest, which in turn help in estimating the fluid flow and thermal properties of the formation. To distinguish this type of heat pulse testing from the in-well heat pulse testing, we refer to it as formation heat pulse testing or simply heat pulse testing. It should be noted that for formation heat pulse testing, thermal perturbation can still be introduced inside the wellbore. However, there is no hydraulic communication between the wellbore and formation for this case to eliminate fluid dynamics inside the wellbore (see Fig. 2.5). The heating source may also be deployed such that it is directly in contact with the formation at the depth where the test is to be conducted. The efficiency of heat dissipation from the heating cable depends on the formation fluid velocity as well as the effective thermal properties of the formation. Previously, formation heat-pulse testing was deployed using two separate cables: one for monitoring and the other for heating. Temperature monitoring using this technique is sensitive to the location of the monitoring cable with respect to the heating cable. Deploying the DTS cable in active mode eliminates the necessity of using two separate cables and improves the accuracy of the temperature results.

Ballard (1996) used an analytical solution developed by Romero (1995) to model the temperature evolution around a heating source of finite length during formation heat pulse testing considering the effect of heat dissipation by advection and conduction mechanisms. In his work, a thin cylindrical heater is buried in the ground at the point where formation fluid velocity is to be estimated. The velocity and the direction of formation fluid flow are estimated using the adopted analytical solution with regression analysis. Diao et al. (2004) provided a simplified solution to the temperature evolution around the heating source assuming a line-source heater, referred to as Moving Infinite Line Source (MILS) solution. They used the developed solution to study the effect of formation fluid flow on the performance of geothermal heat exchanger wells. des Tombe et al. (2019) adopted the MILS solution to estimate the vertical variation of formation fluid flow in an unconsolidated rock aquifer during heat pulse testing. The analytical solution is adopted with regression analysis to infer formation fluid flow along the monitoring cable. Simon et al. (2021) presented graphical interpretation methods using the MILS solution to estimate

formation fluid velocity and thermal properties of the formation without the need for regression analysis. The graphical interpretation methods identify two characteristic heat transport regimes, namely conduction- and advection-dominant. The early-time heat transport regime is conduction-dominant in which the thermal properties of the surrounding formation dominate the temperature behavior, and the late-time heat transport regime is advection-dominant in which groundwater velocity dominates the temperature behavior. Formation thermal properties are estimated using temperature measurements obtained during the conduction-dominant period, while formation fluid velocity is estimated using the stabilized temperature obtained during the advection-dominant period. del Val et al. (2021) extended the previously developed interpretation methods to consider the thermal properties of the heating cable material and the implications of cable installation behind the casing. Their study showed that the thermal resistance of the materials surrounding the A-DTS cable can result in different stabilized temperatures and inaccurate estimation of formation fluid velocity.

To address the depth limitation of the test deployment, Bakker et al. (2015) introduced a new method to install the fiber optic cable using direct push equipment. They performed a heat pulse test with A-DTS cable deployed using the proposed method to assess groundwater velocity in an unconsolidated shallow aquifer (down to 100 m depth). This technique of direct attachment of the heater to the formation should be feasible for shallow aquifers but may be difficult to implement for deeper formations (deeper than 100 m). Consequently, other studies were devoted to enabling formation heat pulse testing at deeper formations. An alternative deployment technique is presented by Coleman et al. (2015) that involves deploying the heating source inside the monitoring well. For this installation, fluid dynamics in the wellbore have to be eliminated by isolating the hydraulic communication between the monitoring wellbore and the surrounding formation. In their field study, they showed the application of heat pulse testing with A-DTS in a borehole that is isolated from the formation with a flexible impermeable fabric liner. The sealing liner eliminates the effects of borehole cross-connection with the formation and restores natural flow conditions prevailed prior to well drilling. Their work enables qualitative assessment of a fractured bedrock aquifer and identification of inflowing fractures at the borehole. Another approach for deploying formation heat pulse testing is presented by Read et al. (2013) in which wellbore fluid is replaced with warm fluid, and temperature decay through the wellbore during the cooling period is monitored with fiber-optic DTS cable. This technique enabled the authors to detect cross-flowing fractures and quantify the crossflow rate. One of the limitations of this technique is possible change of hydraulic head in the wellbore during warm fluid injection, which in turn may cause fluid flow through and around the wellbore.

The previous studies were devoted to investigating the applications of formation heat pulse testing for monitoring groundwater flow (single-phase flow) through water bearing formations. Apart from this, we will extend the application of formation heat pulse testing for monitoring CO₂ plume migration in storage aquifers. New interpretation techniques are developed through extending the MILS solution to consider two-phase flow in the reservoir. The objective of the proposed interpretation methods is to provide spatial estimates of CO₂ saturation, individual phase velocity, and subsurface thermal properties at a monitoring well using temperature data obtained during the heating period.

Chapter 3. Temperature Warmback Analysis for Estimating Injection Profile in Vertical Injection Wells

3.1. Temperature Warmback Analysis During Injection via Vertical Injection Well

In this chapter, the application of temperature warmback analysis for injection profiling through stratified reservoirs completed by a vertical injection well is presented. As a first step, we developed a forward analytical model to describe the temperature profile in the reservoir during the warmback period. Inversion procedure is presented in terms of convenient graphical techniques that adopt the developed model along with the observed temperature data to determine extent of the flooded front inside the reservoir, injection rate, and the geothermal temperature all per individual layer. The analytical model is next validated against a thermally coupled numerical simulation tool. The graphical techniques are then applied to the numerically obtained temperature history to determine inversion results.

3.1.1. Problem Description for Single-Layer Reservoir

In the following, we consider cold fluid injection into a homogenous and isotropic single-layer reservoir with porosity ϕ and uniform thickness h by an injector that is completed through the entire thickness of the reservoir. The reservoir is a single-phase liquid reservoir, and the injection fluid is identical to the in-situ fluid of the reservoir except for its temperature, which is lower than the in-situ fluid temperature. Initial reservoir temperature is T_o and instant thermal equilibrium between injected fluid and rock is assumed. Fluid is injected at a constant rate q and constant injection temperature T_{inj} through a fully penetrating vertical well. The thermal properties of the reservoir are heat capacity of fluid saturated rock $\rho_r C_r$ and thermal conductivity of fluid saturated rock λ_r . The thermal and physical properties are assumed to be constant and uniform throughout the reservoir. During the injection phase, heat is transferred via the bulk fluid movement and the conduction in the flow direction. Fig. 3.1 shows a schematic illustration of the physical model.

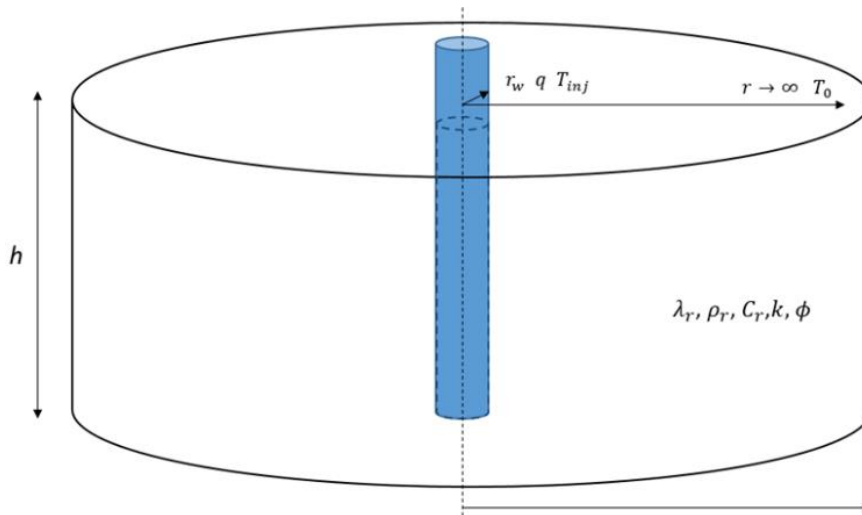


Figure 3. 1. Schematic illustration of the model for a single-layer reservoir.

The energy balance equation for the heat transfer inside the reservoir, which can be derived by combining the energy and mass balance equations, is given by Eq. 3.1 (App 2010, Duru and Horne 2010).

$$\rho_r C_r \frac{\partial T}{\partial t} + u_f \rho_f C_f \frac{\partial T}{\partial r} = \phi \left(\mu_{JT} \rho_f C_f + 1 \right) \frac{\partial P}{\partial t} + \mu_{JT} u_f \rho_f C_f \frac{\partial P}{\partial r} + \frac{1}{r} \frac{\partial}{\partial r} \left(\lambda_r r \frac{\partial T}{\partial r} \right) + \dot{Q} \quad (3.1)$$

where $u_f = \frac{Q}{2\pi r h}$. The first and second terms in LHS of Eq. 3.1 represent the transient temperature change and heat transfer by advection, respectively. The first and the second terms in RHS represent the adiabatic expansion/compression effect and Joule-Thomson cooling/heating effect. The third and fourth terms in RHS represent heat transfer by conduction in the flow direction and heat exchange with the overlying/underlying layers. Neglecting heat gain from the overlying/underlying layers and baro-thermal effects, Eq. 3.1 - in dimensional form - reduces to Eq. 3.2 (Chen and Reddell 1983) in dimensionless form after using the following group of dimensionless definitions.

$$\frac{\partial^2 T_D}{\partial r_D^2} + \frac{1-2\beta}{r_D} \frac{\partial T_D}{\partial r_D} = \frac{\partial T_D}{\partial t_D} \quad (3.1)$$

where:

$$T_D = \frac{T_o - T(r,t)}{T_o - T_{inj}} \quad r_D = \frac{r}{h} \quad t_D = \frac{t \lambda_r}{h^2 \rho_r C_r} \quad \beta = \frac{P_e}{2} = \frac{q \rho_f C_f}{4\pi h \lambda_r}$$

$$\rho_r C_r = \phi \rho_f C_f + (1-\phi) \rho_s C_s \quad \lambda_r = \phi \lambda_f + (1-\phi) \lambda_s$$

The corresponding initial and boundary conditions are:

$$T_D(r_D, 0) = 0 \quad (3.2)$$

$$T_D(r_D \rightarrow 0, t_D) = 1 \quad (3.3)$$

$$\lim_{r_D \rightarrow \infty} \frac{\partial T_D}{\partial r_D} = 0 \quad (3.4)$$

When injection is terminated, fluid movement throughout the reservoir ceases and the governing equation is simplified to the Eq. 3.6 in which the convection term for the heat transfer is dropped.

$$\frac{\partial^2 T_D}{\partial r_D^2} + \frac{1}{r_D} \frac{\partial T_D}{\partial r_D} = \frac{\partial T_D}{\partial \Delta t_D} \quad (3.5)$$

where Δt_D represents the dimensionless shut-in time. Eq. 3.6 is subjected to the following initial and boundary conditions:

$$T_D(r_D, \Delta t_D = 0) = T_D(r_D, t_{Dinj}) \quad (3.6)$$

$$\lim_{r_D \rightarrow 0} \left(r_D \frac{\partial T_D}{\partial r_D} \right) = 0 \quad (3.7)$$

$$\lim_{r_D \rightarrow \infty} \frac{\partial T_D}{\partial r_D} = 0 \quad (3.8)$$

where $T_D(r_D, t_{Dinj})$ represents the temperature distribution at the end of the injection period. The governing equation for heat balance inside the reservoir during the shut-in period, Eq. 3.6, is a heat conduction problem in which the initial condition is described by Eq. 3.7 and the boundary conditions are given by Eq. 3.8 and Eq. 3.9. The solution to the problem is presented in the next section.

3.1.2. Analytical Solution for Single-Layer Reservoir

The initial-boundary value problem during the injection period can be solved using Laplace transform technique. In Laplace domain, the governing equation is simplified into an ODE of the Bessel equation's form. The solution of the problem is obtained in terms of modified Bessel functions of the second kind, and the real-time solution is obtained through inverse Laplace transformation. The solution is a special case of the solution developed by Avdonin (1964) when the heat exchange with overlying/underlying layers is neglected. This assumption is reasonable for short injection periods and relatively thick layers. The solution in the real-time domain is given by Eq. 3.10.

$$T_D = \frac{1}{\Gamma(\beta)} \Gamma\left(\beta, \frac{r_D^2}{4t_D}\right) \quad (3.9)$$

where $\Gamma\left(\beta, \frac{r_D^2}{4t_D}\right)$ is an incomplete Gamma function of β from $\frac{r_D^2}{4t_D}$ to infinity. Based on this solution, the temperature at the beginning of shut-in period is given by (Abramowitz et al. 1988).

$$T_D(r_D, \Delta t_D = 0) = \frac{1}{\Gamma(\beta)} \Gamma\left(\beta, \frac{r_D^2}{4t_{Dinj}}\right) \quad (3.10)$$

The initial-boundary value problem corresponding to the warmback period is described by Eq. 3.6 through Eq. 3.9 where the corresponding initial condition (given by Eq. 3.7) is re-written using Eq. 3.11. The solution of the warmback problem is obtained using Hankel transformation. The resulting temperature response for the warmback period is given by Eq. 3.12.

$$T_D(r_D, \Delta t_D) = \frac{1}{\Gamma(\beta)} \frac{1}{2\Delta t_D} \int_0^\infty x \Gamma\left(\beta, \frac{x^2}{4t_{Dinj}}\right) e^{-\left(\frac{x^2+r_D^2}{4\Delta t_D}\right)} I_o\left(\frac{xr_D}{2\Delta t_D}\right) dx \quad (3.11)$$

The solution for the temperature at the wellbore is obtained by assigning $r_D \rightarrow 0$ in the Eq. 3.12. The sandface temperature solution is given by Eq. 3.16 in dimensionless form and Eq. 3.17 in dimensional form.

$$T_{wD} = 1 - \left(1 + \frac{t_{Dinj}}{\Delta t_D}\right)^{-\beta} \quad (3.13)$$

$$T_w = T_o - (T_o - T_{inj}) \left(1 + \frac{t_{inj}}{\Delta t}\right)^{-\beta} \quad (3.14)$$

It is evident from Eq. 3.14 that the rate of warmback is mainly dependent on the dimensionless convective parameter β which is equivalent $\frac{1}{2}$ Péclet number and the time ratio, $(1 + t_{Dinj}/\Delta t_D)$. We refer to that time ratio as shut-in time ratio, t_R which is analogous to Horner time ratio in the pressure build-up/fall-off testing interpretation (Horner 1951). Through applying the first order derivative to Eq. 3.14 with respect to t_R and multiplying by t_R , the solution is turned into the following convenient form:

$$t_R \left(\frac{dT_w}{dt_R}\right) = \beta (T_{inj} - T_o) t_R^{-\beta} \quad (3.15)$$

3.1.3. Inversion of Warmback Temperature Data

Graphical interpretation techniques of the warmback temperature are introduced using Eq. 3.14 and Eq. 3.15 in the following forms:

1. The first technique is to plot the normalized sandface temperature change $\left(\frac{T_w - T_{inj}}{T_o - T_{inj}}\right)$ versus shut-in time ratio, t_R on a log-log plot. The plotted data are fitted with a straight line with a slope magnitude of β at late shut-in time.
2. Alternatively, the logarithmic derivative of the sandface temperature $t_R \left(\frac{\partial T_w}{\partial t_R}\right)$ is plotted versus shut-in time ratio, t_R on a log-log plot and the plotted data are line-fitted with a slope magnitude of β and vertical axis intercept magnitude of $b = \beta(T_o - T_{inj})$ based on Eq. 3.15. The logarithmic-derivative-based technique is especially useful if accurate estimate of the initial temperature for the layer of interest is not available.

Both graphical techniques should provide parallel lines with same slope magnitude, β . Therefore, both can be applied to the data in a single graph to ensure consistency. The value of β can be used to estimate the injection rate per layer with Eq. 3.16.

$$q = \frac{\lambda_r}{\rho_f C_f} 4\pi h \beta \quad (3.16)$$

The initial temperature can be determined from the intercept, b of the straight line with vertical axis in the second graphical technique using Eq. 3.17.

$$T_o = T_{inj} + \frac{b}{\beta} \quad (3.17)$$

The thermal front at the injection time, t_{inj} can be represented by the radius of influence, R (Shaw-Yang and Hund-Der 2008):

$$R = \sqrt{4\alpha_t t_{inj} \Gamma^{-1} \left(\frac{\epsilon}{T_o - T_{inj}}, \beta \right)} \quad (3.18)$$

where $\alpha_t = \frac{\lambda_r}{\rho_r C_r}$ is the thermal diffusivity, and $\Gamma^{-1}(-)$ is the inverse of the in-complete gamma

function. Radius of influence is the distance from the injection well to the location where the temperature changes by a specified value, ϵ given by the resolution at which the temperature is measured. Shaw-Yang and Hund-Der (2008) used the resolution of 0.5 °C (0.9 °F) in defining R in their study, while we use 0.5 °F in this work.

While our modelling approach was developed for single-layer reservoir, it can also be applied to multilayer reservoir. The required assumption, however, is that the heat gain from overlying/underlying layers is negligible. When this assumption is valid, the above single-layer graphical techniques can be used to obtain the injection rate, the thermal front extent, and the initial geothermal temperature all per individual layer in a multilayer reservoir.

3.1.4. Analytical Models Validation

The developed analytical model is validated against a thermally coupled numerical reservoir simulator (CMG-STARS 2020). A verification case is developed for a multilayer reservoir that consists of nine layers which is completed with a fully penetrating well. Cold water is injected at constant injection rate (4000 bbl/day) and constant injection temperature (60 °F) into the reservoir. The injection is terminated after 0.125 day and the shut-in period is 3 days. During the injection period, water is injected into all the layers where the injected water is distributed among the completed layers according to their flow capacities. The layers have equal thickness of 50 ft and different permeabilities ranging from 10 md to 90 md. The simulation input data are given in Table 3.1.

Fig. 3.2 and Fig. 3.3 illustrate the temperature profiles in the reservoir after 1- and 2-day shut-in periods, respectively for layers 1, 5, and 9. Good match is obtained between the analytical and the numerical results at the specified shut-in times. There is small deviation between the numerical and the analytical results which is around 1 °F due to neglecting heat exchange with the surrounding layers. As indicated, layer 9 exhibits the maximum swept region while layer 1 exhibits the smallest swept region. Fig 3.4 shows the changes of the sandface temperatures for the specified layers. The figure illustrates the rate of warmback for the specified layers indicating that layer 1 exhibits the fastest warmback, while layer 9 exhibits the slowest warmback rate; the behavior that is in accordance with the extent of swept regions indicated previously in Fig. 3.2 and Fig. 3.3.

Table 3. 1. Input data for the synthetic case.

Input data	Value
Initial reservoir temperature (°F)	150
Initial reservoir pressure (psia)	4000
Injected temperature (°F)	60
Injection rate (bbl/day)	4000
Injection time (day)	0.125
Shut-in time (day)	3
Net pay thickness (ft)	50
Porosity (fraction)	0.3
Permeability (md)	10, 20, 30, 40, 50, 60, 70, 80, 90
Reservoir thermal conductivity (Btu/ft/hr/F)	1
Reservoir heat capacity (Btu/ft ³ /F)	43

3.1.5. Inversion Procedure Application

In this section, the graphical techniques presented in section 3.1.3 are used to determine the thermal front propagation, injection rate distribution among the completed layers, and the geothermal temperature for the multilayer reservoir. These techniques are applied to the temperature data obtained through numerical simulation of the previous synthetic case.

Fig. 3.5 illustrates the warmback data inversion for layers 1, 5, and 9 using the proposed graphical techniques. The measured sandface temperatures for the specified layers are fitted with straight lines at the late shut-in times. Early-time deviation of the numerical results from the fitted straight line is obtained due to the adiabatic expansion of reservoir fluids due to pressure relief when injection stops. Table 3.2 shows the results of the graphical techniques including the injection rate, the extent of the thermal front per layer at the end of the injection period, and the geothermal temperature for all the completed layers. The results of the inversion procedures are

in good agreement with the numerical results. The estimation error for the injection rates is $\sim 0.04\%$ and for the geothermal reservoir temperature is $\sim 0.3\%$. Fig. 3.5 illustrates the injection profiling over the multilayer reservoir including all the completed layers. It is obtained that layer 9 admitted the maximum percentage of the injected fluid (16.39%), while layer 1 admitted the minimum percentage of the injected fluid (4.07%).

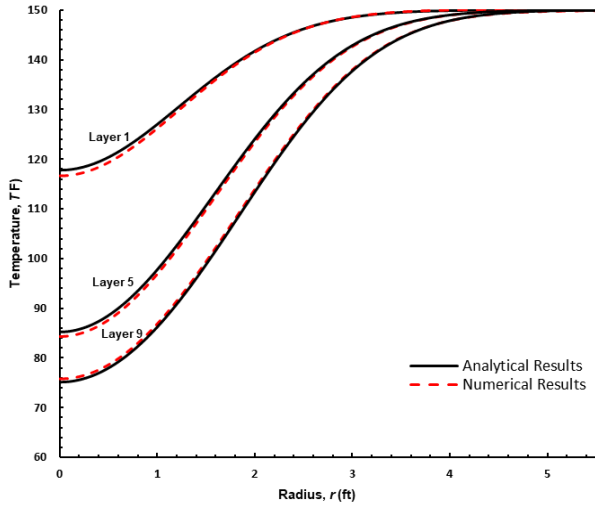


Figure 3. 2. Temperature profiles after a shut-in time of 1 day.

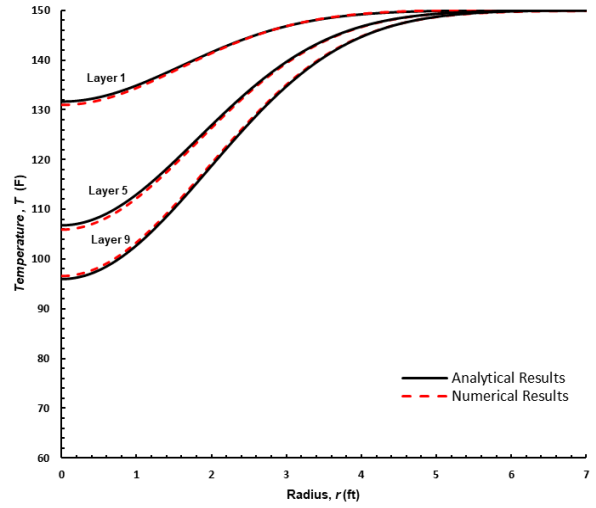


Figure 3. 3. Temperature profiles after a shut-in time of 2 days.

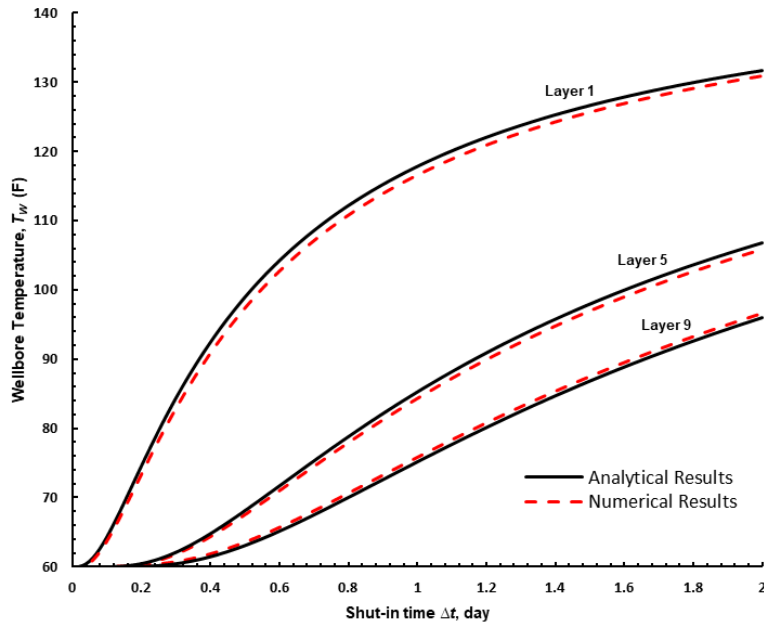


Figure 3. 4. Analytically and numerically calculated sandface temperature during the warmback period.

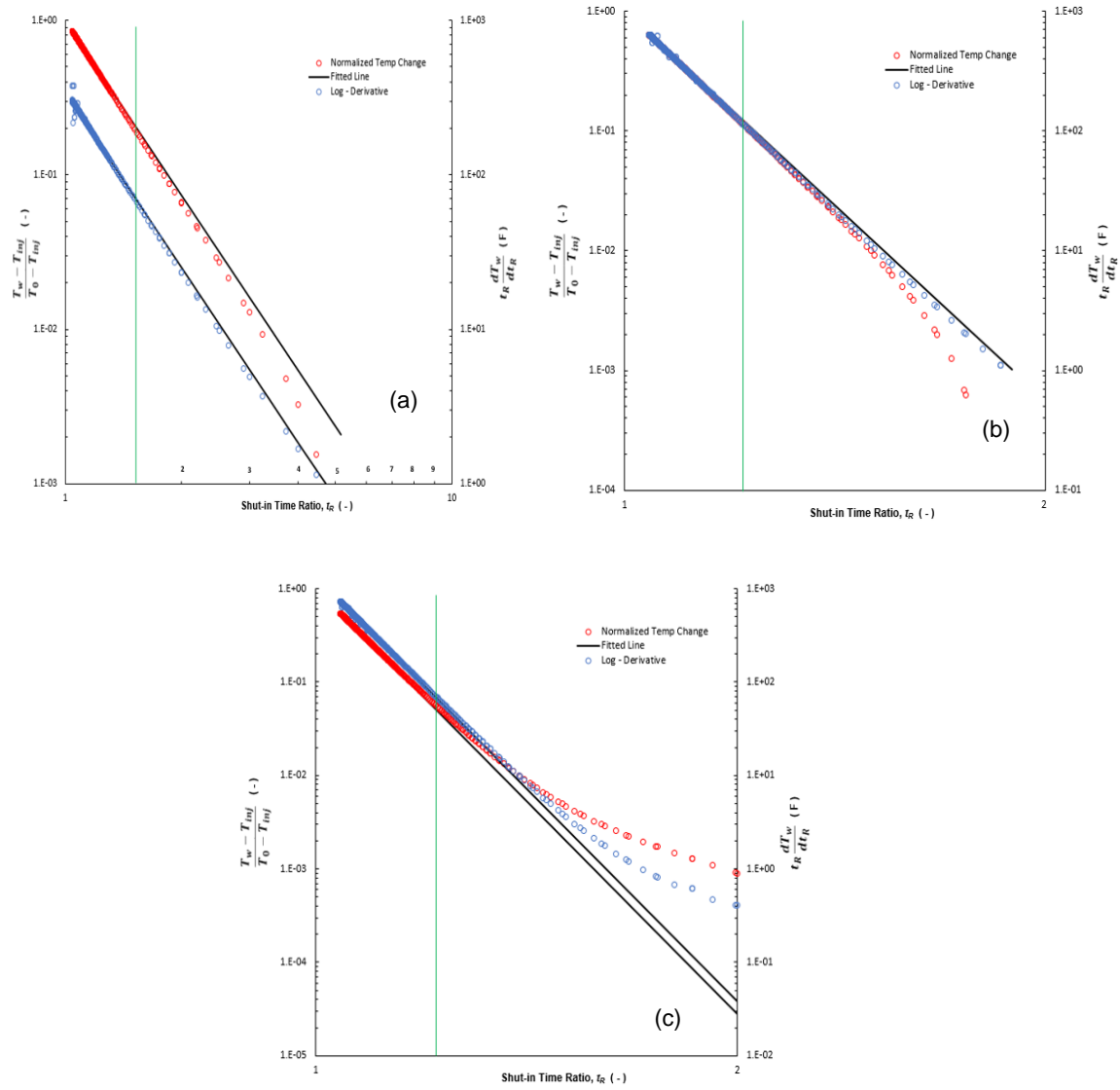


Figure 3. 5. Application of the graphical techniques for: (a) layer 1, (b) layer 5, and (c) layer 9.

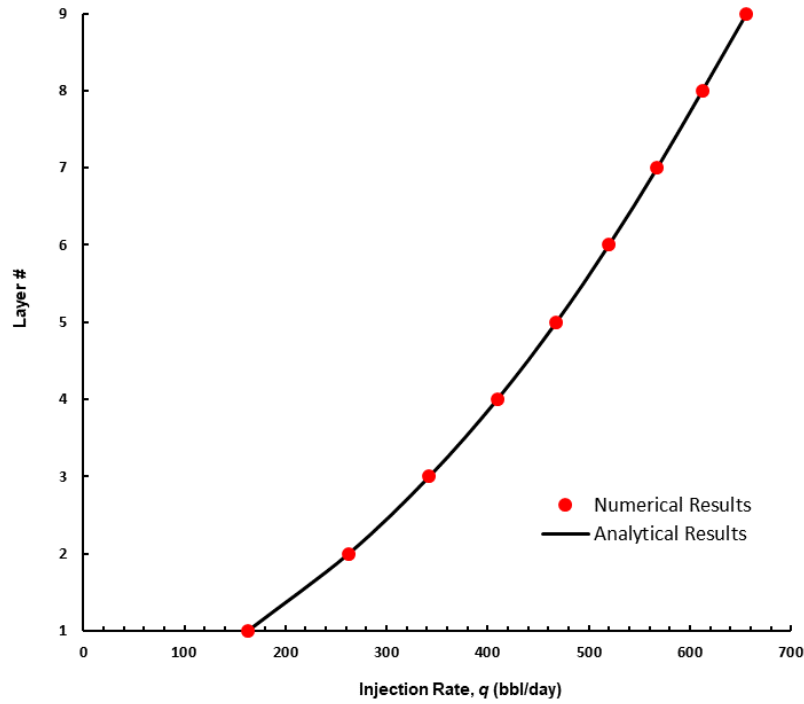


Figure 3. 6. Graphical illustration of the injection rate distribution among the injection layers.

Table 3. 2. Inversion results obtained using the graphical techniques.

Layer	Slope magnitude (Normalized Temp Change)	Slope magnitude (Log Derivative)	Intercept (Log Derivative)	Estimated rate, bbl/day	Actual rate, bbl/day	Error in rate estimation (percent)	Estimated Geothermal Temperature (F)
1	3.759	3.759	338.35	162.92	162.99	0.04	150.011
2	6.057	6.057	545.47	262.52	262.55	0.012	150.056
3	7.894	7.894	712.13	342.14	342.17	0.009	150.212
4	9.445	9.445	854.13	409.37	409.38	0.003	150.432
5	10.86	10.86	978.78	467.66	467.8	0.029	150.127
6	11.99	11.99	1079.4	519.67	519.83	0.032	150.025
7	13.09	13.09	1178.2	567.35	567.43	0.013	150.008
8	14.12	14.12	1271.2	611.99	612.23	0.039	150.028
9	15.13	15.13	1362	655.77	655.63	0.022	150.0198

3.1.6. Parametric Study

In this section, we investigate the effect of fluid after-flow that established after injection ceases on the accuracy of the proposed forward and inverse models. In the proposed solution, the fluid velocity in reservoir is assumed to be zero after injection stops. This assumption may be valid if injection well is shut-in at the bottom. Otherwise, fluid still flows to the reservoir after shut-in due to storage capacity of the injection well. Fig. 3.7 shows bottomhole flow rate for vertical injection well that is completed through a 200 ft-thick reservoir. Water is injected with constant injection rate of 2000 bbl/day and bottomhole injection temperature of 60 °F for 12 hours before injection stops. Initial reservoir temperature is 110 °F and the thermal conductivity of the reservoir is 1 Btu/ft hr °F. Fig. 3.7 illustrates bottomhole fluid flow rate after injection ceases for different wellbore storage coefficients ($C = 0.1, 0.05, \text{ and } 0.01 \text{ bbl/psi}$). It is evident that after-flow period can extend up to 1 hour depending on wellbore storage coefficient. Fig. 3.8 (a) illustrates the numerical and analytical sandface temperature results during forward modeling. The effect of the after-flow on the temperature behavior is negligible because of the short duration of the after-flow and the rapidly diminishing bottomhole flow rate. Good agreement is obtained between the analytical and numerical results which indicates that the effect of after-flow on the accuracy of forward modelling can be negligible. Fig. 3.8 (b) illustrates the application of the proposed graphical technique to the numerical temperature results. Temperature data are fitted with straight line at late shut-in time with slope magnitude of -11. Injection rate is estimated using Eq. 3.16 which gives 1894 bbl/day with an estimation error of ~ 7 percent. Accordingly, the inverse modeling still provides good estimation of injection rate if injection well is subject to after-flow during shut-in period.

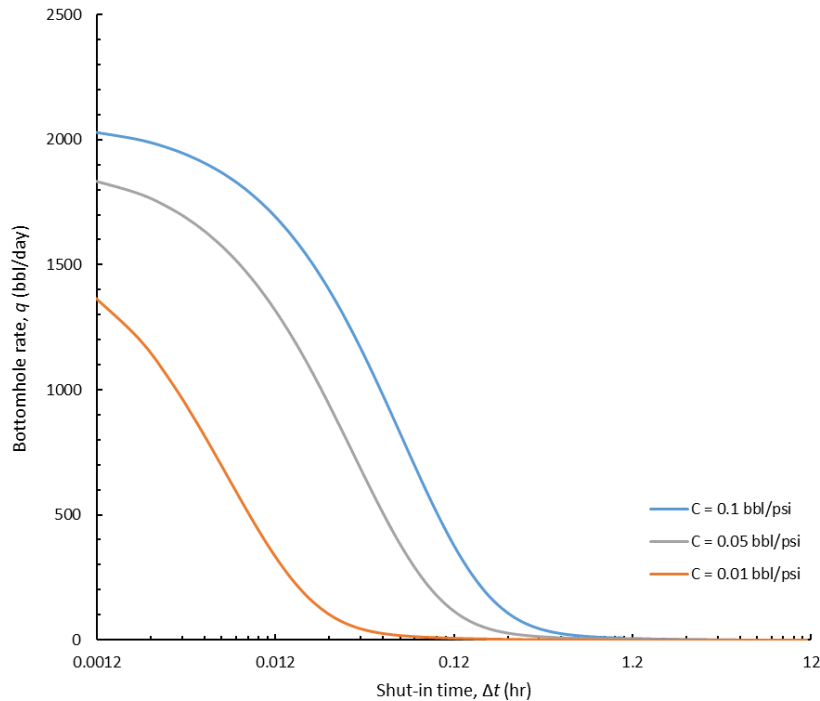


Figure 3. 7. Bottomhole flow rate during the shut-in period at different wellbore storage coefficients.

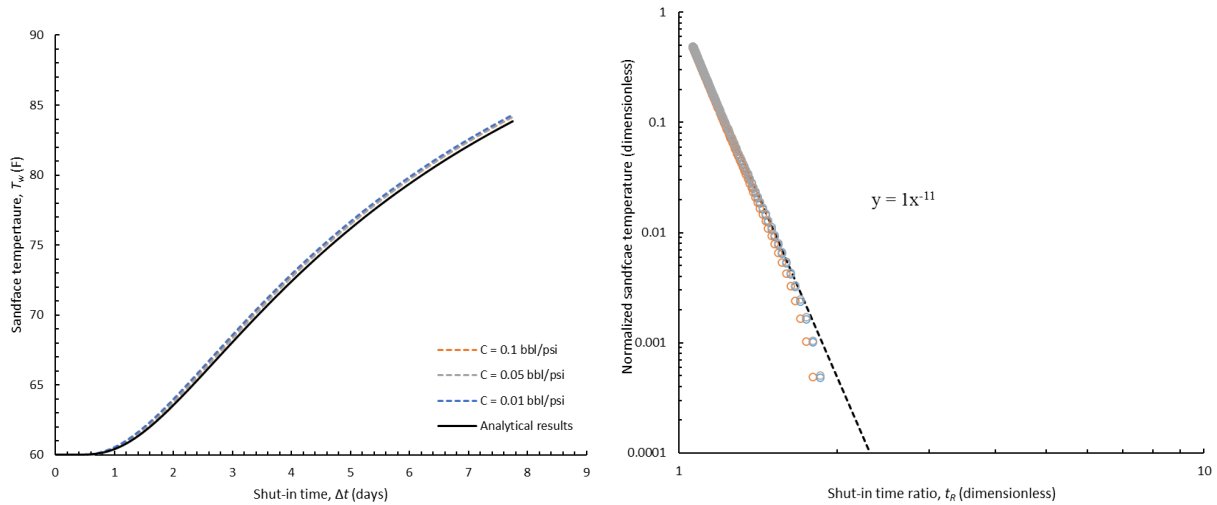


Figure 3. 8. (a) Analytically and numerically calculated sandface temperature during the warmback period considering fluid after-flow, (b) application of the graphical technique to the observed sandface temperature data.

Next, we investigate the effect of thermal properties uncertainty on the estimated injection rate. The thermal properties of reservoir which are responsible for heat transfer in porous medium are effective thermal conductivity and effective heat capacity. Eq. 3.16 indicates that sandface temperature recovery is not dependent on effective heat capacity of formation. Accordingly, the uncertainty of formation thermal conductivity is investigated. Assuming a range of measured reservoir thermal conductivity that follows a normal distribution with mean thermal conductivity identical to the actual value (1 Btu/ft hr F) and standard deviation of 0.25. This range represents formation thermal conductivity values that are within ~ 30 percent estimation error of the actual value (see Fig. 3.9 (a)). Using Eq. 3.16, the estimated injection rate and estimation errors are illustrated on Fig. 3.9 (b) and Fig. 3.9 (c), respectively. The maximum estimation error associated with the proposed range of reservoir thermal conductivities is 28 percent.

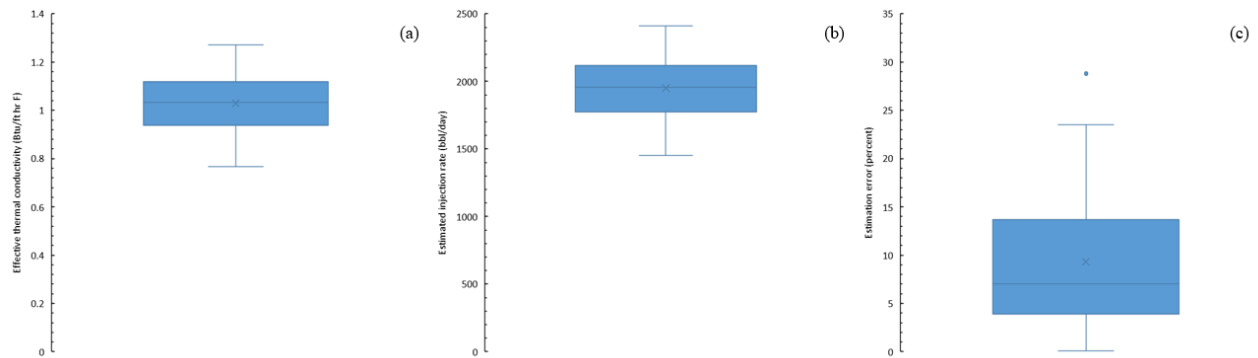


Figure 3. 9. (a) Reservoir thermal conductivity range, (b) estimated injection rate, and (c) estimation errors.

3.2. Warmback Analysis Application for Conventional Reservoirs - Considering Heat Exchange Between Injection Zones

In the previous section, the proposed analytical solution neglects the effect of heat exchange between the injection zones during the injection and shut-in period, which make the proposed solution is valid for short injection and shut-in durations and relatively thick injection zones. If the injection duration extends to relatively long periods (e.g., 1 day or more), an extended shut-in time is required to obtain a pronounced temperature signal during the shut-in period. In general, shut-in period is expected to be longer than injection period during warmback analysis because heat propagation by advection which is dominant during the injection period is more effective than heat diffusion which is dominant during the shut-in period. In this section, we investigated the effect of heat exchange between the injection zones in a stratified reservoir on temperature recovery during the warmback period. Next, new analytical solution is presented to consider the effect of heat exchange between the injection zones during the warmback period. Finally, the proposed analytical solution is casted into simple graphical technique for inversion modeling.

3.2.1. Effect of Heat Exchange Between Injection Zones on the Temperature Recovery

To investigate the significance of heat exchange between the injection zones on temperature recovery, different cases are modeled with and without heat gain from the surrounding strata for different injection rates and different zonal thicknesses. The reservoir properties for the synthetic cases are given in Table 3.3. Fig. 3.7 (a) and (b) show the temperature recovery during the warmback period for different injection rates (100, 500, and 1000 bbl/day) and different formation thicknesses (7, 10, and 15 ft), respectively. It is evident that the effect of heat gain from the surroundings increases as injection rate increases because area of heat exchange with the surrounding strata increases. On the other hand, thin layers exhibit more heat exchange with the surroundings compared with thick layers. Consequently, the effect of heat gain from the surroundings is significant for high operating injection rates and relatively thin injection zones. Accordingly, heat transfer in the transverse direction should be considered during solving the warmback problem for these cases. To simplify the solution of the problem, we considered heat exchange with the surrounding during the shut-in period only. This assumption is feasible for high injection rates and thin injection zones (high Péclet number) because the mechanism of heat transfer by conduction becomes negligible compared with heat transfer by advection as indicated by Platenkamp (1985).

To investigate the significance of neglecting heat gain during the injection period, the contribution of different heat transfer mechanisms to temperature evolution in the reservoir during the injection period ($t = 0.5$ days) using the input data shown in Table 3.3 is illustrated in Fig. 3.11. It is evident that heat transfer by advection is the most dominant mechanism which results in a step change in temperature at the thermal front. On the other hand, heat diffusion in the flow direction smears the thermal shock at the thermal front, which results in a smooth and gradual change in temperature at the thermal front. The mechanism of heat exchange with the surrounding increases the temperature heating upstream of the thermal front slightly without affecting the location of the thermal front.

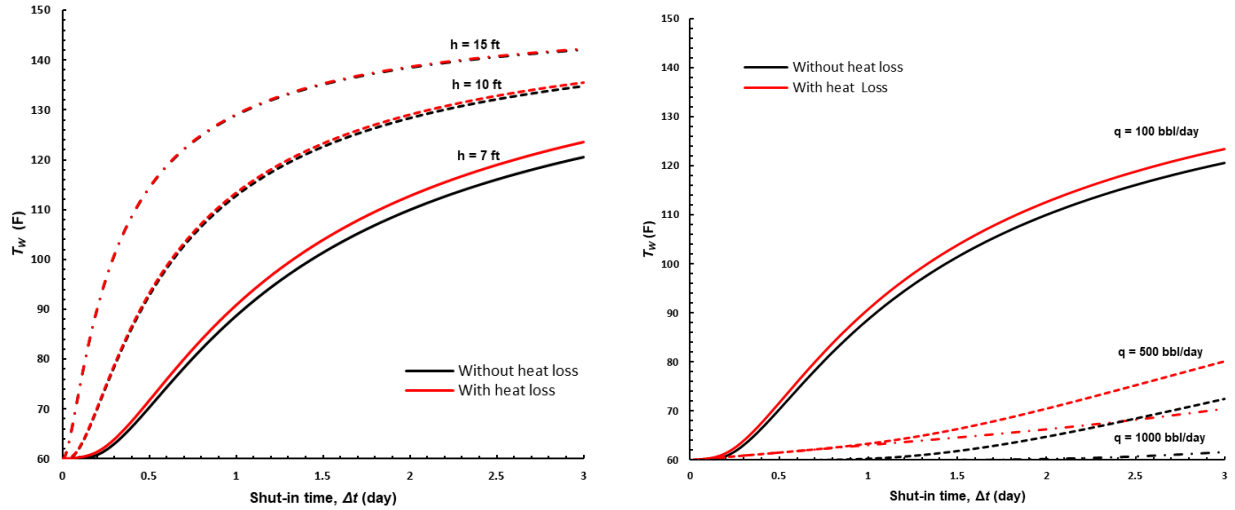


Figure 3. 10. Effect of injection rate and injection zone thickness on temperature recovery with/without considering heat gain from the surrounding strata.

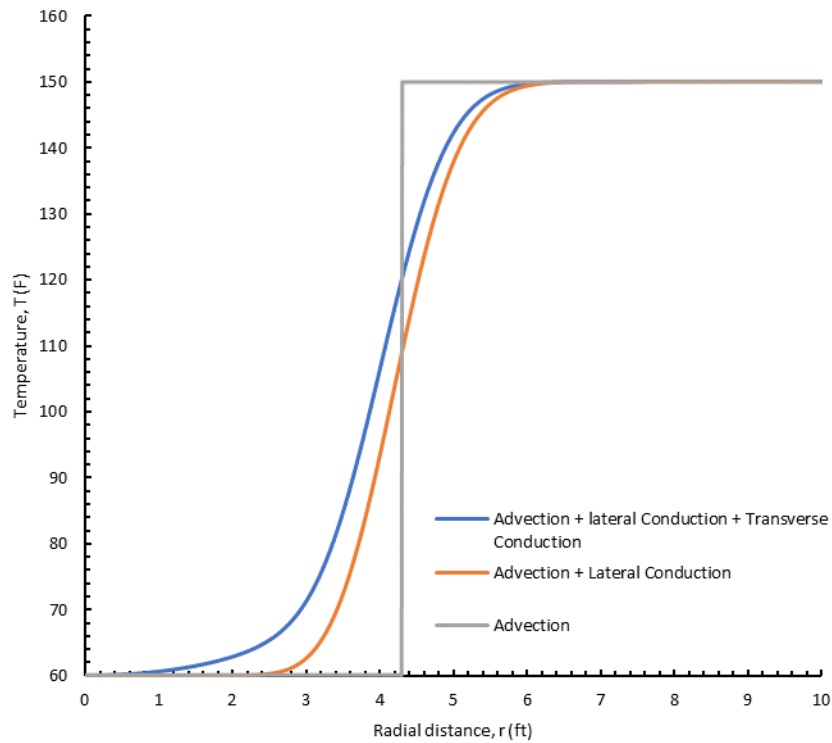


Figure 3. 11. Temperature profile during the injection period ($t = 0.5$ days) considering different heat transfer mechanisms (heat conduction, heat advection, and heat gain from the surrounding strata) (Case 1).

Additionally, the shut-in duration is often longer than the injection duration to obtain pronounced temperature recovery. This is attributed to the slow-acting nature of the heat diffusion mechanism compared with the heat advection mechanism. The extent of heat propagation via

diffusion which is given by $2\sqrt{\alpha_t t}$ (Marín 2010) is much smaller than the extent of heat transfer

by advection which is given by $\sqrt{\frac{1}{\pi h} \left(\frac{\rho_w C_w}{\rho_r C_r} \right) qt}$ (Platenkamp 1985) for the same time interval.

For example, using the input data given in Table 3.3, the radius of heat propagation by advection for injection rate of 100 bbl/day and formation thickness of 10 ft is 12.8 higher than the radius of heat propagation by diffusion for the same time period. Accordingly, heat exchange during the injection period can be neglected without big loss of accuracy.

3.2.2. Problem Description for Single-Layer Reservoir

In the following, we consider a single-layer reservoir sandwiched between an impermeable cap and bed strata. The reservoir layer is homogenous and isotropic with uniform thickness h and porosity ϕ . Cold fluid is injected into the reservoir via a fully penetrating vertical well with constant injection rate q and constant injection temperature T_{inj} . Heat is transferred during injection through heat convection and heat conduction in the flow direction, while it transfers by diffusion (in flow and transverse directions) only during the shut-in period. Fig. 3.12 shows schematic illustration of the physical model.

During the injection period, heat transfer is described by Eq. 3.2, and the solution for temperature propagation in the reservoir is described using Eq. 3.10. During the shut-in period, the heat transport equation is described using Eq. 3.19.

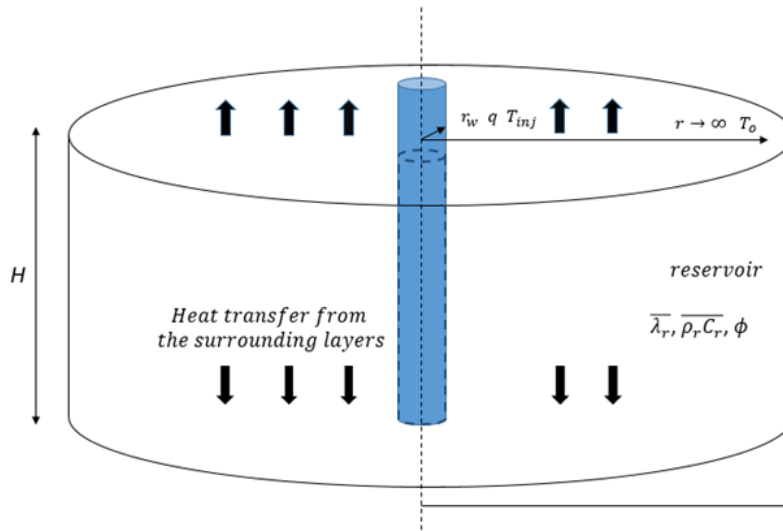


Figure 3. 12. Schematic illustration of the conceptual model for a single-layer reservoir.

$$\frac{\lambda_r}{r} \frac{\partial}{\partial r} \left(r \frac{\partial T}{\partial r} \right) + \lambda_r \frac{\partial^2 T}{\partial z^2} = \rho_r C_r \frac{\partial T}{\partial \Delta t} \quad (3.19)$$

Integrating Eq. 3.19 over the reservoir thickness, the following simplified heat transfer equation is obtained in terms of average temperature over the reservoir's thickness.

$$\frac{\lambda_r}{r} \frac{\partial}{\partial r} \left(r \frac{\partial T}{\partial r} \right) + \frac{\lambda_r}{H} \int_0^H \frac{\partial^2 T}{\partial z^2} dz = \rho_r C_r \frac{\partial T}{\partial \Delta t} \quad (3.20)$$

$$\frac{\lambda_r}{r} \frac{\partial}{\partial r} \left(r \frac{\partial T}{\partial r} \right) + \frac{\lambda_r}{H} \left\{ \left(\frac{\partial T}{\partial z} \right)_{z=H} - \left(\frac{\partial T}{\partial z} \right)_{z=0} \right\} = \rho_r C_r \frac{\partial T}{\partial \Delta t} \quad (3.21)$$

$$\frac{\lambda_r}{r} \frac{\partial}{\partial r} \left(r \frac{\partial T}{\partial r} \right) + \frac{2\lambda_r}{H} \left(\frac{\partial T}{\partial z} \right)_{z=H} = \rho_r C_r \frac{\partial T}{\partial \Delta t} \quad (3.22)$$

Eq. 3.22 can be rewritten such that heat exchange with the surrounding strata is described using convective form of heat gain in terms of overall heat transfer coefficient, U . Overall heat transfer concept can describe heat transfer in the vertical direction to the fluid flow without increasing the problem dimensionality as indicated by Zolotukhin (1979) and Satman et al. (1984). Accordingly, Eq. 3.22 simplifies to the following 1D heat transfer equation.

$$\frac{\lambda_r}{r} \frac{\partial}{\partial r} \left(r \frac{\partial T}{\partial r} \right) + \frac{2U}{H} (T_o - T) = \rho_r C_r \frac{\partial T}{\partial \Delta t} \quad (3.23)$$

Writing the heat transport equation in dimensionless form, Eq. 3.23 becomes:

$$\frac{\partial^2 T_D}{\partial r_D^2} + \frac{1}{r_D} \frac{\partial T_D}{\partial r_D} - \zeta T_D = \frac{\partial T_D}{\partial \Delta t_D} \quad (3.24)$$

where $\zeta = \frac{2H}{\lambda_r} U$. The corresponding initial and boundary conditions are given by:

$$T_D(r_D, \Delta t_D = 0) = \frac{1}{\Gamma(\beta)} \Gamma\left(\beta, \frac{r_D^2}{4t_{injD}}\right) \quad (3.25)$$

$$\lim_{r_D \rightarrow 0} \left(r_D \frac{\partial T_D}{\partial r_D} \right) = 0 \quad (3.26)$$

$$T_D(r_D \rightarrow \infty, \Delta t_D) = 0 \quad (3.27)$$

The solution of the IBVP described by Eq. 3.24 – 3.27 is obtained using Hankel transformation. According to which, the solution is given by:

$$T_D(r_D, \Delta t_D) = \frac{1}{\Gamma(\beta)} \frac{e^{-\zeta \Delta t_D}}{2\Delta t_D} \int_0^\infty x \Gamma\left(\beta, \frac{x^2}{4t_{Dinj}}\right) e^{-\left(\frac{x^2+r_D^2}{4\Delta t_D}\right)} I_0\left(\frac{xr_D}{2\Delta t_D}\right) dx \quad (3.28)$$

The solution for the temperature at the wellbore is obtained by assigning ($r_D \rightarrow 0$) in Eq. 3.28. The sandface temperature solution is described with Eq. 3.29.

$$T_{wD}(\Delta t_D) = e^{-\zeta \Delta t_D} \left(1 - \left(\frac{t_{Dinj} + \Delta t_D}{\Delta t_D} \right)^{-\beta} \right) \quad (3.29)$$

Eq. 3.29 implies that the warmback rate at the sandface is mainly dependent on the dimensionless convective parameter β (or equivalently $1/2$ the Péclet number, Pe) and the dimensionless term ζ . Pe quantifies the effect of injection rate/advection velocity on the warmback rate. As the injection rate increases (high Péclet number), the thermal front propagates deeper in the reservoir during the injection period and consequently the warmback rate decreases. Meanwhile, ζ quantifies the effect of heat gain from the surrounding layers on the temperature recovery during the warmback period, which is analogous to Biot number (Bi) ($= hh_c/\lambda_r$) in heat transfer problems with convection heat loss/gain (Cengel 2014). As overall heat transfer coefficient increases (high Biot number), warmback rate increases. Eq. 3.29 is simplified to the analytical solution given by 3.12 if heat transfer with the surroundings is neglected.

3.2.3. Problem Description for Multilayer Reservoir

In this section, the warmback problem is extended to a stratified reservoir that is composed of n layers with different permeabilities and/or thicknesses that result in different injection rate and thermal front propagation per layer. Fig. 3.13 shows a schematic illustration of the physical model. Heat exchange is considered between the reservoir layers and the surrounding cap and bed strata. The governing equation of the problem during the shut-in period for a multi-layer reservoir is given by Eq. 3.30 for an arbitrary layer, j .

$$\frac{\partial T_{Dj}}{\partial \Delta t_D} = \frac{\partial^2 T_{Dj}}{\partial r_D^2} + \frac{1}{r_D} \frac{\partial T_{Dj}}{\partial r_D} + \zeta_j \left((T_{Dj+1} + T_{Dj-1}) - 2T_{Dj} \right) \quad \text{where } j=1,2,\dots,n \quad (3.30)$$

where $T_{D0} = T_{Dn+1} = 0$. The following group of dimensionless parameters are adopted to rescale the governing equations.

$$T_{Dj} = \frac{T_o - T_j(r, t)}{T_o - T_{inj}} \quad r_D = \frac{nr}{H} \quad \Delta t_D = \frac{n^2 \lambda_r \Delta t}{H^2 \rho_r C_r} \quad H = \sum_{j=1}^n h_j \quad (3.31)$$

$$\zeta_j = \frac{H^2 U}{n^2 \lambda_r h_j}$$

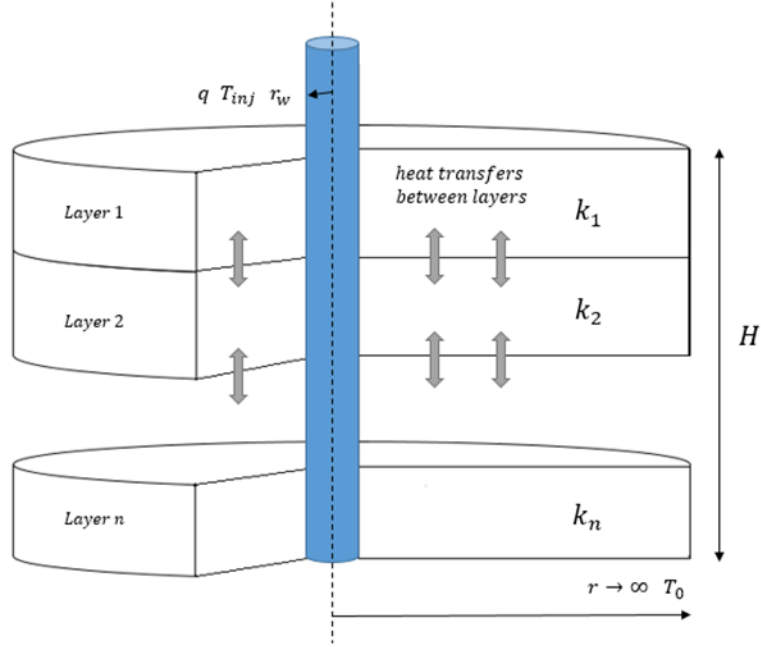


Figure 3. 13. Schematic illustration of the conceptual model for a multilayer reservoir.

The system of governing equations is subject to the following initial and boundary conditions:

$$T_{Dj}(r_D, \Delta t_D = 0) = \frac{1}{\Gamma(\beta_j)} \Gamma\left(\beta_j, \frac{r_D^2}{4t_{Dinj}}\right) \quad (3.32)$$

$$\lim_{r_D \rightarrow 0} \left(r_D \frac{\partial T_{Dj}}{\partial r_D} \right) = 0 \quad (3.33)$$

$$\lim_{r_D \rightarrow \infty} \left(r_D \frac{\partial T_{Dj}}{\partial r_D} \right) = 0 \quad (3.34)$$

The initial-boundary value problem described by Eq. 3.30 – Eq. 3.34 is solved using Hankel transform that transforms the system of PDEs in the real space domain into a linear system of ODEs, described by Eq. 3.35 (in matrix form), in Hankel space domain.

$$\begin{bmatrix}
-(\kappa^2 + 2\zeta_1) & \zeta_1 & 0 & 0 & 0 & 0 & 0 & 0 \\
\zeta_2 & -(\kappa^2 + 2\zeta_2) & \zeta_2 & 0 & 0 & 0 & 0 & 0 \\
0 & \zeta_3 & -(\kappa^2 + 2\zeta_3) & \zeta_3 & 0 & 0 & 0 & 0 \\
0 & 0 & \cdot & \cdot & \cdot & 0 & 0 & 0 \\
0 & 0 & 0 & 0 & \zeta_{n-2} & -(\kappa^2 + 2\zeta_{n-2}) & \zeta_{n-2} & 0 \\
0 & 0 & 0 & 0 & 0 & \zeta_{n-1} & -(\kappa^2 + 2\zeta_{n-1}) & \zeta_{n-1} \\
0 & 0 & 0 & 0 & 0 & 0 & \zeta_n & -(\kappa^2 + 2\zeta_n)
\end{bmatrix}
\begin{bmatrix}
\bar{T}_{D1} \\
\bar{T}_{D2} \\
\bar{T}_{D3} \\
\cdot \\
\bar{T}_{Dn-2} \\
\bar{T}_{Dn-1} \\
\bar{T}_{Dn}
\end{bmatrix}
=
\begin{bmatrix}
\frac{\partial \bar{T}_{D1}}{\partial \Delta t_D} \\
\frac{\partial \bar{T}_{D2}}{\partial \Delta t_D} \\
\frac{\partial \bar{T}_{D3}}{\partial \Delta t_D} \\
\cdot \\
\frac{\partial \bar{T}_{Dn-2}}{\partial \Delta t_D} \\
\frac{\partial \bar{T}_{Dn-1}}{\partial \Delta t_D} \\
\frac{\partial \bar{T}_{Dn}}{\partial \Delta t_D}
\end{bmatrix}
\quad (3.35)$$

The resulting system of equation in Hankel space domain is a linear system of ODEs with an independent variable, Δt_D . The solution can be obtained by solving the following eigenvalue problem:

$$(\mathbf{A} - \bar{\lambda} \mathbf{I}) \mathbf{X} = 0 \quad (3.36)$$

The matrix \mathbf{A} is the square matrix of the coefficients in Eq. 3.35, and \mathbf{I} is an identity matrix. \mathbf{X} and $\bar{\lambda}$ are square and vector matrices of the eigenvectors and eigenvalues of the square matrix \mathbf{A} , respectively. The solution in real-space domain is obtained by using inverse Hankel transformation as follows:

$$\begin{bmatrix}
T_{D1} \\
T_{D2} \\
\cdot \\
T_{Dn-1} \\
T_{Dn}
\end{bmatrix}
=
\frac{1}{2\Delta t_D}
\begin{bmatrix}
X^{(1,1)} e^{\lambda_1 \Delta t_D} & X^{(1,2)} e^{\lambda_2 \Delta t_D} & \cdot & X^{(1,n-1)} e^{\lambda_{n-1} \Delta t_D} & X^{(1,n)} e^{\lambda_n \Delta t_D} \\
X^{(2,1)} e^{\lambda_1 \Delta t_D} & X^{(2,2)} e^{\lambda_2 \Delta t_D} & \cdot & X^{(2,n-1)} e^{\lambda_{n-1} \Delta t_D} & X^{(2,n)} e^{\lambda_n \Delta t_D} \\
\cdot & \cdot & \cdot & \cdot & \cdot \\
X^{(n-1,1)} e^{\lambda_1 \Delta t_D} & X^{(n-1,2)} e^{\lambda_2 \Delta t_D} & \cdot & X^{(n-1,n-1)} e^{\lambda_{n-1} \Delta t_D} & X^{(n-1,n)} e^{\lambda_n \Delta t_D} \\
X^{(n,1)} e^{\lambda_1 \Delta t_D} & X^{(n,2)} e^{\lambda_2 \Delta t_D} & \cdot & X^{(n,n-1)} e^{\lambda_{n-1} \Delta t_D} & X^{(n,n)} e^{\lambda_n \Delta t_D}
\end{bmatrix}
\times
\begin{bmatrix}
X^{(1,1)} & X^{(1,2)} & \cdot & X^{(1,n-1)} & X^{(1,n)} \\
X^{(2,1)} & X^{(2,2)} & \cdot & X^{(2,n-1)} & X^{(2,n)} \\
\cdot & \cdot & \cdot & \cdot & \cdot \\
X^{(n-1,1)} & X^{(n-1,2)} & \cdot & X^{(n-1,n-1)} & X^{(n-1,n)} \\
X^{(n,1)} & X^{(n,2)} & \cdot & X^{(n,n-1)} & X^{(n,n)}
\end{bmatrix}^{-1}
\begin{bmatrix}
I_1 \\
I_2 \\
\cdot \\
I_{n-1} \\
I_n
\end{bmatrix}
\quad (3.37)$$

where $\lambda_j(\zeta_j \Delta t_D) = \bar{\lambda}_j e^{\kappa^2 \Delta t_D}$ and $I_j = \int_0^\infty x T_{Dj}(x, t_{Dinj}) e^{-\left(\frac{x^2 + r_D^2}{4\Delta t_D}\right)} I_o\left(\frac{x r_D}{2\Delta t_D}\right) dx$. The sandface

temperature solutions are obtained by assigning ($r_D \rightarrow 0$) in Eq. 3.37 which are given by:

$$\begin{aligned}
\begin{bmatrix} T_{wD1} \\ T_{wD2} \\ \cdot \\ T_{wDn-1} \\ T_{wDn} \end{bmatrix} &= \begin{bmatrix} X^{(1,1)} e^{\lambda_1 \Delta t_D} & X^{(1,2)} e^{\lambda_2 \Delta t_D} & \cdot & X^{(1,n-1)} e^{\lambda_{n-1} \Delta t_D} & X^{(1,n)} e^{\lambda_n \Delta t_D} \\ X^{(2,1)} e^{\lambda_1 \Delta t_D} & X^{(2,2)} e^{\lambda_2 \Delta t_D} & \cdot & X^{(2,n-1)} e^{\lambda_{n-1} \Delta t_D} & X^{(2,n)} e^{\lambda_n \Delta t_D} \\ \cdot & \cdot & \cdot & \cdot & \cdot \\ X^{(n-1,1)} e^{\lambda_1 \Delta t_D} & X^{(n-1,2)} e^{\lambda_2 \Delta t_D} & \cdot & X^{(n-1,n-1)} e^{\lambda_{n-1} \Delta t_D} & X^{(n-1,n)} e^{\lambda_n \Delta t_D} \\ X^{(n,1)} e^{\lambda_1 \Delta t_D} & X^{(n,2)} e^{\lambda_2 \Delta t_D} & \cdot & X^{(n,n-1)} e^{\lambda_{n-1} \Delta t_D} & X^{(n,n)} e^{\lambda_n \Delta t_D} \end{bmatrix} \\
&\times \begin{bmatrix} X^{(1,1)} & X^{(1,2)} & \cdot & X^{(1,n-1)} & X^{(1,n)} \\ X^{(2,1)} & X^{(2,2)} & \cdot & X^{(2,n-1)} & X^{(2,n)} \\ \cdot & \cdot & \cdot & \cdot & \cdot \\ X^{(n-1,1)} & X^{(n-1,2)} & \cdot & X^{(n-1,n-1)} & X^{(n-1,n)} \\ X^{(n,1)} & X^{(n,2)} & \cdot & X^{(n,n-1)} & X^{(n,n)} \end{bmatrix}^{-1} \begin{bmatrix} 1 - t_{DR}^{-\beta_1} \\ 1 - t_{DR}^{-\beta_2} \\ \cdot \\ 1 - t_{DR}^{-\beta_{n-1}} \\ 1 - t_{DR}^{-\beta_n} \end{bmatrix}
\end{aligned} \tag{3.38}$$

where $t_{DR} = ((t_{Dinj} + \Delta t_D) / \Delta t_D)$. For a reservoir that consists of three layers with equal thicknesses, the temperature solution is given by:

$$\begin{bmatrix} T_{D1} \\ T_{D2} \\ T_{D3} \end{bmatrix} = \frac{1}{2\Delta t_D} \begin{bmatrix} C_1(\Delta t_D) & C_2(\Delta t_D) & C_3(\Delta t_D) \\ C_2(\Delta t_D) & C_4(\Delta t_D) & C_2(\Delta t_D) \\ C_3(\Delta t_D) & C_2(\Delta t_D) & C_1(\Delta t_D) \end{bmatrix} \begin{bmatrix} I_1 \\ I_2 \\ I_3 \end{bmatrix} \tag{3.39}$$

where

$$\begin{aligned}
I_1 &= \int_0^\infty x T_{D1}(x, t_{Dinj}) e^{-\left(\frac{x^2 + r_D^2}{4\Delta t_D}\right)} I_o \left(\frac{x r_D}{2\Delta t_D}\right) dx & I_2 &= \int_0^\infty x T_{D2}(x, t_{Dinj}) e^{-\left(\frac{x^2 + r_D^2}{4\Delta t_D}\right)} I_o \left(\frac{x r_D}{2\Delta t_D}\right) dx \\
I_3 &= \int_0^\infty x T_{D3}(x, t_{Dinj}) e^{-\left(\frac{x^2 + r_D^2}{4\Delta t_D}\right)} I_o \left(\frac{x r_D}{2\Delta t_D}\right) dx
\end{aligned}$$

and

$$\begin{aligned}
C_1(\Delta t_D) &= \frac{1}{4} \left(e^{(-2+\sqrt{2})\zeta \Delta t_D} + 2e^{(-2)\zeta \Delta t_D} + e^{(-2-\sqrt{2})\zeta \Delta t_D} \right) & C_2(\Delta t_D) &= \frac{1}{2\sqrt{2}} \left(e^{(-2+\sqrt{2})\zeta \Delta t_D} - e^{(-2-\sqrt{2})\zeta \Delta t_D} \right) \\
C_3(\Delta t_D) &= \frac{1}{4} \left(e^{(-2+\sqrt{2})\zeta \Delta t_D} - 2e^{(-2)\zeta \Delta t_D} + e^{(-2-\sqrt{2})\zeta \Delta t_D} \right) & C_4(\Delta t_D) &= \frac{1}{2} \left(e^{(-2+\sqrt{2})\zeta \Delta t_D} + e^{(-2-\sqrt{2})\zeta \Delta t_D} \right)
\end{aligned}$$

where $T_{D1}(x, t_{Dinj})$, $T_{D2}(x, t_{Dinj})$, and $T_{D3}(x, t_{Dinj})$ are the dimensionless temperatures in the first, second, and third layer, respectively at the end of the injection period that were described by Eq. 3.32 (r_D is replaced with a dummy integration variable x). The corresponding sandface temperature solutions are described by the following equations:

$$\begin{bmatrix} T_{wD1} \\ T_{wD2} \\ T_{wD3} \end{bmatrix} = \begin{bmatrix} C_1(\Delta t_D) & C_2(\Delta t_D) & C_3(\Delta t_D) \\ C_2(\Delta t_D) & C_4(\Delta t_D) & C_2(\Delta t_D) \\ C_3(\Delta t_D) & C_2(\Delta t_D) & C_1(\Delta t_D) \end{bmatrix} \begin{bmatrix} 1-t_{DR}^{-\beta_1} \\ 1-t_{DR}^{-\beta_2} \\ 1-t_{DR}^{-\beta_3} \end{bmatrix} \quad (3.40)$$

As a step toward adopting the analytical solution in the inversion procedures, the solution described by Eq. 3.40 is rewritten in the following form.

$$\begin{bmatrix} F_1 \\ F_2 \\ \cdot \\ F_{n-1} \\ F_n \end{bmatrix} = \begin{bmatrix} 1 \\ 1 \\ \cdot \\ 1 \\ 1 \end{bmatrix} - \left(\begin{bmatrix} X^{(1,1)}e^{\lambda_1\Delta t_D} & X^{(1,2)}e^{\lambda_2\Delta t_D} & \cdot & X^{(1,n-1)}e^{\lambda_{n-1}\Delta t_D} & X^{(1,n)}e^{\lambda_n\Delta t_D} \\ X^{(2,1)}e^{\lambda_1\Delta t_D} & X^{(2,2)}e^{\lambda_2\Delta t_D} & \cdot & X^{(2,n-1)}e^{\lambda_{n-1}\Delta t_D} & X^{(2,n)}e^{\lambda_n\Delta t_D} \\ \cdot & \cdot & \cdot & \cdot & \cdot \\ X^{(n-1,1)}e^{\lambda_1\Delta t_D} & X^{(n-1,2)}e^{\lambda_2\Delta t_D} & \cdot & X^{(n-1,n-1)}e^{\lambda_{n-1}\Delta t_D} & X^{(n-1,n)}e^{\lambda_n\Delta t_D} \\ X^{(n,1)}e^{\lambda_1\Delta t_D} & X^{(n,2)}e^{\lambda_2\Delta t_D} & \cdot & X^{(n,n-1)}e^{\lambda_{n-1}\Delta t_D} & X^{(n,n)}e^{\lambda_n\Delta t_D} \end{bmatrix}^{-1} \begin{bmatrix} T_{wD1} \\ T_{wD2} \\ \cdot \\ T_{wDn-1} \\ T_{wDn} \end{bmatrix} = \begin{bmatrix} t_{DR}^{-\beta_1} \\ t_{DR}^{-\beta_2} \\ \cdot \\ t_{DR}^{-\beta_{n-1}} \\ t_{DR}^{-\beta_n} \end{bmatrix} \quad (3.41)$$

$$\times \begin{bmatrix} X^{(1,1)} & X^{(1,2)} & \cdot & X^{(1,n-1)} & X^{(1,n)} \\ X^{(2,1)} & X^{(2,2)} & \cdot & X^{(2,n-1)} & X^{(2,n)} \\ \cdot & \cdot & \cdot & \cdot & \cdot \\ X^{(n-1,1)} & X^{(n-1,2)} & \cdot & X^{(n-1,n-1)} & X^{(n-1,n)} \\ X^{(n,1)} & X^{(n,2)} & \cdot & X^{(n,n-1)} & X^{(n,n)} \end{bmatrix}^{-1}$$

The resulting system of equations indicate that the LHS functions (F_j) (that we call plotting functions) are related to the shut-in time ratio, t_{DR} by a power function. Based on that, if the plotting functions are plotted versus the shut-in time ratio on a log-log scale, the plotted data will be fitted with straight lines with slope magnitude equal to β_j that in turn is a function of the corresponding injection rate. For a reservoir composed of three layers of equal thickness, the plotting functions are given by:

$$\begin{bmatrix} 1 - \frac{C_2 T_{wD2} (C_3 - C_1) + C_4 (C_1 T_{wD1} - C_3 T_{wD3}) + C_2^2 (T_{wD3} - T_{wD1})}{(C_1 - C_3)(C_4(C_1 + C_3) - 2C_2^2)} \\ 1 - \frac{T_{wD2} (C_3 + C_1) - C_2 (T_{wD3} + T_{wD1})}{(C_4(C_1 + C_3) - 2C_2^2)} \\ 1 - \frac{C_2 T_{wD2} (C_3 - C_1) - C_4 (C_1 T_{wD1} - C_3 T_{wD3}) - C_2^2 (T_{wD3} - T_{wD1})}{(C_1 - C_3)(C_4(C_1 + C_3) - 2C_2^2)} \end{bmatrix} = \begin{bmatrix} t_{DR}^{-\beta_1} \\ t_{DR}^{-\beta_2} \\ t_{DR}^{-\beta_3} \end{bmatrix} \quad (3.42)$$

where C_j have been defined in Eq. 3.39. To further simplify the graphical technique and make the plotting variables more sensible, an approximation is adopted for relatively long shut-in time. The shut-in time ratio, t_{DR} is simplified by using the binomial expansion for extended shut-in

time to $\left(1 - \beta_j \frac{t_{inj}}{\Delta t}\right)$. With few mathematical manipulations, Eq. 3.42 can be simplified to the following dimensional forms:

$$\left(\frac{\Delta T_1 + \sqrt{2}\Delta T_2 + \Delta T_3}{\Delta T_1 - \Delta T_3}\right) = \left(\frac{q_1 + \sqrt{2}q_2 + q_3}{q_1 - q_3}\right) e^{\left(\frac{\sqrt{2}U}{h\rho_r C_r}\right)\Delta t} \quad (3.43)$$

$$\left(\frac{\Delta T_1 - \sqrt{2}\Delta T_2 + \Delta T_3}{\Delta T_1 - \Delta T_3}\right) = \left(\frac{q_1 - \sqrt{2}q_2 + q_3}{q_1 - q_3}\right) e^{-\left(\frac{\sqrt{2}U}{h\rho_r C_r}\right)\Delta t} \quad (3.44)$$

where $\Delta T_j = T_o - T_{wj}$. Plotting the sandface temperature response described by the LHS functions of Eq. 3.43 and Eq. 3.44 versus shut-in time, Δt in a semi-log scale results in a straight line with

slope magnitude $\left(\frac{\sqrt{2}U}{h\rho_r C_r}\right)$ and vertical intercepts $b_1 = \left(\frac{q_1 + \sqrt{2}q_2 + q_3}{q_1 - q_3}\right)$ and

$b_2 = \left(\frac{q_1 - \sqrt{2}q_2 + q_3}{q_1 - q_3}\right)$. The injection rates can easily be evaluated using the intercepts and the

injection constraint equation as described by the following expressions:

$$q_1 = \left(\frac{b_1 + b_2 + 2}{(\sqrt{2} + 2)b_1 - (\sqrt{2} - 2)b_2}\right) Q \quad q_2 = \left(\frac{b_1 - b_2}{(\sqrt{2} + 1)b_1 - (\sqrt{2} - 1)b_2}\right) Q \quad (3.45)$$

$$q_3 = \left(\frac{b_1 + b_2 - 2}{(\sqrt{2} + 2)b_1 - (\sqrt{2} - 2)b_2}\right) Q$$

The graphical procedures adopted for relatively long shut-in time are simple compared with the first approach and insensitive to the accuracy of the thermal properties and overall heat transfer coefficients. On the other hand, it requires relatively long shut-in time.

3.2.4. Inversion Procedure

The following inversion procedure can be followed to obtain the injection profile and the extent of the thermal front (per layer):

1. Obtain the sandface temperature measurements with shut-in times during the warmback period for the completed layers.

2. Calculate the dimensionless sandface temperatures, T_{wDj} , and the dimensionless shut-in time, Δt_D for the acquired data. The required properties for these calculations are rock and fluid thermal properties, overall heat transfer coefficient, and reservoir layers thicknesses.
3. Calculate the plotting functions represented by the elements of LHS vector of Eq. 3.41 (Eq. 3.42 for the case of three-layer reservoir).
4. Plot the plotting functions, F_j versus the dimensionless shut-in ratio, t_{DR} on a log-log scale. Identify and line-fit the portion of the data showing a linear behavior.
5. Calculate the parameter β_j from the slope. Use β_j to obtain the injection rate per layer with the following equation.

$$q_j = \frac{\lambda_r}{\rho_f C_f} 4\pi h_j \beta_j \quad (3.46)$$

The accuracy of the thermal properties and overall heat transfer coefficient may be questionable. An alternative approach can be adopted such that the shut-in period extends for relatively long period. The plotting functions (e.g., LHS of Eq. 3.43 and Eq. 3.44 for three-layer reservoir case) can be plotted versus shut-in time on a semi-log scale. The vertical intercepts along with the constraint equation of injection rates are solved for the injection rates of the corresponding layers as described by Eq. 3.45 for a three-layer reservoir case.

3.2.5. Analytical Models Validation

The developed analytical model is validated against results obtained using a thermally coupled numerical reservoir simulator (CMG-STARS 2020). The reservoir and fluid properties are given in Table 3.3.

Table 3. 3. Reservoir properties for the synthetic case.

Input data	Value
Initial reservoir temperature (°F)	150
Initial reservoir pressure (psia)	4000
Injected temperature (°F)	60
Injection rate (bbl/day)	500
Injection time (day)	0.125
Shut-in time (day)	3
Net pay thickness (ft)	10
Porosity (fraction)	0.3
Permeability (md)	100, 200, 300
Reservoir thermal conductivity (Btu/ft hr F)	1.7
Overall heat transfer coefficient (Btu/ft ² hr F)	0.218
Reservoir heat capacity (Btu/ft ³ F)	43

In this case, a stratified reservoir that consists of three injection zones is considered. Cold water is injected at constant injection rate (500 bbl/day) and constant injection temperature (60 °F) into the reservoir. The injection is terminated after 0.125 day and the shut-in period is 3 days. During the injection period, water is injected into all the layers through a fully penetrating well where the injected water is distributed among the completed layers according to their flow capacities. The layers have equal thicknesses of 10 ft and different permeabilities 100, 200, and 300 md. Fig. 3.14 (a) and (b) illustrate the temperature profiles in the individual layers of the reservoir after 1 day and 2 days, respectively during the shut-in period. The figures show good match between the analytical and numerical results at the specified shut-in times. Fig. 3.15 illustrates the sandface temperatures of the completed layers during the warmback period. It is obtained that the uppermost layer that has the minimum flow capacity exhibits the fastest rate of temperature recovery, while the lowermost layer that has the maximum flow capacity exhibits the slowest rate of temperature recovery.

3.2.6. Inversion Procedure Application

The graphical technique is applied to the numerical results to obtain the injection profile over the stratified reservoir. Fig. 3.16 illustrates the application of the graphical technique for the numerically calculated sandface temperature of top, middle, and the bottom layer. The numerical results are fitted with straight lines with different slope magnitudes. Early time deviation is obtained for the numerical results of all the layers due to the adiabatic cooling effect at the start of shut in. The early time cooling effect ends at ~3.38 hr, 7 hr, and 10 hr for the top, middle, and bottom layer, respectively. These time intervals are specified by the vertical blue, red, and green lines, respectively in Fig. 3.16, which specify the end of the early cooling period and the start of the dominating temperature warmback behavior.

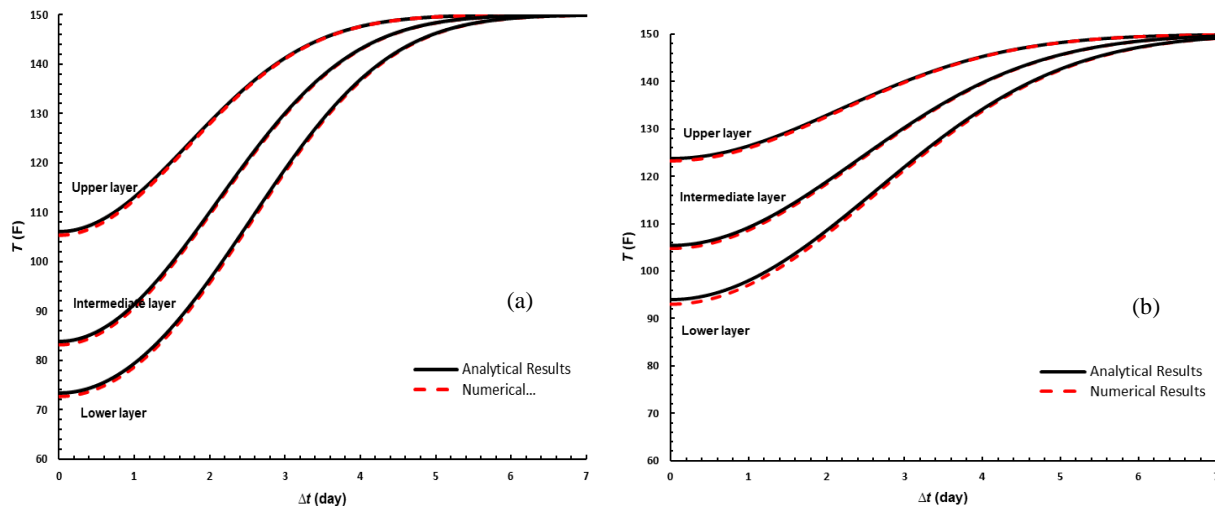


Figure 3. 14. The temperature profiles in the reservoir during the warmback period after: (a) 2 days, (b) 3 days.

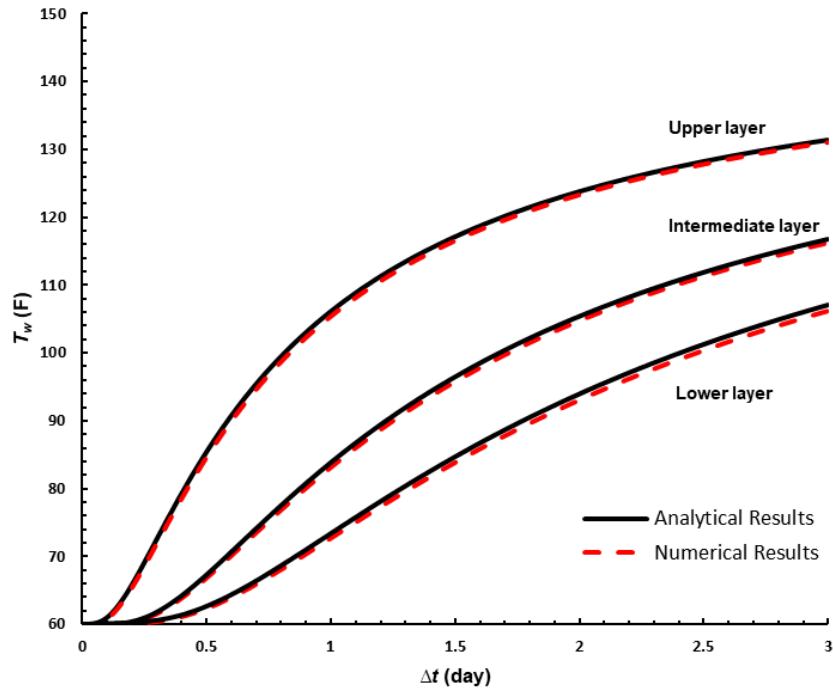


Figure 3. 15. Analytically and numerically calculated sandface temperature during the shut-in period.

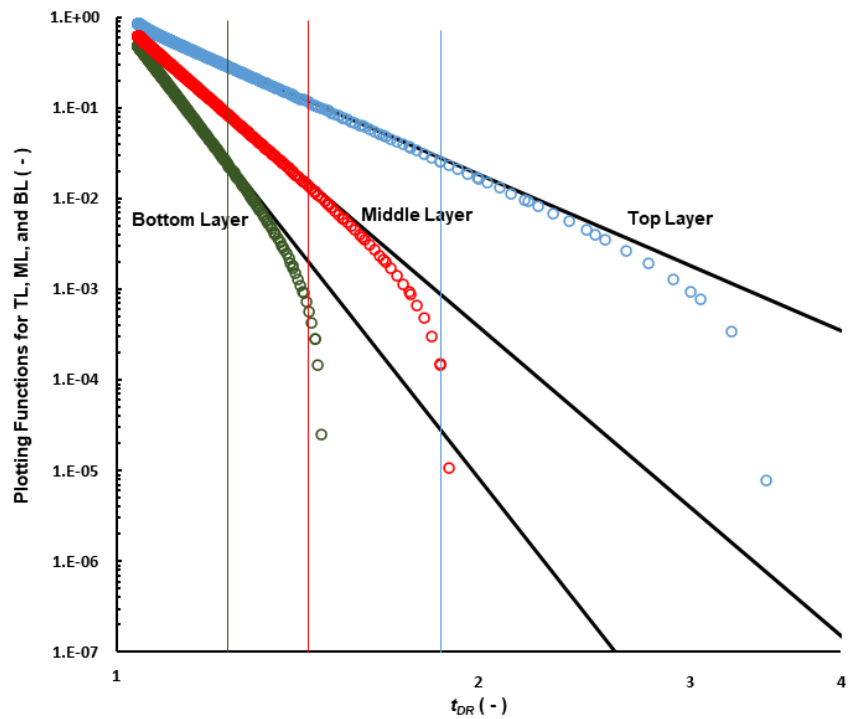


Figure 3. 16. Application of the first graphical technique to the numerical results.

The inversion results are displayed in Table 3.4. The inversion results are in a good agreement with the numerical results with an estimation error for the injection rates are ~ 0.01 percent. Fig. 3.17 illustrates the application of the second graphical technique to the numerical results. The primary and secondary axis illustrates the plotting functions represented by LHS of Eqs. 3.43 and 3.44. Fig. 3.17 indicates that the plotted data are fitted with straight lines after $\Delta t = 2$ days with vertical intercepts $b_1 = 3.633$ and $b_2 = 0.598$. The obtained vertical intercepts are substituted in Eq. 3.45 to obtain the injection profiling. The injection profiling obtained by the second approach is given in Table 3.4.

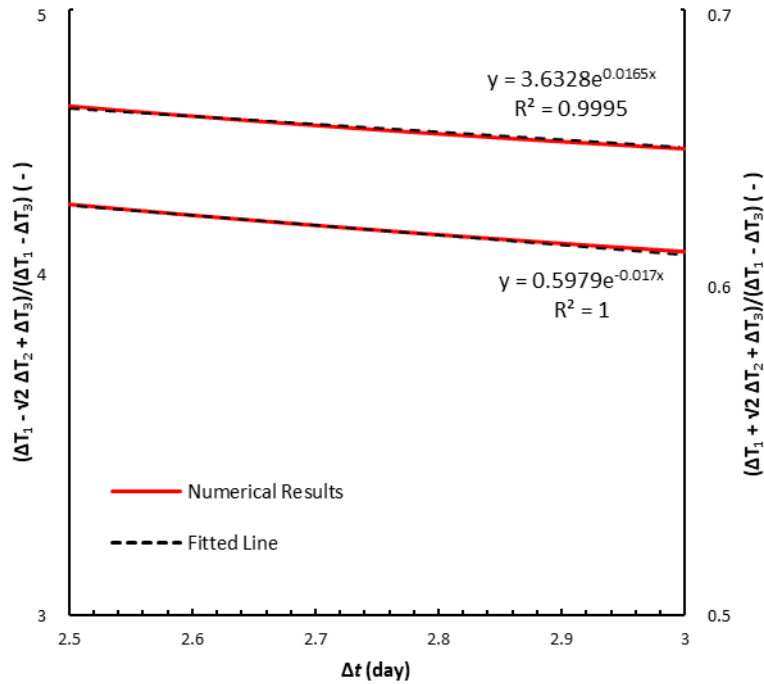


Figure 3. 17. Application of the second graphical technique to the numerical results.

Table 3. 4. Results of the inversion procedures.

Layer	Graphical Technique I			Graphical Technique II		
	Slope magnitude	Estimated rate, bbl/day	Actual rate, bbl/day	Error in rate estimation (percent)	Estimated rate, bbl/day	Error in rate estimation (percent)
1	5.733	84.42	84.416	0.0047	87.455	3.6
2	11.33	166.84	166.85	0.0059	168.269	0.85
3	16.87	248.42	248.41	0.0040	244.276	1.79

Chapter 4. Application of Temperature Warmback Analysis under Variable Injection Rate and Variable Injection Temperature

In this chapter, two major limitations of our previous modeling efforts are addressed by modifications to handle: (1) variable injection rate and variable injection temperature and (2) thermal storage capacity of the wellbore. In Appendix A, a numerical investigation is conducted (using CMG-STARS (2020) and KAPPA-Rubis (2019)) to demonstrate the significance of the aforementioned two limitations and the importance of addressing them. The numerical investigation shows that bottomhole temperature variation is inevitable and can extend over the entire duration of the injection period even for constant surface injection temperature. Additionally, bottomhole rate can be variable, even if the surface injection rate is fixed due to wellbore storage effect at the start of the injection and shut-in periods. Thermal wellbore storage results in different (lower) wellbore temperature compared with the sandface temperature due to the thermal capacity of the wellbore system as well as the thermal resistance of tubing, casing, and cement sheath. This effect can extend over the entire duration of the shut-in period, and it should be considered if the temperature monitoring tool is deployed inside the wellbore especially for short-term injection operations to avoid overestimation of the injection profile during the warmback analysis.

4.1. Injection under Variable Rate and Variable Temperature

In this section, a semi-analytical model is developed to simulate the transient temperature in a reservoir during non-isothermal fluid injection under variable rate and variable temperature (see Fig. 4.1). The governing equation for heat transfer during the injection period in the reservoir considering variable injection rate and variable bottomhole injection temperature is described by the following advection-diffusion equation:

$$\rho_r C_r \frac{\partial T}{\partial t} + \rho_w C_w u_w(t) \frac{\partial T}{\partial r} = \frac{\lambda_r}{r} \frac{\partial}{\partial r} \left(r \frac{\partial T}{\partial r} \right) \quad (4.1)$$

where the advection velocity is given by:

$$u_w(t) = \frac{q(t)}{2\pi r h} \quad (4.2)$$

The governing equation is subject to the following initial and boundary conditions during the injection period.

$$T(r, t = 0) = T_o \quad (4.3)$$

$$T(r = 0, t) = T_{inj}(t) \quad (4.4)$$

$$\lim_{r \rightarrow \infty} \left(\frac{\partial T}{\partial r} \right) = 0 \quad (4.5)$$

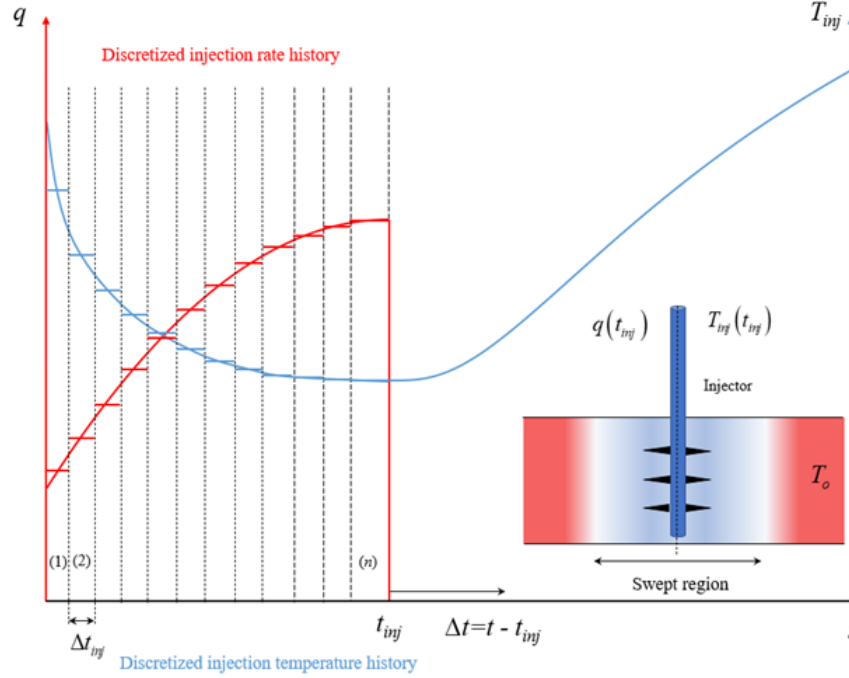


Figure 4. 1. Rate and temperature history during the injection and shut-in periods.

A semi-analytical approach is developed to solve the initial-boundary value problem (IBVP) described by Eq. 4.1 – 4.5. The injection history is discretized into small time steps such that injection rate and injection temperature can be considered constant over a single time step as illustrated in Fig. 4.1. Next, an analytical solution for constant injection rate and constant injection temperature is presented to solve for temperature profile during the time step period. The obtained temperature solution at the end of the time step period is considered as the initial condition during the solution of the next time step. The dimensionless form of the governing equation is as follows:

$$\frac{\partial T_D}{\partial t_D} = \frac{\partial^2 T_D}{\partial r_D^2} + \frac{1-2\beta(t_D)}{r_D} \frac{\partial T_D}{\partial r_D} \quad (4.6)$$

The corresponding initial and boundary conditions are given by:

$$T_D(r_D, t_D = 0) = 0 \quad (4.7)$$

$$T_D(r_D = 0, t_D) = T_{injD}(t_D) \quad (4.8)$$

$$\lim_{r_D \rightarrow \infty} \left(\frac{\partial T_D}{\partial r_D} \right) = 0 \quad (4.9)$$

The details of the solution to the above problem are given in Appendix B, according to which the temperature solution at time step i , where $i = 1, 2, \dots, n$ and n is the number of time steps, is given by:

$$T_{D,i} = \frac{1}{\Gamma(\beta_i)} \Gamma\left(\beta_i, \frac{r_D^2}{4(t_{D,i} - t_{D,i-1})}\right) + \frac{r_D^{\beta_i}}{2(t_{D,i} - t_{D,i-1})} \int_0^\infty u^{1-\beta_i} \exp\left(-\frac{u^2 + r_D^2}{4(t_{D,i} - t_{D,i-1})}\right) I_\beta\left(\frac{ur_D}{2(t_{D,i} - t_{D,i-1})}\right) T_D(u, t_{D,i-1}) du \quad (4.10)$$

where $t_{D,0} = 0$, $T_{D,i} = \left(\frac{T_o - T(t)}{T_o - T_{inj,i}}\right)$, $\beta_i = \frac{\rho_w C_w q_i}{4\pi h \lambda_r}$, and $T_D(u, t_{D,i-1})$ is the temperature solution at the end of the previous time step. The obtained solution constitutes two terms: the first term in the RHS is a solution of the same IBVP but with homogenous initial condition. (i.e., $T_D(r_D, t_D = 0) = 0$) which has been previously developed by Chen and Reddell (1983). The second term in the RHS is a solution of the same IBVP but with homogenous inner boundary condition (i.e., $T_D(r_D = 0, t_D) = 0$).

During the shut-in period, the advection-diffusion equation is simplified to a heat diffusion equation because fluid velocity becomes negligible during the shut-in period. The governing equation for heat transfer during the shut-in period is described by the following equation in dimensionless form:

$$\frac{\partial T_D}{\partial \Delta t_D} = \frac{\partial^2 T_D}{\partial r_D^2} + \frac{1}{r_D} \frac{\partial T_D}{\partial r_D} \quad (4.11)$$

where $\Delta t_D = t_D - t_{injD}$. The corresponding initial and boundary conditions are as follows:

$$T_D(r_D, \Delta t_D = 0) = T_D(r_D, t_D = t_{injD}) \quad (4.12)$$

$$\lim_{r_D \rightarrow 0} \left(\frac{\partial T_D}{\partial r_D}\right) = 0 \quad (4.13)$$

$$\lim_{r_D \rightarrow \infty} \left(\frac{\partial T_D}{\partial r_D}\right) = 0 \quad (4.14)$$

The sandface temperature solution during the warmback period is obtained using Hankel transformation. The details of the solution derivation are given in Appendix C, according to which, the sandface temperature solution is given by:

$$T_{wD}(\Delta t_D) = \frac{1}{2\Delta t_D} \int_0^\infty u \exp\left(-\frac{u^2}{4\Delta t_D}\right) T_D(u, t_D = t_{injD}) du \quad (4.15)$$

Eq. 4.15 describes the sandface temperature solution during the warmback period assuming a negligible size of the wellbore over the injection interval. This assumption is feasible for long

shut-in periods that exceed the early-time effect of the thermal storage capacity of the wellbore. For cases of short shut-in periods (few hours), considering the thermal storage capacity of the wellbore is required. This consideration will be made in the Section 4.3.

4.2. Injection under Variable Rate and Variable Temperature for Advection-dominant Heat Transfer

The problem presented in the previous section can be simplified if the heat transfer during the injection period is purely advection. This assumption is most feasible for short injection periods and high injection rates (i.e., high Péclet number) (LaForce et al. 2014). In this case, the governing equation for heat transfer in the reservoir is simplified to the following transport equation:

$$\frac{\partial T_D}{\partial t_D} + 4\beta(t_D) \frac{\partial T_D}{\partial r_D^2} = 0 \quad (4.16)$$

The corresponding initial and boundary conditions in the dimensionless form are described by Eq. 4.3 - Eq. 4.5. Since the IBVP is homogenous except for the inner boundary condition, superposition can be used to obtain the solution of the advection problem (see the details of the solution derivation in Appendix D). Accordingly, the temperature solution during the injection period is given by:

$$T_D(r_D, t_D) = \sum_{i=0}^{n-1} \left(1 - U \left(r_D^2 - \left\{ r_{TD}(t_D)^2 - r_{TD}(t_{D,i})^2 \right\} \right) \right) \Delta T_{injD,i} \quad (4.17)$$

where $\Delta T_{injD,i} = T_{injD,i+1} - T_{injD,i}$, $\Delta T_{injD,0} = T_{injD,1} - T_{injD,0} = T_{injD,1}$, $r_{TD}(t_D)$ is the dimensionless radius of the thermal front $\left(= \sqrt{\frac{1}{\pi r_w^2 h} \left(\frac{\rho_w C_w}{\rho_r C_r} \right) W_{inj}(t)} \right)$, and W_{inj} is the cumulative injected volume.

During the warmback period, the governing equation for the heat transfer is described by Eq. 4.11. The initial and boundary conditions are described by Eq. 4.12 – 4.14. Using Hankel transformation technique, the solution of the sandface temperature during the warmback period is given by:

$$T_{wD}(\Delta t_D) = \sum_{i=0}^{n-1} \Delta T_{injD,i} \left[1 - \exp \left(-\frac{r_{TD}(t_{injD})^2 - r_{TD}(t_{injD,i})^2}{4\Delta t_D} \right) \right] \quad (4.18)$$

For extended shut-in time, Eq. 4.18 is simplified to the following form:

$$T_{wD}(\Delta t_D) = \sum_{i=0}^{n-1} \Delta T_{injD,i} \frac{\left(r_{TD}(t_{injD})^2 - r_{TD}(t_{injD,i})^2 \right)}{4\Delta t_D} \quad (4.19)$$

Writing this equation in dimensional form gives:

$$\Delta T_w (=T_o - T_w) = \frac{1}{\Delta t} \left(\frac{\rho_w C_w}{4\pi\lambda_r h} \right) \sum_{i=0}^{n-1} \Delta T_{inj,i} (W_{inj}(t_{inj}) - W_{inj}(t_{inj,i})) \quad (4.20)$$

If the time steps are selected for equal temperature change segments, $\Delta T_{inj,seg}$, the following sandface temperature solution is obtained.

$$\Delta T_w (=T_o - T_w) = \frac{\Delta T_{inj,seg}}{\Delta t} \left(\frac{\rho_w C_w}{4\pi\lambda_r h} \right) \sum_{i=0}^{n-1} (W_{inj}(t_{inj}) - W_{inj}(t_{inj,i})) \quad (4.21)$$

The late shut-in time asymptotic solution described by Eq. 4.21 presents a simple form for the sandface temperature that can be put in a simple graphical technique for the inversion purpose as will be shown in Section 4.5. Note that for constant rate, Eq. 4.21 simplifies to:

$$\Delta T_w (=T_o - T_w) = \frac{\Delta T_{inj,seg}}{\Delta t} \left(\frac{\rho_w C_w q}{4\pi\lambda_r h} \right) \sum_{i=0}^{n-1} (t_{inj} - t_{inj,i}) \quad (4.22)$$

As shown in Appendix E, an exact analytical solution can be derived by accounting for both diffusion and advection if the injection rate is assumed constant, while the injection temperature is variable:

$$T_{wD}(\Delta t_D) = \sum_{i=0}^{n-1} \Delta T_{injD,i} \left(1 - \left(1 + \frac{t_{injD} - t_{injD,i}}{\Delta t_D} \right)^{-\beta} \right) \quad (4.23)$$

This solution will be simplified to Eq. 4.22 at late shut-in time (see details in Appendix E). If, in addition to the constant rate, the injection temperature is also fixed, we get:

$$\Delta T_w (=T_o - T_w) = \frac{\Delta T_{inj,seg}}{\Delta t} \left(\frac{\rho_w C_w q}{4\pi\lambda_r h} \right) t_{inj} \quad (4.24)$$

The solution presented for constant rate and constant injection temperature is asymptotically identical to Eq. 4.24. The above solutions are summarized in Table 4.1. The analytical solutions developed so far assume a negligible size of the wellbore system (i.e., line source). This assumption can be valid after sufficient shut-in time. However, if the shut-in period is short (few hours), the thermal storage capacity of the wellbore interferes with the temperature behavior. In this case, the thermal storage capacity of the wellbore must be considered during solving the warmback problem. In the next section, the energy balance equation of the wellbore is solved along with the governing equation of heat transfer in the reservoir to account for this effect.

Table 4. 1. Summary of the closed-form analytical solutions and the corresponding asymptotic forms.

	Constant q , constant T_{inj}	Constant q , variable T_{inj}	Variable q , variable T_{inj}
Solution	$\frac{T_o - T_w}{T_o - T_{inj}} = 1 - \left(1 + \frac{t_{inj}}{\Delta t}\right)^{\left(\frac{\rho_w C_w q}{4\pi\lambda_r h}\right)}$	$\frac{T_o - T_w}{\Delta T_{inj,seg}} = \sum_{j=0}^{n-1} \left(1 - \left(1 + \frac{t_{inj} - t_{inj,j}}{\Delta t}\right)^{\left(\frac{\rho_w C_w q}{4\pi\lambda_r h}\right)}\right)$	$\frac{T_o - T_w}{\Delta T_{inj,seg}} = \sum_{i=0}^{n-1} 1 - \exp\left(-\frac{1}{\Delta t} \left(\frac{\rho_w C_w}{4\pi\lambda_r h}\right) (W_{inj}(t_{inj}) - W_{inj}(t_{inj,i}))\right)$
Late-time solution	$\frac{T_o - T_w}{T_o - T_{inj}} = \left(\frac{\rho_w C_w q}{4\pi\lambda_r h}\right) \left(\frac{t_{inj}}{\Delta t}\right)$	$\frac{T_o - T_w}{\Delta T_{inj,seg}} = \left(\frac{\rho_w C_w q}{4\pi\lambda_r h}\right) \frac{\sum_{j=0}^{n-1} (t_{inj} - t_{inj,j})}{\Delta t}$	$\frac{T_o - T_w}{\Delta T_{inj,seg}} = \left(\frac{\rho_w C_w}{4\pi\lambda_r h}\right) \frac{\sum_{i=0}^{n-1} (W_{inj}(t_{inj}) - W_{inj}(t_{inj,i}))}{\Delta t}$

4.3. Accounting for the Wellbore System

In this section, an analytical solution for the warmback period is presented considering the energy balance equation of the wellbore over the injection interval. The solution is developed for two types of well completions: cased-hole and open-hole. The solution accounts for the effects of the thermal storage capacity of the wellbore for the open hole. For the cased hole, it also accounts for the thermal resistances of the tubing, casing, and cement sheath that separate the temperature measurement tool from the sandface. The governing equation that describes heat transfer in the reservoir during the shut-in period is given by Eq. 4.11. The corresponding initial and outer boundary conditions are described by Eq. 4.12 and Eq. 4.14; respectively, however, the inner boundary condition is modified to be as follows:

$$\left(r_D \frac{\partial T_D}{\partial r_D} \right) \Big|_{r_D=1} = Q_D \quad (4.25)$$

where Q_D is the dimensionless rate of heat transfer at the reservoir-wellbore interface

$$\left(\frac{Q}{2\pi h \lambda_r (T_{inj} - T_o)} \right). \text{ The obtained IBVP is a heat conduction problem in radial coordinates that is}$$

subject to a non-homogenous initial condition and a non-homogenous inner boundary condition. According to Özışık (1980), superposition principle can be used to obtain the solution. The solution of the IBVP has to be a summation of solutions of two different heat conduction problems: the first problem is identical to the above heat conduction problem but with a homogenous initial condition. The second one is identical to the above heat conduction problem but with a homogenous inner boundary condition. Since the radius of the wellbore is small, the line-source assumption can be adopted (Li and Lai 2015). The solution is then given by:

$$T_D(r_D, \Delta t_D) = -\frac{Q_D}{2} E_1 \left(\frac{r_D^2}{4\Delta t_D} \right) + \frac{1}{2\Delta t_D} \int_0^\infty u \exp \left(-\frac{u^2 + r_D^2}{4\Delta t_D} \right) I_o \left(\frac{ur_D}{2\Delta t_D} \right) T_D(u, t_D = t_{injD}) du \quad (4.26)$$

where $E_1\left(\frac{r_D^2}{4\Delta t_D}\right) = \int_{\frac{r_D^2}{4\Delta t_D}}^{\infty} \frac{e^{-u}}{u} du$ and $T_D(u, t_D = t_{injD})$ is the temperature solution at the end of the

injection period. Accordingly, the sandface temperature solution is given by Eq. 4.27 by assigning $r_D = 1$ in the first term of Eq. 4.26 and $r_D \rightarrow 0$ in the second term of Eq. 4.26.

$$T_D(r_D = 1, \Delta t_D) = Q_D I_1(\Delta t_D) + I_2(\Delta t_D) \quad (4.27)$$

where

$$I_1(\Delta t_D) = -\frac{1}{2} E_1\left(\frac{1}{4\Delta t_D}\right) \quad (4.28)$$

$$I_2(\Delta t_D) = \begin{cases} 1 - \left(\frac{t_{injD} + \Delta t_D}{\Delta t_D}\right)^{-\beta} & \text{for constant } q \text{ and constant } T_{inj} \\ \sum_0^{n-1} \Delta T_{injD,i} \left(1 - \left(1 + \frac{t_{injD} - t_{injD,i}}{\Delta t_D}\right)^{-\beta}\right) & \text{for constant } q \text{ and variable } T_{inj} \\ \frac{1}{2\Delta t_D} \int_0^{\infty} u \exp\left(-\frac{u^2}{4\Delta t_D}\right) T_D(u, t_D = t_{injD}) du & \text{for variable } q \text{ and variable } T_{inj} \\ \sum_{i=0}^{n-1} \Delta T_{injD,i} \left[1 - \exp\left(-\frac{r_{TD}(t_{injD})^2 - r_{TD}(t_{injD,i})^2}{4\Delta t_D}\right)\right] & \text{for variable } q \text{ and variable } T_{inj} \end{cases} \quad (4.29)$$

(Section 4.1)

(Section 4.2)

If the heat flux at the reservoir/wellbore interface (Q_D) is neglected (i.e., isolated boundary condition), the solution described by Eq. 4.27 is simplified to the solutions presented in the previous section. The first term of Eq. 4.27 dominates the wellbore temperature solution at the early shut-in time, while the second term dominates the temperature solution at the late shut-in time. Hasan and Kabir (2012) provided a simple yet an accurate expression for $I_1(\Delta t_D)$ given by the following equation:

$$I_1(\Delta t_D) = -\ln\left[e^{-0.2\Delta t_D} + (1.5 - 0.3719e^{-0.2\Delta t_D})\sqrt{\Delta t_D}\right] \quad (4.30)$$

Eq. 4.30 is proved to be accurate especially at early shut-in time. The energy balance equation of the wellbore over the injection interval is described by Eq. 4.31.

$$V_{wb} \rho_w C_w \frac{\partial T_{wb}}{\partial \Delta t} = Q \quad (4.31)$$

where Q represents the rate of heat transfer from the reservoir to the wellbore and $V_{wb} (= \pi r_w^2 h)$ is wellbore volume over the injection interval. Writing this equation in dimensionless form gives:

$$\frac{\partial T_{wbD}}{\partial \Delta t_D} = \theta Q_D \quad (4.32)$$

where $\theta = 2 \frac{\rho_r C_r}{\rho_w C_w}$. The rate of heat transfer Q for open-hole and cased-hole completions are given by (Ramey 1962):

$$Q = 2\pi h \lambda_r \left(r \frac{\partial T}{\partial r} \right) \Big|_{r=r_w} \quad \text{for open-hole} \quad (4.33)$$

$$Q = 2\pi r_w h U_T (T|_{r=r_w} - T_{wb}) \quad \text{for cased-hole} \quad (4.34)$$

where U_T is the overall heat transfer coefficient which is defined for tubing and casing by (Ramey 1962):

$$U_T|_{r=r_i} = \left(\frac{1}{h_{ii}} + \frac{r_{ii} \ln \frac{r_{io}}{r_{ii}}}{k_t} + \frac{r_{ii}}{r_{io} h_a} + \frac{r_{ii} \ln \frac{r_{co}}{r_{ci}}}{k_c} + \frac{r_{ii} \ln \frac{r_{wb}}{r_{co}}}{k_{cem}} \right)^{-1} \quad (4.35)$$

$$U_T|_{r=r_{ci}} = \left(\frac{1}{h_{ci}} + \frac{r_{ci} \ln \frac{r_{co}}{r_{ci}}}{k_c} + \frac{r_{ci} \ln \frac{r_{wb}}{r_{co}}}{k_{cem}} \right)^{-1} \quad (4.36)$$

In dimensionless form, Eq. 4.33 and Eq. 4.34 become:

$$Q_D = \left(r_D \frac{\partial T_D}{\partial r_D} \right) \Big|_{r_D=1} \quad \text{for open-hole} \quad (4.37)$$

$$Q_D = a_3 (T_D(r_D=1) - T_{wbD}) \quad \text{for cased-hole} \quad (4.38)$$

where $a_3 = \frac{r_w U_T}{\lambda_r}$. The governing equation of the wellbore temperature for cased-hole completion is obtained by substituting Eq. 4.38 into Eq. 4.27. The resulting equation relates the wellbore temperature, T_{wbD} with the sandface temperature, $T_D(r_D=1)$. Next, it is substituted into Eq. 4.32 and the following governing equation of the wellbore temperature, T_{wbD} is obtained:

$$\frac{\partial T_{wbD}}{\partial \Delta t_D} + \theta a_3 \left(\frac{1}{(1 - a_3 I_1(\Delta t_D))} \right) T_{wbD} = \theta a_3 \left(\frac{I_2(\Delta t_D)}{(1 - a_3 I_1(\Delta t_D))} \right) \quad (4.39)$$

The solution of Eq. 4.39 subject to the initial condition $T_{wbD}(\Delta t_D = 0) = 1$ is as follows (Kreyszig 2009).

$$T_{wbD}(\Delta t_D) = e^{-h(\Delta t_D)} \left(\int_0^{\Delta t_D} e^{h(\tau)} r(\tau) d\tau + 1 \right) \quad (4.40)$$

where $h(\Delta t_D) = \int_0^{\Delta t_D} \frac{\theta a_3}{1 - a_3 I_1(u)} du$ and $r(\Delta t_D) = \frac{\theta a_3 I_2(\Delta t_D)}{1 - a_3 I_1(\Delta t_D)}$. For the case of open-hole completion, the energy balance equation of the wellbore is obtained by replacing Q_d in Eq. 4.32 with that in Eq. 4.27 keeping in mind that the sandface temperature, $T_D(r_D = 1)$ is identical to the wellbore temperature, T_{wbD} in the case of open-hole completion. Accordingly, the following governing equation of wellbore temperature is obtained:

$$T_{wbD}(\Delta t_D) = e^{-h(\Delta t_D)} \left(\int_0^{\Delta t_D} e^{h(\tau)} r(\tau) d\tau + 1 \right) \quad (4.41)$$

where $h(\Delta t_D) = - \int_0^{\Delta t_D} \frac{\theta}{I_1(u)} du$, $r(\Delta t_D) = -\theta \frac{I_2(\Delta t_D)}{I_1(\Delta t_D)}$.

4.4. Forward Modeling

In this section, forward modeling procedure is presented to evaluate the temperature profile in the reservoir during the injection and the shut-in periods. Since the analytical solutions developed for variable rate – variable temperature and constant rate – variable temperature are presented in a closed form, forward modeling procedure using these solutions is straightforward. However, the semi-analytical solution is not presented in a closed form and consequently, the discretization approach discussed earlier is required to obtain the temperature solution.

The procedure consists of few steps: the first step is to discretize the rate and temperature history during the injection period such that the rate and temperature are constant during the time step period. Next, Eq. 4.10 is used to obtain the temperature profile at the end of the time step period. The obtained temperature profile is used as the initial condition while solving for the reservoir temperature in the next time step. This procedure is repeated up to the end of the injection period. Finally, Eq. 4.15 is used to solve for the sandface temperature during the shut-in period considering the temperature profile obtained at the end of the injection period as the initial condition. Fig. 4.2 illustrates a flow diagram of the forward modeling procedure. Time step selection is subject to the engineering judgment; small time steps should be selected at time intervals of rapid change in either injection rate or injection temperature, while larger time steps can be selected for time intervals of slight changes of temperature or rate.

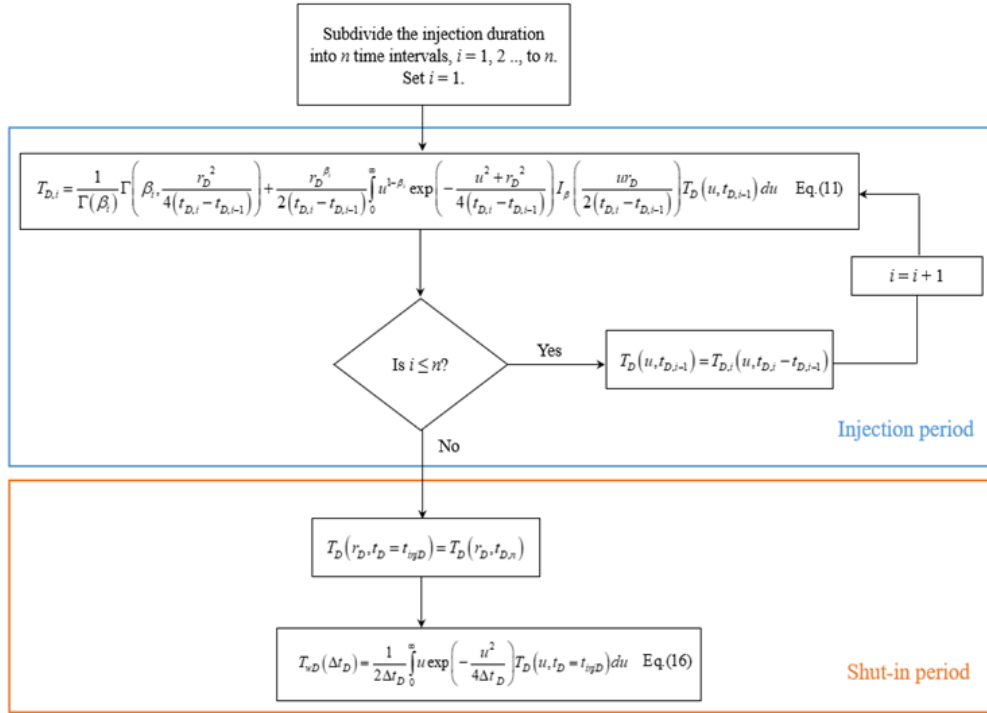


Figure 4. 2. Flow chart of the solution procedure using the semi-analytical solution for injection under variable-rate and variable-temperature and the subsequent warmback period.

4.5. Inverse Modeling

Inverse modeling aims at evaluating the injection profile over a stratified reservoir that is completed by a commingled injection well using the sandface temperature data. The solution procedure presented in the previous section is adopted with an optimization routine to solve for the correct injection profile. The optimization tool iterates on the injection profile that provides sandface temperature solution with the best match with the observed temperature data during the warmback period. In this work, Genetic Algorithm (GA) is used for the optimization process. In general, the traditional optimization routines converge to local minimum solutions; however, GA can get out of the local minimum solutions and reach the global minimum solution because of its special features (Wh et al. 1992). The fitness function that is used to evaluate the accuracy of the solution is described by Eq. 4.42.

$$\text{RMSE} = \sqrt{\frac{\sum_{j=1}^m (T_{w,cal}(j) - T_{w,obs}(j))^2}{m}} \quad (4.42)$$

where $j=1, 2, \dots, m$ indicates the j^{th} measured temperature during the warmback period, while m is the number of the temperature measurements. Numerical inversion using GA minimization is required when using the semi-analytical solution as the forward model. This technique is valid for any shut-in durations. However, graphical inversion can be applied if the solution presented in Section 4.2 is used which assumes negligible heat conduction compared with advection.

Consequently, the following procedure can be used to infer the injection profile assuming uniform injection temperature over the injection interval.

- Divide the injection history into time periods with equal temperature change segments, $\Delta T_{inj,seg}$.
- Plot the sandface temperature change, $\Delta T_w (= T_o - T_w(\Delta t))$ during the shut-in period versus the shut-in time, Δt on a log-log scale and identify the data to be fitted with a negative unit slope straight line.
- Determine the intercept of the fitted line with the vertical axis, b at $\Delta t = 1$. The following summation can be estimated.

$$\sum_{i=0}^{n-1} (W_{inj}(t_{inj}) - W_{inj}(t_{inj,i})) = \frac{b}{\Delta T_{inj,seg}} \times \left(\frac{4\pi\lambda_r h}{\rho_w C_w} \right) \quad (4.43)$$

The estimated summation in Eq. 4.43 is not intuitively useful, however it can be used to estimate the injection profile according to the following (see the details in Appendix D).

$$\frac{W_{inj,j}}{W_{inj,j+1}} = \frac{\left(\sum_{i=0}^{n-1} (W_{inj}(t_{inj}) - W_{inj}(t_{inj,i})) \right)_j}{\left(\sum_{i=0}^{n-1} (W_{inj}(t_{inj}) - W_{inj}(t_{inj,i})) \right)_{j+1}} = \frac{b_j}{b_{j+1}} \times \frac{\left(\frac{4\pi\lambda_r h}{\rho_w C_w} \right)_j}{\left(\frac{4\pi\lambda_r h}{\rho_w C_w} \right)_{j+1}} \quad (4.44)$$

For the case of constant rate and variable temperature, the same procedure as above can be followed because the late shut-in time asymptotic solution given by Eq. 4.22 is a special case of the asymptotic solution for variable rate – variable temperature when injection rate is fixed. This can be proved by using the above procedure with Eq. 4.22 in place of Eq. 4.21. Accordingly, the late shut-in time asymptotic behavior of the sandface temperature is mainly dependent on the cumulative injected volume and the magnitude of injection temperature change, $(T_o - T_{inj,n})$ regardless of the injection rate and injection temperature history. However, at early shut-in time, temperature recovery is strongly dependent on the injection temperature and injection rate history. Consequently, the proposed graphical technique should be used only for extended shut-in time; otherwise, the semi-analytical model with regression analysis should be used to evaluate the injection profile.

The previous procedure assumes negligible wellbore fluid interventions on the temperature recovery. This is feasible when the fiber optic cable is cemented behind the production casing and/or shut-in time is extended for long period. For the case of short shut-in periods in which the effect of the thermal wellbore storage cannot be overlooked, the analytical solutions developed considering thermal wellbore storage should be used with the help of regression analysis to infer the injection profile.

4.6. Validation with Numerical Results

In this section, the forward models presented in this work are validated against the thermal compositional reservoir simulator CMG-STAR3 (2020) using different scenarios for water injection. The inversion procedures are applied to the numerical data obtained from the synthetic cases and the obtained inversion results are compared with those obtained from the numerical simulation tool. The input data for the synthetic cases are given in Table 4.2. The first case is presented for a stratified reservoir that consists of five layers with different permeabilities ranging from 300 md (uppermost layer) to 100 md (lowermost layer). The reservoir is subject to a short-term injection of 0.25 days under a constant rate of 400 bbl/day and variable temperature. The injection temperature declines exponentially from 150 °F with a decline rate of 0.8514 hour⁻¹ and stabilizes at 120 °F at the end of the injection period (see Fig. 4.3). Finally, injection stops to allow for the warmback. Injection temperature history is discretized into small time steps of equal temperature segments ($\Delta T_{inj,seg} = 2$ °F) as shown in Fig. 4.3. Finer time steps are used at the early injection time when temperature declines steeply, while larger time steps are adopted at the late injection time when temperature declines gently.

Fig. 4.4 (a) and (b) illustrate the temperature profiles in the reservoir for the uppermost and lowermost layers, respectively during the injection period at $t = 0.125$ and 0.25 days. The thermal front propagates deeper in the uppermost layer which has higher injectivity compared with the lowermost layer. Fig. 4.4 (c) and (d) illustrate how the temperature perturbation dissipates by the effect of heat diffusion in the reservoir during the warmback period at $\Delta t = 1, 2,$ and 3 days. Fig. 4.5 illustrates the sandface temperature recovery for the injection zones during the warmback period. It is evident from Fig. 4.5 that the temperature of the uppermost layer that has the highest permeability ($k = 300$ md) rebounds slowly compared with the other layers which have lower permeabilities. On the other hand, the temperature of the lowermost layer which has the minimum permeability ($k = 100$ md) recovers quickly compared with the other layers.

Case 1 is modified into Case 2 by allowing for injection rate variation. For Case 2, the injection rate declines exponentially from 700 bbl/day with a decline rate of 0.6 hour⁻¹ and stabilizes at 400 bbl/day by the end of the injection period, while the injection temperature is identical to that presented in Fig. 4.3 (see Fig. 4.6). Finally, injection stops after 6 hours to allow for the warmback. In this case, both rate and temperature change smoothly during the injection period which is the most likely scenario in actual injection operations. The forward modeling procedure described in Section 4.4 is adopted to evaluate reservoir temperature during the injection and shut-in periods. The injection history is discretized into 12 time-steps (single-step = 0.5 hr) as shown in Fig. 4.6. Fig. 4.7 (a) and (b) illustrate the temperature profiles in the uppermost and lowermost layers, respectively during the injection period at $t = 0.125$ and 0.25 days. Fig. 4.7 (c) and (d) illustrate the temperature profiles in the uppermost and lowermost layers, respectively during the warmback period at $\Delta t = 1, 2,$ and 3 days. Fig. 4.8 illustrates the sandface temperature recovery for the injection zones during the warmback period. The perfect match between the analytical and numerical results indicates that the adopted discretization of the injection history is sufficient and there is no need for finer discretization. In the next section, the inversion procedure will be used to evaluate injection rates or the injection profile for the synthetic cases presented in this section.

Table 4. 2. Input data for the validation cases (empty cells indicate identical properties to the left column).

Input data	Case 1	Case 2
Initial temperature, T_o (F)	150	-
Initial pressure, p_o (psi)	1500	-
Reservoir thickness, h (ft)	200	-
Porosity, ϕ (fraction)	0.3	-
Permeability, k (md)	300,250,20,150,100	300,250,20,150,100
Reservoir thermal conductivity, λ_r (Btu/ft hr F)	1.39	1.39
Rock heat capacity, C_r (Btu/lbm F)	0.12	-
Rock density, ρ_r (lbm/ft ³)	165	-
Water heat capacity, C_w (Btu/lbm F)	1	-
Water density, ρ_w (lbm/ft ³)	6.24	-
Residual oil saturation behind flooded front, S_{or} (fraction)	0	-
Injection time, t_{inj} (hours)	6	6
Injection rate, q (bbl/day)	400	variable
Number of grids (n_x , n_y , and n_z)	10,000 \times 1 \times 5	
Grid size (ft.)	Logarithmic growth from 0.001 to 0.65	

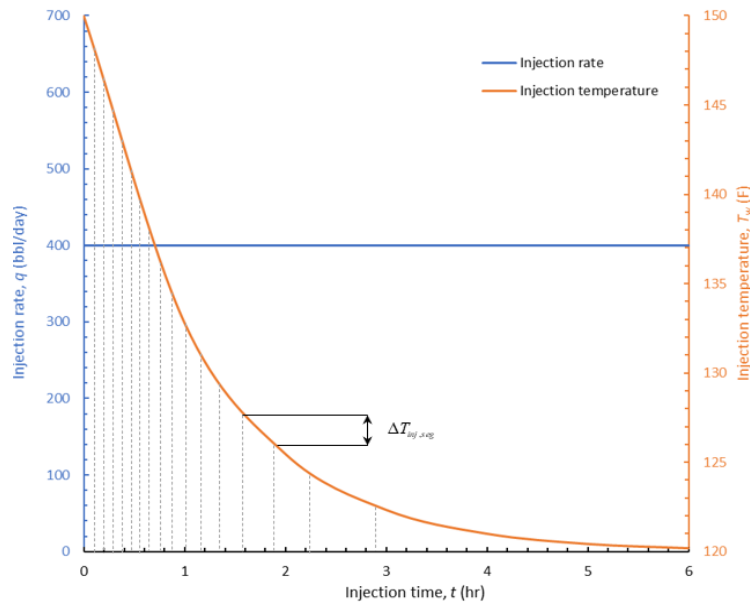


Figure 4. 3. Injection rate and injection temperature history during the injection period (Case 1).

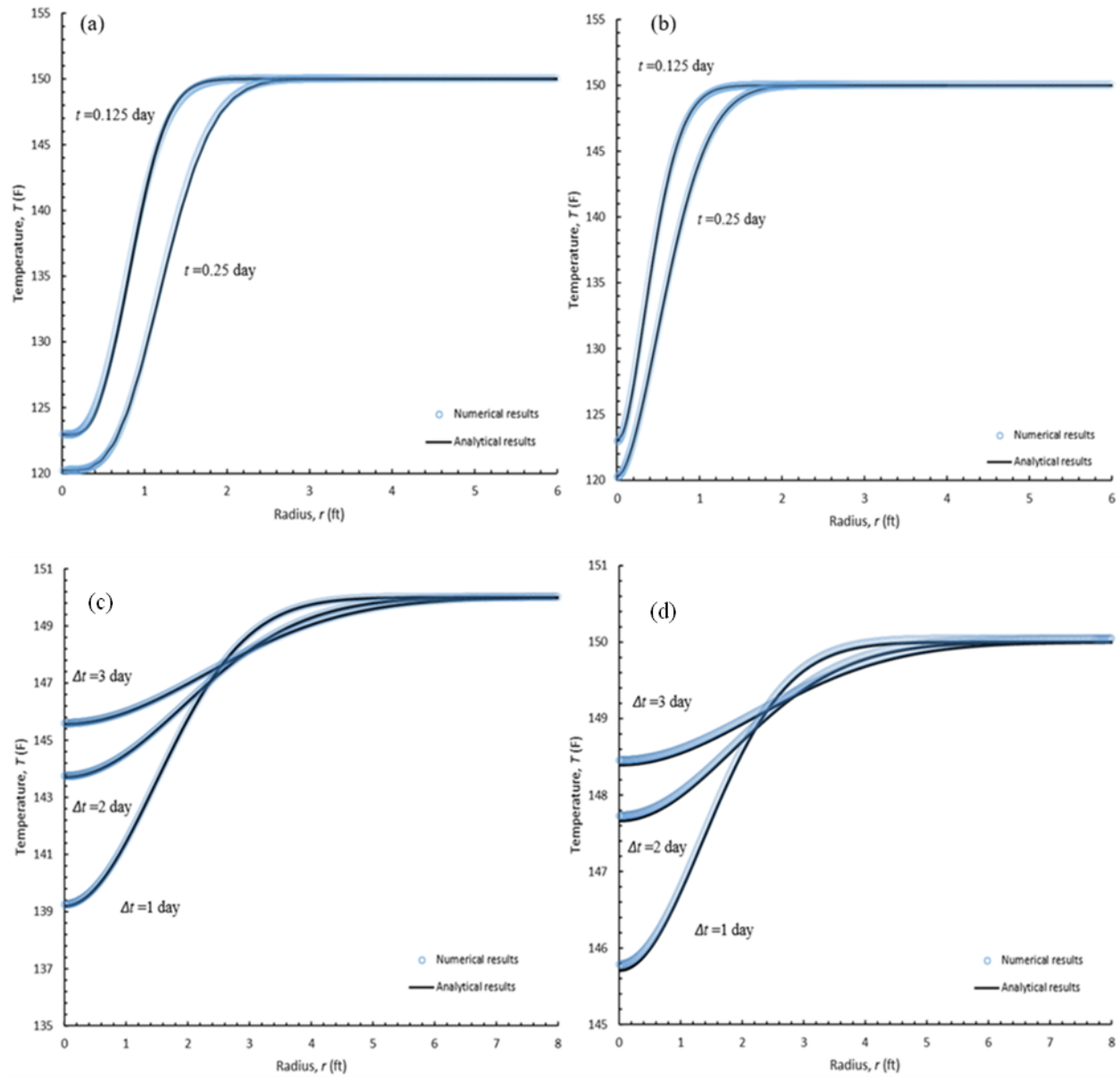


Figure 4. 4. Temperature profile during the injection period (a and b) and the shut-in period (c and d) for the uppermost layer and lowermost layer, respectively (Case 1).

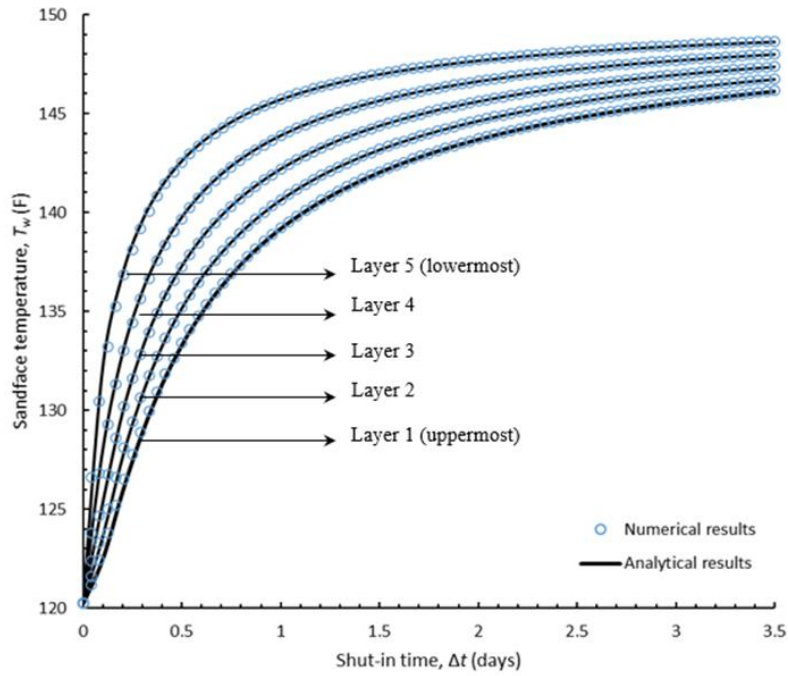


Figure 4. 5. Sandface temperature recovery during the warmback period at the injection layers (Case 1).

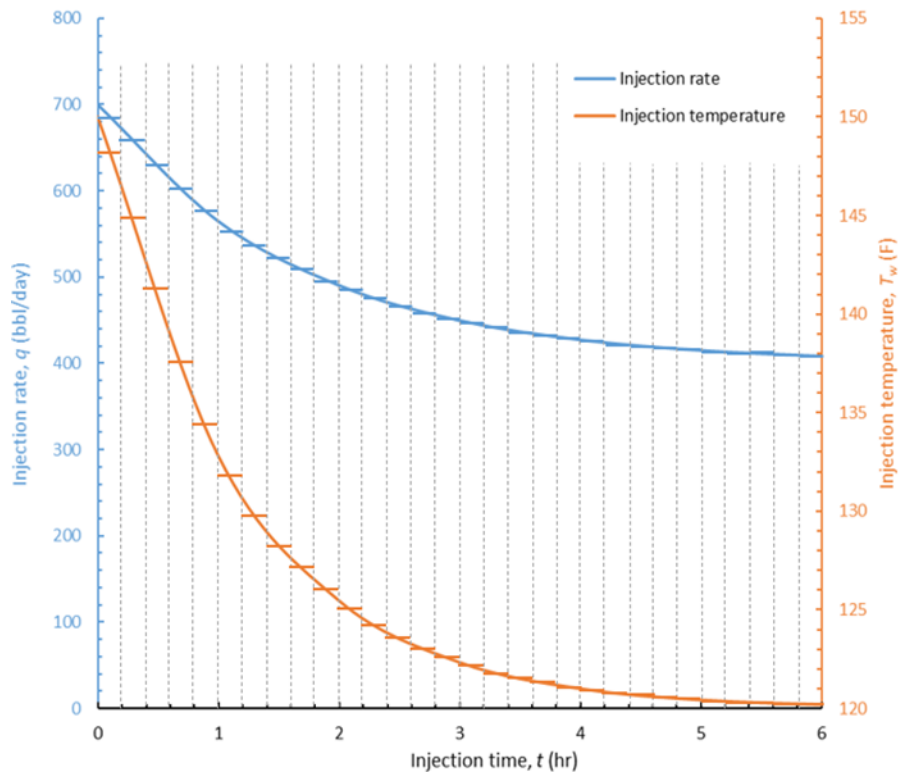


Figure 4. 6. Injection rate and injection temperature history during the injection period (Case 2).

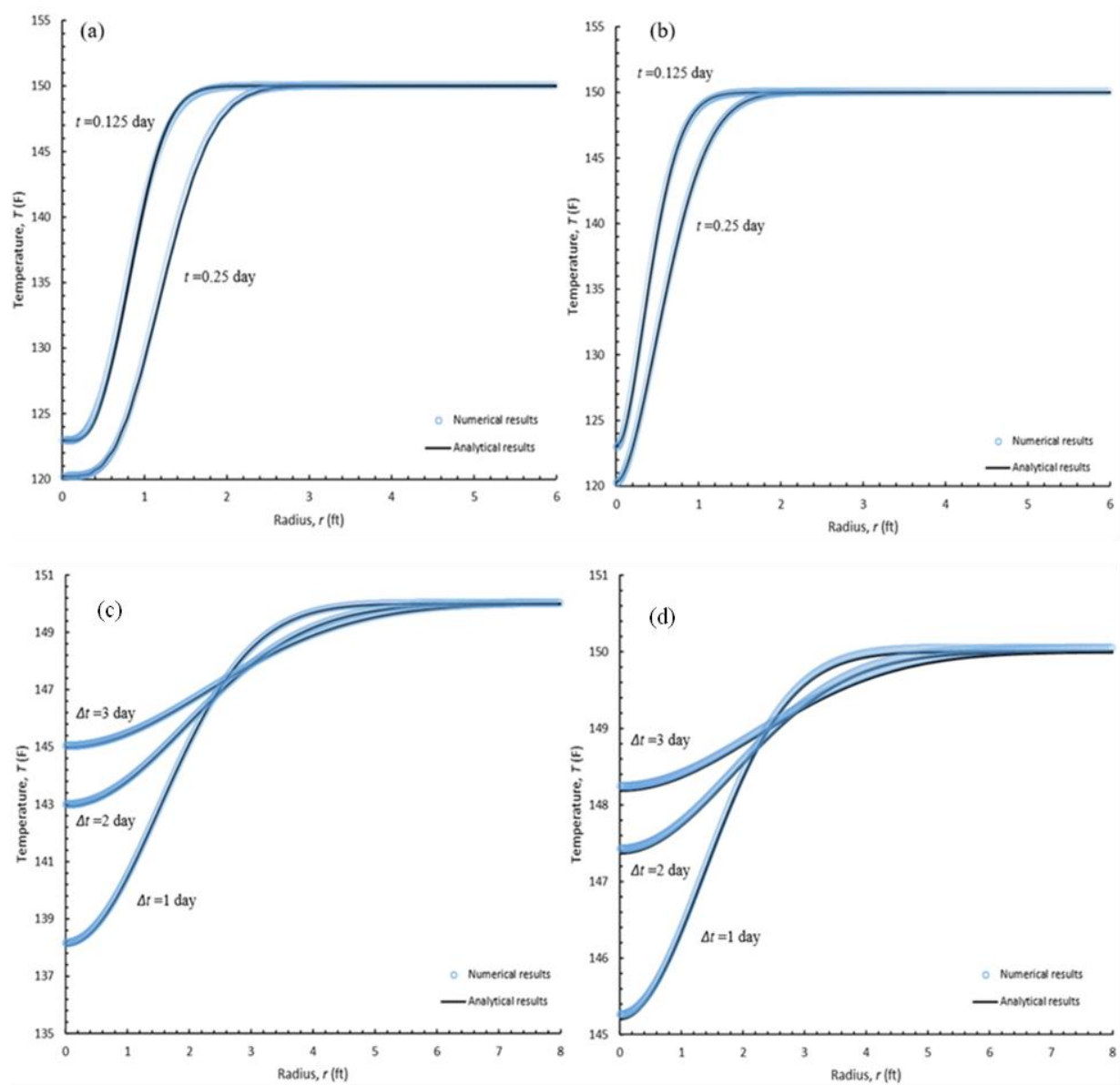


Figure 4. 7. Temperature profile during the injection period (a and b) and the shut-in period (c and d) for the uppermost layer and lowermost layer, respectively (Case 2).

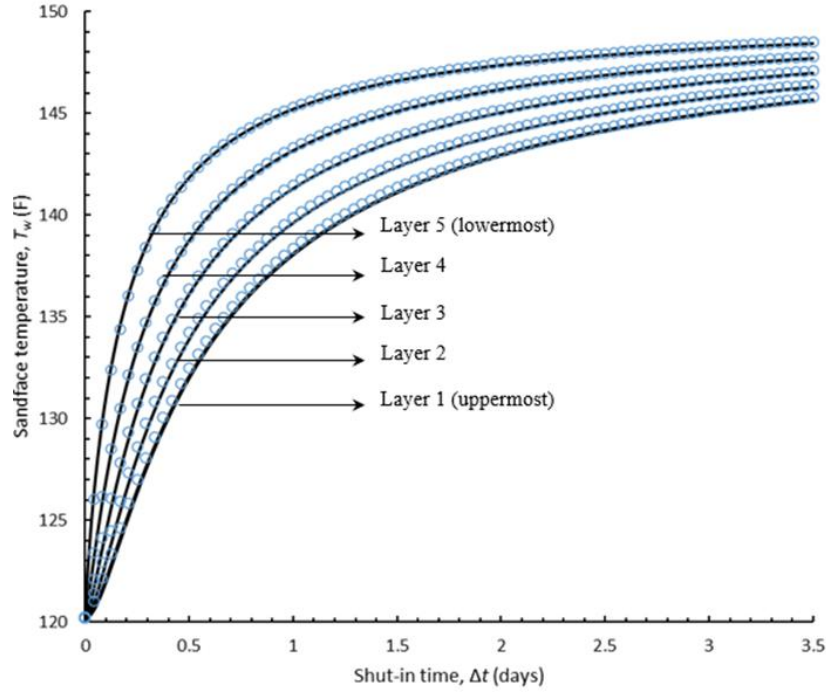


Figure 4. 8. Sandface temperature recovery during the warmback period at the injection zones (Case 2).

4.7. Inversion Procedure Application

In this section, the inversion procedures will be used to infer the injection profile for Cases 1 and 2. The numerical results of the sandface temperature history for these cases are analyzed using the inversion techniques to obtain the injection rates or injection profile. In Case 1, the graphical technique presented in Section 4.5 is applied to the sandface temperature results to infer the injection profile. The sandface temperature change ($= T_o - T_w(\Delta t)$) for every zone is plotted versus the shut-in time on a log-log scale. Fig. 4.9 (a) illustrates the application of the graphical technique for the numerical results. The data are fitted with straight lines with negative unit slope at the late shut-in time. The intercept of the fitted line with the vertical axis at $\Delta t = 1$ day is estimated for each zone, and Eq. 4.44 is used to obtain the corresponding injection rates. Table 4.3 summarizes the inversion results for Case 1. A good match is obtained between the numerical results and the values obtained using the graphical technique.

In Case 2, the graphical technique and the regression analysis are used for inverse modeling. The graphical technique presented in Section 4.5 is applied to the numerical results as illustrated in Fig. 4.9 (b). The plotted data are fitted with straight lines with negative unit slopes at the late shut-in time ($\Delta t > 3$ days). The intercept of the fitted line with the vertical axis at $\Delta t = 1$ day is estimated for each zone and Eq. 4.44 is used to obtain the corresponding injection rates. The inversion results obtained from the graphical technique are given in Table 4.3. As for the regression analysis approach, Genetic algorithm is used to iterate on the injection profile over the stratified reservoir. Fig. 4.10 (a) illustrates the injection history for the injection zones of the stratified reservoir as obtained from the regression analysis. Very good match is obtained between the numerical and the analytical results. Fig. 4.10 (b) illustrates the solution progress during the regression analysis. The inversion results using the regression technique are also given

in Table 4.3. Overall, good agreement is obtained between the numerical results and the inversion results. Based on the inversion results shown in Table 4.3, regression analysis provides slightly more accurate results compared with the graphical technique. Additionally, a relatively long shut-in time ($\Delta t > 3$ days) is required for the graphical technique to provide accurate results compared with the regression analysis that is applicable for any shut-in time durations.

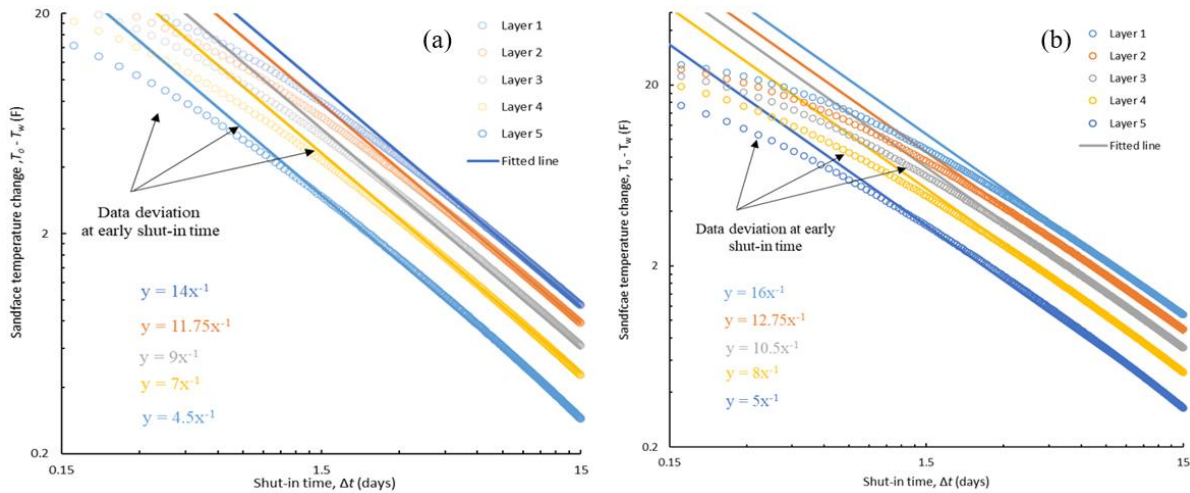


Figure 4. 9. Application of the graphical technique to the observed sandface temperature data of (a) Case 1, and (b) Case 2.

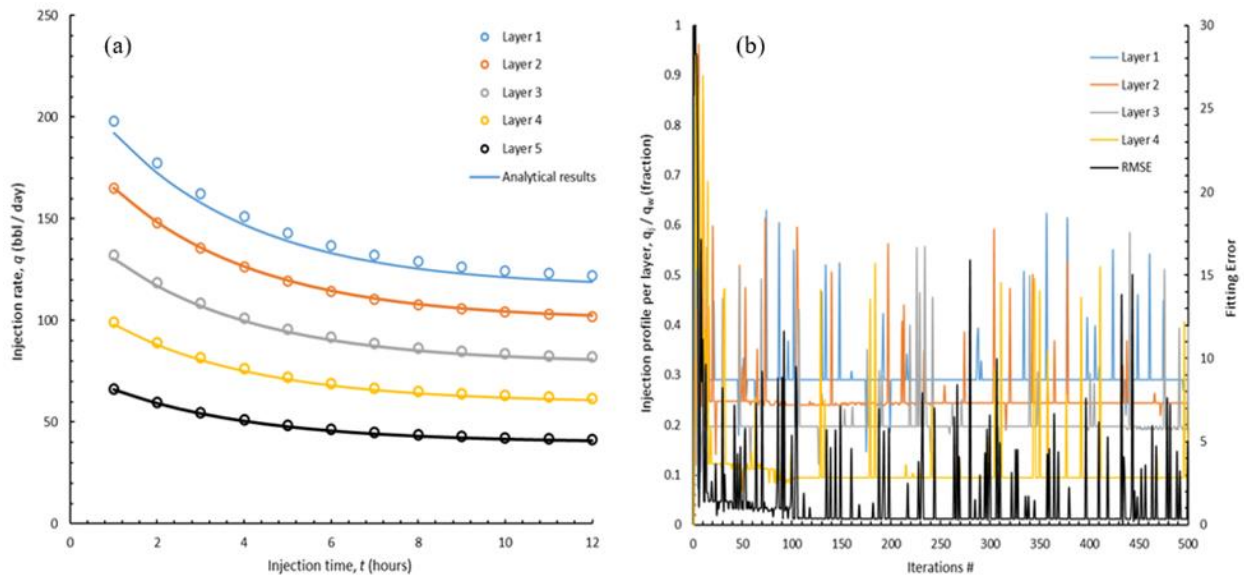


Figure 4. 10. Regression analysis results for Case 2: (a) Injection profile estimation (b) solution progress during the regression analysis.

Table 4. 3. Inversion results for Cases 1 and 2.

Zone	Case 1			Case 2		
	Injection rate per zone (bbl / day)					
	Analytical approach	Numerical results	Error (%)	Analytical results	Numerical results	Error (%)
Zone 1	121.081	119.092	1.670	0.306	0.300	2.189
Zone 2	101.621	99.613	2.017	0.244	0.250	2.337
Zone 3	77.838	80.070	2.788	0.201	0.200	0.460
Zone 4	60.540	60.459	0.135	0.153	0.150	1.952
Zone 5	38.919	40.766	4.531	0.096	0.100	4.560
Sum				1	1	

Chapter 5. Applications of Temperature Warmback Analysis for Injection Profile in Horizontal Wells

Water flooding using horizontal injection wells dates back to 1990, and it has been successfully utilized in many oilfields. The applications of horizontal injector-producer pattern to develop reservoirs with low permeability and small thickness can maintain reservoir pressure, improve recovery factor and decrease injection pressure (LING et al. 2008). The objective of this chapter is to develop an analytical approach to quantitatively estimate injection profile along the lateral of horizontal injection well using temperature data obtained during the warmback period.

The proposed analytical model solves heat transport equation in the reservoir during injection and shut-in periods assuming *linear* fluid flow and heat transport in the reservoir. Heat transfer by convection, conduction along flow direction, and heat exchange with the surrounding strata are considered during solving the heat transport equation. The developed solution is displayed in appropriate type curves that can be used to evaluate injection profile and the effective injection intervals of the horizontal well through type curve matching. The proposed solution and inversion procedure are validated against a thermally-coupled numerical reservoir simulator, CMG-STAR3 (2020).

5.1. Problem Description

A mathematical model is developed herein to simulate the transient temperature distribution during non-isothermal fluid injection into reservoir via horizontal well. Cold fluid is injected through horizontal well that is completed at mid-thickness of a reservoir which is bounded from above and below by impermeable cap and bed strata, respectively. Fig. 5.1 gives schematic illustration of the physical model. The assumptions adopted to formulate the problem are as follows:

- The reservoir is homogenous, isotropic, and of infinite extent in the lateral direction with uniform thickness, h . Heat is transferred via bulk fluid movement and heat conduction in lateral direction. Heat transfer with the surrounding is evident due to temperature gradient in the traverse direction, and reservoir thermal conductivity in traverse direction is assumed to be infinity.
- Fluid flow is linear with negligible flow into transverse direction. This assumption is valid for relatively thin layers which are suitable candidate for horizontal well completions. For anisotropic reservoirs of limited thickness whose vertical to horizontal permeability ratio is low, the effect of vertical flow by buoyance is therefore negligible.
- The surrounding cap and bed strata are assumed to be homogenous, isotropic, and impermeable. Heat transfer through the surroundings is caused solely by conduction due to temperature gradient in traverse direction with negligible heat transfer in the lateral direction.
- Fluid is injected with constant injection rate, q and constant injection temperature, T_{inj} .
- Thermal properties of reservoir and surrounding impermeable rock, such as effective heat capacity $\rho_r C_r = \phi \rho_w C_w + (1 - \phi) \rho_s C_s$ and effective thermal conductivity $\lambda_r = \phi \lambda_w + (1 - \phi) \lambda_s$ are assumed to be uniform and constant.

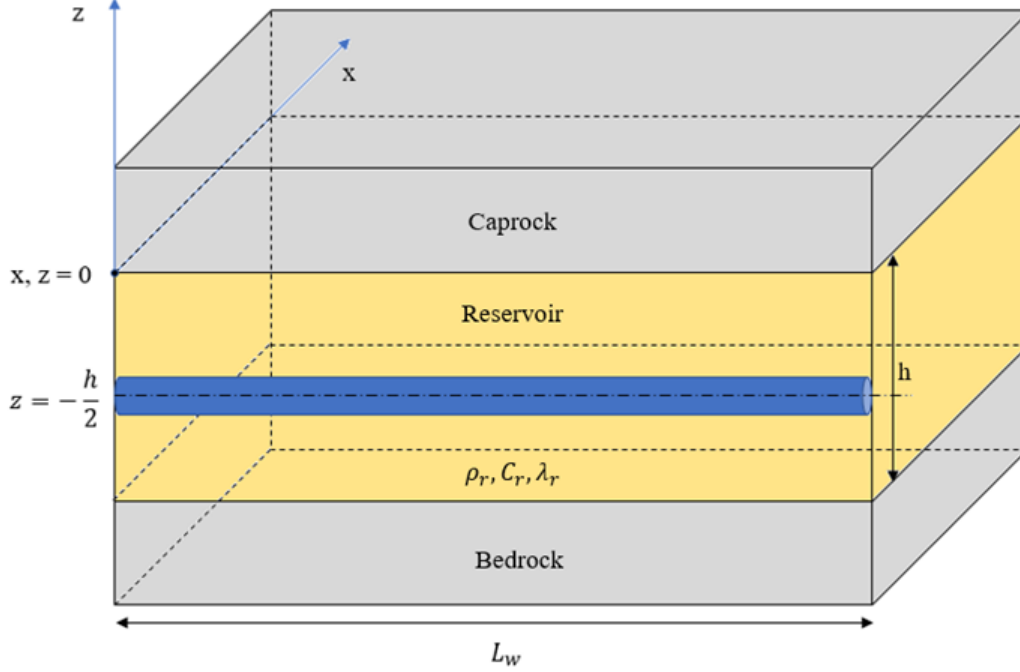


Figure 5. 1. Schematic illustration of the conceptual model showing a horizontal injection well completed through an injection zone which is sandwiched between an impermeable cap and bed strata.

The governing equation for heat transfer in the injection zone during the injection period is described by Eq. 5.1.

$$\rho_r C_r \frac{\partial T}{\partial t} + \rho_w C_w u_w \frac{\partial T}{\partial x} = \lambda_r \frac{\partial^2 T}{\partial x^2} + \frac{2\lambda_r}{h} \frac{\partial T_m}{\partial z} \Big|_{z=0} \quad (5.1)$$

where $u_w = q/hL_w$. The governing equation for the surrounding strata is described by the following heat conduction equation:

$$\lambda_r \frac{\partial^2 T_m}{\partial z^2} = \rho_r C_r \frac{\partial T_m}{\partial t} \quad (5.2)$$

The governing equations are subject to the following initial and boundary conditions for reservoir and surrounding strata, respectively:

$$T(x, t = 0) = T_o \quad (5.3)$$

$$T(x = 0, t) = T_{inj} \quad (5.4)$$

$$\lim_{x \rightarrow \infty} \frac{\partial T}{\partial x} = 0 \quad (5.5)$$

$$T_m(x, z, t = 0) = T_o \quad (5.6)$$

$$\lim_{z \rightarrow \infty} \frac{\partial T_m}{\partial z} = 0 \quad (5.7)$$

$$T_m(x, z = 0, t) = T(x, t) \quad (5.8)$$

After injection stops, fluid movement in the reservoir ceases and heat transfer in the reservoir and the surrounding strata are governed solely by conduction due to temperature gradient in lateral and transverse directions. The Initial-Boundary Value Problems (IBVP's) for the reservoir and the surrounding strata during the shut-in period are described by the following equations:

$$\rho_r C_r \frac{\partial T}{\partial \Delta t} = \lambda_r \frac{\partial^2 T}{\partial x^2} + \frac{2\lambda_r}{h} \frac{\partial T_m}{\partial z} \Big|_{z=0} \quad (5.9)$$

$$\lambda_r \frac{\partial^2 T_m}{\partial z^2} = \rho_r C_r \frac{\partial T_m}{\partial \Delta t} \quad (5.10)$$

$$T(x, \Delta t = 0) = T(x, t = t_{inj}) \quad (5.11)$$

$$T(x, \Delta t = 0) = T(x, t = t_{inj}) \quad (5.12)$$

$$\lim_{x \rightarrow 0} \frac{\partial T}{\partial x} = 0 \quad (5.13)$$

$$\lim_{x \rightarrow \infty} \frac{\partial T}{\partial x} = 0 \quad (5.14)$$

$$T_m(x, z, \Delta t = 0) = T_m(x, z, t = t_{inj}) \quad (5.15)$$

$$\lim_{z \rightarrow \infty} \frac{\partial T_m}{\partial z} = 0 \quad (5.16)$$

$$T_m(x, z = 0, \Delta t) = T(x, \Delta t) \quad (5.17)$$

where $\Delta t = t - t_{inj}$. The following definitions of dimensionless properties are introduced:

$$T_D = \frac{T_o - T}{T_o - T_{inj}} \quad T_{mD} = \frac{T_o - T_m}{T_o - T_{inj}} \quad x_D = \frac{4\lambda_r}{\rho_w C_w u_w h^2} x \quad t_D = \frac{4\lambda_r}{\rho_r C_r h^2} t \quad z_D = \frac{2z}{h} \quad (5.18)$$

$$\beta = \rho_w C_w u_w \frac{h}{2\lambda_r}$$

The corresponding initial-boundary value problems during the injection period in the dimensionless form are given below:

$$\frac{\partial T_D}{\partial t_D} + \frac{\partial T_D}{\partial x_D} = \frac{1}{\beta^2} \frac{\partial^2 T_D}{\partial x_D^2} + \frac{\partial T_{mD}}{\partial z_D} \Big|_{z_D=0} \quad (5.19)$$

$$\frac{\partial T_{mD}}{\partial t_D} = \frac{\partial^2 T_{mD}}{\partial z_D^2} \quad (5.20)$$

$$T_{mD}(x_D, z_D, t_D = 0) = 0 \quad (5.21)$$

$$\lim_{z_D \rightarrow \infty} \frac{\partial T_{mD}}{\partial z_D} = 0 \quad (5.22)$$

$$T_{mD}(x_D, z_D = 0, t_D) = T_D(x_D, t_D) \quad (5.23)$$

$$T_D(x_D, t_D = 0) = 0 \quad (5.24)$$

$$T_D(x_D = 0, t_D) = 1 \quad (5.25)$$

$$\lim_{x_D \rightarrow \infty} \frac{\partial T_D}{\partial x_D} = 0 \quad (5.26)$$

The initial-boundary value problems during the shut-in period in dimensionless form are given below:

$$\frac{\partial T_D}{\partial \Delta t_D} = \frac{1}{\beta^2} \frac{\partial^2 T_D}{\partial x_D^2} + \frac{\partial T_{mD}}{\partial z_D} \Big|_{z_D=0} \quad (5.27)$$

$$\frac{\partial T_{mD}}{\partial \Delta t_D} = \frac{\partial^2 T_{mD}}{\partial z_D^2} \quad (5.28)$$

$$T_D(x_D, \Delta t_D = 0) = T_D(x_D, t_D = t_{Dinj}) \quad (5.29)$$

$$\lim_{x_D \rightarrow 0} \frac{\partial T_D}{\partial x_D} = 0 \quad (5.30)$$

$$\lim_{x_D \rightarrow \infty} \frac{\partial T_D}{\partial x_D} = 0 \quad (5.31)$$

$$T_{mD}(x_D, z_D, \Delta t_D = 0) = T_{mD}(x_D, z_D, t_D = t_{Dinj}) \quad (5.32)$$

$$\lim_{z_D \rightarrow \infty} \frac{\partial T_{mD}}{\partial z_D} = 0 \quad (5.33)$$

$$T_{mD}(x_D, z_D = 0, \Delta t_D) = T_D(x_D, \Delta t_D) \quad (5.34)$$

The solution procedure is as follows: an analytical solution for the injection period's IBVPs (Eq. 5.19 – Eq. 5.26) is obtained using Laplace transformation technique. Then, the resulting solution is used to describe the initial conditions (Eq. 5.27 and Eq. 5.34) for the IBVPs during shut in. Finally, double Laplace transformation technique is adopted to obtain the temperature solution during the shut-in period. As for the solution of the IBVP during the injection period, Laplace transformation defined by Eq. 5.35 is used to obtain the temperature solution for reservoir and the surrounding strata as described by Eq. 5.36 and Eq. 5.37, respectively. Details of solution derivation are given in the Appendix F.

$$\mathcal{L}_s \{T_D(x_D, t_D)\} = \bar{T}_D(x_D, s) = \int_0^{\infty} e^{-st_D} T_D(x_D, t_D) dt_D \quad (5.35)$$

$$T_D(x_D, t_D) = \int_0^{t_D} \frac{\beta x_D}{2\sqrt{\pi\tau^3}} \operatorname{erfc}\left(\frac{\tau}{2\sqrt{t_D - \tau}}\right) e^{-\left(\frac{\beta^2(x_D - \tau)^2}{4\tau}\right)} d\tau \quad (5.36)$$

$$T_{mD}(x_D, z_D, t_D) = \frac{z_D}{2\sqrt{\pi}} \int_0^{t_D} \frac{e^{-\left(\frac{z_D^2}{4\kappa}\right)}}{\sqrt{\kappa^3}} T_D(x_D, t_D - \kappa) d\kappa \quad \text{for } z_D > 0 \quad (5.37)$$

The analytical solution for IBVPs during shut-in period (Eq. 5.27- Eq. 5.34) are obtained using double Laplace transformation defined by Eq. 5.38 (Debnath 2016). The solution for reservoir temperature during shut-in period is described by Eq. 5.39. Details of solution derivation are given in the Appendix F.

$$\mathcal{L}_{s,p} \{T_D(x_D, t_{Dinj}, \Delta t_D)\} = \bar{\bar{T}}_D(x_D, s, p) = \int_0^{\infty} \int_0^{\infty} e^{-st_D - p\Delta t_D} T_D(x_D, t_D, \Delta t_D) dt_D d\Delta t_D \quad (5.38)$$

$$T_D = \frac{1}{2\sqrt{\pi}} \mathcal{L}_s^{-1} \left\{ \begin{array}{l} \frac{G(s)}{s} \left(I_1(s, \Delta t_D) + \int_0^{\Delta t_D} F(s, x) I_1(s, \Delta t_D - x) dx \right) + \\ \frac{1}{s} \exp(\beta G(s) x_D) \left(I_2(s, \Delta t_D) + \int_0^{\Delta t_D} F(s, x) I_2(s, \Delta t_D - x) dx \right) \end{array} \right\} \quad (5.39)$$

where

$$I_1(s, \Delta t_D) = \int_0^{\Delta t_D} \int_0^u \frac{1}{\sqrt{\pi\tau}} \frac{ue^{-G(s)(u-\tau)}}{\sqrt{(\Delta t_D - u)^3}} \exp\left(-\frac{u^2}{4(\Delta t_D - u)}\right) e^{\left(\frac{(\beta x_D)^2}{4\tau}\right)} d\tau du$$

$$G(s) = \frac{\beta}{2} \left(1 - \sqrt{1 + 4\beta^{-2}(\sqrt{s} + s)}\right) \quad I_2(s, \Delta t_D) = \int_0^{\Delta t_D} \frac{ue^{-G(s)u}}{\sqrt{(\Delta t_D - u)^3}} \exp\left(-\frac{u^2}{4(\Delta t_D - u)}\right) du$$

$$F(s, x) = \left(\frac{1}{\sqrt{\pi x}} - \sqrt{s} e^{sx} \operatorname{erfc}(\sqrt{sx})\right)$$

Sandface temperature solution during shut-in period is described by the following equation which is obtained by assigning ($x_D \rightarrow 0$) in Eq. 5.39.

$$T_{wD}(\Delta t_D) = \frac{1}{2\sqrt{\pi}} \mathcal{L}_s^{-1} \left\{ \frac{1}{s} \left(I_3(s, \Delta t_D) + \int_0^{\Delta t_D} F(s, x) I_3(s, \Delta t_D - x) dx \right) \right\} \quad (5.40)$$

where

$$I_3(s, \Delta t_D) = \int_0^{\Delta t_D} \frac{u}{\sqrt{(\Delta t_D - u)^3}} \exp\left(-\frac{u^2}{4(\Delta t_D - u)}\right) e^{-G(s)^2 u} \operatorname{erfc}(G(s)\sqrt{u}) du$$

It is obtained from Eq. 5.40 that sandface temperature mainly depends on β which is equivalent to $1/2$ Péclet number, $\left(\operatorname{Pe} = \frac{v_w h}{\alpha_t}\right)$ where v_w is the advection velocity $\left(v_w = \frac{\rho_w C_w}{\rho_r C_r} u_w\right)$ and α_t is

thermal diffusivity $\left(\alpha_t = \frac{\lambda_r}{\rho_r C_r}\right)$. Thus, velocity of fluid flow throughout reservoir or

equivalently, the injection rate can be evaluated given the sandface temperature history during shut-in period. Inverse Laplace transformation in Eq. 5.40 is obtained numerically using Stehfest algorithm (Stehfest 1970).

5.2. Inversion Procedure

In this section, inversion procedure is introduced to evaluate the injection profile along the lateral section of the wellbore using the developed analytical solution assuming reservoir thickness and thermal diffusivity are known. The analytical solution is used to construct type curves in which dimensionless sandface temperature, $1 - T_{wD}$ and the logarithmic derivative of the dimensionless sandface temperature, $\Delta t_D (\partial T_{wD} / \partial \Delta t_D)$ are plotted versus dimensionless shut-in time, Δt_D at different values of Péclet number (expressed in terms of β). Different type curves can be constructed for different injection times. Fig. 5.1 illustrates type curves of sandface temperature at $t_{Dinj} = 0.01$. Inversion procedure follows the steps below:

- Divide the lateral section of wellbore into equal intervals with length, ΔL_w .
- Obtain sandface temperature history at the first interval during shut-in period.

- Construct type curves of the sandface temperature solution using Eq. 5.40 at a dimensionless injection time, t_{Dinj} which corresponds to the operating injection time using Eq. 5.18.
- Plot sandface temperature change, $\Delta T_w (= T_w - T_{inj})$ and the logarithmic derivative of the sandface temperature, $\Delta t (\partial T_w / \partial \Delta t)$ versus shut-in time, Δt on a log-log scale. The graph should be in the same mesh size as that of the developed type curves in step 3.
- Select arbitrary shut-in time (e.g., 1 day) and evaluate the corresponding dimensionless shut-in time using Eq. 5.18.
- Slide the sandface temperature plot on type curves vertically such that the dimensionless shut-in time evaluated in step 5 coincide with the corresponding shut-in time until the best match is obtained.
- Estimate the effective heat capacity and the effective thermal conductivity of the flooded region using average water saturation behind the flooded front using the following equations:

$$\rho_r C_r = \phi (\bar{S}_w \rho_w C_w + (1 - \bar{S}_w) \rho_o C_o) + (1 - \phi) \rho_s C_s \quad (5.41)$$

$$\lambda_r = \phi (\bar{S}_w \lambda_w + (1 - \bar{S}_w) \lambda_o) + (1 - \phi) \lambda_s \quad (5.42)$$

- Use β value of the type-curve that provides the best match to evaluate injection rate at the interval of interest using Eq. 5.18.

$$q = \frac{2\lambda_r \beta_{MP}}{\rho_w C_w} \Delta L_w \quad (5.43)$$

- Select an arbitrary point $((1 - T_{wD})|_{MP}, \Delta T_w|_{MP})$ and evaluate initial reservoir temperature using the following equation:

$$T_o = T_{inj} + \frac{\Delta T_w|_{MP}}{(1 - T_{wD})|_{MP}} \quad (5.44)$$

- Repeat steps 2 – 9 with the next interval up to the end of the lateral section of wellbore.

It is clear from Fig. 5.2 that at high injection rates (high β), temperature solutions are indistinguishable at early shut-in times. In this case, effect of heat transfer by conduction in the lateral direction is negligible compared with heat gain from the surrounding strata because thermal front propagation is deeper into the reservoir for high injection rates. In this case, it is recommended to shut-in for relatively long shut-in time so that effect of heat conduction in the lateral direction dominate heat transfer mechanisms in the reservoir.

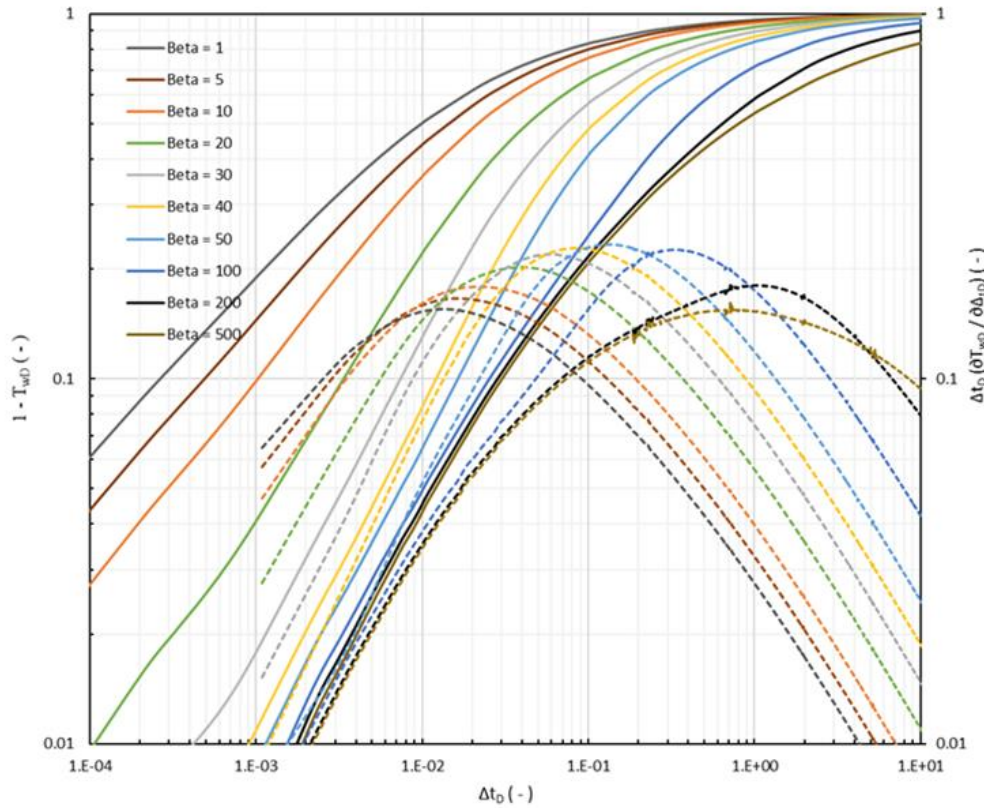


Figure 5. 2. Type curves for sandface temperature solution at $t_{Dinj} = 0.01$.

5.3. Validation Results

In this section, validation of the analytical solutions and application of the inversion procedure are introduced for a synthetic case that is modelled using a thermally-coupled numerical reservoir simulator, CMG-STARS (2020). The input data of the synthetic case is tabulated in Table 5.1. In this case, water is injected along the horizontal well into a heterogeneous reservoir in which permeability changes (500, 400, 300, 200, and 100 md at 50, 100, 150, 200, and 250 ft) along wellbore from heel to toe. Reservoir can be divided into 5 intervals with different injectivities. Fig 5.3 illustrates temperature profiles for first, third, and fifth intervals of reservoir. Temperature profiles are illustrated at different times during injection (6, 12, 18, and 24 hr). Good agreement is obtained between the analytical and the numerical results. Fig. 5.4 provides visual illustration of the thermal front propagation for all intervals by the end of injection period. This case is designed to mimic the real field situation in which the majority of fluid injection may be located at the heel and decreases progressively toward the toe.

After injection stops, temperature disturbance dissipates into the reservoir via heat conduction and temperature starts to equilibrate throughout the reservoir. Fig. 5.5 illustrates the corresponding sandface temperature profiles during the shut-in period for 1st, 3rd, and 5th intervals. It is obtained that rate of warmback for 1st interval is slower than other intervals due to its high injectivity. On the other hand, rate of warmback for 5th interval is higher because of its lowest injectivity. Fig. 5.6 provides graphical illustration of sandface temperature profile along

wellbore for all completed intervals. It is evident that warmback increases along the wellbore from heel to toe which confirms the non-uniform injection profile established along wellbore.

Table 5. 1. Input data for the synthetic case.

Input data	Value
Initial reservoir temperature, T_o (F)	200
Injection temperature, T_{inj} (F)	60
Injection rate, q (bbl / day)	5000
Lateral section length, L_w (ft)	250
Reservoir thickness, h (ft)	15
Injection time, t_{inj} (day)	1
Injected fluid density, ρ_w (lbm / ft ³)	63.4
Injected fluid heat capacity, C_w (Btu/lbm F)	1
Reservoir effective heat capacity, $\rho_r C_r$ (Btu/ft ³ F)	39.3
Reservoir effective thermal conductivity, λ_r (Btu/ft hr F)	1
Permeability, k (md)	500,400,300,200,100
Porosity, ϕ (fraction)	0.15
Water saturation behind flooded front (fraction)	1
Grid cells $n_x \times n_y \times n_z$	4000 \times 10 \times 1
Grid size (dx, dy, dz) (ft)	0.1, 25, 15
Grid cell type	Uniform

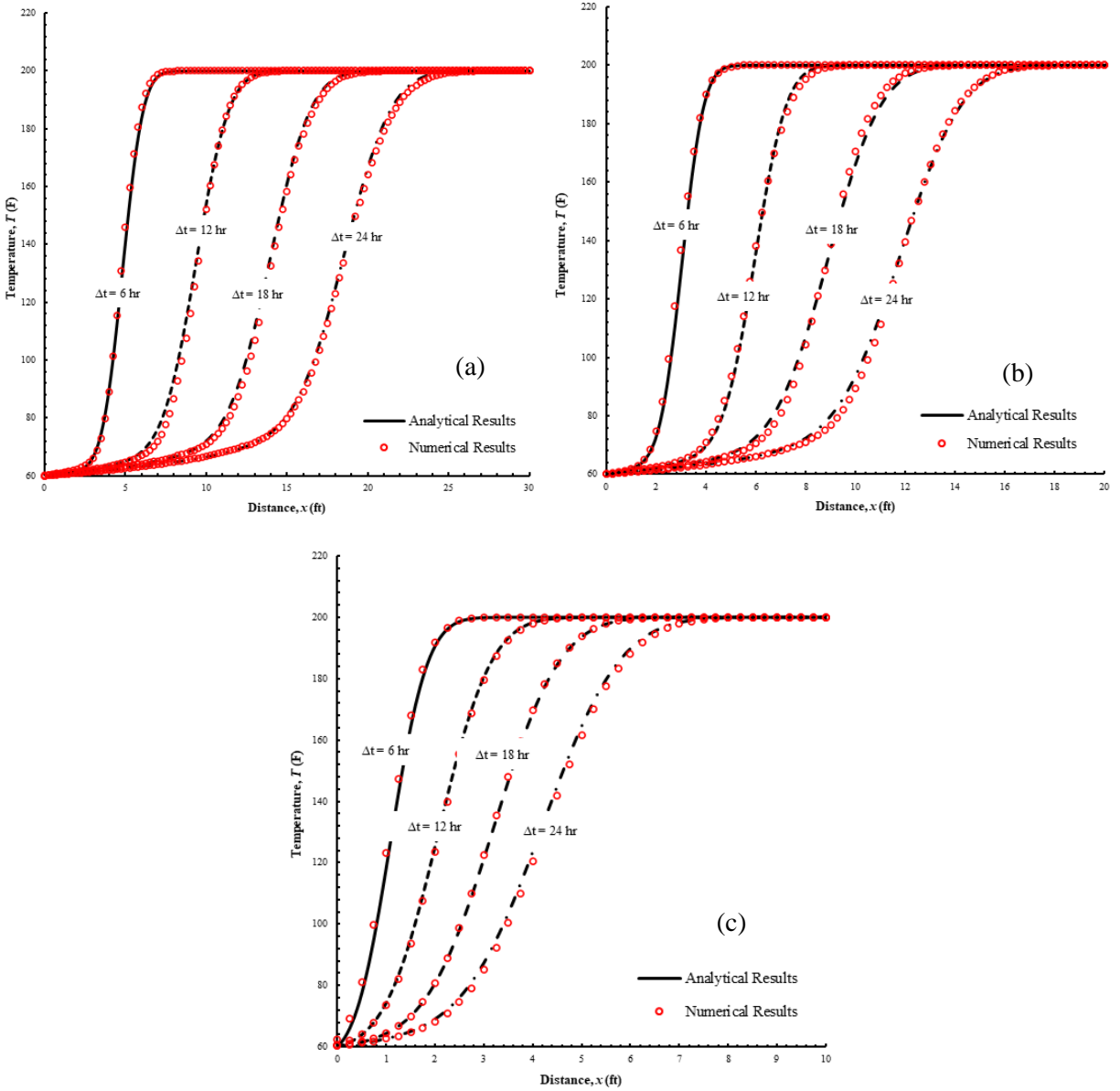


Figure 5. 3. Temperature profile during the injection period for (a) 1st interval, (b) 3rd interval, and (c) 5th interval.

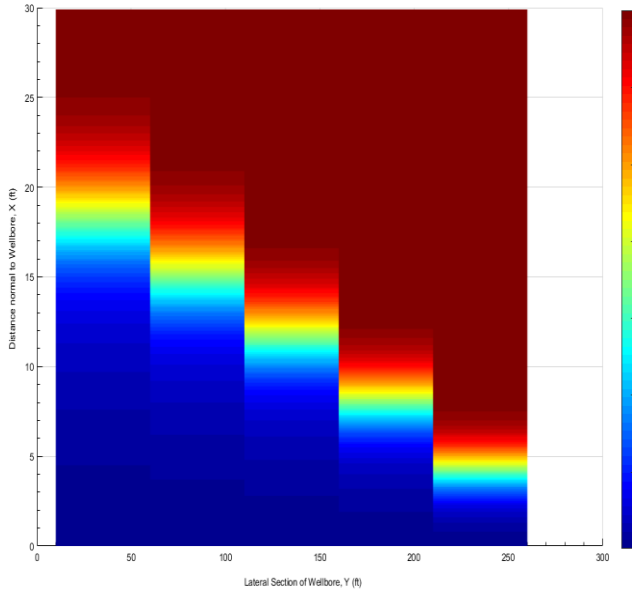


Figure 5. 4. Visual illustration of thermal fronts propagation at end of the injection period.

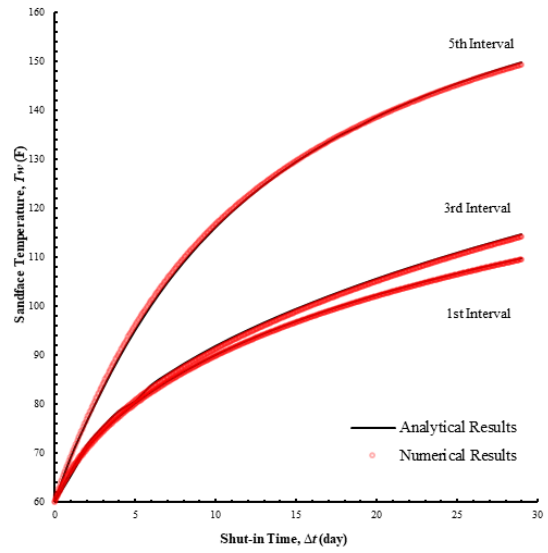


Figure 5. 5. Sandface temperature recovery during the shut-in period.

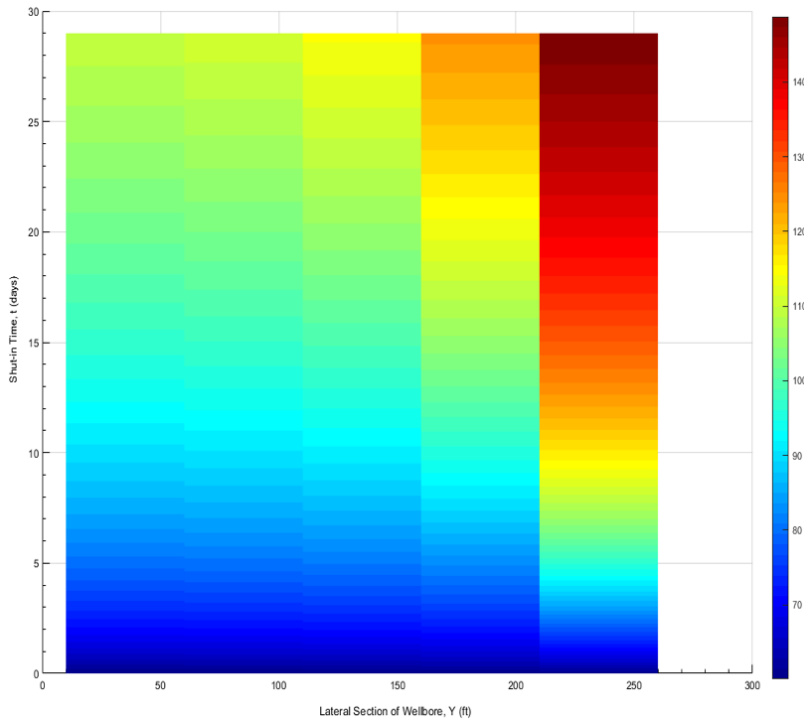


Figure 5. 6. Visual illustration of temperature warmback along the lateral of the horizontal well.

5.4. Inversion Procedure Application

In this section, the inversion procedure is applied to estimate the injection profile along the wellbore using the sandface temperature history. Sandface temperature history for each interval is used to evaluate the local injection rate through type curve matching using Fig. 5.2.

Type curves illustrated in Fig. 5.7 are developed for injection time of 1 day ($t_{Dinj}=0.01$) and the input data given in Table 5.1. The inversion procedure is illustrated for two arbitrary intervals which are 1st interval which has the highest injectivity and 5th interval which has the lowest injectivity. Inversion procedure is as follows:

- Sandface temperature change and the logarithmic derivative of sandface temperature for 1st and 5th intervals are plotted versus shut-in time on a log-log scale. Scales of the developed plots have to be the same as those of Fig. 5.2.
- Select arbitrary shut-in time (e.g., 1 day) and evaluate the corresponding dimensionless shut-in time using Eq. 5.18.
- Shift sandface temperature history plot over type curves vertically as illustrated in Fig. 5.7 and Fig. 5.8 for 1st and 5th intervals, respectively such that the dimensionless shut-in time evaluated in step 5 coincide with the corresponding shut-in time until best match is obtained.
- Use Eq. 5.43 to evaluate the local injection rate for the interval of interest using β of the matched type -curve.
- Select a match point, $(\Delta T_w|_{MP}, (1-T_{wD})|_{MP})$ and estimate initial temperature using Eq. 5.44. Table 5.2 illustrates the inversion results for all intervals.

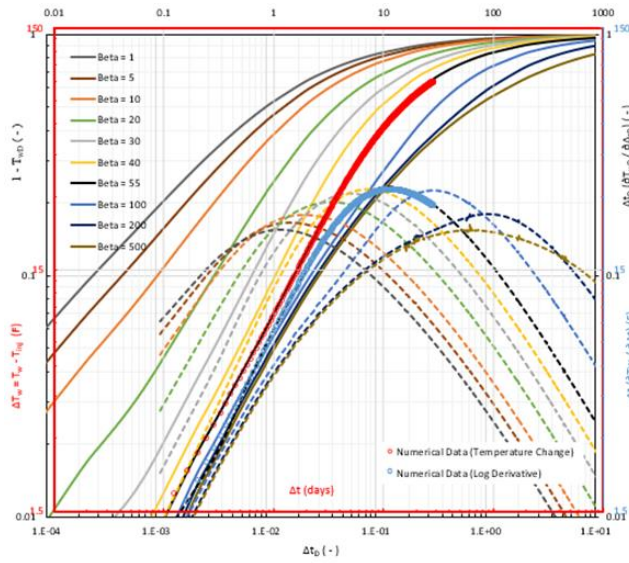


Figure 5. 7. Application of the inversion procedure on 1st interval.

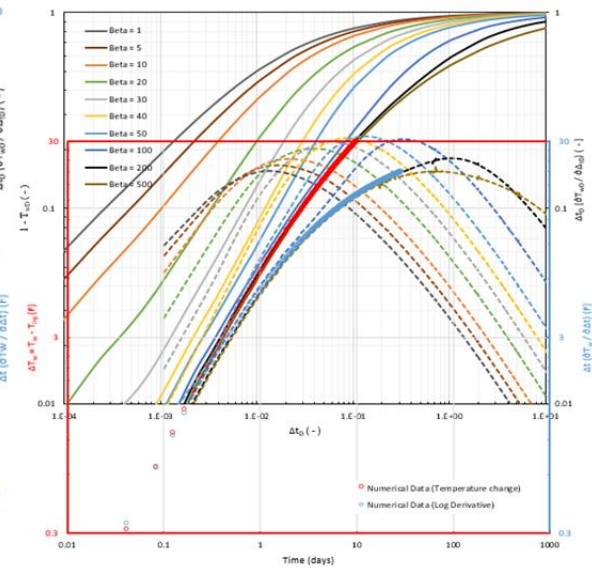


Figure 5. 8. Application of the inversion procedure on 5th interval.

Table 5. 2. Inversion results for the synthetic case.

Interval	β (-)	Estimated rate (bbl/day)	Rate estimation error (%)	Estimated initial temperature (F)	Initial temperature estimation error (%)
1	240	1617.37	0.81	204.4	2.2
2	195	1314.12	0.14	199.1	0.45
3	150	1010.86	0.30	197.6	1.2
4	100	673.91	3.38	198	1
5	55	370.65	0.56	213.5	6.75

Chapter 6. Warmback Analysis Application for Hydraulic Fracture Characterization

Temperature monitoring has been used in last decades for monitoring and diagnosis of hydraulic fracture treatments in Multi-stage Fractured Horizontal Wells (MFHW). The distinct temperature signal obtained along the lateral during stimulation and post-stimulation reveal important information about fracture effectiveness, fracture locations, degree of isolation between fracture stages, and the geometry and propagation of the created fractures. In this chapter, temperature warmback analysis is presented as a temperature monitoring technique for characterizing created fractures. New analytical approach is presented to characterize transverse fractures created along horizontal well using temperature recovery data obtained after the fracture treatment. The analytical model describes the transient temperature evolution in the fracture and the surrounding matrix during fracture propagation (injection phase) and the warmback periods. The analytical solution considers heat transfer via convection and conduction in the created fracture, while heat is transferred only via heat conduction in the surrounding matrix. Inversion procedures are presented using graphical techniques to estimate the dimensions of the fracture such as fracture half-length and fracture width. In addition, the initial geothermal temperature can also be obtained. The analytical approach is validated against a thermally-coupled numerical reservoir simulator, CMG-STARS (2020). The inversion procedures are applied to the observed numerical temperature data to estimate fracture dimensions.

6.1. Problem Description

In the following, we consider a horizontal well with multiple transverse fractures completed in a tight reservoir as illustrated in Fig. 6.1. The reservoir and fracture domains are homogenous and isotropic with constant thermal properties. Cooler stimulation fluid is injected for fracture creation at constant injection rate q per fracture and constant injection temperature T_{inj} . Fluid flow in the fracture is linear with negligible leak-off to the surrounding matrix. Heat is transferred in the flow direction via bulk fluid movement (convection) and from the surrounding matrix via heat conduction. In the matrix, heat is solely transferred by conduction in the direction perpendicular to the fracture plane.

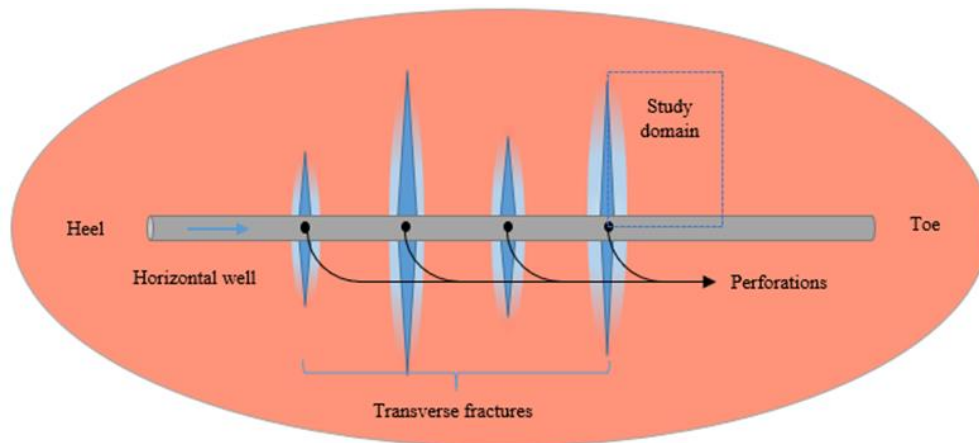


Figure 6. 1. Schematic illustration of a horizontal with multiple transverse fractures.

After fluid injection stops, fracture propagation terminates and the temperature in the fracture increases due to heat flux from the surrounding matrix. The rate of temperature increase depends on the dimensions of the created fracture and the thermal properties of the injected fluid and reservoir rock. Due to symmetric nature of the problem, one quarter of the fracture is considered to be the model domain as illustrated in Fig. 6.2. As the effect of fluid leak-off is neglected, the problem can be simplified to a convection-diffusion problem in the fracture. The governing equation that describes transient temperature within the hydraulic fracture during fracture treatment is described by the following equation:

$$\rho_r C_r \frac{\partial T}{\partial t} + \rho_w C_w u_w \frac{\partial T}{\partial x} = \frac{2}{w_f} \lambda_m \frac{\partial T_m}{\partial y} \Big|_{y=0} \quad (6.1)$$

where $u_w = \left(\frac{q}{2w_f h_f} \right)$. The governing equation for the transient temperature in the surrounding matrix is described by the following equation:

$$\rho_m C_m \frac{\partial T_m}{\partial t} = \lambda_m \frac{\partial^2 T_m}{\partial y^2} \quad (6.2)$$

The governing equation for the transient temperature in the hydraulic fracture (Eq. 6.1) is subject to the following initial and boundary conditions:

$$T(x, t = 0) = T_o \quad (6.3)$$

$$T(x = 0, t) = T_{inj} \quad (6.4)$$

The governing equation for the surrounding matrix (Eq. 6.2) is subject to the following initial and boundary conditions:

$$T_m(x, y, t = 0) = T_o \quad (6.5)$$

$$T_m(x, y = 0, t) = T(x, t) \quad (6.6)$$

$$\lim_{y \rightarrow \infty} \frac{\partial T_m(x, y, t)}{\partial y} = 0 \quad (6.7)$$

After injection stops, temperature in the fracture warms back due to heat flux from the surrounding matrix. The governing equation for the transient temperature within the created fracture during the warmback period is simplified to the following heat conduction equation:

$$\rho_r C_r \frac{\partial T}{\partial \Delta t} = \frac{2}{w_f} \lambda_m \frac{\partial T_m}{\partial y} \Big|_{y=0} \quad (6.8)$$

The governing equation for the transient temperature in the surrounding matrix during the shut-in period is described by the following equation:

$$\rho_m C_m \frac{\partial T_m}{\partial \Delta t} = \lambda_m \frac{\partial^2 T_m}{\partial y^2} \quad (6.9)$$

The governing equations (Eq. 6.8 and Eq. 6.9) are subject to the following initial and boundary conditions:

$$T(x, \Delta t = 0) = T(x, t_{inj}) \quad (6.10)$$

$$T_m(x, y, \Delta t = 0) = T_m(x, y, t = t_{inj}) \quad (6.11)$$

$$T_m(x, y = 0, \Delta t) = T(x, \Delta t) \quad (6.12)$$

$$\lim_{y \rightarrow \infty} \frac{\partial T_m(x, y, \Delta t)}{\partial y} = 0 \quad (6.13)$$

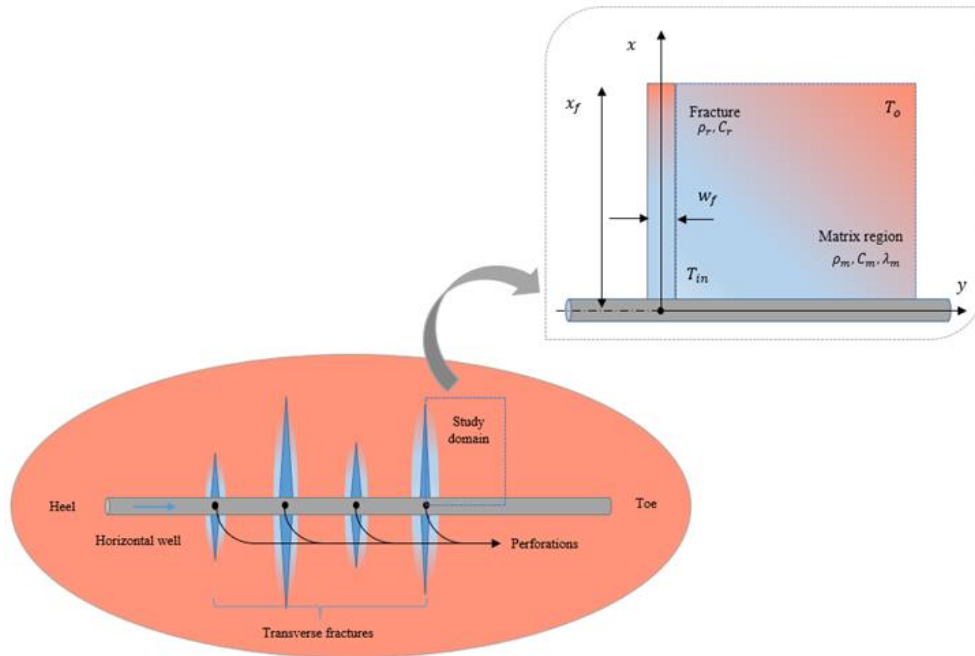


Figure 6. 2. Schematic illustration of the problem showing the study domain (one quarter of the transverse fracture).

The initial-value problem described by Eq. 6.1– 6.13 is re-written using the following group of dimensionless parameters:

$$T_D = \frac{T - T_o}{T_{inj} - T_o} \quad T_{mD} = \frac{T_m - T_o}{T_{inj} - T_o} \quad y_D = \frac{2y}{w_f} \quad x_D = \frac{4\lambda_m}{\rho_w C_w u_w w_f^2} x \quad (6.14)$$

$$t_D = \frac{4\lambda_m}{\rho_r C_r w_f^2} t \quad \Delta t_D = \frac{4\lambda_m}{\rho_r C_r w_f^2} \Delta t \quad \theta = \frac{\rho_m C_m}{\rho_r C_r}$$

The corresponding dimensionless form of the initial-boundary value problem during injection phase is as follows:

$$\frac{\partial T_D}{\partial t_D} + \frac{\partial T_D}{\partial x_D} = \frac{\partial T_{mD}}{\partial y_D} \Big|_{y_D=0} \quad (6.15)$$

$$\frac{\partial^2 T_{mD}}{\partial y_D^2} = \theta \frac{\partial T_{mD}}{\partial t_D} \quad (6.16)$$

The corresponding initial and boundary conditions are as follows:

$$T_D(x_D, t_D = 0) = 0 \quad (6.17)$$

$$T_D(x_D = 0, t_D) = 1 \quad (6.18)$$

$$T_{mD}(x_D, y_D, t_D = 0) = 0 \quad (6.19)$$

$$T_{mD}(x_D, y_D = 0, t_D) = T_D(x_D, t_D) \quad (6.20)$$

$$\lim_{y_D \rightarrow \infty} \frac{\partial T_{mD}(x_D, y_D, t_D)}{\partial y_D} = 0 \quad (6.21)$$

The solution of the initial-boundary value problem described by Eq. 6.15– 6.21 was obtained using Laplace transformation technique (Lauwerier 1955). The solution for the temperature in fracture and surrounding matrix are described by Eq. 6.22 and Eq. 6.23, respectively.

$$T_D = \operatorname{erfc} \left(\frac{\sqrt{\theta} x_D}{2\sqrt{t_D - x_D}} \right) U(t_D - x_D) \quad (6.22)$$

$$T_{mD} = \operatorname{erfc} \left(\frac{\sqrt{\theta} (x_D + y_D)}{2\sqrt{t_D - x_D}} \right) U(t_D - x_D) \quad (6.23)$$

The dimensionless forms of the governing equations of transient temperature for fracture and matrix during warmback period are described by Eq. 6.24 and Eq. 6.25, respectively.

$$\frac{\partial T_D}{\partial \Delta t_D} = \frac{\partial T_{mD}}{\partial y_D} \Big|_{y_D=0} \quad (6.24)$$

$$\frac{\partial^2 T_{mD}}{\partial y_D^2} = \theta \frac{\partial T_{mD}}{\partial \Delta t_D} \quad (6.25)$$

The corresponding initial and boundary conditions are as follows:

$$T_D(x_D, \Delta t_D = 0) = \operatorname{erfc}\left(\frac{\sqrt{\theta}x_D}{2\sqrt{t_{Dinj} - x_D}}\right)U(t_{Dinj} - x_D) \quad (6.26)$$

$$T_D(x_{Df}, \Delta t_D) = 0 \quad (6.27)$$

$$T_{mD}(x_D, y_D, \Delta t_D = 0) = \operatorname{erfc}\left(\frac{\sqrt{\theta}(x_D + y_D)}{2\sqrt{t_{Dinj} - x_D}}\right)U(t_{Dinj} - x_D) \quad (6.28)$$

$$T_{mD}(x_D, y_D = 0, \Delta t_D) = T_D(x_D, \Delta t_D) \quad (6.29)$$

$$\lim_{y_D \rightarrow \infty} \frac{\partial T_{mD}(x_D, y_D, \Delta t_D)}{\partial y_D} = 0 \quad (6.30)$$

The analytical solution for the transient temperature during the warmback period is obtained using Laplace transformation technique. The analytical solutions for the fracture and the matrix during warmback period are described by Eq. 6.31 and Eq. 6.32, respectively:

$$T_D = \left(\operatorname{erfc}(\beta) - \frac{\sqrt{\theta}e^{-\beta^2}}{2\pi\alpha\beta^2} \int_0^{\Delta t_D} \frac{1}{\sqrt{\tau^3}} \left\{ 1 - \sqrt{\pi}F(\tau) \operatorname{erfc}(F(\tau))e^{F(\tau)^2} \right\} \right) U(t_{Dinj} - x_D) \quad (6.31)$$

$$\times F(\tau)^2 \left(1 - e^{\theta(\Delta t_D - \tau)} \operatorname{erfc}(\sqrt{\theta(\Delta t_D - \tau)}) \right) d\tau$$

$$T_{mD} = \operatorname{erfc}\left(\frac{y_D\sqrt{\theta}}{2\sqrt{t_{Dinj}}}\right) - \frac{\sqrt{t_{Dinj}}}{\pi} \int_0^{\Delta t_D} \left\{ \frac{\operatorname{erfc}\left(\frac{y_D\sqrt{\theta}}{2\sqrt{\Delta t_D - \tau}}\right) - e^{\theta y_D} e^{\theta(\Delta t_D - \tau)} \operatorname{erfc}\left(\sqrt{\theta(\Delta t_D - \tau)} + \frac{y_D\sqrt{\theta}}{2\sqrt{\Delta t_D - \tau}}\right)}{\sqrt{\tau}(\tau + t_{Dinj})} \right\} d\tau \quad (6.32)$$

$$+ \frac{1}{2\sqrt{\pi t_{Dinj}}} \int_0^{\infty} \left\{ \exp\left(-\frac{(u - y_D\sqrt{\theta})^2}{4t_{Dinj}}\right) - \exp\left(-\frac{(u + y_D\sqrt{\theta})^2}{4t_{Dinj}}\right) \right\} \operatorname{erfc}\left(\frac{u}{2\sqrt{\Delta t_D}}\right) du$$

where $F(\tau) = \left(2\alpha\beta\sqrt{\frac{\tau}{\theta + 4\alpha^2\tau}}\right)$, $\alpha = \left(\frac{\sqrt{\theta}}{2\sqrt{t_{Dinj} - x_D}}\right)$, and $\beta = \left(\frac{\sqrt{\theta}x_D}{2\sqrt{t_{Dinj} - x_D}}\right)$. The sandface

temperature solution in the fracture domain can be obtained by assigning ($x_D \rightarrow 0$) in Eq. 6.32 as follows:

$$T_{wD} = 1 - \frac{\sqrt{\theta}}{2\pi\alpha} \int_0^{\Delta t_D} \frac{1 - e^{-\theta(\Delta t_D - \tau)} \operatorname{erfc}\left(\sqrt{\theta(\Delta t_D - \tau)}\right)}{\sqrt{\tau} \left(\tau + \frac{\theta}{4\alpha^2}\right)} d\tau \quad (6.33)$$

The solution described by Eq. 6.33 can be presented in the form of type curves in which dimensionless sandface temperature, T_{wD} is plotted versus dimensionless shut-in time at different dimensionless injection times. The type curves are illustrated in Fig. 6.3 for different injection times. The developed type curves will be used for fracture and reservoir characterization in the next section. Fig. 6.3 indicates that the sensitivity of sandface temperature to fracture width decreases for high t_{Dinj} (small fracture widths).

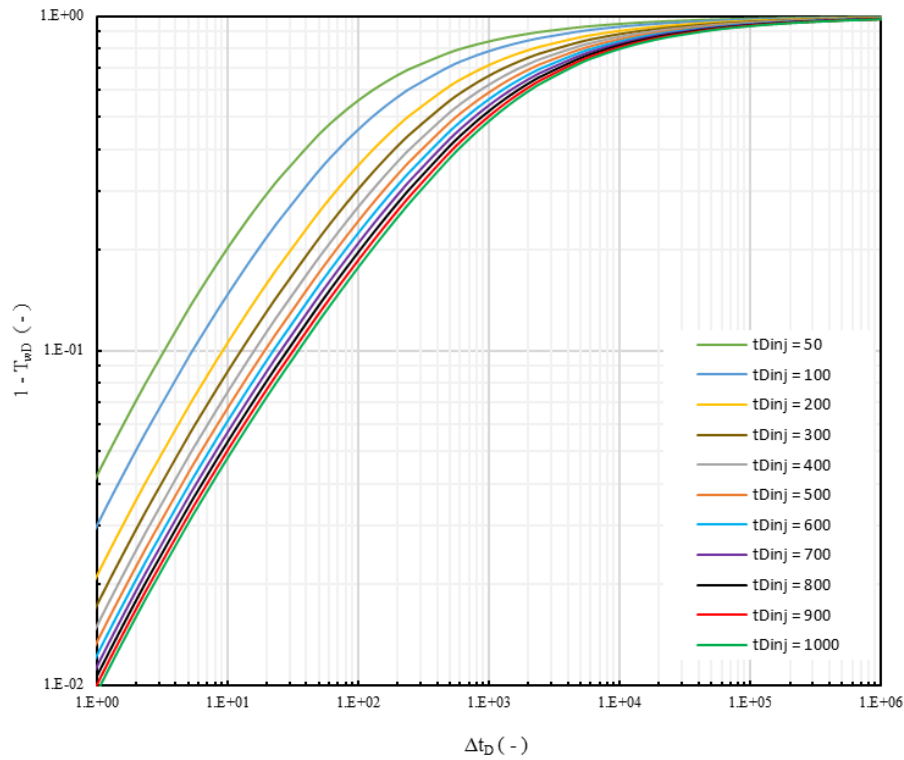


Figure 6. 3. Type curves of sandface temperature during the warmback period.

Late-time asymptotic solution of the sandface temperature at fracture can be obtained by assigning $\left(\frac{\Delta t_D}{t_{Dinj}} \rightarrow \infty\right)$ in Eq. 6.33 as described by Eq. 6.34 (dimensionless form) and Eq. 6.35 (in dimensional form).

$$T_{wD} = \left(1 + \frac{2\sqrt{\theta t_{Dinj}}}{\sqrt{\pi}}\right) \frac{1}{\sqrt{\pi\theta\Delta t_D}} \quad (6.34)$$

$$T_w = T_o - (T_o - T_{inj}) \frac{1}{\pi \sqrt{\theta}} \left(\sqrt{\pi} \sqrt{\frac{w_f^2}{4\alpha_t}} + 2\sqrt{\theta t_{inj}} \right) \frac{1}{\sqrt{\Delta t}} \quad (6.35)$$

where α_t is the thermal diffusivity of fracture system ($= \lambda_m / \rho_r C_r$). In the next section, late-time solution is recasted into a simple graphical technique for inversion purpose.

6.2. Inversion Procedure

In this section, inversion procedures are presented to determine the fracture dimensions and estimate the initial reservoir temperature using the measured temperature history during the warmback period. The measured sandface temperature at perforations is used to infer the fracture width, fracture half-length, and initial reservoir temperature. Two independent approaches are used for inversion: (1) regression analysis using optimization routines and (2) graphical approach using analytical solution – based type curves.

Inversion procedure using regression analysis

Levenberg – Marquardt optimization routine (Press et al.) is for regression analysis. Levenberg – Marquardt is a least square curve fitting solver that solves for the fracture width iteratively such that sum of the squares of the deviations is minimized as described with the following equation:

$$S(w_f, T_o) = \arg \min_{w_f, T_o} \sum_{i=1}^m \left(T_{w(obs)}(\Delta t_i) - T_{w(cal)}(\Delta t_i, w_f, T_o) \right)^2 \quad (6.36)$$

To start the minimization, an initial estimate of fracture width and initial reservoir temperature has to be provided. Next, the optimizer updates the initial estimate to $(w_f + \Delta w_f, T_o + \Delta T_o)$ in which the term, $(\Delta w_f, \Delta T_o)$ are obtained by evaluating the following function $T_{w(cal)}(\Delta t, w_f + \Delta w_f, T_o + \Delta T_o)$ which is calculated by linearization as follows:

$$T_{w(cal)}(\Delta t_i, w_f + \Delta w_f, T_o + \Delta T_o) \approx T_{w(cal)}(\Delta t_i) + \left. \frac{\partial T_{w(cal)}(\Delta t_i)}{\partial w_f} \right|_{T_o} \Delta w_f + \left. \frac{\partial T_{w(cal)}(\Delta t_i)}{\partial T_o} \right|_{w_f} \Delta T_o \quad (6.37)$$

The solution of the minimization problem is obtained when the gradients approaches zero. After substituting into Eq. 6.36 with Eq. 6.37, the function to be minimized takes the following matrix form:

$$S(w_f, T_o) = \arg \min_{w_f, T_o} \sum_{i=1}^m \left(T_{w(obs)}(\Delta t_i) - T_{w(cal)}(\Delta t_i, w_f, T_o) - J\delta \right)^2 \quad (6.38)$$

The vector matrix, δ represents the solution update and the row matrix, J represents the matrix of gradient at the current iteration. Values of δ that provide the minimum value of Eq. 6.38 is

obtained by taking the derivative of Eq. 6.38 with respect to δ and equates the derivative with zero as illustrated in Eq. 6.39 (in matrix form).

$$(J^T J) \delta = J^T (T_{w(obs)} - T_{w(cal)}) \quad (6.39)$$

The resulting system of equations is linear system which can easily be solved for δ . Levenberg improved Eq. 6.39 to take the following damped form:

$$(J^T J + \lambda I) \delta = J^T (T_{w(obs)} - T_{w(cal)}) \quad (6.40)$$

where I is an identity matrix. The non-negative damping parameter, λ is adjusted every iteration to control rate of the reduction of the residual, $S(w_f, T_o)$. An initial estimates of fracture width and initial reservoir temperature are provided to the optimization routine along with the observed history of sandface temperature and the input data for the analytical solution. Next, the optimum values of the unknowns are obtained within few minutes.

Inversion procedure using graphical techniques

The second approach for inversion procedure is through graphical technique interpretation. Although using optimization inversion is sufficient, graphical techniques may be preferred by a field analyst. Analytical solution – based type curves are developed and presented in Fig. 6.3. Before starting type curve matching, initial estimate of initial reservoir temperature can be helpful to avoid non-unique match problem. Initial estimation of T_o can be obtained by using conventional temperature buildup technique at non-perforated region of cased hole (Xu 1990). Conventional temperature buildup technique is implemented at inter-stages non-perforated regions which exhibit quick warmback rate compared with perforated regions. The inversion procedure is as follows:

- Obtain sandface temperature at perforation during the warmback period.
- Plot the change of the measured sandface temperature, $(= T_w - T_{inj})$ versus shut-in time, Δt on a log-log scale. Use the same mesh size as that in the type curves given in Fig. 6.3.
- Select an arbitrary point in the plotted data, e.g., $(T_w - T_{inj} = 100)$ and calculate the corresponding dimensionless value, $\left(1 - T_{wD} = \frac{100}{T_o - T_{inj}}\right)$ using estimated value of initial reservoir temperature.
- Match the plotted data with type curves horizontally such that the selected point $(T_w - T_{inj} = 100)$ coincides with the corresponding dimensionless value until the best match is obtained. Determine the appropriate matched curve, t_{DinjMP} and select an arbitrary match point. The fracture width can be obtained by the following equation using the matching point's abscissas.

$$w_f = \sqrt{\frac{4\Delta t_{MP}\alpha_t}{\Delta t_{DMP}}} \quad (6.41)$$

- Fracture half-length can be obtained using injection rate by:

$$x_f = \left(\frac{q}{2h_f w_f} \right) \left(\frac{t_{DinjMP}}{\Delta t_{DMP}} \right) \Delta t_{MP} \quad (6.42)$$

- Initial reservoir temperature can be re-estimated using the following equation.

$$T_o = T_{inj} + \frac{\Delta T_w|_{MP}}{(1 - T_{wD})|_{MP}} \quad (6.43)$$

Alternatively, and/or if non-unique match is encountered during type curve matching, the following straight-line inversion approach can be used:

- Plot the sandface temperature versus $\left(\frac{1}{\sqrt{\Delta t}} \right)$ on Cartesian scales.
- Identify the data that are fitted with straight line and evaluate the slope of the fitted line, m .
- Extrapolate the fitted line to $\left(\frac{1}{\sqrt{\Delta t}} = 0 \right)$, which is equivalent to an infinite shut-in period. The extrapolated temperature value is the initial temperature, T_o .
- The fracture width can be estimated using the following equation:

$$w_f = \left\{ \frac{m\pi\sqrt{\theta}}{T_o - T_{inj}} - 2\sqrt{\theta t_{inj}} \right\} \sqrt{\frac{4\alpha_t}{\pi}} \quad (6.44)$$

- Fracture half-length is estimated using the following equation:

$$x_f = \frac{qt_{inj}}{2h_f w_f} \quad (6.45)$$

6.3. Validation Results

The analytical solution is validated against numerically obtained results from a thermally coupled reservoir simulator. The input data of the synthetic cases are detailed in Table 6.1. The input data for the first case are relevant to a field case presented by Ugueto et al. (2016). In this case, fluid is injected at 12.5 bbl/min rate for 105 minutes in an ultra-tight reservoir with 0.583 μD permeability and fracture permeability of 500 D. Then, injection is stopped to allow warmback for 8 hours.

Fig. 6.4 (a) illustrates the temperature profile in the created fracture during the warmback period at different times (2, 4, 6, and 8 hours). The fracture temperature increases due to heat

flux from the surrounding warm matrix. The rate of temperature recovery depends mainly on the thermal properties of the surrounding matrix and width of the created fracture. Fig. 6.4 (b) shows the transient temperature profile in the surrounding matrix during the warmback period. The temperature profile in the surrounding matrix exhibits relatively flat distribution due to the thermal diffusion inside the reservoir. Matrix temperature at fracture face increases significantly from the prevailing injection temperature to ~ 145 °F at the end of shut-in period. The rate of temperature recovery decreases toward fracture tip. Fig. 6.5 illustrates the evolution of the temperature at the perforation. Perforation temperature increases significantly from the prevailing injection temperature 60 °F to more than 100 °F after 1 hour. Consequently, the early-time temperature measurements can be adopted for fracture characterization without need for long shut-in periods. Fig. 6.6 shows 3D illustration of the temperature evolution during the warmback period in the fracture and surrounding matrix.

The input data for the second case is relevant to DFIT and is given in Table 6.1. The data of DFIT are field data presented by Liu et al. (2020) from which the averaged pumping information are adopted. In this case, fluid is injected at 5 bbl/min for 12 minutes. Then, injection stops for few days to allow for fracture closure and pressure fall-off. Given the extended time of fracture closure, analyzing sandface temperature after injection stops can infer the characteristics of the created fracture at the end of injection because the warmback attains immediately after injection stops. Fig. 6.7 illustrates the temperature profile in the created fracture and the surrounding matrix during the warmback period at different shut-in times (15, 30, 45, 60 minutes). Throughout the fracture, temperature increases continuously due to heat flux from the surrounding warm matrix. Maximum temperature variation is observed at near wellbore region due to the relatively high temperature gradient in the surrounding matrix. In the surrounding matrix, temperature profile exhibits relatively flat distribution with time due to thermal equilibration in the reservoir. Fig. 6.8 illustrates sandface temperature evolution during the warmback period. Temperature at the perforation increases to ~ 160 °F after only 1 hour of the start of shut-in period. Temperature warmback for this case is higher compared with fracture treatment in case 1 due to limited injection time and the relatively smaller fracture width. Spatiotemporal visualizations of temperature evolution throughout the fracture and the surrounding matrix are shown on the 3D plots illustrated in Fig. 6.9.

Table 6. 1. Input data for the validation cases.

	Case 1	Case 2
Initial reservoir temperature (°F)	180	200
Initial reservoir pressure (psi)	3560	4650
Reservoir depth (ft)	7656	10,000
Injected fluid temperature (°F)	60	60
Effective heat capacity of fracture (Btu/ft ³ F)	37	59
Effective heat capacity of matrix (Btu/ft ³ F)	31	33
Effective thermal conductivity of fracture / matrix (Btu/ft hr F)	1	2
Injected fluid density (lb. / ft ³)	62.4	62.4
Injected fluid heat capacity (Btu/lb. F)	1	1
Injected flow rate per fracture (bbl/min)	12.5	5
Fracture width (ft)	0.02	0.01
Fracture height (ft)	200	100
Total injection time (minute)	105	12
Reservoir permeability (micro-Darcy)	0.583	0.1
Fracture permeability (Darcy)	500	60
Matrix porosity (fraction)	0.042	0.01

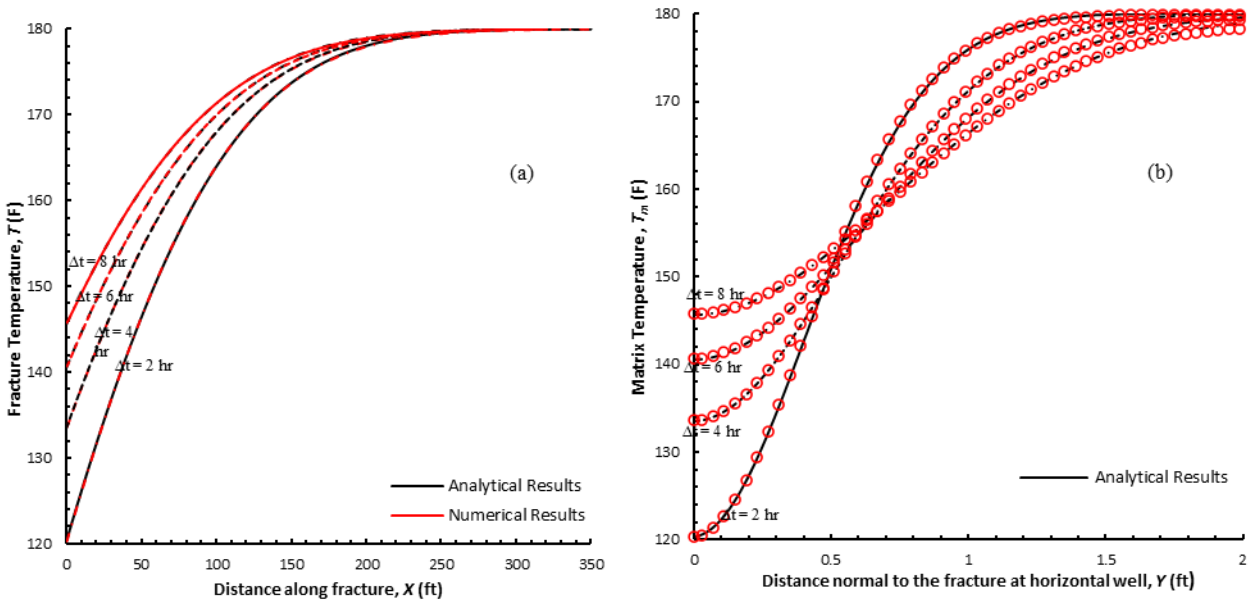


Figure 6. 4. Temperature profile in (a) the fracture plane and (b) the surrounding matrix during the warmback period (Case 1).

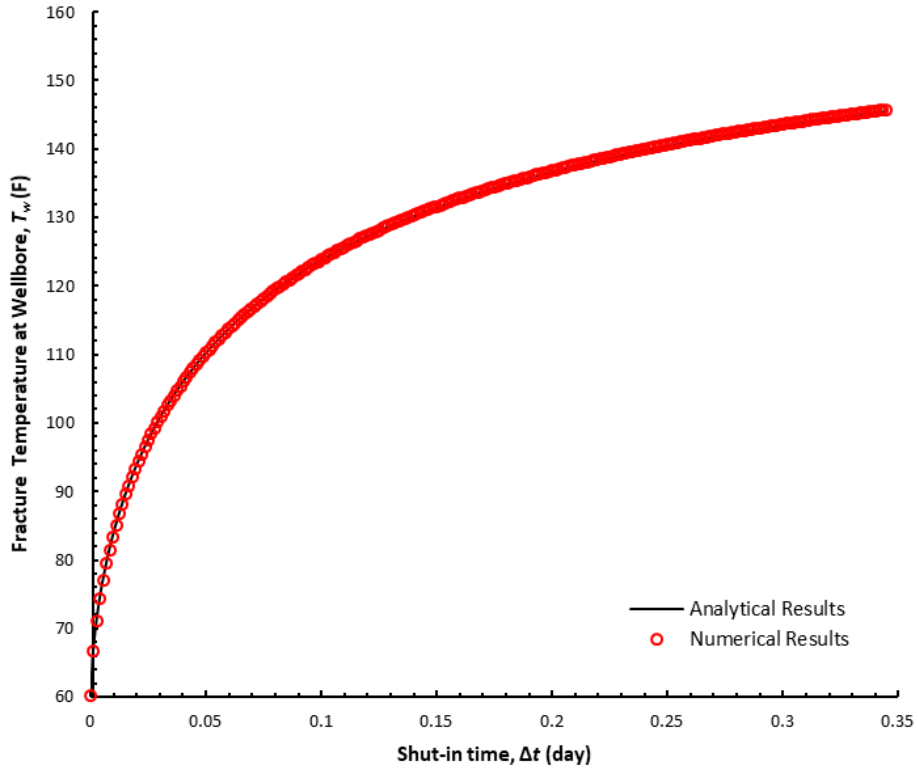


Figure 6. 5. Analytically and numerically calculated temperature at the perforation during the warmback period (Case 1).

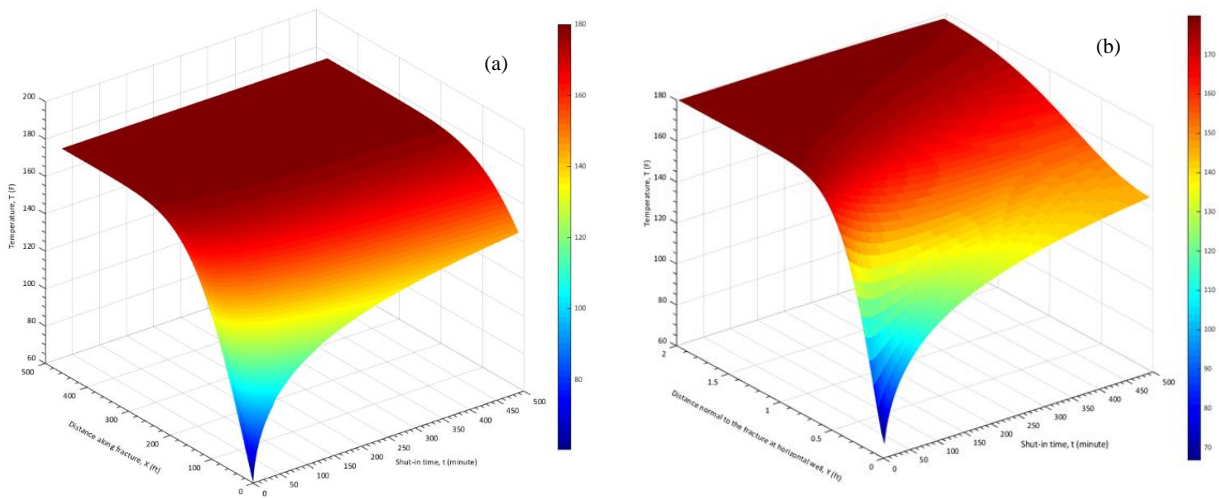


Figure 6. 6. 3D map showing a spatiotemporal temperature evolution in (a) the fracture plane and (b) the surrounding matrix during the warmback period (Case 1).

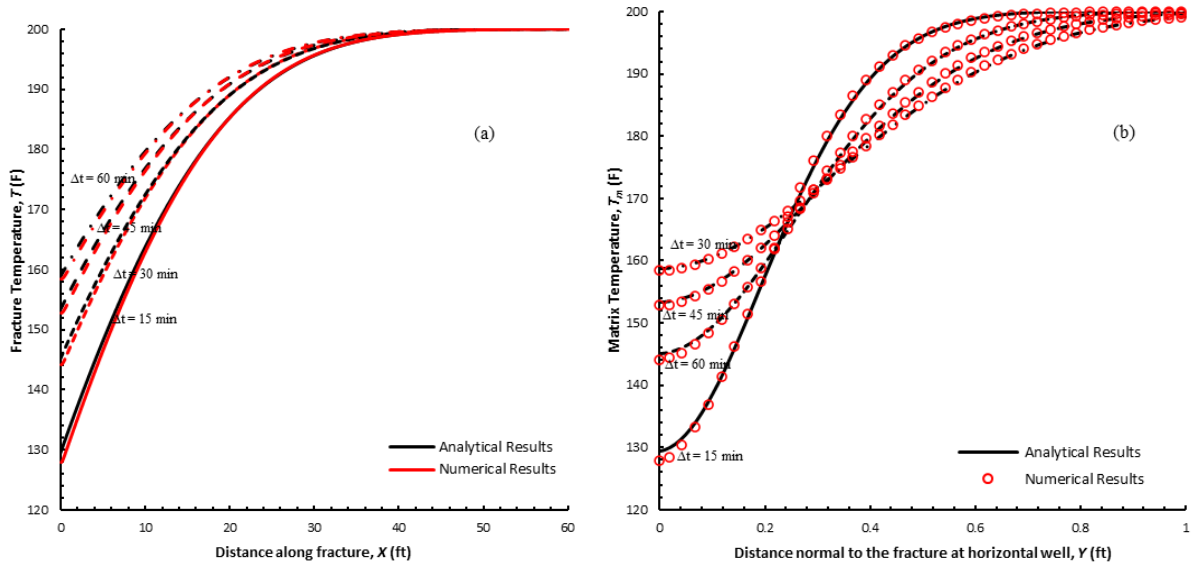


Figure 6. 7. Temperature profile in (a) the fracture plane and (b) the surrounding matrix during the warmback period (Case 2).

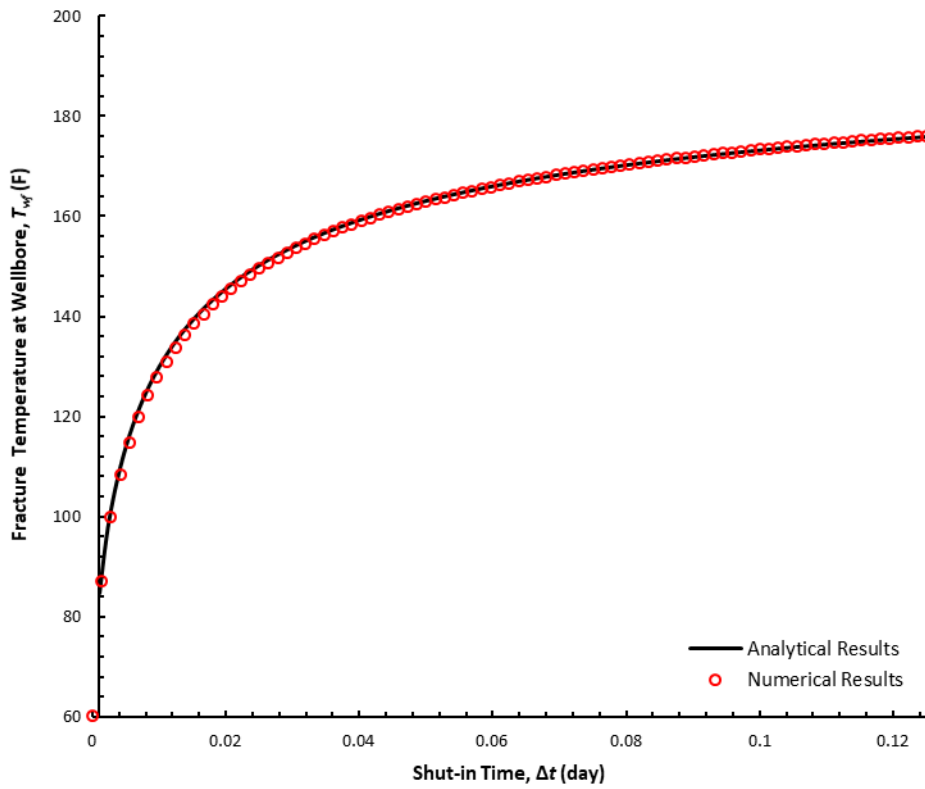


Figure 6. 8. Analytically and numerically calculated sandface temperature at perforations during the warmback period (Case 2).

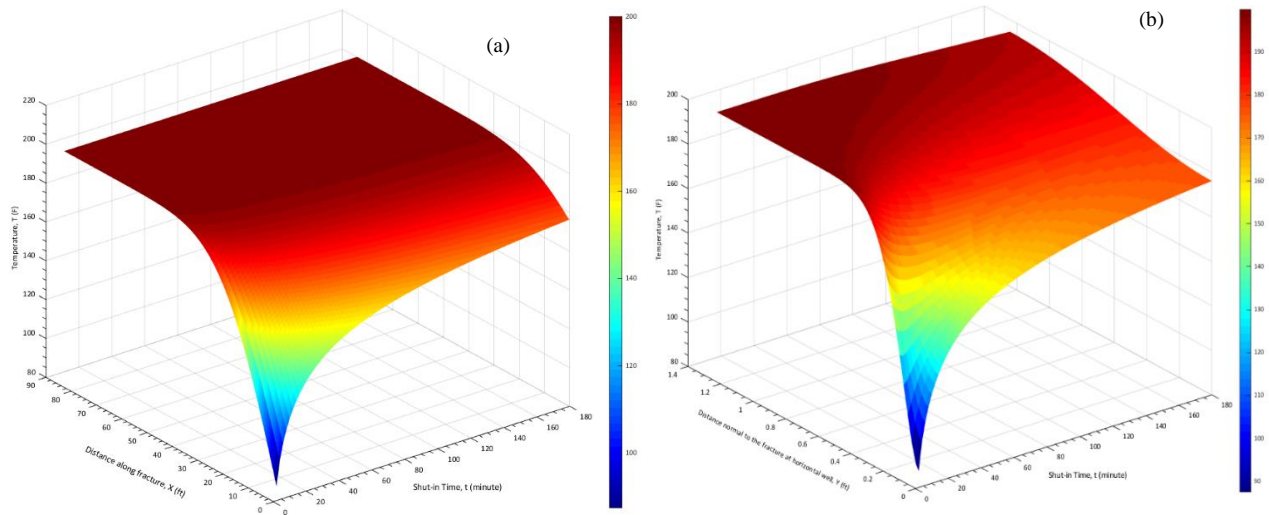


Figure 6. 9. 3D map of a spatiotemporal temperature evolution in (a) the fracture plane and (b) the surrounding matrix during the warmback period (Case 2).

6.4. Inversion procedure for fracture geometry

In this section, inversion procedure is used to obtain the created fracture dimensions using temperature data obtained at the perforation during the warmback period for the presented synthetic cases. Optimization process is used to estimate fracture width and initial reservoir temperature using Levenberg – Marquardt optimization routine. Fig. 6.10 (a) and (b) illustrate the fitting accuracy during the optimization process for case 1 and case 2, respectively. Fitting error is evaluated using root mean square error scheme. The estimated values of fracture width, initial reservoir temperature, and fracture half-length are presented in Table 6.2. Graphical approach has also been used for inversion procedure, and it provides inversion results which are in good agreement with optimization approach. Fig. 6.11 (a) illustrates the type-curve matching of the numerically obtained perforation temperature data for case 1. Using the results obtained from the type-curve matching process, the fracture characteristics (fracture width and fracture half-length) as well as initial reservoir temperature are obtained using Eq. 6.41– Eq. 6.43. The inversion results for the first case are displayed in Table 6.2. Good agreement is obtained with the actual results. For the second synthetic case, the same procedure is followed. Fig. 6.11 (b) illustrates the type-curve matching process for case 2, and its corresponding inversion results are shown in Table 6.2. Application of graphical techniques for late-time solution is illustrated in Fig. 6.12 for case 1 and case 2. The corresponding inversion results are illustrated in Table 6.2.

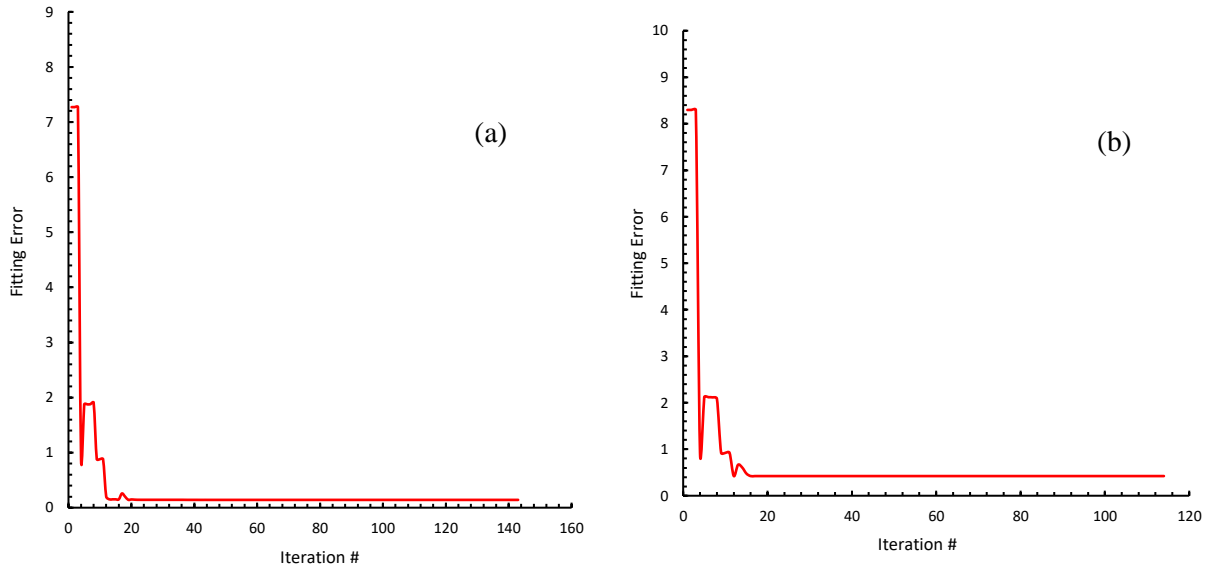


Figure 6. 10. Solution fitness progress during the optimization process: (a) Case 1 (b) Case 2.

Table 6. 2. Inversion results for the validation cases.

	Case 1				Case 2			
	Optimization Results*							
	Result		Fitting error		Result		Fitting error	
Fracture width (ft)	0.0195		0.141		0.0124		0.423	
Fracture half-length (ft)	944.76				135.84			
Initial reservoir temperature (F)	180.48				199.75			
	Graphical Techniques Results							
	Type curves		Straight-line		Type curves		Straight-line	
	Result	Estimation error (percent)	Result	Estimation error (percent)	Result	Estimation error (percent)	Result	Estimation error (percent)
Fracture width (ft)	0.0198	0.766	0.0199	0.002	0.0098	2.41	0.0097	2.154
Fracture half-length (ft)	928	0.765	921.22	0.01	172.59	2.46	172.15	2.193
Initial reservoir temperature (F)	178.96	0.576	180	0.0	192.25	3.88	200	0.0

* Estimation errors in optimization results section are evaluated using root mean square error.

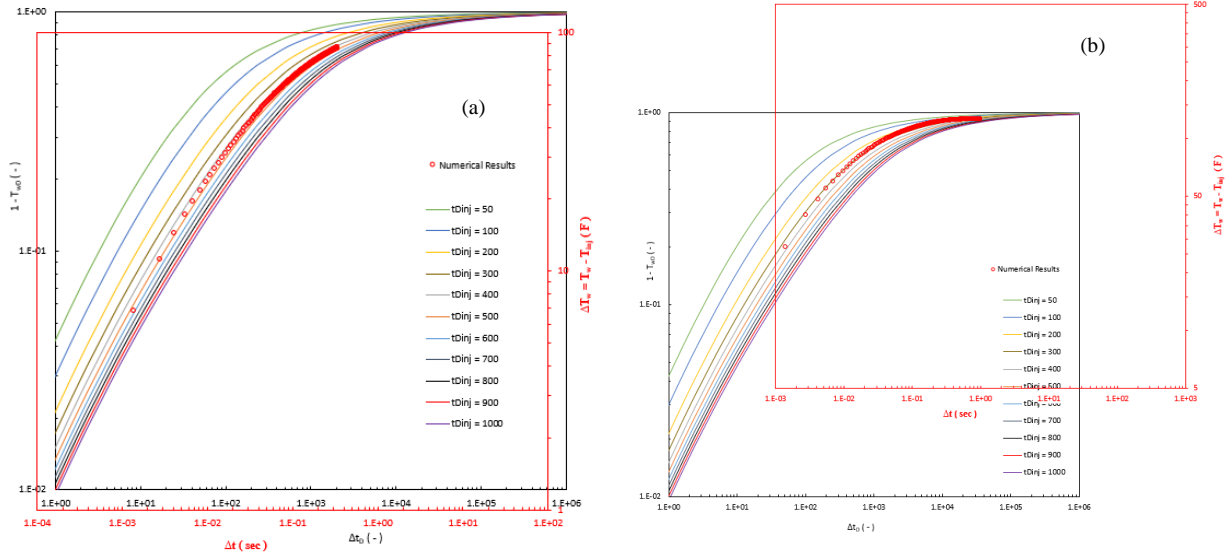


Figure 6. 11. Type-curve matching of sandface temperature results: (a) Case 1, (b) Case 2.

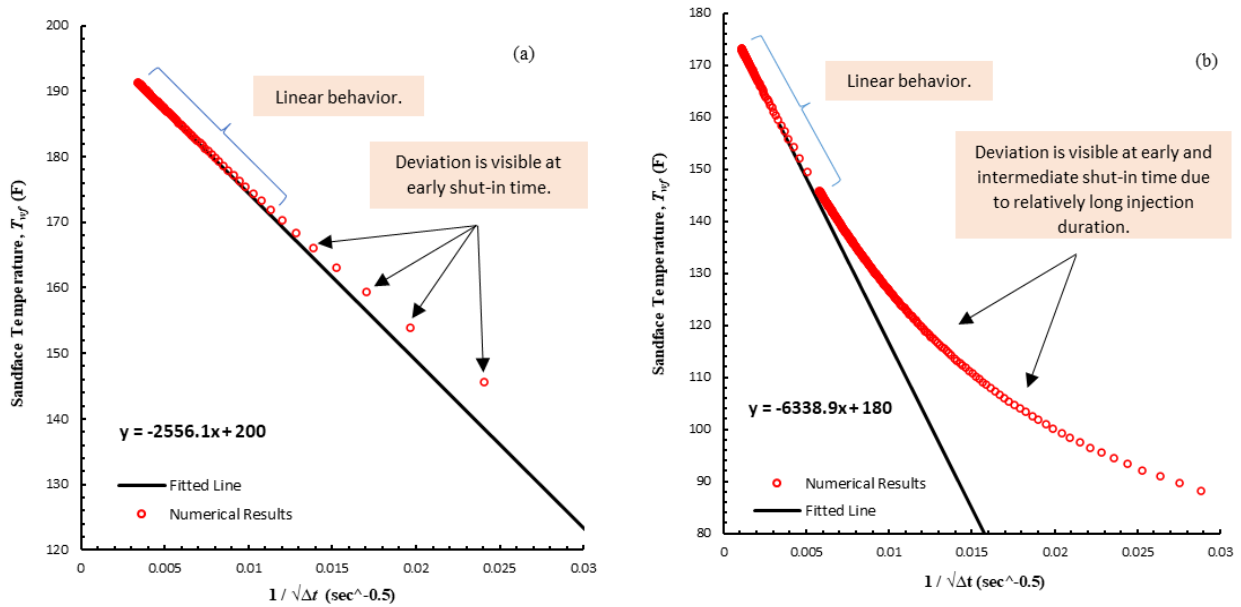


Figure 6. 12. Application of late-time graphical interpretation technique: (a) Case 1, (b) Case 2.

Chapter 7. Application of Temperature Warmback Analysis for Allocating CO₂ Injection Rate and Plume Extent Evaluation using Temperature Warmback Analysis

In this chapter, we will extend the application of temperature warmback analysis for estimating injection profile through CO₂ injection wells and estimate CO₂ plume extent during Geological CO₂ Storage (GCS). Monitoring CO₂ injection profile during CO₂ storage in deep saline aquifers is important to assess the vertical heterogeneity of the target reservoir and maximize the potential storage capacity of the reservoir. Temperature warmback analysis has recently been used for monitoring CO₂ during GCS (Mawalkar et al. 2019), however, its application is restricted to providing qualitative indication of flow profile and injection well integrity. The analytical models developed previously assume single-phase flow in the reservoir during injection activity and consequently they neglect the effect of flowing fluids saturation on temperature recovery. This assumption may be valid for liquid-liquid displacement process in which the contrast between the thermal properties of the displaced (e.g., oil) and displacing (e.g., water) is not significant. For the applications of gas injection in liquid bearing formations such as CO₂ injection in deep saline aquifers, this assumption can be violated. Consequently, new analytical solution is required to consider temperature and CO₂ saturation evolutions during and shortly after CO₂ injection.

7.1. Forward Modeling

In this section, novel analytical model is developed to model temperature and CO₂ evolution during and shortly after CO₂ injection in deep saline aquifer. The solution is developed through solving coupled mass and heat conservation equations during CO₂ flow in the porous medium. The following assumptions are made during formulating and solving the problem:

- CO₂ is injected with constant injection rate, q and constant injection temperature, T_{inj} in an aquifer with initial temperature, T_o for an injection duration, t_{inj} . Then, injection stops to allow for the temperature recovery (see Fig. 7.1).
- The aquifer consists of multiple layers. Each layer is assumed to be homogenous, isotropic, and of an infinite extent in the lateral direction with a uniform thickness, h . However, the aquifer can be vertically heterogeneous (i.e., the properties of the layers are different).
- Fluid flow is assumed to be 1D radial flow.
- Fluid displacement is immiscible; no mass transfer occurs between the displacing and the displaced fluids.
- Heat transfers in the flow direction by advection and conduction. Heat exchange with the surrounding strata is negligible during the injection and shut-in periods.
- No phase change occurs over the displacement length (Dindoruk and Dindoruk 2008).
- Fractional-flow curve is a function of saturation and temperature only (Bratvold and Horne 1989).
- Capillary and gravity forces are neglected during the injection and shut-in periods (Bratvold and Horne 1989).
- Energy contributions from kinetics and stresses/pressure are neglected.

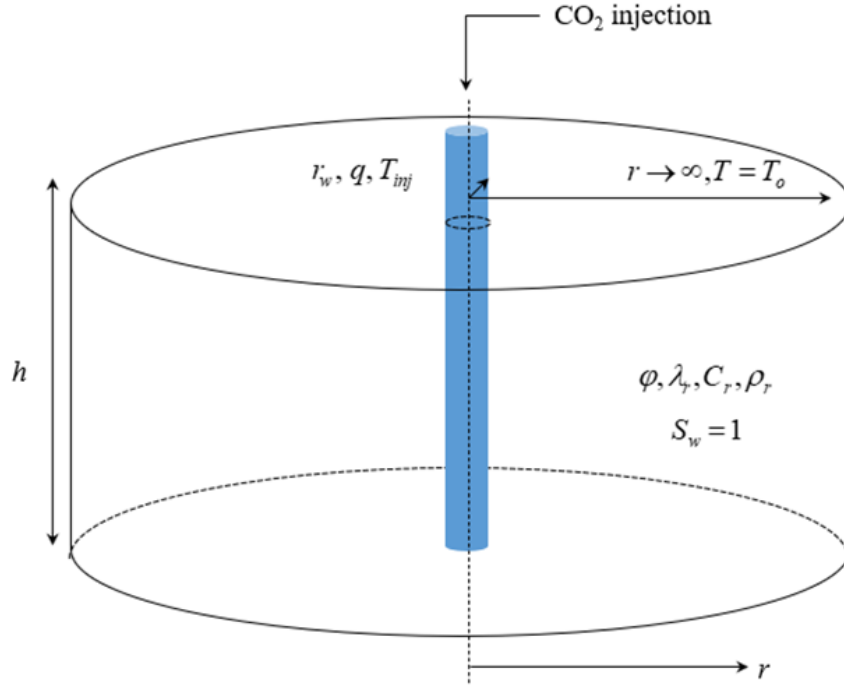


Figure 7. 1. Schematic illustration of the physical model for a single-layer reservoir.

The mass conservation equation for flowing CO₂ in the reservoir is given by:

$$\frac{\partial}{\partial t}(\phi \rho_g S_g) + \frac{1}{r} \frac{\partial}{\partial r}(r \rho_g u_g) = 0 \quad (7.1)$$

where $u_g = q_g / A = q_g / (2\pi r h)$ is gas phase velocity, ρ_g is gas phase density, S_g is gas phase saturation, and ϕ is formation porosity. Using the assumption of incompressible fluid flow, which is feasible for the brine and the supercritical state nature of the injected CO₂, the mass conservation equation is simplified to the following form (Buckley and Leverett 1942),

$$\frac{\partial S_g}{\partial t} + \left(\frac{q}{\pi h \phi} \right) \frac{\partial f_g}{\partial r^2} = 0 \quad (7.2)$$

The volumetric fractional flow is the ratio of CO₂-rich gaseous phase velocity to the mixture (brine + CO₂) velocity, which is given by:

$$f_g(S_g, T) = \frac{u_g}{u} = \frac{\frac{k_{rg}}{\mu_g}}{\frac{k_{rg}}{\mu_g} + \frac{k_{rw}}{\mu_w}} = \frac{1}{1 + \left(\frac{k_{rw}}{k_{rg}} \right) \left(\frac{\mu_g}{\mu_w} \right)} \quad (7.3)$$

Since the fractional flow of CO₂ is only a function of CO₂ saturation and temperature due to the temperature dependency of viscosity ratio and the saturation dependency of relative permeability (Dindoruk and Dindoruk 2008), respectively, the mass conservation equation can be written in the following form using the chain rule,

$$\frac{\partial S_g}{\partial t} + \left(\frac{q}{\pi h \phi} \right) \left(\frac{\partial f_g}{\partial S_g} \frac{\partial S_g}{\partial r^2} + \frac{\partial f_g}{\partial T} \frac{\partial T}{\partial r^2} \right) = 0 \quad (7.4)$$

The energy balance equation for an immiscible CO₂-brine displacement is described by the following equation assuming advection-dominant heat transfer in the reservoir (Duru and Horne 2010, App 2010, Mao and Zeidouni 2017),

$$\frac{\partial}{\partial t} (\rho_t C_t T) + \frac{\partial}{\partial r} (\rho_t C_t u_t T) = 0 \quad (7.5)$$

where

$$\rho_t C_t = \phi (\rho_g C_g S_g + \rho_w C_w (1 - S_g)) + (1 - \phi) \rho_r C_r \quad (7.6)$$

$$\rho_t C_t u_t = (\rho_g C_g u_g + \rho_w C_w u_w) = (\rho_g C_g f_g + \rho_w C_w (1 - f_g)) u \quad (7.7)$$

Assuming that porosity is constant, that fluids have constant density and heat capacity, and the change in the total thermal conductivity is negligible, the governing equation is simplified to the following form after few manipulations:

$$\left(S_g + \frac{\rho_w C_w + \left(\frac{1 - \phi}{\phi} \right) \rho_r C_r}{\rho_g C_g - \rho_w C_w} \right) \frac{\partial T}{\partial t} + \left(f_g + \frac{\rho_w C_w}{\rho_g C_g - \rho_w C_w} \right) \left(\frac{q}{\pi h \phi} \right) \frac{\partial T}{\partial r^2} = 0 \quad (7.8)$$

Eq. 7.5 and Eq. 7.8 constitute coupled hyperbolic partial differential equations. The mass and heat conservation equations are subject to the following initial and boundary conditions:

$$S_g (r, t = 0) = 0 \quad (7.9)$$

$$S_g (r = r_w, t) = 1 - S_{wr} \quad (7.10)$$

$$T (r, t = 0) = T_o \quad (7.11)$$

$$T (r = r_w, t) = T_{inj} \quad (7.12)$$

The above problem has been solved by Bratvold and Horne (1989) in which the authors used the method of characteristics to solve the coupled non-linear hyperbolic conservation equations. The details of their solution procedure are presented in Appendix G for completeness. According to which the temperature and saturation profiles at the end of the injection period are obtained (see Fig. G.2). The temperature profile obtained during the injection period is characterized by step change in the temperature at the thermal front from the injection temperature to initial aquifer temperature. During the shut-in period, the governing equation for heat transfer in the reservoir is described by the following equation:

$$\left(S_g + \frac{\rho_w C_w + \left(\frac{1-\phi}{\phi} \right) \rho_r C_r}{\rho_g C_g - \rho_w C_w} \right) \frac{\partial T}{\partial t} = \left(\frac{\lambda_g - \lambda_w}{\rho_g C_g - \rho_w C_w} \right) \left(S_g + \frac{\lambda_w + \left(\frac{1-\phi}{\phi} \right) \lambda_r}{(\lambda_g - \lambda_w)} \right) \frac{1}{r} \frac{\partial}{\partial r} \left(r \frac{\partial T}{\partial r} \right) \quad (7.13)$$

The corresponding initial and boundary conditions are given by:

$$T(r, \Delta t = 0) = T(r, t = t_{inj}) \quad (7.14)$$

$$T(r = r_w, t) = T_{inj} \quad (7.15)$$

$$\lim_{r \rightarrow \infty} \left(\frac{\partial T}{\partial r} \right) = 0 \quad (7.16)$$

The IBVP is rescaled using the following dimensionless parameters:

$$\begin{aligned} T_D &= \frac{T - T_{inj}}{T_o - T_{inj}} & t_D &= \frac{qt}{\phi \pi r_w^2 h} & r_D &= \frac{r}{r_w} & \alpha &= \frac{\rho_w C_w}{\rho_g C_g - \rho_w C_w} & g &= \frac{f_g + \alpha}{S_g + \beta} \\ \beta &= \frac{\rho_w C_w + \left(\frac{1-\phi}{\phi} \right) \rho_r C_r}{\rho_g C_g - \rho_w C_w} & \eta &= \frac{\lambda_g - \lambda_w}{\rho_g C_g - \rho_w C_w} & \gamma &= \frac{\lambda_w + \left(\frac{1-\phi}{\phi} \right) \lambda_r}{(\lambda_g - \lambda_w)} & \chi &= \frac{q}{\pi h \phi \eta} \end{aligned} \quad (7.17)$$

The governing equation of the heat diffusion (Eq. 7.13) in dimensionless form is given by:

$$\frac{\partial^2 T_D}{\partial r_D^2} + \frac{1}{r_D} \frac{\partial T_D}{\partial r_D} = \theta(r_D) \frac{\partial T_D}{\partial \Delta t_D} \quad (7.18)$$

where $\theta(r_D) = \left(\frac{S_g(r_D) + \beta}{S_g(r_D) + \gamma} \right) \chi$ and $\Delta t_D = t_D - t_{injD}$. The corresponding initial and boundary conditions are given by:

$$T_D(r_D, \Delta t_D = 0) = T_D(r_D, t_D = t_{injD}) \quad (7.19)$$

$$\lim_{r_D \rightarrow 0} \left(\frac{\partial T_D}{\partial r_D} \right) = 0 \quad (7.20)$$

$$\lim_{r_D \rightarrow \infty} \left(\frac{\partial T_D}{\partial r_D} \right) = 0 \quad (7.21)$$

The governing equation described by Eq. 7.18 is a heat diffusion equation with a spatially variable coefficient. The problem is solved by discretizing the aquifer into three regions (see Fig. 7.2) in which the coefficient, $\theta(r_D)$ is constant per region and evaluated at the average saturation within the region. Region 1 extends from the injection well to the thermal front. Region 2 extends from the thermal front to the saturation front. Region 3 extends from the saturation front to the outer boundary of the reservoir. In this solution, the effect of heat diffusion during the injection period is neglected for simplicity. Consequently, temperature profile is described by step change in the temperature at the thermal front where the temperature upstream of the thermal front is identical to the injection temperature (region 1), and the temperature downstream of the thermal front is identical to the initial aquifer temperature (region 2 and region 3). Accordingly, governing equations for heat transfer during the shut-in period for the discretized regions are given by:

$$\frac{\partial^2 T_{D,1}}{\partial r_D^2} + \frac{1}{r_D} \frac{\partial T_{D,1}}{\partial r_D} = \theta_1 \frac{\partial T_{D,1}}{\partial \Delta t_D} \quad 0 \leq r_D < r_{TD} \quad (7.22)$$

$$\frac{\partial^2 T_{D,2}}{\partial r_D^2} + \frac{1}{r_D} \frac{\partial T_{D,2}}{\partial r_D} = \theta_2 \frac{\partial T_{D,2}}{\partial \Delta t_D} \quad r_{TD} \leq r_D < r_{SD} \quad (7.23)$$

$$\frac{\partial^2 T_{D,3}}{\partial r_D^2} + \frac{1}{r_D} \frac{\partial T_{D,3}}{\partial r_D} = \theta_3 \frac{\partial T_{D,3}}{\partial \Delta t_D} \quad r_{SD} \leq r_D < \infty \quad (7.24)$$

The corresponding initial conditions are given by:

$$T_{D,1}(r_D, \Delta t_D = 0) = 0 \quad (7.25)$$

$$T_{D,2}(r_D, \Delta t_D = 0) = 1 \quad (7.26)$$

$$T_{D,3}(r_D, \Delta t_D = 0) = 1 \quad (7.27)$$

The innermost and outermost boundary conditions are well described using thermally isolated boundary conditions which are given by:

$$\lim_{r_D \rightarrow 0} \left(\frac{\partial T_{D,1}}{\partial r_D} \right) = 0 \quad (7.28)$$

$$\lim_{r_D \rightarrow \infty} \left(\frac{\partial T_{D,3}}{\partial r_D} \right) = 0 \quad (7.29)$$

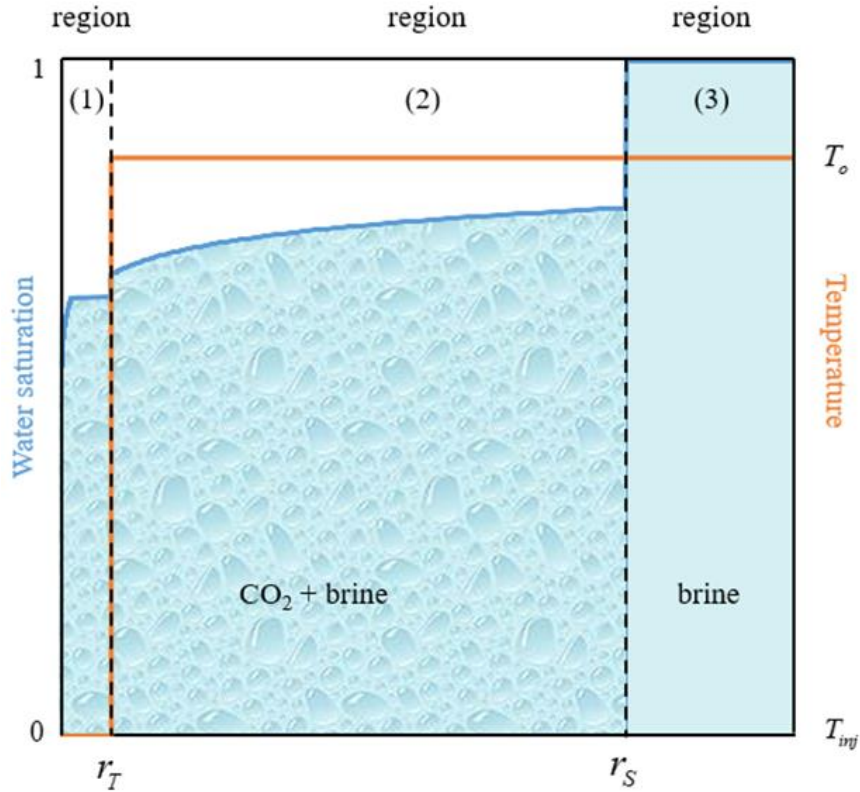


Figure 7. 2. Schematic illustration of the three-region model showing the temperature and saturation profiles at the end of the injection period as obtained from Bratvold and Horne (1989)'s solution.

The boundary conditions at the interfaces of the regions are described through the conservation of heat flux and the continuity of temperature, which are given by:

$$R_{12} \left(\frac{\partial T_{D,1}}{\partial r_D} \right)_{r_D=r_{TD}} = \left(\frac{\partial T_{D,2}}{\partial r_D} \right)_{r_D=r_{TD}} \quad (7.30)$$

$$T_{D,1}(r_D = r_{TD}, \Delta t_D) = T_{D,2}(r_D = r_{TD}, \Delta t_D) \quad (7.31)$$

$$R_{23} \left(\frac{\partial T_{D,2}}{\partial r_D} \right)_{r_D=r_{SD}} = \left(\frac{\partial T_{D,3}}{\partial r_D} \right)_{r_D=r_{SD}} \quad (7.32)$$

$$T_{D,2}(r_D = r_{SD}, \Delta t_D) = T_{D,3}(r_D = r_{SD}, \Delta t_D) \quad (7.33)$$

where $R_{ij} = \varepsilon_i / \varepsilon_j$ and $\varepsilon_i = \left(S_{gi} + \frac{\lambda_w + ((1-\phi)/\phi)\lambda_r}{\lambda_g - \lambda_w} \right)$. The solution of the IBVP described by Eq.

7.22 -7.33 is obtained using Laplace transformation technique. In Laplace domain, the solution of the governing equations are obtained in terms of the modified Bessel functions, which is given by:

$$T_{D,1}(r_D, \Delta t_D) = \mathcal{L}^{-1} \left\{ c_1(s) I_o(r_D \sqrt{s\theta_1}) \right\} \quad (7.34)$$

$$T_{D,2}(r_D, \Delta t_D) = 1 + \mathcal{L}^{-1} \left\{ c_3(s) I_o(r_D \sqrt{s\theta_2}) + c_4(s) K_o(r_D \sqrt{s\theta_2}) \right\} \quad (7.35)$$

$$T_{D,3}(r_D, \Delta t_D) = 1 + \mathcal{L}^{-1} \left\{ c_6(s) K_o(r_D \sqrt{s\theta_3}) \right\} \quad (7.36)$$

where

$$\begin{aligned} \Phi = & \theta_2 R_{23} K_o(r_{SD} \sqrt{s\theta_3}) \left[I_1(r_{SD} \sqrt{s\theta_2}) K_1(r_{TD} \sqrt{s\theta_2}) - I_1(r_{TD} \sqrt{s\theta_2}) K_1(r_{SD} \sqrt{s\theta_2}) \right] \\ & + \sqrt{\theta_2} \sqrt{\theta_3} K_1(r_{SD} \sqrt{s\theta_3}) \left[I_1(r_{TD} \sqrt{s\theta_2}) K_o(r_{SD} \sqrt{s\theta_2}) + I_o(r_{SD} \sqrt{s\theta_2}) K_1(r_{TD} \sqrt{s\theta_2}) \right] \end{aligned} \quad (7.37)$$

$$\Omega = R_{12} \sqrt{\theta_1} I_1(r_{TD} \sqrt{s\theta_1}) \left[\sqrt{\theta_3} K_o(r_{SD} \sqrt{s\theta_2}) K_1(r_{SD} \sqrt{s\theta_3}) - R_{23} \sqrt{\theta_2} K_o(r_{SD} \sqrt{s\theta_3}) K_1(r_{SD} \sqrt{s\theta_2}) \right] \quad (7.38)$$

$$X = -R_{12} \sqrt{\theta_1} I_1(r_{TD} \sqrt{s\theta_1}) \left[\sqrt{\theta_3} I_o(r_{SD} \sqrt{s\theta_2}) K_1(r_{SD} \sqrt{s\theta_3}) + R_{23} \sqrt{\theta_2} K_o(r_{SD} \sqrt{s\theta_3}) I_1(r_{SD} \sqrt{s\theta_2}) \right] \quad (7.39)$$

$$\Theta = -\frac{R_{12} R_{23} \sqrt{\theta_1}}{r_{SD} \sqrt{s}} I_1(r_{TD} \sqrt{s\theta_1}) \quad (7.40)$$

$$\Psi = s \left\{ \begin{aligned} & R_{12} \sqrt{\theta_1} I_1(r_{TD} \sqrt{s\theta_1}) \left[\begin{aligned} & R_{23} \sqrt{\theta_2} K_o(r_{SD} \sqrt{s\theta_3}) \left(I_1(r_{SD} \sqrt{s\theta_2}) K_o(r_{TD} \sqrt{s\theta_2}) + I_o(r_{TD} \sqrt{s\theta_2}) K_1(r_{SD} \sqrt{s\theta_2}) \right) \\ & \sqrt{\theta_3} K_1(r_{SD} \sqrt{s\theta_3}) \left(I_o(r_{SD} \sqrt{s\theta_2}) K_o(r_{TD} \sqrt{s\theta_2}) - I_o(r_{TD} \sqrt{s\theta_2}) K_o(r_{SD} \sqrt{s\theta_2}) \right) \end{aligned} \right] \\ & + \sqrt{\theta_2} I_o(r_{TD} \sqrt{s\theta_1}) \left[\begin{aligned} & R_{23} \sqrt{\theta_2} K_o(r_{SD} \sqrt{s\theta_3}) \left(I_1(r_{SD} \sqrt{s\theta_2}) K_1(r_{TD} \sqrt{s\theta_2}) - I_1(r_{TD} \sqrt{s\theta_2}) K_1(r_{SD} \sqrt{s\theta_2}) \right) \\ & + \sqrt{\theta_3} K_1(r_{SD} \sqrt{s\theta_3}) \left(I_1(r_{TD} \sqrt{s\theta_2}) K_o(r_{SD} \sqrt{s\theta_2}) + I_o(r_{SD} \sqrt{s\theta_2}) K_1(r_{TD} \sqrt{s\theta_2}) \right) \end{aligned} \right] \end{aligned} \right\} \quad (7.41)$$

The sandface temperature solution is obtained by assigning $r_D \rightarrow 0$ in Eq. 7.34, which yields:

$$T_{wD}(\Delta t_D) = \mathcal{L}^{-1} \left\{ \frac{\Phi}{\Psi} \right\} \quad (7.42)$$

At early shut-in times, an asymptotic solution of the sandface temperature can be obtained using the following asymptotic expansions of the modified Bessel functions at large argument (Abramowitz et al. 1988),

$$\lim_{z \rightarrow \infty} I_\nu(z) = \frac{e^z}{\sqrt{2\pi z}} \quad (7.43)$$

$$\lim_{z \rightarrow \infty} K_\nu(z) = \sqrt{\frac{\pi}{2z}} e^{-z} \quad (7.44)$$

Consequently, the early-time asymptotic solution in Laplace domain is given by:

$$T_{wD}(\Delta t_D) \approx \mathcal{L}^{-1} \left\{ \frac{\sqrt{\pi\sqrt{\theta_1}}}{\sqrt{2}} \sqrt{r_{TD}} \frac{1}{s^{\frac{3}{4}}} e^{(-r_{TD}\sqrt{s\theta_1})} \right\} \quad (7.45)$$

The corresponding early-time asymptotic solution in the real-time domain is obtained using inverse Laplace transformation (Abramowitz et al. 1988), which is given by:

$$T_{wD}(\Delta t_D) = \left(\frac{r_{TD}\sqrt{\theta_1}}{2\sqrt{\pi}} \right) \frac{e^{-\left(\frac{\theta_1 r_{TD}^2}{8\Delta t_D}\right)}}{\sqrt{\Delta t_D}} K_{\frac{1}{4}} \left(\frac{\theta_1 r_{TD}^2}{8\Delta t_D} \right) \approx e^{-\left(\frac{\theta_1 r_{TD}^2}{4\Delta t_D}\right)} \quad (7.46)$$

The above equation is re-written below in a dimensional form using the dimensionless group given by Eq. 7.17,

$$\Delta T_w(\Delta t) = (T_o - T_{inj}) e^{-\frac{1}{4} \left(\frac{\bar{S}_{g1} + \beta}{\bar{S}_{g1} + \gamma} \right) \frac{r_f^2}{\eta \Delta t}} \quad (7.47)$$

where \bar{S}_{g1} is the average gas saturation within region 1. Eq. 7.47 is identical to the temperature solution for a single region reservoir which has thermal properties and fluid saturation identical to the innermost region. This indicates that at the early shut-in time, the properties of the innermost region dominate the temperature recovery at injection well. The early-time asymptotic solution presents a simple form for the temperature recovery at the shut-in period which can be

casted into a simple graphical technique for the inverse modeling as will be shown in the next section.

7.2. Inverse Modeling

In this section, inversion procedures are presented using the analytical solutions developed in Section 7.1 to estimate the injection profile, the radius of the saturation front, the radius of the thermal front, and the initial geotherm prior to CO₂ injection. Inverse modeling is done using the early-time asymptotic solution given by Eq. 7.47. The inversion procedure is as follows:

- Construct the solution of the advection problem using Bratvold and Horne (1989)'s procedure as illustrated in Appendix G. The solution describes the temperature and gas saturation profiles at the end of the injection period versus the similarity variable ζ , similar to Fig G.1 (b) in Appendix G and Figs. 7.3 (b) in the validation section.
- Plot the change in the sandface temperature, $\Delta T_w(\Delta t) (= T_w(\Delta t) - T_{inj})$ for the layer of interest versus $1/\Delta t$ on a semi-log scale such that the temperature change is plotted on the logarithmic scale.
- Identify the portion of the plotted data to be fitted with a straight line.
- Estimate the slope, m and the intercept with the vertical axis, b of the fitted line.
- The initial temperature of the layer of interest is estimated by:

$$T_o = T_{inj} + b \quad (7.48)$$

- The location of the thermal front is estimated by:

$$r_T = \sqrt{4\eta \left(\frac{\bar{S}_{g1} + \gamma}{\bar{S}_{g1} + \beta} \right) |m|} \quad (7.49)$$

where η , γ , and β are given by Eq. 7.17, and the fluid properties are estimated at the initial conditions. The average gas saturation within the near wellbore region, \bar{S}_{g1} can be obtained by averaging the saturation values located upstream of the thermal front in the S_g - ζ profile obtained in the first step.

- The injection rate at the layer of interest is estimated using Eq. 7.50, where ζ_T is the velocity of the thermal front which is given by $(f_g(S_{g1}) + \alpha)/(S_{g1} + \beta)$ or $(f_g(S_{g2}) + \alpha)/(S_{g2} + \beta)$, S_{g1} is the gas saturation upstream of the thermal front, S_{g2} is the gas saturation downstream of the thermal front, and α and β are given by Eq. 7.17. S_{g1} is obtained from the intercept of the thermal tangent with f_g - S_g plot at the injection temperature and S_{g2} is obtained from the tangent point of the thermal tangent on f_g - S_g plot at the initial temperature.

$$q = \frac{1}{\zeta_T} \left(\frac{\pi r_T^2 h \phi}{t_{inj}} \right) \quad (7.50)$$

- The radius of the saturation front is estimated using Eq. 7.51, where ζ_{S_g} is the velocity of the saturation front which is given by the slope of the saturation tangent with f_g - S_g plot at the initial temperature.

$$r_{S_g} = \sqrt{\left(\frac{qt_{inj}}{\pi h \phi}\right)} \zeta_{S_g} \quad (7.51)$$

The results of the developed forward and inverse models presented in Section 7.1 – 7.2 are validated against numerical results in the next sections to demonstrate their validity.

7.3. Solution Validation

In this section, the developed forward model is validated against the results of the numerical reservoir simulator; TOUGH3/ECO2N. TOUGH3 is a numerical simulator capable of simulating nonisothermal multiphase and multicomponent fluid flow in multidimensional porous media (Jung et al. 2018). ECO2N is a fluid property module implemented in TOUGH3 that estimates the thermophysical properties of brine and CO₂ system (Pruess 2005). The synthetic case is presented for a heterogeneous multi-zone aquifer that is subject to CO₂ injection via a commingled injection well (see Table 7.1). CO₂ is injected at a bottomhole temperature lower than the initial reservoir temperature. Then, injection stops to allow for temperature recovery. In this case, a 5-layer aquifer with different permeability per layer ($k = 900, 700, 500, 300, \text{ and } 100$ md) is subject to cold CO₂ injection at a constant injection rate of 460 m³/day and a constant bottomhole injection temperature of 20 °C (see Table 7.1). Each layer is 10-m thick. The injection profile as obtained from the numerical model is 165, 129, 92, 55 and 18 m³/day for the injection layers from the top to the bottom of the aquifer. The analytical models presented in Section 7.1 are used to model the transient temperature during the injection and the shut-in periods in each layer. First, the solution procedure presented in Appendix G is used to solve the advection problem. Fig. 7.3 (a) illustrates the f_g - S_g plots at the initial reservoir temperature and the bottomhole injection temperature with the characteristic curves. Fig. 7.3 (b) illustrates the derivative of the fractional flow curves along with the established solution.

Fig. 7.4 (a) shows the transient temperature and CO₂ saturation profiles at the end of the injection period for the layer 1 (uppermost layer) as obtained from TOUGH3 and the analytical solution. The extent of CO₂ plume propagation by the end of the injection period is 15.5 m while the extent of the thermal front is 3.5 m.

Table 7. 1. Input data for the synthetic case.

Feature	Value	Unit
Initial temperature, T_o	65	°C
Injection temperature, T_{inj}	20	°C
Injection rate, q	460	m ³ /day
Injection period, t_{inj}	3	days
Reservoir thickness, h	50	m
Residual water saturation, S_{wr}	0.3	fraction
Residual CO ₂ saturation, S_{gr}	0.05	fraction
Porosity, ϕ	0.25	fraction
Permeability, k	100, 300, 500, 700, and 900	md
Water density, ρ_w	991	kg/m ³
CO ₂ density, ρ_g	724	kg/m ³
Rock density, ρ_r	2650	kg/m ³
Water heat capacity, C_w	4143.6	J/kg K
CO ₂ heat capacity, C_g	2501	J/kg K
Rock heat capacity, C_r	1000	J/kg K
Effective thermal conductivity,	2	W/m K
CO ₂ and water viscosity at T_o	0.06 – 0.438	cp
CO ₂ and water viscosity at T_{inj}	0.095 – 0.886	cp

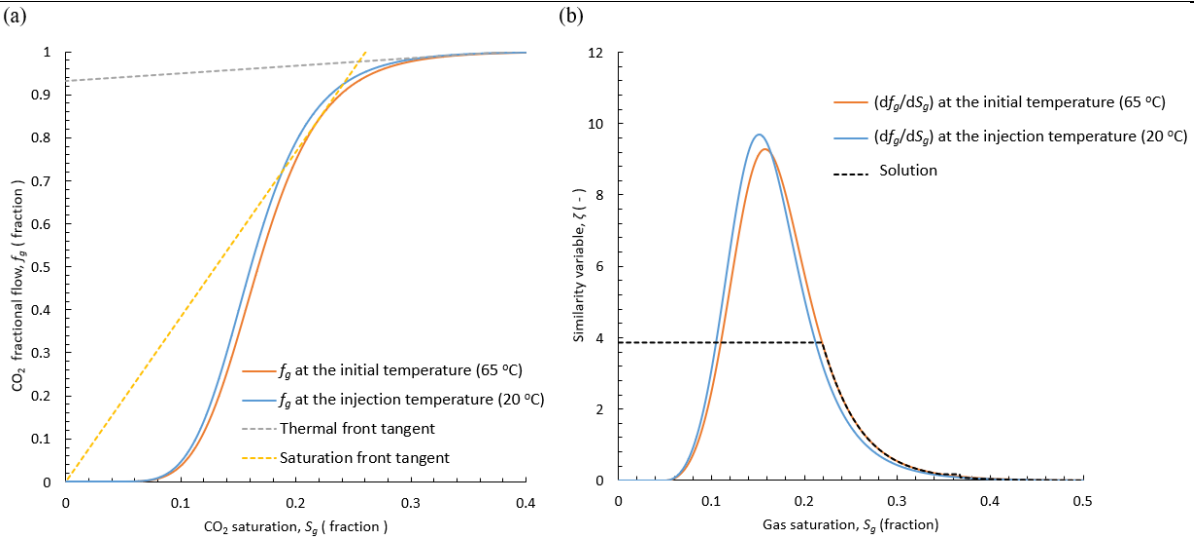


Figure 7. 3. (a) f_g - S_g plots with the characteristic curves (b) slopes of the fractional flow curves along with the saturation solution in terms of the similarity variable defined by Eq. G.9.

Fig. 7.4 (b) illustrates the temperature profiles in layer 1 during the warmback period at $\Delta t = 7, 14, 21,$ and 30 days. Fig. 7.5 illustrates the sandface temperature recovery over the injection zones during the warmback period. Different rates of temperature recovery are obtained during the shut-in period due to the different injectivities of the injection layers. Layer 5, which has the lowest permeability ($k = 100$ md), accepts the lowest percentage of the injected volume and consequently exhibits the highest temperature rebound during the shut-in period. On the other hand, layer 1 which has the highest permeability ($k = 900$ md), accepts most of the injected volume, and consequently, exhibits the lowest temperature rebound during the shut-in period. The temperature recovery for layer 1 is 8 °C compared with 38 °C for layer 5 at $\Delta t = 30$ days. Based on these observations, the characteristics of the temperature recovery reflect the injection profile and the distribution of the injected CO_2 over the reservoir thickness.

It is obtained from Fig. 7.5 that the three-region solution provides underestimated temperature results at the early shut-in time because it neglects the effect of heat transfer by conduction during the injection period. As the injection rate increases, the relative contribution of advection mechanism compared with the conduction mechanism, known as Péclet number, increases. This is why the deviation in the results obtained using three-region solution and multi-region solution decreases as injection rate increases from layer 5 ($18 \text{ m}^3/\text{day}$) to layer 1 ($165 \text{ m}^3/\text{day}$). In the next section, the inversion procedure presented in Section 7.2 is used to infer the injection profile and the distribution of the CO_2 over the aquifer thickness.

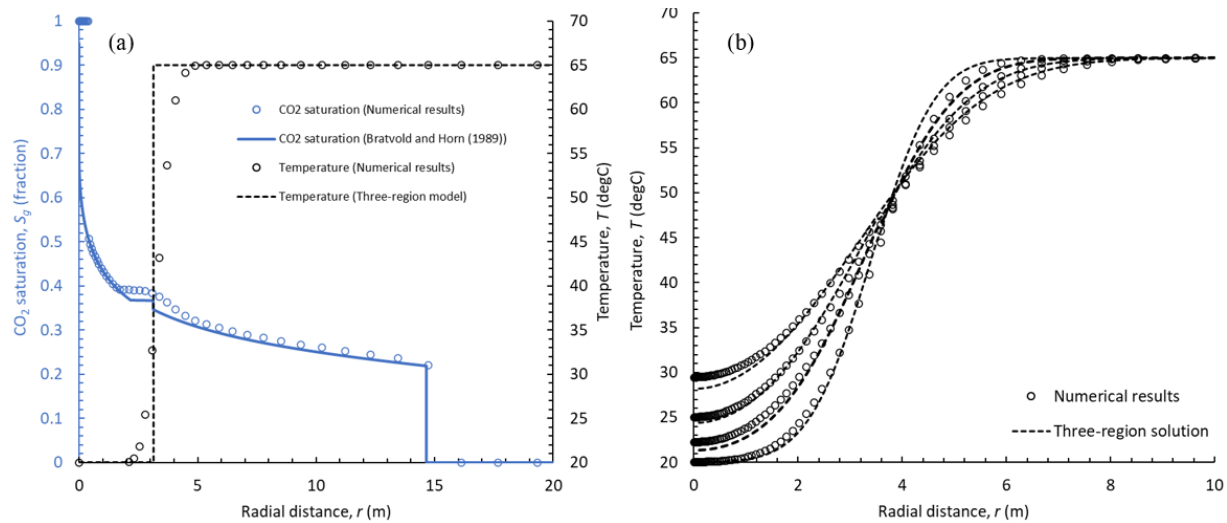


Figure 7. 4. (a) Transient temperature profile at the end of the injection period (b) transient temperature profile during the warmback period obtained using TOUGH3 and the three-region analytical solution (layer 1).

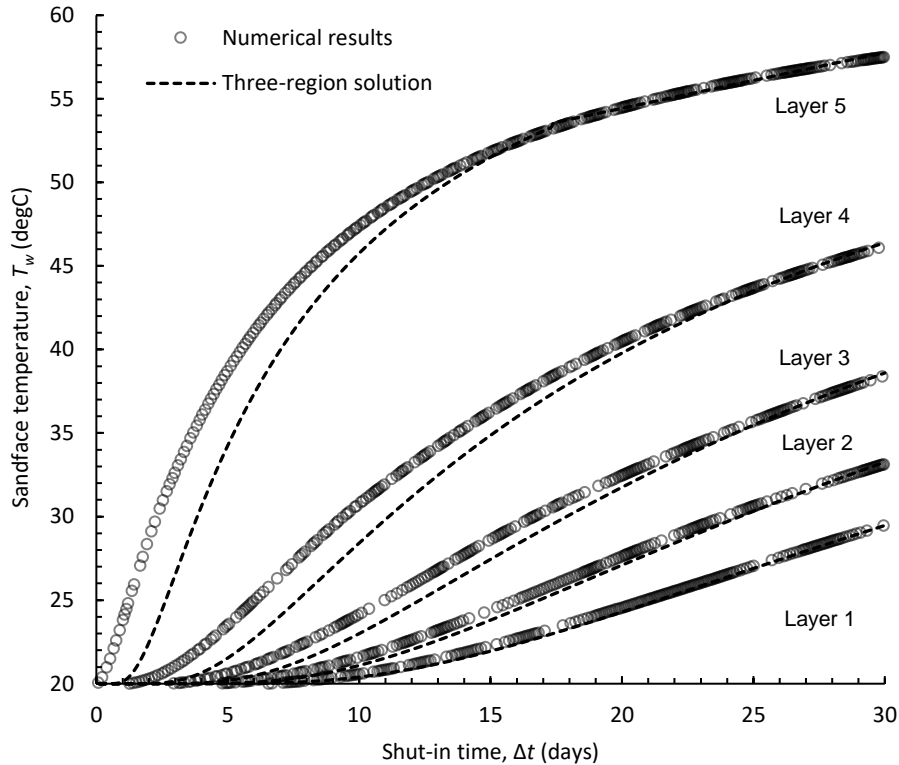


Figure 7. 5. Transient sandface temperature during the warmback period obtained using TOUGH3 and the three-region analytical solution.

7.4. Inverse Modeling Application

In this section, the inversion procedure introduced in Section 7.2 is used for the inverse modeling. Fig. 7.6 shows the application of the graphical technique for the numerical temperature results. Disagreement is evident between the asymptotic solution and the numerical results at the early shut-in time. This can be attributed to neglecting the effect of heat conduction during the injection period and the adiabatic expansion of CO₂ at the sandface region when injection stops which results in slight decrease in the temperature signal before the warmback. The corresponding inversion results are given in Table 7.2, respectively. It is obtained that the graphical technique is simple and yet provides inversion results with good accuracy compared with the numerical results.

In the next paragraphs, the significance of the assumptions made during developing the analytical solution is discussed. First, we assumed that fluid flow geometry around the injection well is radial. This assumption is likely for a fully penetrating vertical well given the high viscous forces around the well which can effectively displace the fluids to allow for radial flow. However, radial flow may not develop if the injection zone is highly heterogeneous and/or anisotropic. We also neglected the mutual dissolution (i.e., mass exchange) between the injected CO₂ and aqueous brine in the reservoir. This assumption is inherent in Bratvold and Horne (1989)'s solution which is used in our work to obtain the temperature and saturation profiles during the injection period.

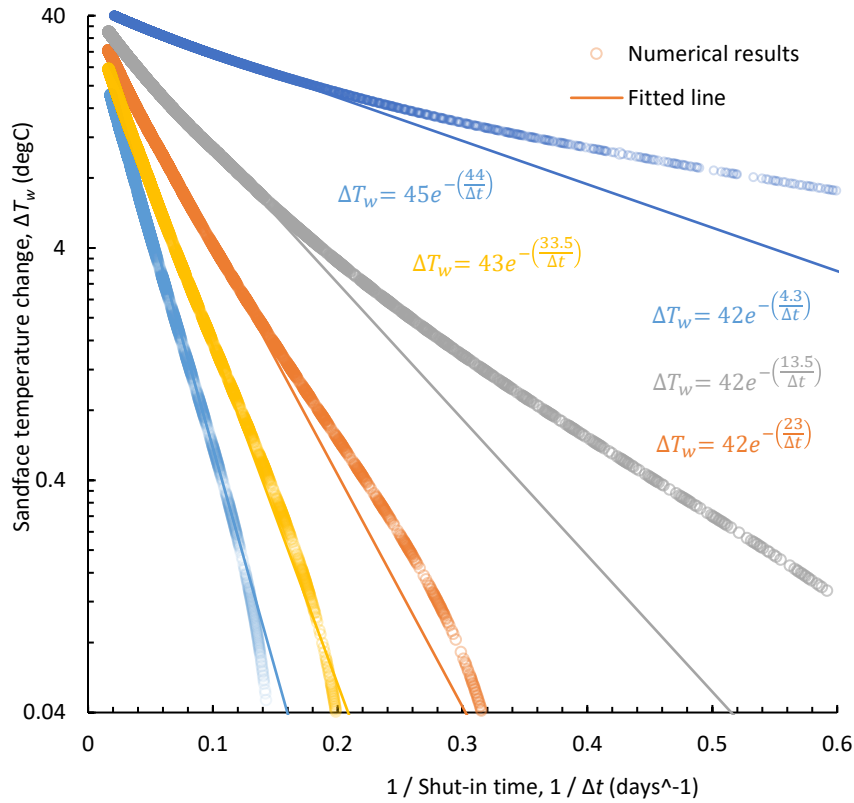


Figure 7. 6. Application of the graphical technique for the numerical sandface temperature data.

Table 7. 2. Inversion results obtained using the graphical technique.

	Layer 1	Layer 2	Layer 3	Layer 4	Layer 5
Initial temperature (°C)	65 (0%)	63 (3.1 %)	62 (4.62%)	62 (4.62%)	62 (4.62%)
Radius of thermal front (m)	3.36 (6.13 %)	2.93 (7.4 %)	2.43 (6.52 %)	1.86 (6.4 %)	1.051 (3.5 %)
Injection rate (m ³ / day)	168.2 (1.67 %)	128 (0.48 %)	87.9 (4.34 %)	51.6 (6.42 %)	16.44 (1.67 %)
Radius of saturation front (m)	15.76 (2.37 %)	13.75 (3.24 %)	11.39 (4.97 %)	8.73 (6 %)	4.93 (8.45 %)

Accordingly, the size of dry-out region is neglected. Despite that neglecting the dry-out region may affect the pressure evolution, however temperature is shown to be slightly affected. This

assumption is feasible for the application of the proposed technique because temperature warmback analysis is generally limited to short injection durations (few days); and consequently, the obtained size of the dry-out region is limited. In Case 1, the size of dry-out region is shown to be small (0.4 m) compared with the size of the two-phase region (15 m) after 3 days of CO₂ injection. Additionally, a good agreement is obtained between the analytical results and those obtained numerically as shown in Fig. 7.4 which demonstrates that feasibility of this assumption. Neglecting the mutual dissolution between the displacing and displaced phases also results in negligible contribution of specific hydrothermal processes such as water vaporization and CO₂ dissolution. According to Han et al. (2010), the contribution of water vaporization and CO₂ dissolution can be up to 1 °C which is of negligible effect compared with heat transfer by advection.

Besides, the solution presented in this work neglects the effect of heat exchange with the surrounding strata. This assumption is invalid for extended injection and shut-in durations (Hashish and Zeidouni 2021). However, the application of the warmback analysis is generally limited to short injection durations (few days). Injecting for a long injection period may not be practical anyway because extended shut-in time would be required to obtain a pronounced warmback signal. The shorter the injection duration, the more pronounced the temperature recovery that can be obtained during the warmback period. A short shut-in duration is also desirable to avoid extended pause in injection activity.

Chapter 8. Application of In-well and Formation Heat Pulse Testing for CO₂ Plume Monitoring

In this chapter, we will introduce the applications of heat pulse testing for monitoring CO₂ plume migration through storage aquifers. Two types of heat pulse testing are presented in this study which are in-well and formation heat pulse testing. In heat pulse testing, a distributed heating source is deployed within a monitoring well (in-well testing) or embedded in direct contact with the porous medium of the monitoring zone (formation testing). Temperature evolution during the heating period is monitored with fiber optic DTS cable which depends on the velocity of the surrounding fluids and heat conduction through porous medium. Analyzing the temperature data obtained during in-well and formation heat pulse testing in this chapter enables estimating subsurface fluid velocity, detecting CO₂ arrival, and providing spatial estimates of CO₂ saturation in the adjacent porous medium and formation thermal properties. The application of in-well and formation heat pulse testing is presented in sections 8.1 and 8.2, respectively.

8.1. In-well Heat Pulse Testing

In this section, new approach is presented to estimate the lateral velocity of brine (before CO₂ arrival) and velocity of CO₂ (after CO₂ arrival) as well as indicating CO₂ arrival using in-well heat pulse test. The heater can be deployed through the wellbore using a wireline or a small diameter tubing (coiled tubing). The heating source can be an electrical heater that constitutes a thermal coil with high electrical resistance which is shielded in a container made of conductive material such as Aluminum or Copper (see Fig. 8.1 (a)). Alternatively, the heating source can constitute a thermal coil that is wrapped around a small diameter tubing that can be deployed in the wellbore (see Fig. 8.1 (b)). The latter scenario, known as a pump down system, has been proposed by Liu et al. (2013) to obtain temperature signal during heat pulse testing with high spatial resolution.

Temperature heating is monitored using DTS cable which can be wrapped around the heating source. When electrical current passes through the thermal coil, electrical power is transformed into thermal energy. Flowing fluid across the downhole heater conveys the heat generated by the heater to the surroundings and reduces its surface temperature to a stabilized value which depends mainly on two competing effects: the electrical power supplied to the heater and heat loss by advection due to flowing fluid movement across the heater. To estimate the flowing fluid velocity, Joule effect is used to estimate the rate of heat released from the downhole heater, q given by Eq. 8.1. The rate of the generated heat is controlled by modifying the electrical power, P supplied to the heating cable which is considered as a design factor during heat pulse testing.

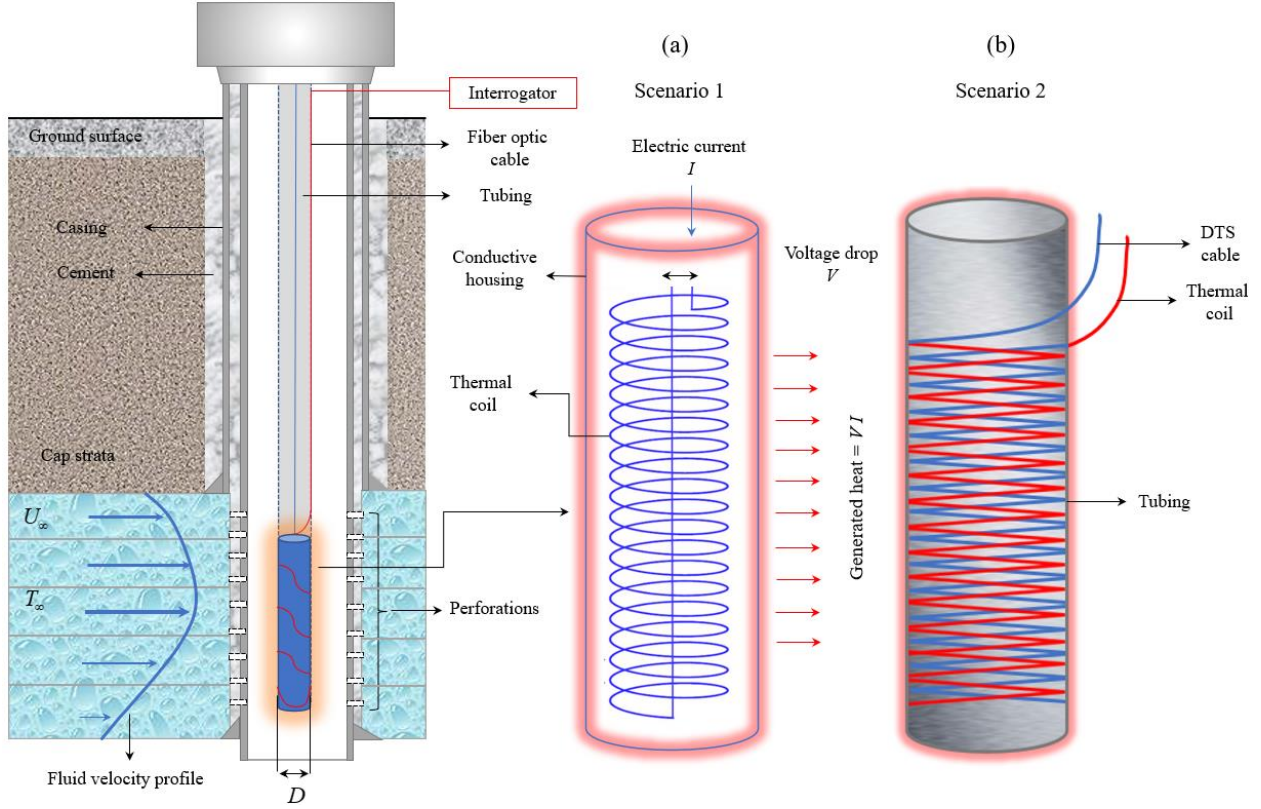


Figure 8. 1. Schematic illustration of the downhole electrical heater: (a) In the first scenario, the heater constitutes a thermal coil that is shielded in a conductive housing (b) in the second scenario, the thermal coil is wrapped around a deployed tubing. In both scenarios, the fiber optic cable is wrapped around the heater/tubing to increase the resolution of temperature measurements.

$$q = P = I \times V = I^2 \times R \quad (8.1)$$

where I is the magnitude of the electrical current that passes through the thermal coil, V is the voltage drop, and R is the thermal resistance of the thermal coil. The rate of heat released from the heating source is related to the convective heat transfer coefficient, h using Newton's law of cooling (described by Eq. 8.2) which is given by:

$$q = Ah(T_s - T_\infty) \quad (8.2)$$

where A is the surface area of the heater, T_s is the surface temperature of the heater when heat transfer reaches steady state conditions, and T_∞ is the temperature of the surrounding fluid. Heat transfer coefficient, h depends on fluid properties such as dynamic viscosity, thermal conductivity, mass density, and specific heat capacity. Additionally, the geometry and the roughness of the solid surface are among the factors that affect the convection heat transfer mechanism (Cengel 2014). Another factor that affects convective heat loss from the heater is the fluid flow regime. Fluid flow across a cylinder involves different flow regimes that range from laminar flow at low Reynolds numbers to fully turbulent flow at high Reynolds numbers. Due to the complicated flow patterns that establish across the cylinder, analytical modeling of the

problem is difficult. Rather, numerical or experimental models are required to model the fluid and heat flow across a cylinder. Numerous correlations were developed based on experimental observations to estimate the average heat transfer coefficient during external fluid flow across a cylinder, and they are classified into two categories according to the method by which fluid properties are estimated (Sparrow et al. 2004). In the first category, fluid properties are evaluated at the film temperature which is the arithmetic average of surface temperature and free stream temperature, such as Morgan (1975) and Churchill and Bernstein (1977). In the second category, fluid properties are estimated as a function of the free stream temperature, such as Žukauskas (1972), Whitaker (2014), and Sparrow et al. (2004).

Churchill and Bernstein (1977) correlation, given by Eq. 8.3, is used in this work to estimate convection heat transfer coefficient for fluid flow across a circular cylinder. The correlation is accurate and quite comprehensive because it covers all the range of Reynolds number for fluid flow across a circular cylinder, and it is applicable for both gas and liquid flow.

$$\text{Nu} = \frac{hD}{\lambda} = 0.3 + \frac{0.62 \text{Re}^{1/2} \text{Pr}^{1/3}}{\left[1 + (0.4/\text{Pr})^{2/3}\right]^{1/4}} \left[1 + \left(\frac{\text{Re}}{282,000}\right)^{5/8}\right]^{4/5} \quad (8.3)$$

where Nu is local Nusselt number around the periphery of the heater ($= hD/\lambda$), Pr is Prandtl number ($= \mu C_p/\lambda$) and Re is Reynolds number ($= \rho U_\infty D/\mu$). ρ is the fluid density, μ is the fluid viscosity, C_p is the fluid heat capacity, λ is the thermal conductivity of the surrounding fluid, U_∞ is the fluid velocity, and D is the external diameter of the heater. Nusselt number is a dimensionless number that describes the enhancement of heat transfer through the thermal boundary layer by convection compared with the heat transfer by conduction. Different rates of heat generations can be obtained by changing the supplied electrical power to the heater through using a variable-output transformer.

$$P = V \times I = q = Ah(T_s - T_\infty) \quad (8.4)$$

Accordingly, the convective heat transfer coefficient can be estimated by:

$$h = \frac{P}{A(T_s - T_\infty)} \quad (8.5)$$

Nonuniform surface temperature is obtained across the periphery of the heater due to variability of heat transfer across the cylinder (see Fig. 8.2). To estimate the average heat transfer coefficient, two approaches may be followed. The first method is to estimate the numerical integration of the local h values along the periphery of the heater using the following equation:

$$\bar{h} = \frac{1}{A} \int_0^A h(A) dA \quad (8.6)$$

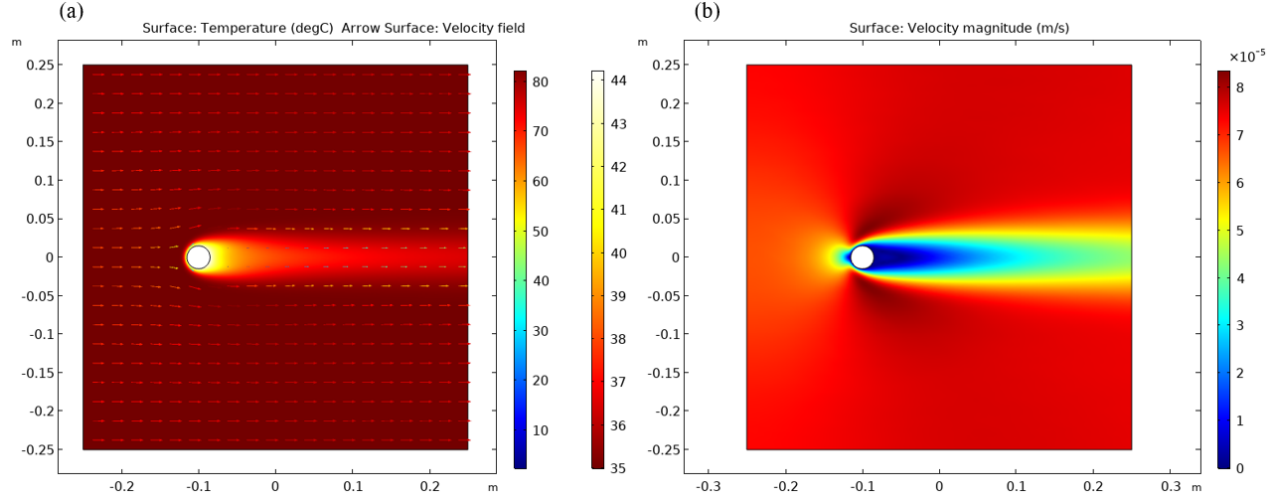


Figure 8. 2. Temperature (left) and velocity (right) evolutions in the flow stream around the heating source for the single-phase CO₂ case described in the Application section.

The second method is to evaluate the average temperature along the periphery of the heater using Eq. 8.7, and then evaluate the average heat transfer coefficient using Eq. 8.8. The second method provides relatively accurate results (Churchill and Bernstein 1977), and it is used in this work.

$$\bar{T}_s = \frac{1}{A} \int_0^A T_s(A) dA \quad (8.7)$$

$$\bar{h} = \frac{P}{A(\bar{T}_s - T_\infty)} \quad (8.8)$$

Our proposed methodology involves creating a series of heat pulses by changing the electrical power supplied to the heater and measuring the corresponding stabilized temperature signal. The average heat transfer coefficient is then obtained using Eq. 8.8. Next, the velocity of the flowing fluid is estimated using Eq. 8.3 where the fluid properties are evaluated at the film temperature which is the arithmetic average of the surface and flowing fluid temperature. Finally, the flowing fluid velocity is estimated as the average of the values obtained at the different heat pulses.

One of the complications associated with the applicability of in-well heat pulse test to detect CO₂ arrival is the immediate upward migration of CO₂ to shallower intervals of the wellbore when CO₂ gets inside the wellbore. This may result in temperature increase at the shallower intervals at which CO₂ accumulate which results in false indication of the breakthrough zones. To avoid this problem, a multilevel temperature monitoring system should be used. In this system, each monitoring zone is separated from other monitoring zones at the well through isolating packers. Multilevel temperature and pressure monitoring is novel in the context of GCS; however, it has been used for long time for groundwater hydrology and contamination studies (Pickens et al. 1978). It was proposed by Strandli and Benson (2013) for pressure and temperature monitoring in GCS projects to increase the vertical resolution of the pressure and temperature measurements at monitoring wells.

8.1.1. Methodology Validation

In this section, the proposed approach is validated. We obtained the average temperatures at various fluid velocities for single-phase brine and single-phase CO₂ using numerical simulation and based on the correlation (Eq. 8.3). COMSOL Multiphysics is adopted to model the problem of the conjugate heat transfer during fluid flow across a cylinder (COMSOL 2018). To validate the feasibility of using the correlation in our methodology, the problem is modeled using both techniques for the conditions encountered during GCS. First, two synthetic cases are presented for single-phase brine and single-phase CO₂ flow across the heater to illustrate the application of the proposed technique to estimate the downhole fluid velocity before and after CO₂ arrival. Next, different cases are presented for two-phase flow of CO₂ and brine across the heater at different CO₂ saturations. The obtained temperature results for single-phase brine, single-phase CO₂, and two-phase flow scenarios are analyzed to investigate the sensitivity of the heater temperature to CO₂ intrusion and fluid velocity.

To obtain realistic values of the boundary conditions such as pressure, temperature, and fluid velocity at the monitoring well, we used TOUGH3-ECO2N to model 1D radial flow of supercritical CO₂ in deep saline aquifer. The reservoir properties and operating conditions adopted in this study are given in Table 8.1. Initial pressure and temperature conditions are estimated using $p = 1 + 0.1z$ and $T = 15 + 0.025z$, respectively with p in bars, T in degrees C, and z in meter (Doughty 2008). Fig. 8.3 illustrates brine and CO₂ mass flow rate (left) and pressure and CO₂ saturation (right) at the monitoring well during CO₂ injection as obtained from TOUGH3-ECO2N. Before CO₂ arrival, flow is single-phase brine at the monitoring well at mass flow rate of 140 kg/s. When CO₂ reaches the monitoring well, brine mass flow rate diminishes sharply, and CO₂ mass flow rate increases to a stabilized value of 100 kg/s. Despite that CO₂ saturation in the reservoir increases to ~0.2 after CO₂ arrival, the fluid flow at the wellbore becomes fully CO₂ shortly after CO₂ arrival. Consequently, fluid flow inside the monitoring well can be considered single-phase CO₂ soon after CO₂ arrival. Pressure, temperature, and brine/CO₂ velocity obtained using TOUGH3 are used as inlet boundary conditions while modeling the problem using COMSOL Multiphysics (see Fig. 8.4). Brine and supercritical CO₂ properties used in COMSOL Multiphysics are estimated at the obtained pressure and temperature conditions using NIST webbook (NIST, 2021). The estimated velocity of the brine before CO₂ arrival is constant and equals ~ 40 $\mu\text{m/s}$ at pressure of 110 bar, while the stabilized CO₂ velocity after CO₂ arrival equals 35 $\mu\text{m/s}$.

Brine/CO₂ velocity can change as a function of the operating injection rate, location of the monitoring well, thickness of the injection zone, and the pressure and temperature conditions of the aquifer. Additionally, the fluid velocity within the monitoring well can be higher than the interstitial velocity of the fluid inside the formation as will be discussed in the discussion section. In COMSOL Multiphysics, fluid flow across the heater is assumed to be linear because the injector is located far from the monitoring well. Additionally, we consider the wellbore domain only while modeling the temperature evolution during the heat pulse test. It is evident from Fig. 8.2 that the temperature evolution is limited to the region surrounding the heating cable/source (within few centimeters from the heating cable). Consequently, the effect of the environment outside the monitoring well such as casing, cement sheath, and the porous media can be neglected. This assumption may be violated for extended heating period through which the surrounding porous media can affect the temperature evolution.

Table 8. 1. Input data for the synthetic case.

Feature	value	Feature	Value
Initial temperature, °C	35	Aquifer porosity, fraction	0.12
Initial pressure, bar	81	Aquifer horizontal permeability, md	500
Brine salinity, fraction	0.15	Aquifer vertical permeability, md	50
Bottomhole injection temperature, °C	35	Aquifer rock compressibility, MPa ⁻¹	3.4 × 10 ⁻⁵
Injection rate, kg/s	100	Aquifer outer radius, km	100
Location of monitoring well, m	100	Effective thermal conductivity, W/m K	2.51
Aquifer thickness, m	50	Rock heat capacity, J/kg K	920

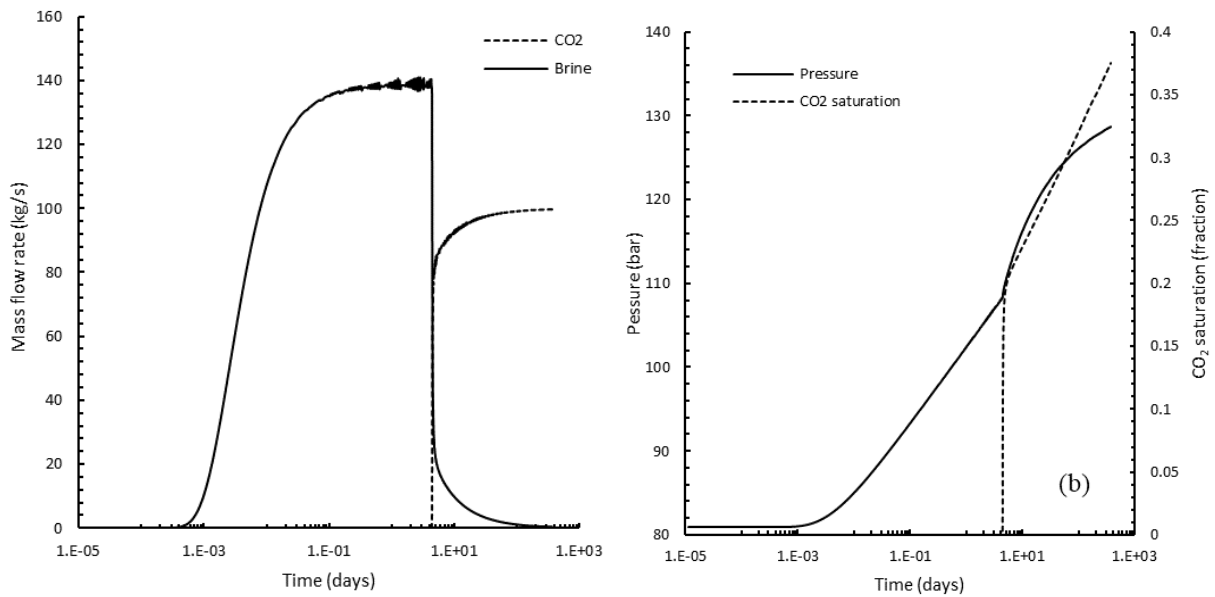


Figure 8. 3. (a) Brine and CO₂ mass flow rate and (b) pressure and CO₂ saturation at the monitoring well during CO₂ injection in deep saline aquifer.

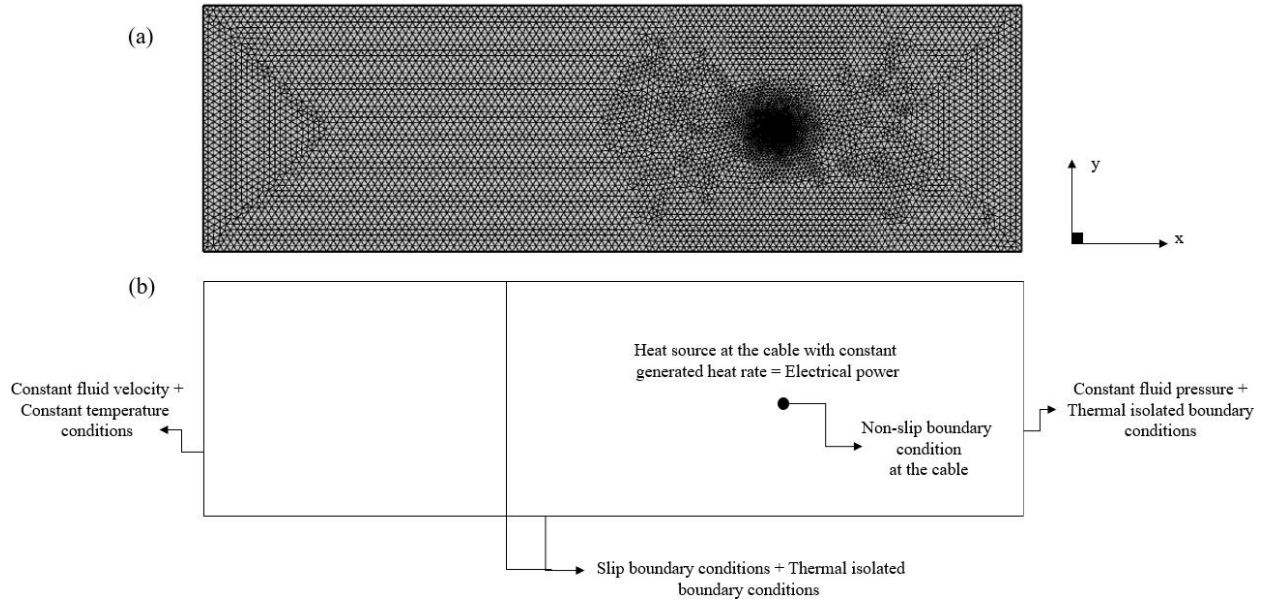


Figure 8. 4. Schematic illustration of the numerical model in COMSOL Multiphysics platform showing: (a) grid discretization (b) boundary conditions.

Fig. 8.5 illustrates the temperature results obtained using Churchill and Bernstein (1977)'s correlation and COMSOL simulation for a heater of diameter 3 cm and electrical power of 10 W/m which is subject to single-phase brine (shown in black color) and single-phase CO₂ (shown in red) at velocity of 20 - 140 μm/s, ambient temperature of 35 ° C, and ambient pressure of 110 bar. The electrical power supplied to the heater should be controlled to mitigate the effect of heat transfer by natural convection and avoid damaging the fiber optic cable. Simon et al. (2021) suggested injecting electrical power in the range of 15 – 35 W/m, that is high enough to improve the resolution of the temperature measurements without triggering the natural convection effect. Temperature results illustrated in Fig. 8.5 represent the stabilized temperature which is obtained after the heat exchange between the heater and the surrounding fluids reaches steady state condition. The steady state conditions can attain after few minutes or hours depending on the surrounding fluid velocity and the heater diameter as will be discussed in the discussion section. It is evident from Fig. 8.5 that the stabilized surface temperature of the downhole heater is sensitive to the velocity of the surrounding fluid and the type of the surrounding fluid inside the wellbore. Stabilized temperature decreases as flowing fluid velocity increases because higher fluid velocity decreases the thermal boundary layer in the fluid surrounding the heater. At high flowing fluid velocity, the sensitivity diminishes because thermal boundary layer decreases to the minimum. Besides, it is obtained that the stabilized temperature of the heater for single-phase CO₂ is much higher than that obtained for single-phase brine.

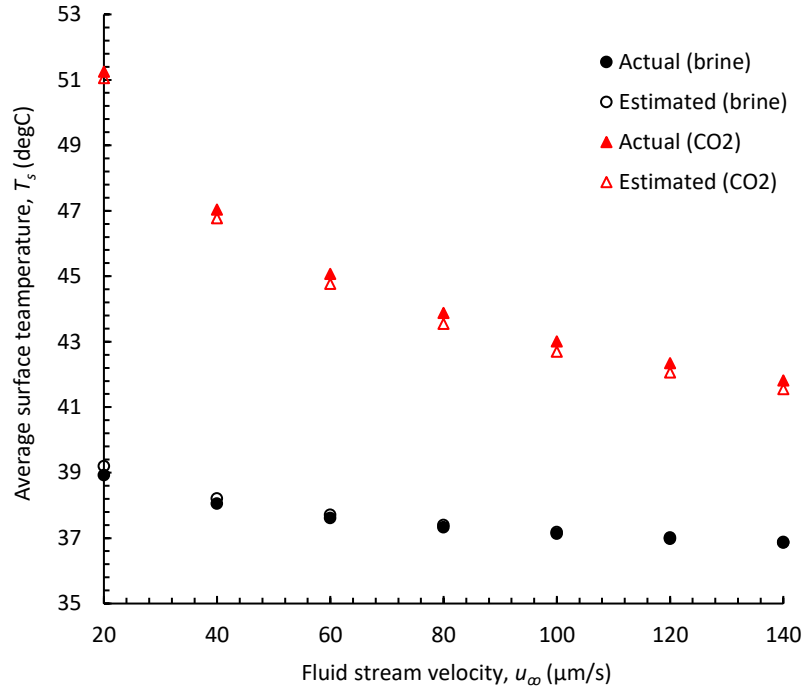


Figure 8. 5. Temperature results of the downhole heater using COMSOL Multiphysics simulation tool and Churchill and Bernstein (1977)’s correlation at external fluid velocity of 20 - 140 $\mu\text{m/s}$ for a single-phase brine scenario (shown in black color) and a single-phase CO₂ scenario (shown in red color).

For example, at flowing fluid velocity of 20 $\mu\text{m/s}$, the observed stabilized temperature for single-phase brine flow is 39 °C compared with 51 °C for the case of single-phase CO₂ flow. High temperature heating is obtained because supercritical CO₂ has lower thermal conductivity and consequently lower heat transfer coefficient compared with the in-situ brine. Consequently, CO₂ arrival can be identified from the increase in the stabilized temperature beyond the base value observed prior to CO₂ arrival. The results obtained using the correlation are in good agreement with the numerical results for single-phase brine and single-phase CO₂ scenarios with a maximum estimation error of 0.7 percent.

8.1.2. Application

To illustrate how the proposed methodology is used for estimating the downhole fluid velocity, a heat pulse test is conducted in which a series of electrical powers (5 – 50 W/m) is supplied, and the corresponding stabilized temperature is obtained for two different scenarios: single-phase brine and single-phase CO₂. Fig. 8.6 (a) shows the temperature-power plot for the single-phase brine and single-phase CO₂ cases. In these cases, the ambient temperature is 35 °C, the velocity of the surrounding fluid stream is 80 $\mu\text{m/s}$ (for single-phase brine) and 70 $\mu\text{m/s}$ (for single-phase CO₂), respectively, and the diameter of the downhole heater is 3 cm. Relatively high velocity is used because fluid velocity in the borehole of the monitoring well can be higher than the interstitial fluid velocity as will be discussed in the discussion section. At each pulse, average heat transfer coefficient, h is estimated using Eq. 8.8 and the flowing fluid velocity is estimated accordingly using Eq. 8.3. Fig. 8.6 (b) shows the estimated fluid velocity using the

proposed technique compared with those obtained numerically at each heat pulse for single-phase brine and single-phase CO₂ cases. The maximum estimation error for single-phase brine scenario is 5 percent which corresponds to the heat power of 5 W/m. Brine velocity is estimated as the average of the estimated values which yields 82.3 μm/s (estimation error of ~ 2.9 percent). The maximum estimation error for the single-phase CO₂ case is 7 percent which corresponds to the heat power of 50 W/m. CO₂ velocity is estimated as the average of the estimated values which yields 65 μm/s (estimation error of ~ 7.3 percent).

To illustrate the application of the proposed technique to detect CO₂ arrival, convective heat transfer during two-phase flow across the downhole heater is modeled using COMSOL Multiphysics to show the sensitivity of the temperature signal to CO₂ saturation. Different cases are modeled for different CO₂ saturations (0.2, 0.4, 0.6, 0.8, and 1) and the corresponding temperature response is monitored. The temperature and the velocity of the surrounding fluid stream are 35 °C and 80 μm/s, respectively, and the diameter of downhole heater is 3 cm. Higher surface temperature is obtained during CO₂ arrival as shown in Fig. 8.7 because the heat transfer coefficient, h for CO₂ is much lower than the corresponding heat transfer coefficient of the brine. This is evident from Eq. 8.3 which indicates that the convection heat transfer coefficient is most sensitive to the thermal conductivity of the surrounding fluid. Because the thermal conductivity of supercritical CO₂ (~ 0.08 W/m K) is one order of magnitude lower than thermal conductivity of the in-situ brine (~ 0.6 W/m K), the convection heat transfer coefficient for CO₂ is much lower than the in-situ brine. The increase in the surface temperature of the downhole heater at CO₂ arrival is clear and should be readily detectable to identify CO₂ arrival.

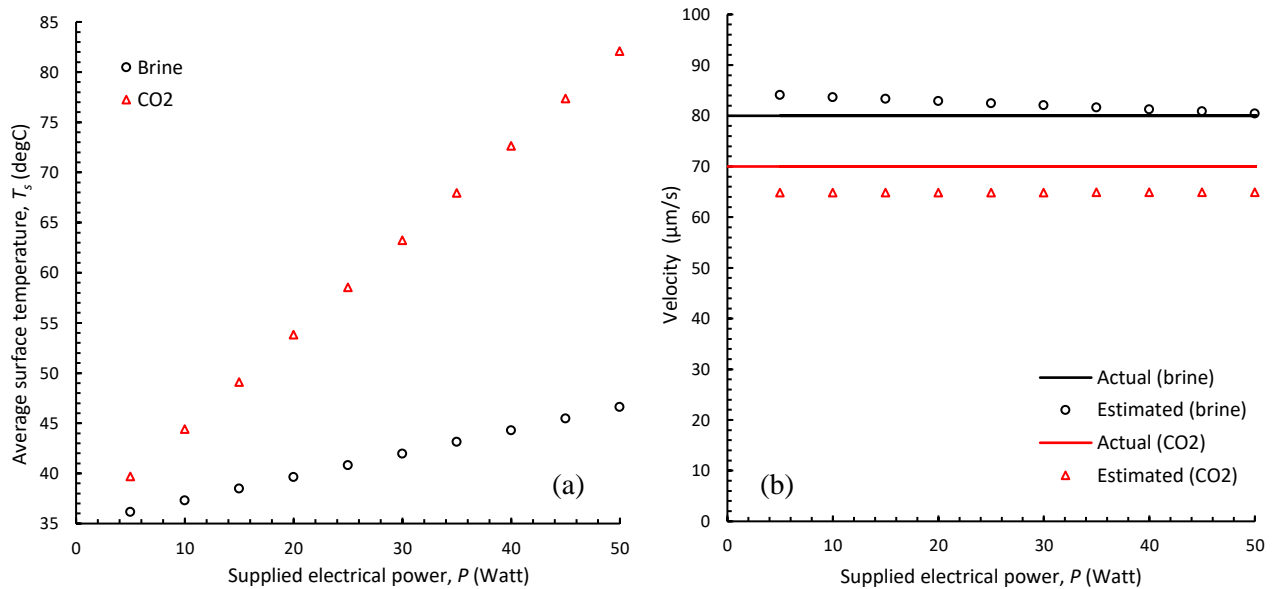


Figure 8. 6. (a) Average surface temperature versus electrical power for 10 different heat pulses (b) estimated fluid velocity obtained using Churchill and Bernstein (1977)'s correlation compared with those obtained numerically for 10 different heat pulses for single-phase brine and single-phase CO₂ scenarios.

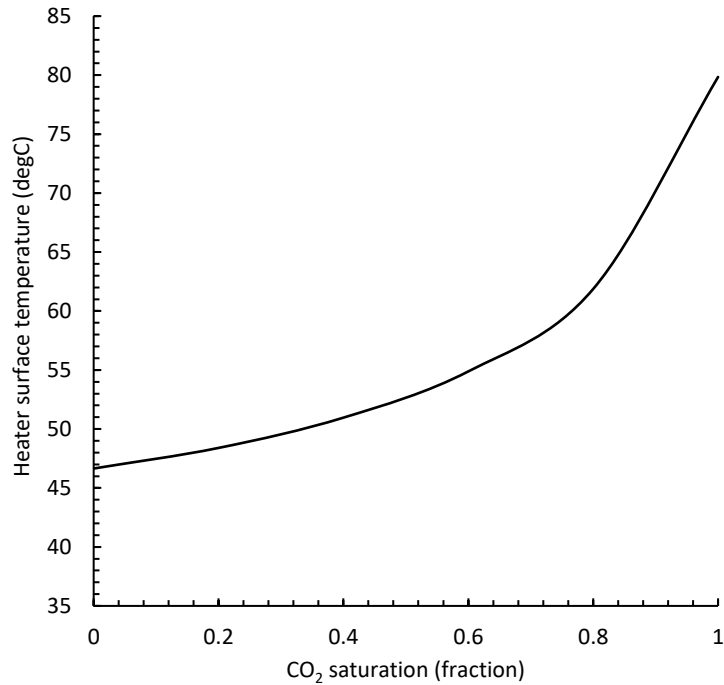


Figure 8. 7. Heater temperature for flowing fluid velocity = 80 $\mu\text{m/s}$ during CO₂ arrival at different CO₂ saturations.

8.1.3. Discussion

In this section, we discuss the applicability of the proposed technique and the validity of the involved assumptions. The proposed technique is used for estimating downhole fluid velocity and detecting CO₂ arrival at a monitoring well during CO₂ storage in GCS projects. It involves three steps; in the first step, the average stabilized temperature of the heater is obtained when the heater is switched on. In the second step, the average heat transfer coefficient for the heat loss from the surface of the heater is calculated using Newton's law of cooling given that the stabilized temperature of the heater (obtained from the first step), the rate of the generated heat, and the temperature of the surrounding fluids are estimated. In the last step, Churchill and Bernstein (1977)'s correlation is adopted to estimate the flowing fluid velocity in terms of the estimated convective heat transfer coefficient. The first and second steps have been widely used while studying the mechanism of heat transfer by convection and estimating the corresponding heat transfer coefficient (Moreira et al. 2019). Churchill and Bernstein (1977)'s correlation has been used in the third step to describe the velocity dependency of heat transfer coefficient because it covers the entire range of Reynolds number for fluid flow across a circular cylinder, and it is applicable for a wide range of Péclet numbers, $Pe = Re Pr > 0.2$ (Lienhard and John 2005, Bird et al. 2006, Cengel 2014). The assumptions adopted in the proposed technique are:

- (1) Surrounding fluid flow is turbulence/disturbance free.
- (2) Steady state conditions attain shortly after the downhole heater is switched on.
- (3) Effect of natural convection from the downhole heater is negligible.
- (4) Effect of heat transfer by radiation from the downhole heater is negligible.
- (5) Fluid flow across the heating source is lateral.

The first assumption is inherent in Churchill and Bernstein (1977)'s correlation, and it implies that the flowing fluid far upstream of the downhole heater should be turbulence free, that is, before the heater has a chance to deflect, slow down or compress the flowing fluid. This assumption is feasible for fluid flow in porous media at the location of the monitoring well because the fluid velocity is generally small (in the order of 10 – 100 $\mu\text{m/s}$) and Reynolds number is generally less than 0.2. Consequently, laminar flow dominates the flow behavior in the porous media at the monitoring well. However, fluid velocity can be disturbed as fluid gets inside the wellbore because the presence of the well as a high permeability conduit allows the short-circuiting of the flow. To investigate the validity of this assumption, the velocity distribution inside the wellbore is modelled using COMSOL Multiphysics assuming single-phase brine. Fig. 8.8 illustrates the velocity evolution within the wellbore in which the borehole is modeled as porous media with porosity 0.99 and higher equivalent permeability compared with the permeability of the surrounding formation (see Table 8.1). This approach for wellbore modeling is known as Equivalent Porous Media (EPM) (Wang et al. 2018, Hu et al. 2012, Feng et al. 2017) and has been used to model pressure and temperature variation in the wellbore environment. The equivalent permeability adopted for the borehole is $3.16 \times 10^{-6} \text{m}^2$ which is the same value used by Hu et al. (2011) and Wang et al. (2018). Fixed mass flow rate conditions are specified at the inlet and outlet boundaries of the numerical model in COMSOL which are representative to the mass flow rate (140 kg/s) obtained from TOUGH3-ECO2N at the monitoring well (see Fig. 8.3). It is evident that the velocity of fluid in the borehole is uniform and higher than the fluid velocity in the surrounding formation. The magnitude of velocity in wellbore is $\sim 80 \mu\text{m/s}$ compared with $\sim 40 \mu\text{m/s}$ which is the fluid velocity in the surrounding formation. As the fluid approaches the wellbore from the left, streamlines converge toward the wellbore system which has higher permeability. Consequently, the spacing between the streamlines decreases, and the fluid velocity increases. When fluid moves outward from the right side, streamlines diverge, and the fluid velocity decreases again. In this case, Reynolds number for fluid flow in the wellbore is $16 \left(= \frac{\rho U_{\infty} D}{\mu} = \frac{1000 \times 8 \times 10^{-5} \times 0.2}{0.001} \right)$, which is much lower than 2000, where U_{∞} is the real flow velocity (m/s), ρ is the fluid density (kg/m^3), D is the wellbore diameter (m), and μ is the fluid viscosity (Pa s). Despite that the observed velocity in the wellbore is different from the interstitial fluid velocity in the surrounding porous media, the variation of estimated fluid velocity at different depths in the wellbore reflects the vertical heterogeneity of the surrounding formation. Formations with high permeability (thief zones) will result in higher wellbore fluid velocity and vice versa.

In the second assumption, the temperature of the downhole heater is assumed to reach steady state conditions shortly after the downhole heater is switched on. To demonstrate the significance of this assumption, transient heat transfer during the heat pulse test is modeled to show the temperature evolution of the downhole heater versus time. Fig. 8.9 (a) illustrates the change of the heater's temperature during the transient period for different flowing brine velocities (40, 80, and 120 $\mu\text{m/s}$), heater diameter of 3 cm and electrical power of 10 W/m. As the flowing fluid velocity decreases, the time it takes for the heater's temperature to stabilize increases. At flowing fluid velocity of 120, 80, and 40 $\mu\text{m/s}$, the steady state temperature attains after 0.5, 1.5, and 3 hours, respectively. Fig. 8.9 (b) illustrates the effect of the heater size on the transient temperature evolution for flowing fluid velocity of 40 $\mu\text{m/s}$, electrical power of 10 W/m, and heater diameter of 1, 2, 3, 4, and 5 cm. As expected, the stabilization time decreases as

the diameter of the heater decreases. Steady state conditions attain after ~1, 1.5, 3, 5, and 7 hours for $D = 1, 2, 3, 4,$ and 5 cm, respectively. Accordingly, the transient period can extend to few hours for small flowing fluid velocity and large heater diameter. This should not restrict the applicability of this technique because the heat pulse test is designed for a monitoring well. Consequently, the duration of the test does not interrupt CO_2 injection activity. On the other hand, the stabilized time for in-well heat pulse test obtained in this work is generally much lower than the stabilized time if the heating source is in contact with the formation. del Val et al. (2021) showed that the stabilized temperature for a heat source which is directly contacted with the formation may be attained after days to weeks which renders the heat pulse test time-consuming and increases the possibility of fiber-optic cable damage because of the excessive heating.

The third assumption is inherent in Churchill and Bernstein (1977)'s correlation which neglects the effect of heat transfer by natural convection from the downhole heater in the wellbore. Natural convection is driven by the temperature gradient in the vertical direction inside the wellbore. The fluid at the bottom of the wellbore which is maintained at higher temperature has lower density compared with the fluid maintained at the upper sections of wellbore which has lower temperature (Ruan et al. 2013). The established density gradient along the wellbore drives fluid flow upward by the effect of buoyancy. Since the increase of temperature during the heat pulse test is within few degrees (~ 2 °C for electrical power of 10 W/m for single-phase brine scenario), the contribution of the natural convection to fluid flow in the wellbore can be neglected. To mitigate the effect of natural convection, Simon et al. (2021) suggested limiting the electrical power supplied to the heating source to $10 - 35 \text{ W/m}$.

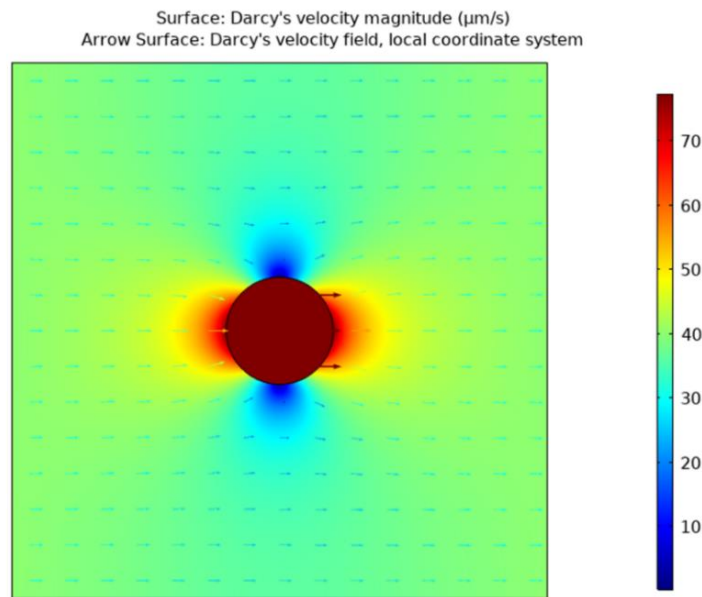


Figure 8. 8. Velocity evolution in the borehole and the surrounding formation (single-phase brine).

The fourth assumption implies neglecting heat transfer by radiation from the downhole heater during the heat pulse test. This assumption is feasible for relatively high h , $h \geq 30 \text{ W m}^{-2}\text{K}^{-1}$ and small emissivity coefficient, ε compared with the ideal black body coefficient ($\varepsilon = 1$)

(Conti et al. 2014). The estimated value of convection heat transfer coefficient, h for the single-phase brine case is $45 \text{ W/m}^2 \text{ K}$. Additionally, the emissivity of the conductive housing (e.g., Aluminum or Copper) is very small ($\sim 0.09 - 0.03$), accordingly it is feasible to neglect the contribution of the heat radiation mechanism. To investigate the significance of this assumption, two cases are modeled for heat transfer during single-phase brine flow over a heater with and without considering heat loss by radiation. The surface temperatures obtained for an electrical power of 10 W/m , diameter of 3 cm , surface emissivity of 0.1 , and surrounding flowing fluid velocity of $80 \mu\text{m/s}$ with and without considering the heat loss by radiation are 37.359 and $37.374 \text{ }^\circ\text{C}$, respectively. Consequently, the contribution of radiation to the heat loss is negligible compared with heat transfer by forced convection.

The last assumption in our work is that fluid flow across the heating source is lateral such that the flow direction is normal to the heating source. However, fluid flow at the monitoring well may not be fully lateral (1) because the storage zone may be inclined with some degree to the monitoring well, and/or (2) because the flow is gravity dominant which is especially relevant away from the injection well (where the viscous forces are weak) as the gravity forces become significant assuming sufficiently high gravity number. To investigate the effect of fluid flow inclination on the temperature signal and the estimated velocity, different cases are modeled for in-well heat pulse testing for single-phase brine and single-phase CO_2 scenarios at different zonal inclinations, $\theta = 0, 5, 10,$ and 15° (see Fig. 8.10). The stabilized temperatures observed for both cases are illustrated in Fig. 8.10 (a) at $\theta = 0, 5, 10,$ and 15° at supplied electrical power of 10 W/m . The maximum deviation in the stabilized temperature due to the flow inclination is less than 9 percent for single-phase brine and single-phase CO_2 . The estimated velocities are also given in Fig. 8.10 (b) according to which the maximum estimation error is less than 15 percent. Overall, the assumptions involved in the proposed technique are feasible and they do not limit the accuracy and applicability of this technique.

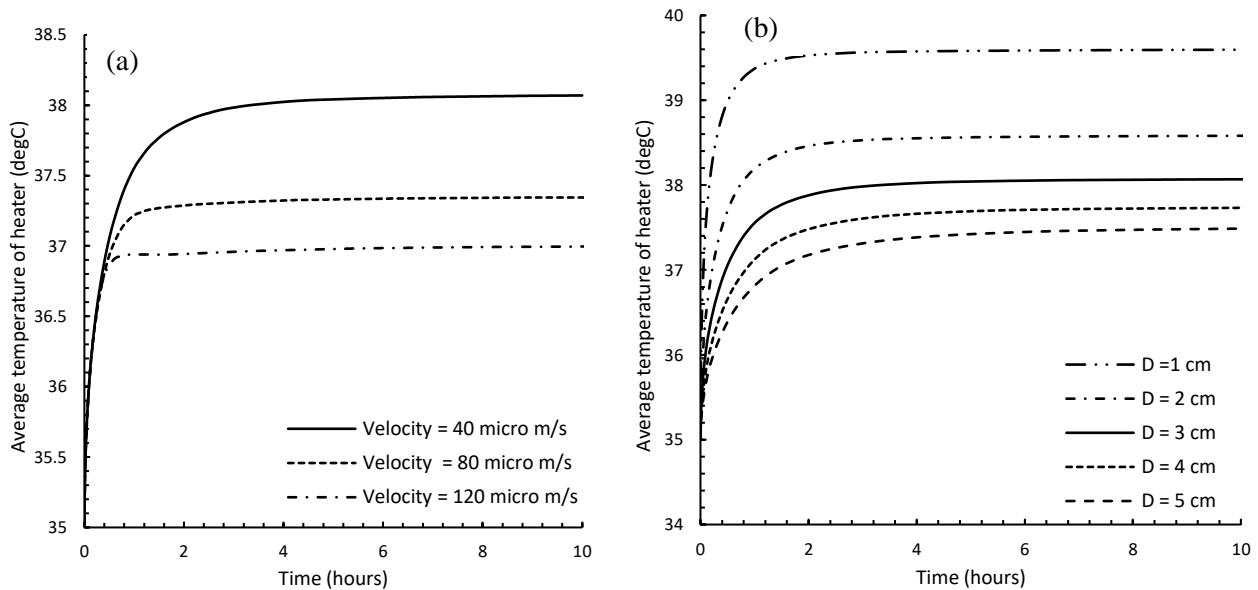


Figure 8.9. Transient evolution of downhole heater temperature after the heater is switched on at different: (a) fluid velocity, and (b) heater diameter (single-phase brine).

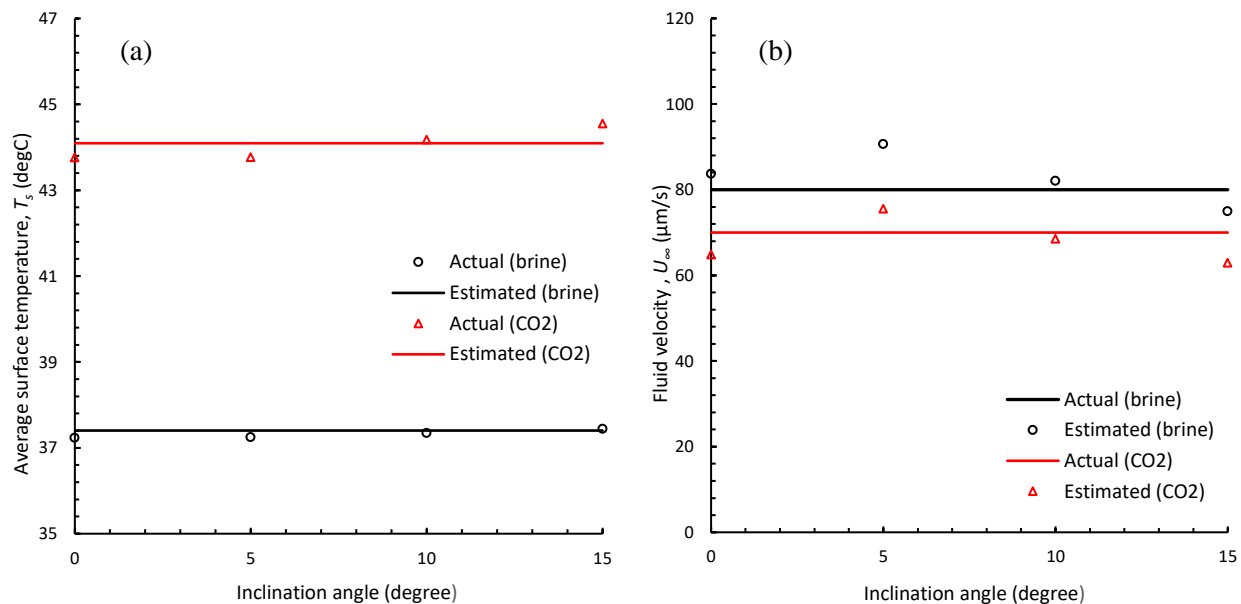


Figure 8. 10. (a) Stabilized temperature and (b) estimated velocity versus flow inclination for single-phase brine and single-phase CO₂ cases.

8.2. Formation Heat Pulse Testing

In this section, we show the application of formation heat pulse testing for monitoring CO₂ plume migration in deep saline aquifer. In this test, the heating source is embedded in direct contact with the porous medium of the monitoring zone. Besides, the heating source can be deployed within a monitoring well, however the wellbore should be hydraulically isolated from the monitoring zone. To interpret and design the proposed heat pulse testing, new graphical interpretation techniques are presented. The interpretation methods are developed through extending the Moving Instantaneous Line Source (MILS) solution, developed by Diao et al. (2004), to consider two-phase flow (gaseous CO₂ and aqueous brine) in the porous medium during heat pulse testing. The objective of the proposed interpretation methods is to provide spatial estimates of CO₂ saturation, individual phase velocity, and subsurface thermal properties at the monitoring zone/well. Temperature results are produced using the new analytical solution and compared with those obtained from a thermal compositional simulation tool. The proposed interpretation methods are applied to the numerical temperature data for inverse modeling.

8.2.1. Forward Modeling

Consider a DTS cable embedded into the formation in active mode (see Fig. 8.11 (b)). The temperature buildup during the heating period depends on the heat dissipation efficiency of the surrounding porous medium. Higher thermal conductivity of the porous medium results in higher rate of released heat from the heating cable, and consequently, lower temperature buildup. With fluid flow in the porous rock, advection partly controls temperature buildup by dissipating the heat generated from the heating cable. The higher the fluid velocity through the porous rock, the lower the temperature buildup. The following assumptions are made during formulating and solving the problem:

- Fluid flow around the heating cable is linear two-phase fluid flow in x -direction. This assumption is feasible for fluid flow at a monitoring well/cable located far from the injection well (Eskilson 1987).
- The heating cable is considered as a heating line-source in z -direction perpendicular to the fluid flow direction (Diao et al. 2004).
- Fluids' saturations and velocities are considered constant during the formation heat pulse test.
- Formation porosity and thermal properties are constant and uniform.
- Heat transfers from the heating cable through the porous rock by advection and conduction mechanisms.
- Effect of heat transfer by natural convection is negligible (Ballard 1996).

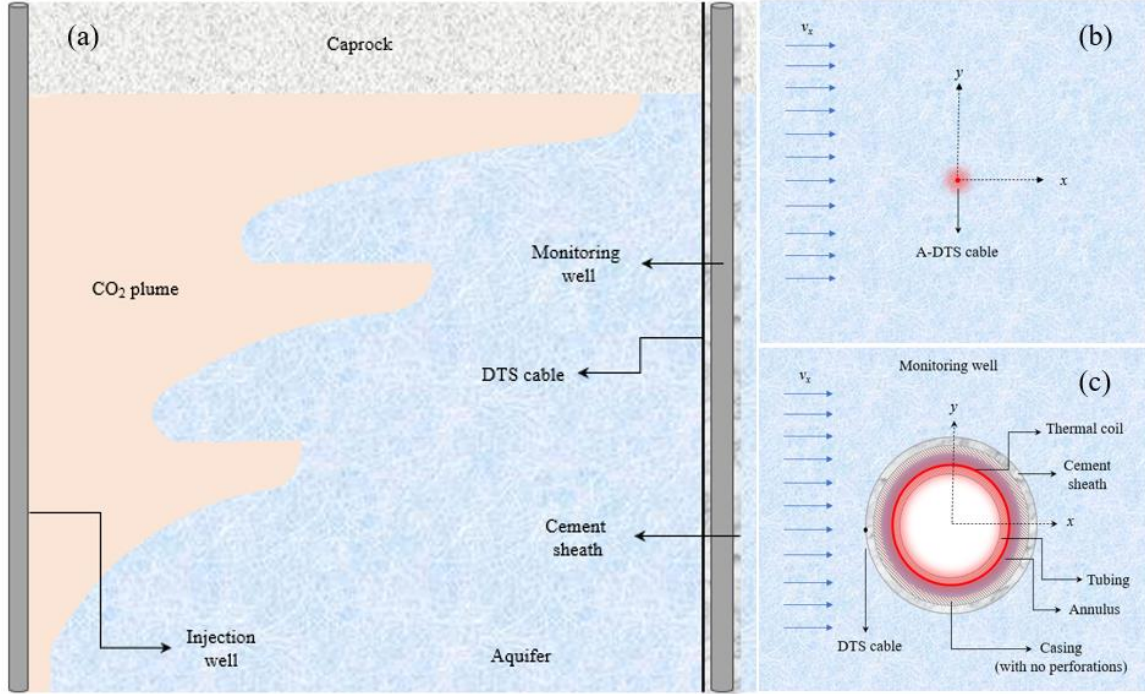


Figure 8. 11. Description of the problem: (a) Schematic illustrating a CO₂ plume, injection well, and monitoring well (b) schematic cross section showing the A-DTS cable as a heating source with indication of fluid flow across the cable and (c) schematic cross-section showing the scenario in which the heating source is deployed inside the monitoring well. In this case, the heating source constitutes a deployed tubing over which a heating cable is wrapped, and the monitoring DTS cable is cemented behind the casing at the cement/formation interface.

Accordingly, the transport of heat in porous medium from a line-heat source during two-phase fluid flow is described by (App 2010, Duru and Horne 2010):

$$\begin{aligned} \frac{\partial}{\partial t} (\phi (\rho_c \hat{H}_c S_c + \rho_w \hat{H}_w S_w) + (1 - \phi) \rho_r H_r) + \frac{\partial}{\partial x} (\rho_c \hat{H}_c v_c + \rho_w \hat{H}_w v_w) \\ = \lambda_e \left(\frac{\partial^2 T}{\partial x^2} + \frac{\partial^2 T}{\partial y^2} \right) + dq \delta(x) \delta(y) \delta(t) \end{aligned} \quad (8.9)$$

where \hat{H} is the specific enthalpy, T_o is the initial temperature, ρ is the fluid density, S_w and S_c are brine and CO₂ saturation, respectively, v is the fluid velocity, λ_e is the effective thermal conductivity of the formation, ϕ is the formation porosity, dq is the heat released per unit length of the cable, and $\delta(-)$ is Dirac delta function. Writing the specific enthalpy in terms of temperature change and the fluid velocity in terms of fractional flow, Eq. 8.9 is simplified after few manipulations to the following form (Diao et al. 2004):

$$\frac{\partial T}{\partial t} + u_T \frac{\partial T}{\partial x} = \alpha_e \left(\frac{\partial^2 T}{\partial x^2} + \frac{\partial^2 T}{\partial y^2} \right) + \frac{dq}{\rho_e C_e} \delta(x) \delta(y) \delta(t) \quad (8.10)$$

where

$$u_T = \left(\frac{\rho_C f_C C_C + \rho_W f_W C_W}{\rho_e C_e} \right) v_T \quad (8.11)$$

and v_T is the total velocity of the fluids ($= v_w + v_c$), $f_w (= v_w/v_T)$ and $f_c (= v_c/v_T)$ are the fractional flow terms of brine and CO₂, respectively, $\alpha_e (= \lambda_e/\rho_e C_e)$ is the effective thermal diffusivity of the formation, and $\rho_e C_e$ is the effective heat capacity of the formation. The effective (bulk) properties of the formation can be estimated using different averaging techniques such as arithmetic, harmonic, and geometric averaging. Generally, arithmetic and harmonic means represent the maximum and the minimum boundaries for means, respectively. The geometric mean lies in between these ranges, and it works well for layered (sedimentary) rocks (Hurter et al. 2007). Geometric mean has been widely used for calculating the effective thermal conductivity, while the arithmetic mean was used for calculating the effective heat capacity (Buntebarth and Schopper 1998). The effective thermal properties are given by:

$$\lambda_e = (\lambda_w^{S_w} \times \lambda_c^{S_c})^\phi \lambda_r^{(1-\phi)} \quad (8.12)$$

$$\rho_e C_e = \phi(\rho_C S_C C_C + \rho_W S_W C_W) + (1 - \phi)\rho_r C_r \quad (8.13)$$

Considering these effective properties, the single-phase analytical solution developed by Diao et al. (2004) can now be adopted for the two-phase CO₂-brine system according to which the transient temperature during the formation heat pulse testing is described by:

$$\Delta T(x, y, t) = \frac{P}{4\pi\lambda_e} \exp\left[\frac{xu_T}{2\alpha_e}\right] \int_0^t \frac{1}{\tau} \exp\left[-\frac{x^2 + y^2}{4\alpha_e\tau} - \frac{u_T^2\tau}{4\alpha_e}\right] d\tau \quad (8.14)$$

where $\Delta T = T - T_o$, $P (= dq/dt)$ is the supplied electrical power. The resulting solution can be written as follows:

$$\Delta T(x, y, t) = \frac{P}{4\pi\lambda_e} \exp\left[\frac{xu_T}{2\alpha_e}\right] \int_{\frac{x^2+y^2}{4\alpha_e t}}^{\infty} \frac{1}{\psi} \exp\left[-\psi - \frac{u_T^2}{16\alpha_e^2} \left(\frac{x^2 + y^2}{\psi}\right)\right] d\psi \quad (8.15)$$

using the transformation $\psi = \frac{x^2+y^2}{4\alpha_e t}$. The temperature evolution during the heating period is controlled by heat diffusion at early times and then becomes dominated by heat advection at late time. Heat transfer by advection limits the temperature increase and results in temperature stabilization at late-time (Diao et al. 2004). At early times in which heat conduction is dominant, the temperature solution is simplified to the following by assigning $u_T \rightarrow 0$:

$$\Delta T(r, t) = -\frac{P}{4\pi\lambda_e} \text{Ei}\left(-\frac{r^2}{4\alpha_e t}\right) \quad (8.16)$$

where $\text{Ei}\left(-\frac{r^2}{4\alpha_e t}\right)$ is the exponential integral function, and $r^2 = x^2 + y^2$. The temperature solution given by Eq. 8.16 is analogous to the solution provided for heat conduction from a line-heating source that supplies constant heat rate, $P(= dq/dt)$ in a homogenous infinite medium, initially at thermal equilibrium (T_o everywhere) (Carslaw and Jaeger (1959)). Transient temperature at the heating source can be simplified further using the logarithmic approximation of the exponential integral function when $\frac{r^2}{4\alpha_e t} \ll 1$. According to which, the temperature at the surface of the heating cable during the conduction-dominant period is given by:

$$\Delta T(r_c, t) = \frac{P}{4\pi\lambda_e} \ln\left(\frac{2.2458\alpha_e t}{r_c^2}\right) \quad (8.17)$$

where r_c is the radius of the cable. Eq. 8.17 plots as a straight line on a semi-log graph of temperature change, ΔT versus log-time. The slope of the straight line, m_f and the intercept, b_f , with the ΔT -axis at $t = 1$ can be used to estimate the effective thermal properties of the formation as follows:

$$\lambda_e = \frac{P}{4\pi m_f} \quad (8.18)$$

$$\alpha_e = \frac{r_c^2}{2.2458} e^{\left(\frac{b_f}{m_f}\right)} \quad (8.19)$$

$$\rho_e C_e = \frac{\lambda_e}{\alpha_e} \quad (8.20)$$

Average CO₂ saturation during the formation heat pulse test can then be estimated using the definition of the effective thermal conductivity, given by Eq. 8.12, after reformulating it into the following form:

$$S_c = \frac{\frac{1}{\phi} \ln\left(\frac{\lambda_e}{\lambda_r(1-\phi)}\right) - \ln \lambda_w}{\ln \lambda_c - \ln \lambda_w} \quad (8.21)$$

The thermal conductivity of brine and CO₂ can be estimated at the average pressure and temperature conditions during the testing period. Eq. 8.21 requires a prior knowledge of the rock thermal conductivity. To estimate the thermal properties of the formation rock, heat pulse testing can be conducted before CO₂ arrival when fluid flow in the surrounding formation is single-phase brine. Accordingly, the traditional interpretation technique can be used to estimate rock

thermal conductivity and rock volumetric heat capacity using Eq. 8.22 and Eq. 8.23, respectively.

$$\lambda_r = \left(\frac{\lambda_e}{\lambda_w^\phi} \right)^{\frac{1}{1-\phi}} \quad (8.22)$$

$$\rho_r C_r = \left(\frac{\rho_e C_e}{(\rho_w C_w)^\phi} \right)^{\frac{1}{1-\phi}} \quad (8.23)$$

At late time, heat transfer from the heating source becomes advection dominant. The steady-state temperature solution at the advection-dominant period is obtained by assigning $t \rightarrow \infty$ in Eq. Eq. 8.15 or replacing the lower limit of the integration with zero, which is given by:

$$\Delta T(r) = \frac{P}{2\pi\lambda_e} \exp\left[\frac{xu_T}{2\alpha_e}\right] K_0\left(\frac{u_T r}{2\alpha_e}\right) \quad (8.24)$$

where K_0 is modified Bessel function of the second kind of zeroth order. Using the following approximation $e^x K_0(x) \approx K_0(x)$ for $x \ll 1$, Eq. 8.24 is simplified to the following form:

$$\Delta T(r) = \frac{P}{2\pi\lambda_e} K_0\left(\frac{u_T r}{2\alpha_e}\right) \quad (8.25)$$

The temperature solution at the heating cable during the advection-dominant period can be simplified further using the logarithmic approximation of the modified Bessel function when $u_T r / 2\alpha_e \rightarrow 0$ (Abramowitz et al. 1988). Accordingly, the cable temperature during the advection-dominant period is given by:

$$\Delta T(r_c) = \frac{P}{2\pi\lambda_e} \ln\left(\frac{2.2458\alpha_e}{u_T r_c}\right) \quad (8.26)$$

Therefore, the late-time stabilized temperature can be line-fitted with a horizontal zero-slope line. Let t_i be the time at which the horizontal fitted line intersects the straight line fitted by the early time data. The advection velocity of the mixture (brine and CO₂) can be estimated using t_i . By equating Eq. 8.17 (for conduction-dominant period) with Eq. 8.27 (for advection-dominant period), the following expression for advection velocity is obtained:

$$u_T = 1.4986 \sqrt{\frac{\alpha_e}{t_i}} \quad (8.27)$$

The flow velocity of the mixture (brine and CO₂) is then given by:

$$v_T = 1.4986 \left(\frac{\rho_e C_e}{f_C \rho_C C_C + f_w \rho_w C_w} \right) \sqrt{\frac{\alpha_e}{t_i}} \quad (8.28)$$

The velocities of CO₂ and brine can then be obtained at the estimated CO₂ saturation as follows:

$$v_C = \frac{v_T}{1 + \left(\frac{k_{rw}}{k_{rc}} \right) \left(\frac{\mu_C}{\mu_w} \right)} \quad (8.29)$$

$$v_w = v_T - v_C \quad (8.30)$$

where k_{rw} and k_{rc} are the effective permeability of rock to brine and CO₂, respectively. μ_w and μ_c are the viscosity of brine and CO₂, respectively.

8.2.2. Inverse Modeling

Based on the above, the following steps are proposed to interpret the temperature data obtained during heat pulse testing:

1. Conduct formation heat pulse testing before CO₂ arrival.
2. Plot temperature evolution, $\Delta T = T - T_o$ versus log time on a semi-log plot. Identify the temperature data to be fitted by straight line during the conduction-dominant period and by a zero-slope horizontal line during advection-dominant period.
3. Read the slope, m_f and intercept, b_f of the fitted line during the conduction-dominant period, and the time at the intercept of the fitted lines during the conduction- and advection-dominant periods, t_i .
4. Use Eq. 8.18 – 8.20 to estimate the effective thermal properties of the brine saturated formation.
5. The thermal conductivity and heat capacity of the formation rock are estimated using Eq. 8.22 and Eq. 8.23, respectively.
6. Conduct formation heat pulse testing after CO₂ arrival.
7. Plot temperature evolution, $\Delta T = T - T_o$ versus log time on a semi-log plot. Identify the temperature data to be fitted by straight line during the conduction-dominant period and by a zero-slope horizontal line during advection-dominant period.
8. Read the slope, m_f and intercept, b_f of the fitted line during the conduction-dominant period, and the time at the intercept of the fitted lines during the conduction- and advection-dominant periods, t_i .

9. Use Eq. 8.18– 8.20 to estimate the effective thermal properties of the formation.
10. Using the rock thermal conductivity estimated in step 5, obtain the average CO₂ saturation using Eq. 8.21. Brine and CO₂ thermal conductivities are available from tables or can be estimated using EOS at the average pressure and temperature conditions during the heat pulse test.
11. Total and individual phases velocities are estimated using Eq. 8.28 – 8.30 where fractional flow terms are obtained using fractional flow curves at the average CO₂ saturation obtained in Step 10.

The analytical solution and interpretation methodology introduced so far consider the first deployment technique of heat pulse testing in which A-DTS is embedded in direct contact with the formation. In the second deployment technique, formation heat pulse test is implemented using a separated distributed heating source deployed within a monitoring well, and the monitoring cable (passive DTS cable) is deployed behind the casing and directly in contact with the formation. In this case, the presented analytical solution and interpretation methods are still usable, however the radius at which the monitoring cable is located from the heating source should be used instead of cable radius. The thermal resistances of wellbore fluid, casing, and cement sheath do not affect the observed temperature signal at the monitoring cable because it is cemented behind the casing at formation/cement interface (see Fig. 8.11 (c)). For proper implementation of heat pulse testing using the second deployment technique, the monitoring well must have no hydraulic communication with the formation to isolate the intervention effects of fluid flow inside the monitoring well. If the casing is perforated, the borehole of the monitoring well can be isolated using impermeable fabric liner as proposed by Coleman et al. (2015). The heating source in this case may constitute a deployed tubing over which a heating coil is wrapped as proposed by Liu et al. (2013) (see Fig. 8.11 (c)). To minimize the thermal storage capacity of the wellbore and the density-driven flow in the annular space, the size of the annulus between the deployed tubing and the inner wall of the casing should be minimized. In Liu et al. (2013)'s work, the annular space is restricted to 0.2 cm to mitigate heat transfer by natural convection inside the wellbore. In the next section, the results of the analytical solution and the interpretation methods are validated against numerical results to demonstrate their validity.

8.2.3. Validation and Application of the Interpretation Methodology

In this section, the analytical results obtained using the proposed forward model are validated against numerical results obtained using the thermal compositional simulation tool, CMG-STARs (2020). The graphical interpretation methods are used to interpret the numerically obtained temperature results and estimate formation thermal properties, formation fluid velocity, and fluid saturation at the monitoring well/cable. Temperature behavior is analyzed before and after CO₂ arrival to show the sensitivity of temperature signal to CO₂ arrival. The input data for the synthetic cases are given in Table 8.2.

Table 8. 2. Input data for the synthetic case (before and after CO₂ arrival).

Feature		Value
Initial temperature, °C		60
Initial pressure, MPa		25
Cable radius, mm		0.55
Fluid velocity, μm/s (m/day)		36.20 (3.128) (before CO ₂ arrival) 35.43 (3.061) (after CO ₂ arrival)
Supplied power, W/m		5
Formation porosity, fraction		0.3
Water density, kg/m ³		995.18
Water heat capacity, J/kg K		4132.1
Water thermal conductivity, W/m K		0.579
CO ₂ density, kg/m ³		732.76
CO ₂ thermal conductivity, W/m K		0.0694
Rock density, Kg/m ³		2650
Rock heat capacity, J/kg K		887.4
Rock thermal conductivity, W/m K		4
Relative Permeability Parameters using Corey's model	n	2
	m	2
	S_{wi}	0.4
	k_{rgo}	0.33

In this case, heat pulse test is deployed using an A-DTS cable of 1.1 mm diameter that is embedded in direct contact with the reservoir's porous medium. The storage reservoir is heterogenous reservoir that constitutes high permeability streak with a width of 10 m and a permeability of 1 Darcy, while the formation permeability is 10 md (see Fig. 8.12 (a)). The reservoir has uniform thickness of 10 m and initial pressure and temperature conditions of 250 bar and 60 °C, respectively. The A-DTS cable is located 50 m away from the injection well within the high permeability streak. CO₂ is injected into the reservoir at a constant injection rate of 0.01 m³/s (864 m³/day) and constant injection temperature of 60 °C. A 2D Cartesian model that consists of 20,604 grid cells is used while building the numerical model. Size of grid cells decreases logarithmically toward the injection well and A-DTS cable in x - and y -directions (see Fig. 8.12 (b)). Fig. 8.13 illustrates the relative permeability curves and fractional flow curve for CO₂ at the reservoir conditions. Relative permeability curves are constructed using Corey's model (Corey 1954) with $S_{wi} = 0.4$, $k_{rgo} = 0.33$, and $m = n = 2$. CO₂ and brine viscosities are estimated at the average pressure and temperature conditions during the testing period which are 0.016 and 0.46 cp, respectively. The rock and fluid properties are given in Table 8.2.

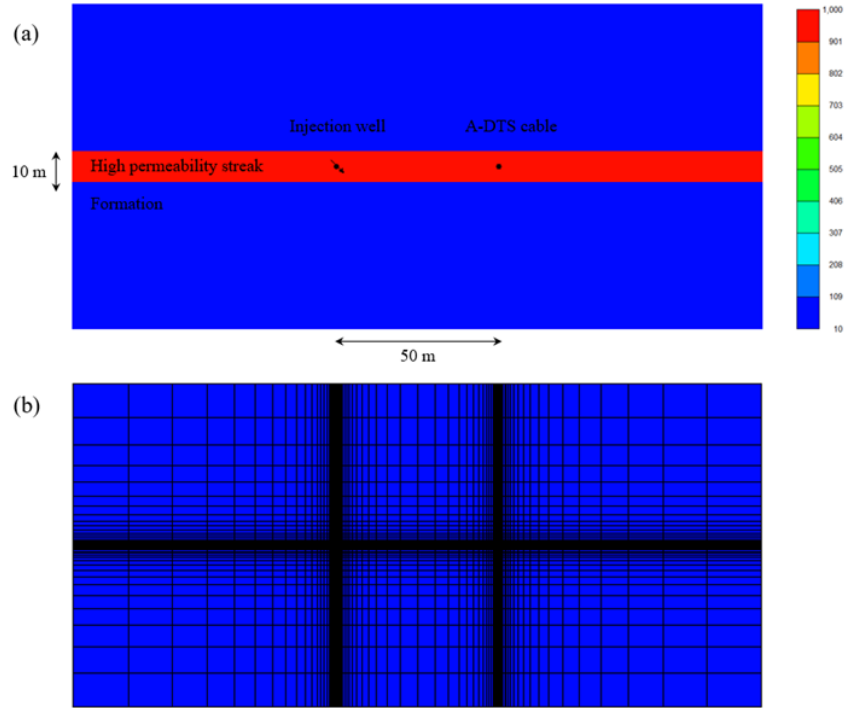


Figure 8. 12. Schematic illustration of the numerical model showing: (a) storage aquifer and the high permeability streak with indication of the injection well and the A-DTS cable (b) grid discretization.

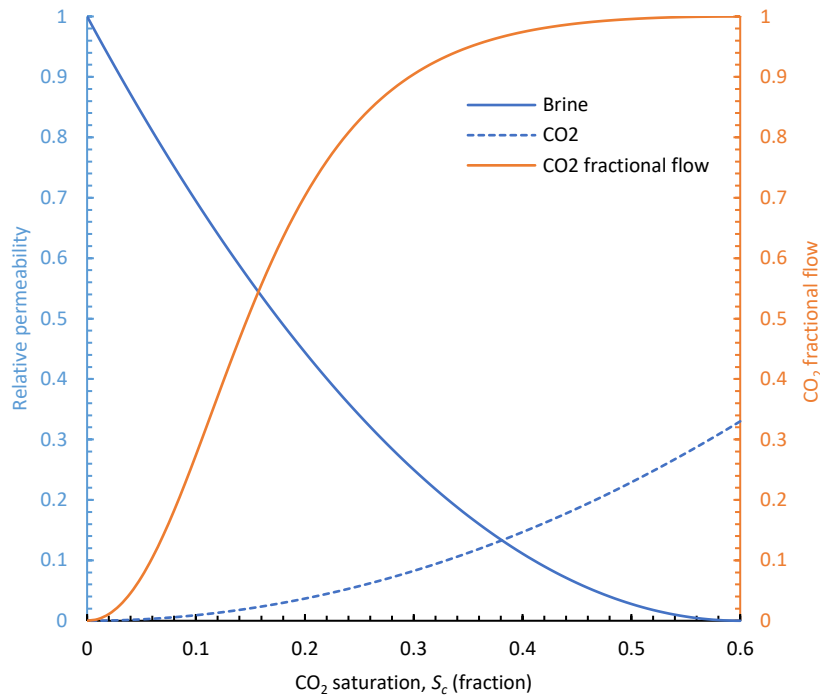


Figure 8. 13. Relative permeability curves constructed using Corey's model (Corey 1954) and CO₂ fractional flow curve.

Heat pulse testing is modelled before and after CO₂ arrival at the A-DTS cable. Fluid velocity, CO₂ velocity, CO₂ saturation, and temperature evolutions during heat pulse tests are shown in Fig. 8.14 as obtained from the numerical simulation. Slight increase in the temperature is observed before heating starts due to Joule-Thomson expansion of the flowing brine. Because brine has negative Joule-Thomson coefficient, it warms as it expands while it flows through porous medium (Stauffer et al. 2014). Before CO₂ arrival, heat pulse test is conducted after 6 hours from the start of CO₂ injection in order to estimate thermal properties of the formation rock. The electrical power supplied to the A-DTS cable is 5 W/m. Heat pulse testing extends to 12 hours, and then heating stops. After CO₂ arrival, heat pulse test is conducted again to monitor CO₂ plume propagation. In this second test, heating starts 5 days after the start of CO₂ injection and extends for two days until temperature stabilizes. Fig. 8.15 illustrates a semi-log plot of temperature buildup during the heat pulse test before CO₂ arrival. Temperature increases linearly during the formation conduction-dominant period before it stabilizes at $t = 1$ hour when the heat generated by the cable is fully dissipated by fluid advection. The temperature increase at the stabilization time is 1.45 °C. The observed temperature signal is controlled by the supplied electrical power which is a design factor during heat pulse testing. Higher electrical power results in higher temperature heating. The temperature behavior obtained using the analytical solution is illustrated on the same figure which shows good agreement with the numerical results. Two fitted lines are shown for the conduction- and advection-dominant periods. The slope and intercept of the fitted line during the conduction-dominant period are 0.18 °C and 0.31°C, respectively. The slope and intercept values are used for estimating the effective thermal properties of the formation using Eq. 8.18 – 8.20 as follows:

$$\lambda_e = \frac{P}{4\pi m_f} = \frac{5}{4\pi \times 0.1777} = 2.239 \text{ W/m K}$$

$$\alpha_e = \frac{r_c^2}{2.2458} e^{\left(\frac{b_f}{m_f}\right)} = \frac{0.00055^2}{2.2458} e^{\left(\frac{0.305}{0.1777}\right)} = 7.498 \times 10^{-7} \text{ m}^2/\text{s}$$

$$\rho_e C_e = \frac{\lambda_e}{\alpha_e} = \frac{2.239}{7.498 \times 10^{-7}} = 2.987 \times 10^6 \text{ J/m}^3\text{K}$$

The thermal conductivity and heat capacity of the formation rock are estimated accordingly using Eq. 8.22 – 8.23 as follows:

$$\lambda_r = \left(\frac{\lambda_e}{\lambda_w \phi}\right)^{\frac{1}{1-\phi}} = \left(\frac{2.239}{0.579^{0.3}}\right)^{\frac{1}{1-0.3}} = 4 \text{ W/m K}$$

$$\rho_r C_r = \left(\frac{\rho_e C_e}{(\rho_w C_w) \phi}\right)^{\frac{1}{1-\phi}} = \left(\frac{2.987 \times 10^6}{(4.113 \times 10^6)^{0.3}}\right)^{\frac{1}{1-0.3}} = 2.604 \times 10^6 \text{ J/m}^3\text{K}$$

The velocity of brine flow around the heating cable is estimated using Eq. 8.28 (assuming gas saturation and gas fractional flow equal to zero) in which t_i is depicted from Fig. 8.15 at $t = 636.4$ s as follows:

$$v_w = v_T = 1.4986 \left(\frac{\rho_e C_e}{\rho_w C_w} \right) \sqrt{\frac{\alpha_e}{t_i}} = 1.4986 \left(\frac{2.987 \times 10^6}{4.113 \times 10^6} \right) \sqrt{\frac{7.498 \times 10^{-7}}{636.4}}$$

$$= 37.36 \mu\text{m/s} \text{ (3.23 m/day)}$$

Table 8.3 shows the inversion results with the estimation errors. Good agreement is obtained between the graphical interpretation results and those provided to the simulation tool with a maximum estimation error of 11 percent.

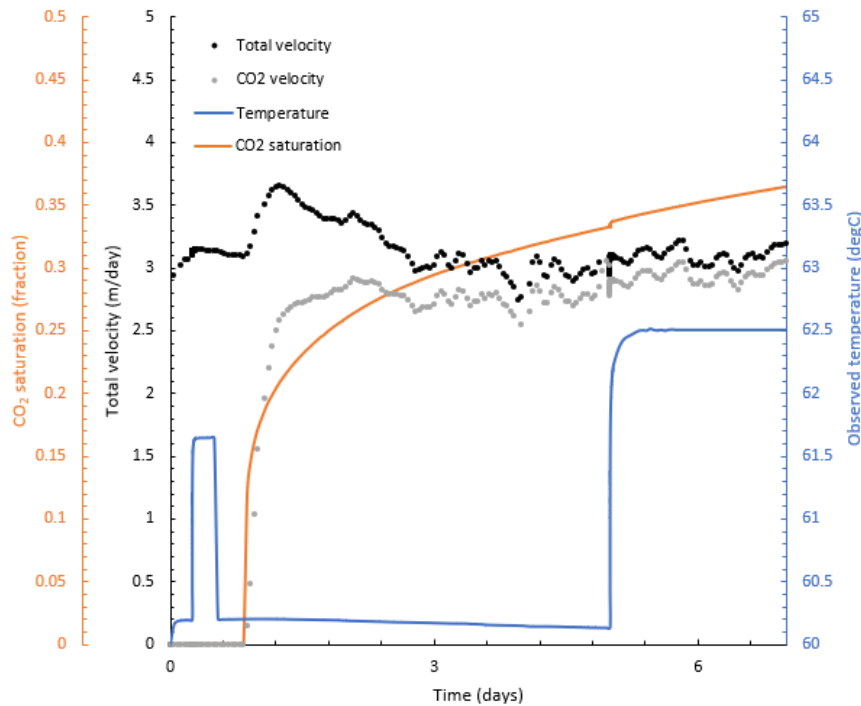


Figure 8. 14. Total velocity, CO₂ velocity, CO₂ saturation, and temperature evolutions during the heat pulse tests.

After CO₂ arrival, formation heat pulse test is modeled during two-phase flow conditions. Slight increase in the CO₂ saturation and velocity is depicted upon the start of heating which is attributed to the expansion of CO₂ adjacent to the heating source by the effect of temperature heating. In the case of two-phase flow, temperature stabilized at 62.51 °C after 18 hours since the test begun. Fig. 8.16 illustrates the temperature evolution obtained during the heat pulse test before and after CO₂ arrival. As observed, higher rate of temperature buildup is observed after CO₂ arrival which results in higher stabilized temperature rise (2.37 °C) compared with the stabilized temperature rise observed before CO₂ arrival (1.45 °C). Also, temperature stabilization before CO₂ arrival attains within 1 hour after the start of test, while it extends to 18 hours after CO₂ arrival. Since the thermal conductivity of supercritical CO₂ (~0.07 W/m K) is one order of magnitude less than that of the aqueous brine phase (~0.6 W/m K), the intrusion of CO₂ decreases the effective thermal conductivity of the surrounding porous medium which in turn decreases the rate of heat dissipation from the heating source.

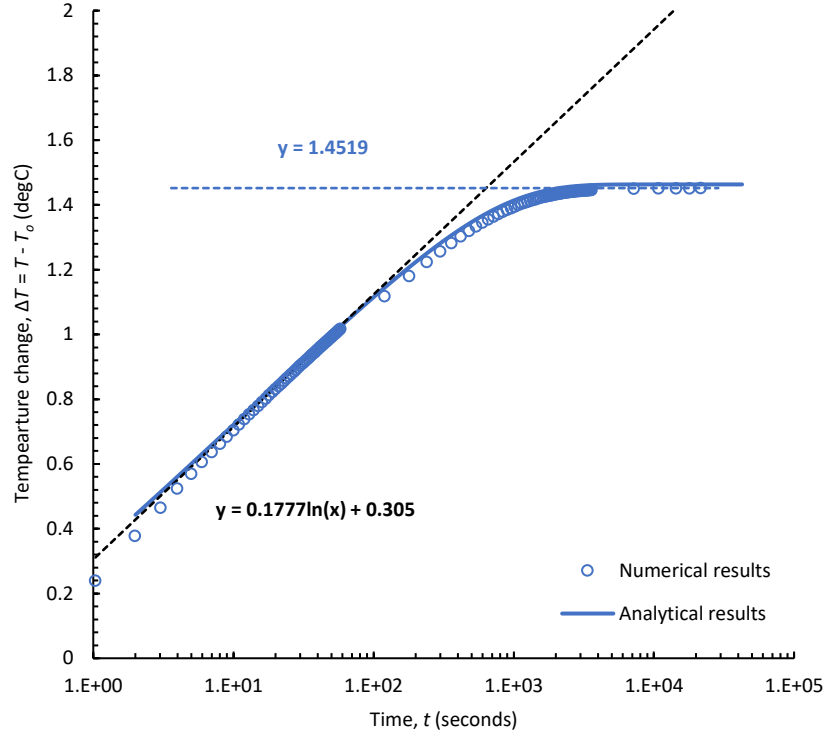


Figure 8. 15. Temperature buildup during the heat pulse test (before CO₂ arrival).

Consequently, higher stabilized temperature is observed after CO₂ arrival due to the reduction of the conduction heat transfer efficiency. Additionally, the replacement of the in-situ brine with the supercritical CO₂ decreases the velocity of heat transfer by advection (Platenkamp 1985). Rate of heat transfer by advection is mainly governed by the advection velocity which is the velocity of thermal plume propagation from the heating source caused by fluid movement. Advection velocity is lower than flowing fluid velocity (Darcy velocity) by a factor, known as a retardation factor $\phi(\rho_f C_f / \rho_e C_e)$ (see Eq. 8.28). Consequently, intrusion of CO₂, which has lower volumetric heat capacity, decreases the retardation factor and the advection velocity, and as such the contribution of advection heat transfer mechanism becomes less effective, and longer stabilization time is obtained. This implies that monitoring the temperature response during formation heat pulse test before and after CO₂ arrival can effectively identify the time of CO₂ arrival. Fig. 8.16 illustrates the semi-log plot of temperature buildup during the heat pulse test after CO₂ arrival as obtained from the numerical simulation and the analytical solution with the fitted lines during the conduction- and advection-dominant periods. The slope and the intercept of the fitted line during the conduction-dominant period are read from Fig. 8.16 which are 0.22 °C and 0.36 °C, respectively. The effective thermal properties of the formation are estimated using Eq. 8.18 – 8.20 as follows:

$$\lambda_e = \frac{P}{4\pi m_f} = \frac{5}{4\pi \times 0.2205} = 1.804 \text{ W/m K}$$

$$\alpha_e = \frac{r_c^2}{2.2458} e^{\left(\frac{b_f}{m_f}\right)} = \frac{0.00055^2}{2.2458} e^{\left(\frac{0.355}{0.2205}\right)} = 6.738 \times 10^{-7} \text{ m}^2/\text{s}$$

$$\rho_e C_e = \frac{\lambda_e}{\alpha_e} = \frac{1.804}{6.738 \times 10^{-7}} = 2.678 \times 10^6 \text{ J/m}^3\text{K}$$

Eq. 8.21 is used to estimate average CO₂ saturation during the testing period as follows:

$$S_c = \frac{\frac{1}{\phi} \ln \left(\frac{\lambda_e}{\lambda_r^{(1-\phi)}} \right) - \ln \lambda_w}{\ln \lambda_c - \ln \lambda_w} = \frac{\frac{1}{0.3} \ln \left(\frac{1.804}{4^{(1-0.3)}} \right) - \ln(0.579)}{\ln(0.0694) - \ln(0.579)} = 0.339$$

Since the thermal conductivity of the rock has been estimated during heat pulse testing before CO₂ arrival, only the thermal conductivities of CO₂ and brine are required in Eq. 8.21 which are estimated using EOS tool at average pressure and temperature conditions during the heating period. The total velocity of the fluid mixture (CO₂ and brine) is estimated using Eq. 8.28 in which t_i is depicted from Fig. 8.16 at $t = 9491$ s as follows:

$$\begin{aligned} v_T &= 1.4986 \left(\frac{\rho_e C_e}{f_C \rho_C C_C + f_W \rho_W C_W} \right) \sqrt{\frac{\alpha_e}{t_i}} \\ &= 1.4986 \left(\frac{2.678 \times 10^6}{0.941 \times 732.76 \times 1177.7 + 0.0586 \times 995.18 \times 4132.1} \right) \sqrt{\frac{6.738 \times 10^{-7}}{9491}} \\ &= 32.1 \text{ } \mu\text{m/s (2.77 m/day)} \end{aligned}$$

Brine and CO₂ fractional flow terms are obtained at the estimated average CO₂ saturation from Fig. 8.13. CO₂ and brine velocities after CO₂ arrival are estimated using Eq. 8.29 – 8.30 as follows:

$$v_C = v_T \times f_g = 32.1 \times 0.941 = 30.2 \text{ } \mu\text{m/s (2.61 m/day)}$$

$$v_w = v_T - v_C = 32.1 - 30.2 = 1.88 \text{ } \mu\text{m/s (0.162 m/day)}$$

The phases' velocities observed after CO₂ arrival indicate that fluid flow becomes almost single-phase CO₂ after CO₂ arrival at the A-DTS cable. This can be attributed to the rapid increase in the CO₂ fractional flow curve from 0 to 1 through the change in CO₂ saturation from 0.0 to 0.4 as observed in Fig. 8.13. The inversion results are given in Table 8.3 which show good agreement with those obtained from the numerical simulation.

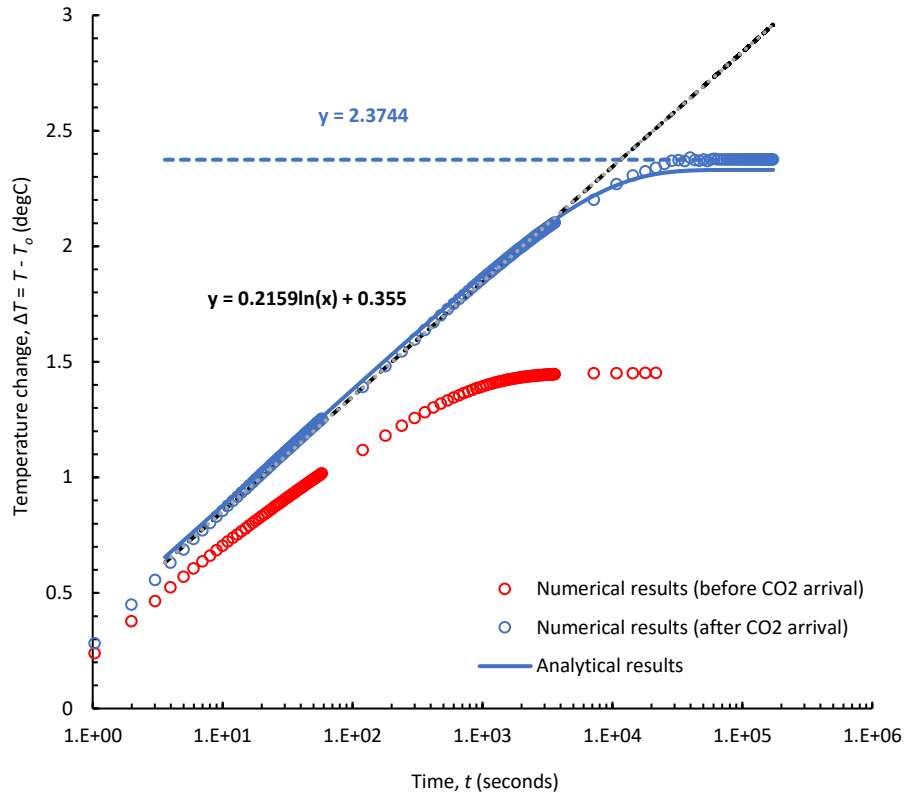


Figure 8. 16. Temperature buildup during the heat pulse test (before and after CO₂ arrival).

Table 8. 3. Inversion results obtained using the graphical interpretation methods with the estimation errors in parentheses (before and after CO₂ arrival).

	(Before CO ₂ arrival)	(After CO ₂ arrival)
Thermal conductivity of formation, W/m K	2.24 (0.004 %)	1.80 (0.005 %)
Heat capacity of formation, J/m ³ K	2.99×10^6 (3.28 %)	2.68×10^6 (5.06 %)
Total fluid velocity, m/day	3.23 (3.19 %)	2.77 (9.40 %)
CO ₂ velocity, m/day	NA	2.61 (9.38 %)
Brine velocity, m/day	3.23	0.16 (9.70 %)
CO ₂ saturation, fraction	NA	0.34 (0.018 %)
Rock Thermal conductivity, W/m K	4.00 (0.005 %)	
Rock heat capacity, J/m ³ K	2.60×10^6 (10.74 %)	

Chapter 9. Application of Passive Temperature Monitoring for Tracking CO₂ Migration

In this chapter, we will show the applications of passive temperature monitoring for tracking CO₂ migration in subsurface and detecting CO₂ migration from the storage aquifer via improperly abandoned wells. In section 9.1, we will study the potential effects of different factors that can affect the established temperature heating at the plume front. CO₂ migration in a storage aquifer is monitored through tracking the warming wave that migrates contemporaneously with the plume front. Temperature heating at the plume front is exclusively caused by exothermic CO₂ dissolution into the in-situ brine. We will study the effects of aquifer outer boundary conditions, injection history, level, and location of the temperature monitoring tool on the established temperature signal. In section 9.2, we will study CO₂ migration from the storage aquifer via improperly abandoned wells. The objective of this study is to investigate the feasibility of using temperature and pressure monitoring at surface to detect CO₂ migration through abandoned wells.

9.1. Monitoring CO₂ Migration in Storage Aquifer

A 2D radial numerical model is used to model temperature evolution for two different outer boundary conditions, namely infinite-acting (open) and no-flow (closed). Additionally, temperature and saturation measurements at different levels of the monitoring wells are analyzed for both cases to investigate the variation of temperature and saturation distributions over the aquifer thickness. Besides, the sensitivity of the temperature signal to injection history is investigated considering different injection scenarios. Finally, the sensitivity of the temperature measurements to the location of the temperature sensor is investigated using a coupled wellbore-reservoir system for two different scenarios. In the first scenario, the temperature sensor (e.g., the fiber optic cable) is cemented outside the casing. In the second scenario, the temperature sensor is located inside the wellbore. Throughout this study, the interrelationships between pressure, temperature, and CO₂ saturation during CO₂ plume evolution are investigated under boundary-dominated flow conditions.

9.1.1. Methods

Non-isothermal numerical simulations are performed using TOUGH3 simulator compiled with ECO2 fluid property module; which is a general-purpose numerical simulation tool for modeling fluid and heat transport of multiphase and multicomponent fluid mixtures in porous media (Jung et al. 2018). To model temperature monitoring inside the monitoring well, T2Well/ECO2N simulation tool is used which is an integrated simulation tool capable of accounting for fluid flow dynamics in both the wellbore and reservoir subdomains (Pan and Oldenburg 2014, Pan 2011).

The problem of CO₂ injection in a saline aquifer is investigated using input data adopted from Pruess et al. (2002) with slight modifications. CO₂ is injected at a constant injection rate (10 kg/s – 315,360 MT/y) and constant bottomhole temperature of 65 °C for 5 years into a saline aquifer via a vertical well which is completed over the entire thickness of the reservoir. Bottomhole injection temperature is set equal to the initial reservoir temperature to isolate the anthropogenic contribution of the injected CO₂ on temperature evolution. The aquifer has a

uniform thickness of 50 m and a radial extent of 5 km (base case) (see Figure 9.1 (a)). The injection well comprises a single grid cell with a radius of 0.3 m and represents the inner boundary of the reservoir model. Beyond the injection well, the reservoir is discretized into 700 grid cells with a logarithmically increasing Δr from 0.3 m to 5 km. To simulate the semi-infinite far-field dimension, 134 grid cells with logarithmically increasing Δr from 5 km to 100 km are implemented. The high resolution of the grids near the injection well is chosen to minimize the non-physical spike of the pressure results at the early-time period (Mathias et al. 2013) (see Figure 9.1 (b)). The burial depth of the reservoir is assumed to be 2000 m and the overlying layer acts as a seal, but it is not considered in the model. In the vertical direction, the reservoir is uniformly discretized into 30 grid cells.

For the initial reservoir conditions, initial pressure and temperature are estimated using $p = 1 + 0.1z$ and $T = 15 + 0.025z$, respectively, with p in bars, T in degrees C, and z in meter (Doughty 2008). The salinity of the brine is 0.15 halite mass fraction. The reservoir is assumed to be homogenous with a porosity of 0.12 fraction, lateral, and vertical permeability of 500 md and 50 md, respectively. The density, thermal conductivity, and the heat capacity of the rock are 2600 kg/m^3 , $2.51 \text{ W/m } ^\circ\text{C}$, and $920 \text{ J/kg } ^\circ\text{C}$.

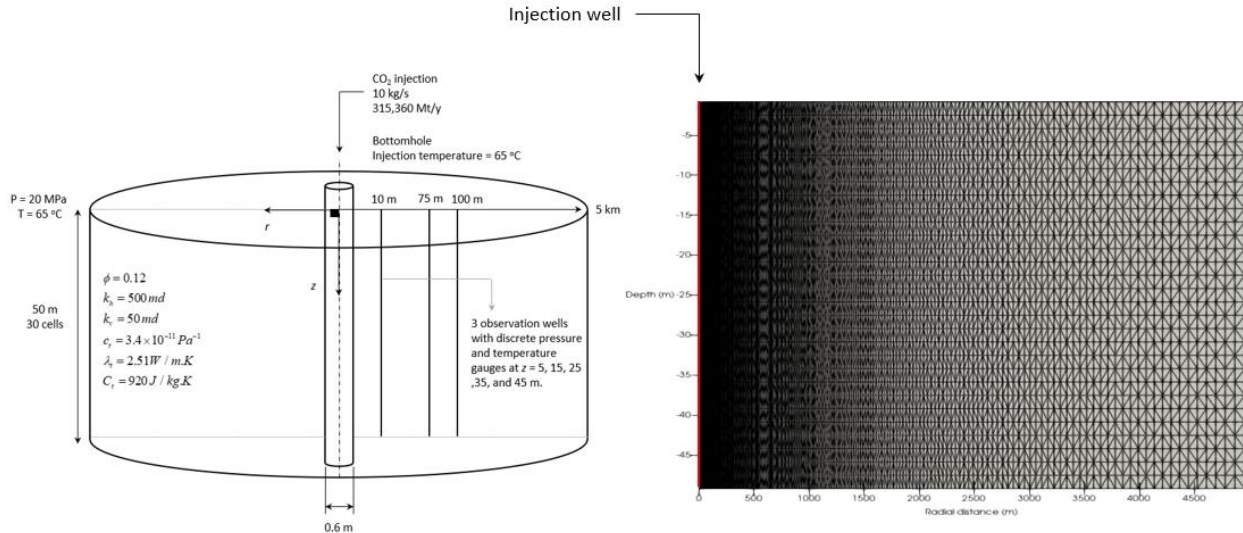


Figure 9. 1. (a) Schematic diagram of the 2D radial model showing the locations of the injection and observation wells (b) logarithmic discretization of the 2D symmetric radial model.

To account for the interfering effects of the CO₂ and the brine occupying the same pore space, Corey's model (Corey 1954) and van Genuchten's model (van Genuchten 1980) described by Eq. 9.1 – 9.3, are used to evaluate the relative permeability and capillary pressure, respectively. The parameters for the 2D radial simulation model are shown in Table 9.1. A total of three observation wells are considered at radial distances of 10, 75, and 100 m, respectively, from the injection well. The observation wells are used to track CO₂ plume migration and monitor pressure, temperature, and CO₂ saturation changes at various depths.

$$k_{rI} = \sqrt{S^*} \left(1 - \left(1 - [S^*]^{1/\lambda} \right)^\lambda \right)^2 \quad \text{where } S^* = (S_l - S_{lr}) / (1 - S_{lr}) \quad (9.1)$$

$$k_{rg} = (1 - \hat{S}^2)(1 - \hat{S})^2 \quad \text{where } \hat{S} = (S_l - S_{lr}) / (1 - S_{gr} - S_{lr}) \quad (9.2)$$

$$P_c = -P_o \left(\left[S^* \right]^{\frac{1}{\lambda}} - 1 \right)^{1-\lambda} \quad (9.3)$$

Table 9. 1. 2D radial model properties.

Input Data	Value	Unit	
CO ₂ injection temperature	65	°C	
Injection time	5	years	
Injection rate	10	kg/s	
Initial reservoir temperature	65 – 66.25	°C	
Reservoir thickness	50	m	
Reservoir lateral extent	5 - 100	km	
Reservoir depth	2000	m	
Model type	Infinite-acting model /Closed model		
Well representation	Single grid with 0.3 m in radius which represents inner boundary		
Grids number in <i>r</i> - and <i>z</i> - directions	834 and 30	-	
Wellbore radius	0.3	m	
Grid size in radial direction	Logarithmically increasing Δr from 0.3 to 5 - 100 km		
Grid size in <i>z</i> - direction	1.667	m	
Initial reservoir pressure	19.75-20.25	MPa	
Water salinity (halite)	150,000	ppm	
Horizontal / vertical Porosity	5×10^{-13} , 5×10^{-14}	m ²	
	0.12	fraction	
	λ	0.457	-
Relative permeability parameters	S_{lr}	0.3	fraction
	S_{is}	1	fraction
	S_{gr}	0.05	fraction
	λ	0.457	-
Capillary pressure parameters	S_{lr}	0.0	fraction
	P_o	0.01961	MPa
	S_{is}	0.999	fraction

9.1.2. Results and Discussion

Figure 9.2 (a) and (b) illustrate the pressure and temperature profiles throughout the aquifer after 5 years of CO₂ injection using an infinite-acting reservoir model and a closed-reservoir model of different aquifer sizes ($r_e = 5 - 100$ km) at the uppermost layer ($z = 5$ m). During boundary-dominated flow conditions, pressure increases excessively throughout the aquifer due to the limited size/storage capacity compared with the infinite-acting reservoir model. The magnitude of the pressure buildup after 5 years of CO₂ injection for a closed aquifer of size $r_e = 5$ km is 10.6 MPa which is much higher than the corresponding pressure buildup for semi-infinite aquifer model which can exceed the fracture pressure of the aquifer at the injection well. On the other hand, temperature exhibits slight increase as the aquifer model becomes bounded and its size decreases. The increase in temperature are attributed to different factors which are:

- Adiabatic compression of CO₂ and brine triggered by the excessive increase of the aquifer's pressure. The contribution of adiabatic compression to the temperature signal is described by Eq. 9.4 (Duru and Horne 2010, Mao and Zeidouni 2017). Given that the adiabatic compression coefficients for CO₂, η_{CO_2} and brine, η_w are of different magnitudes, non-uniform heating is obtained because of the non-uniform saturation distribution throughout the aquifer.

$$\frac{\partial T}{\partial t} = \phi \left\{ \frac{\rho_w C_w S_w \eta_w + \rho_{CO_2} C_{CO_2} (1 - S_w) \eta_{CO_2}}{\phi (\rho_w C_w S_w + \rho_{CO_2} C_{CO_2} (1 - S_w)) + (1 - \phi) \rho_r C_r} \right\} \frac{\partial p}{\partial t} \quad (9.4)$$

where

$$\eta_w = \mu_{JT_w} + \frac{1}{\rho_w C_w} \text{ and } \eta_{CO_2} = \mu_{JT_{CO_2}} + \frac{1}{\rho_{CO_2} C_{CO_2}}$$

- Enhancement of heat of dissolution in the two-phase region triggered by the increase of CO₂ solubility in the in-situ brine as aquifer's pressure increases (Carroll et al. 1991). The increase in CO₂ dissolution is one order of magnitude higher than the increase in water solubility in flowing CO₂ (see Figure 9.2 (b)). Consequently, more heat is released due to the exothermic reaction of CO₂ dissolution. Temperature increases as CO₂ saturation increases toward the trailing edge of the two-phase region. The maximum temperature increase is located at 174 m.
- Increased reservoir pressure also decreases the JT coefficient for CO₂, which mitigates the cooling effect caused by CO₂ JT expansion in the dry-out region. JT coefficient for CO₂ decreases from 1.224 °C/MPa at 20 MPa to 0.455 °C/MPa at 30 MPa. Consequently, the temperature gradient within the dry-out region decreases as the aquifer's pressure increases.

Additionally, upward migration of CO₂ increases the temperature at shallower zones due to convective heat transfer from the deeper zones which have higher geotherm. However, this effect

is not restricted to the closed reservoir. Accordingly, closed boundary condition implies relatively different temperature behavior where adiabatic compression of aquifer fluids as well as increased CO₂ solubility increases the characteristic temperature profile.

Figure 9.2 (c) illustrates CO₂ saturation profiles for the infinite-acting and closed reservoirs ($r_e = 5 - 100$ km) at the uppermost layer ($z = 5$ m) after 5 years of CO₂ injection. The size of the plume shrinks for closed reservoirs as the size of reservoir decreases. This can be attributed to the increase in the CO₂ solubility in the in-situ brine within the two-phase region due to the excessive increase in pressure. Accordingly, the amount of free CO₂ within the two-phase region decreases compared with semi-infinite acting system. Additionally, the excessive increase in the pressure during boundary-dominated flow conditions increases the density of CO₂. This has two consequences. First, the same mass would take less volume for a smaller-size aquifer, and therefore the plume size becomes smaller. Second, the buoyancy effect, which is driven by CO₂-brine density difference, weakens. Consequently, the upward migration of CO₂ to shallower zones ($z < 25$ m) is mitigated, which also results in a smaller extent of CO₂ plume in shallower zones. Overall, a delay of CO₂ arrival time compared with the infinite-acting reservoir case is observed. The extent of CO₂ front is 874 m and 1003 m for closed ($r_e = 5$ km) and infinite-acting reservoir models, respectively.

Three observation wells (OWs) are considered to observe pressure, temperature, and saturation variation at different radial distances and vertical depths. Figure 9.3 illustrates the pressure and temperature history at three observation wells located at 10, 75, and 100 m from the injection well at $z = 5$ m assuming infinite-acting reservoir (left) and closed reservoir (right) models. The discontinuity in the pressure and temperature behavior indicates the arrival of CO₂ front (0.001, 0.053, and 0.880 years for OW1, OW2, and OW3). Before CO₂ arrival, pressure results follow straight lines with identical slopes when plotted on a semi-log scale during the transient flow regime. Since only brine is flowing across the observation points, the pressure behavior is well described by the logarithmic approximation of Ei – function solution to the diffusivity equation (Lee et al. 2003). After CO₂ arrival, pressure increases more steeply because of the reduction of the total mobility of the flowing fluids, which is caused by the two-phase flow effect. Steep reduction in water relative permeability and water mobility is observed upon CO₂ arrival, which exceeds the increase in total mobility caused by the intrusion of the highly mobile CO₂. As CO₂ saturation increases, the increase in CO₂ mobility exceeds the reduction of water mobility and thus, the total mobility of flowing fluids increases again. This effect results in a lower rate of pressure buildup as injection proceeds. Finally, pressure decreases toward the end of the injection period. Vilarrasa et al. (2010) noted that pressure decreases because the pressure drop in the two-phase region due to the relative permeability impairment gets distributed over a larger area as the size of the CO₂ plume increases. The following expression is provided by Vilarrasa et al. (2010) for BHP variation during CO₂ injection, which is a time derivative of the pressure drop in the three regions that establish during CO₂ flow in a saline aquifer.

$$\frac{dp_{inj}}{dt} = \frac{d}{dt} [\Delta p_1 + \Delta p_2 + \Delta p_3] = \frac{Q}{2\pi} \left[\frac{\mu_{CO_2}}{khR_i(t)} - \frac{1}{R_i^2(t)\gamma} \right] \quad (9.5)$$

where R_i is the radius of interference between CO₂ and in-situ brine and γ is the leakage coefficient that characterizes the pressure drop within the two-phase region. This term is

equivalent to the harmonic average of permeabilities within the two-phase region. For shallow propagation of CO₂ plume (i.e., small R_i), the derivative is negative because the second term (negative) is inversely proportional to R_i^2 and will be greater than the other term (positive), which is inversely proportional to R_i . Consequently, injection pressure decreases at small R_i . At long injection time, when $R_i > \frac{kh}{\mu_{CO_2}\gamma}$, injection pressure increases back again.

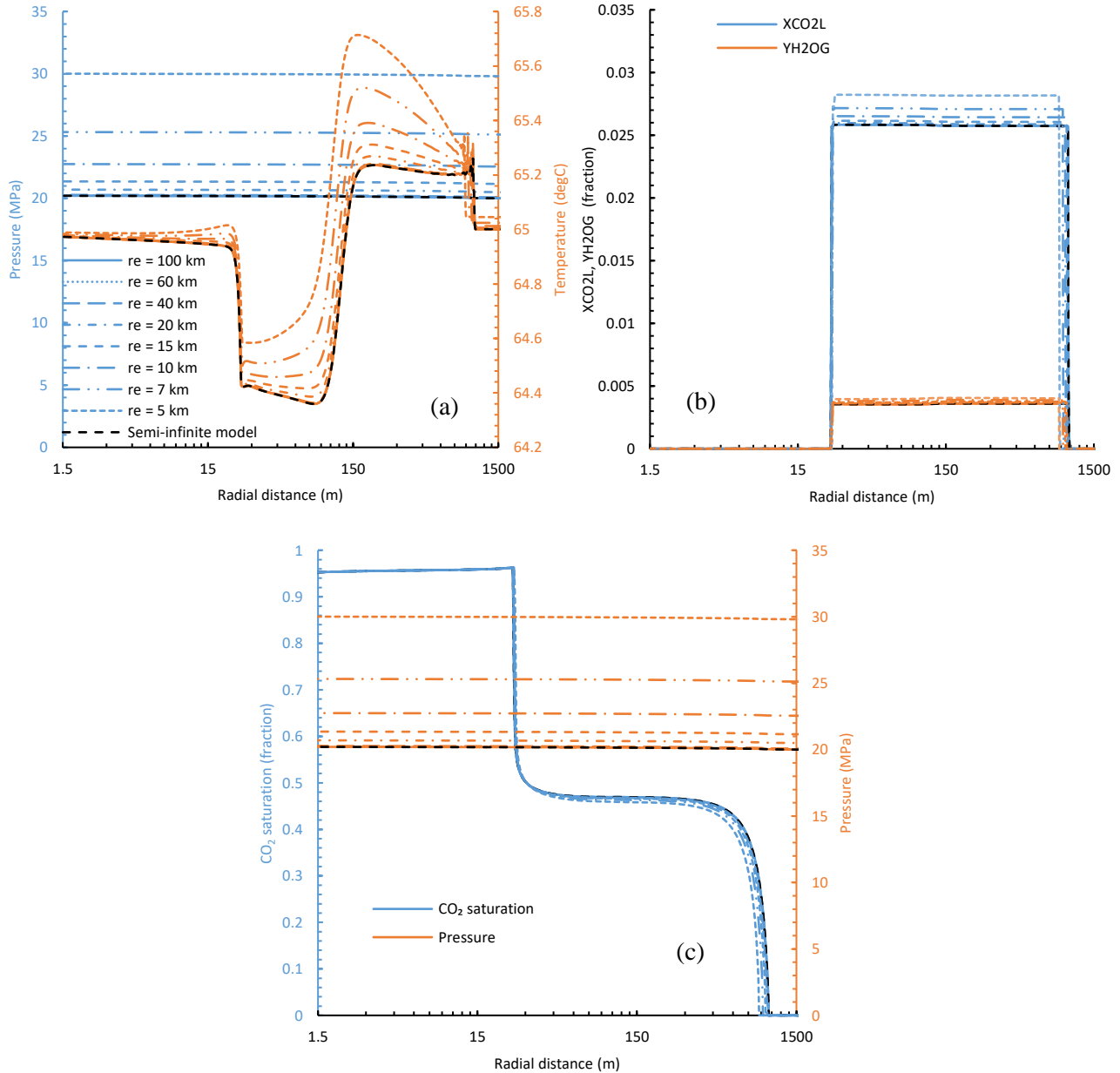


Figure 9. 2. (a) Pressure and temperature (b) mutual solubility (c) CO₂ saturation profiles in the aquifer after 5 year of CO₂ injection for a closed reservoir at different sizes ($r_e = 5 - 100$ km) and an open reservoir model at $z = 5$ m.

CO₂ arrival can be detected using temperature monitoring through tracking the warming front caused by CO₂ dissolution in the brine at the plume front. The temperature increase at the warming front is ~ 0.3 °C as illustrated in Figure 9.3 (left). This anomaly increases to 0.4 °C at $r = 100$ m due to upward migration of CO₂ from warmer and deeper zones governed by gravity. In the vicinity of the well ($r=10$ m), the flow is dominated by viscous forces and gravity is muted. After the warm-up effect of CO₂ dissolution is felt at the observation wells, temperature decreases due to water vaporization and finally temperature increases back to the initial aquifer temperature when water vaporization ceases. Temperature recovery is not visible in OW2 and OW3 which are located far away from the injection well. Figure 9.3 (right) illustrates pressure and temperature variations at the observation wells for the closed reservoir scenario ($r_e = 5$ km). The pressure deviates upward from the transient pressure trend when the boundary-dominated flow (BDF) regime prevails at ~0.03 years. Start of BDF is indicated by replotting pressure behavior at OW1 assuming infinite-acting model (red line). The departure of the black solid line, which represents pressure behavior for closed reservoir, from the dashed red line indicates the start of the boundary dominated flow period. The linear behavior on the semi-log pressure graph corresponding to infinite-acting flow, which has been observed in Fig 9.3 (left) is no longer visible after 0.03 years. The CO₂ arrival may no longer be detected by deviation from the linear behavior on the semi-log pressure graph. Excessive increase in aquifer pressure during BDF is expected because of the limited storage capacity of the aquifer. At OW2 and OW3, temperature exhibits gradual increase after the warming front is felt due to the adiabatic compression of aquifer fluids as well as the increase in heat released by CO₂ dissolution. Such an effect is not visible at OW1 because CO₂ arrival time (0.001 years) at OW1 is less than the time of BDF (0.03 years).

Figure 9.4 (a) illustrates CO₂ saturation and temperature results at OW1 at different levels ($z = 5, 15, 25, 35,$ and 45 m) for the infinite-acting reservoir case. Temperature profiles shifted upward as depth increases due to the geothermal gradient. Temperature and CO₂ saturation results show that CO₂ front/warming front arrives at the same time at all the monitoring intervals, which indicate that the effect of buoyancy is negligible at OW1 ($r = 10$ m) because the viscous force is the dominating force near the injection well. For the closed reservoir case ($r_e = 5$ km), Figure 9.4 (b) indicates similar results compared with the infinite-acting scenario because CO₂ arrival time at OW1 (~ 0.001 years) is much lower than the BDF time (~ 0.03 years). Figure 9.4 (c) illustrates CO₂ saturation and temperature results at OW2 ($r = 75$ m) at the different monitoring levels for the infinite-acting reservoir case. It is observed that CO₂ arrival time increases as the monitoring depth increases because of gravity segregation. CO₂ saturation at $z = 45$ m and $z = 35$ m decrease at $t = 0.87$ years and 3.12 years, respectively due to upward migration of CO₂. CO₂ migration increases the temperature at shallower monitoring depths slightly due to heat transfer by convection from lower zones with higher temperature to the upper zones with lower temperature. Figure 9.4 (d) illustrates the corresponding CO₂ saturation and temperature results for the closed reservoir case. It is obtained that temperature observations at all monitoring levels shift upward after warming front arrival, which indicates that BDF prevails.

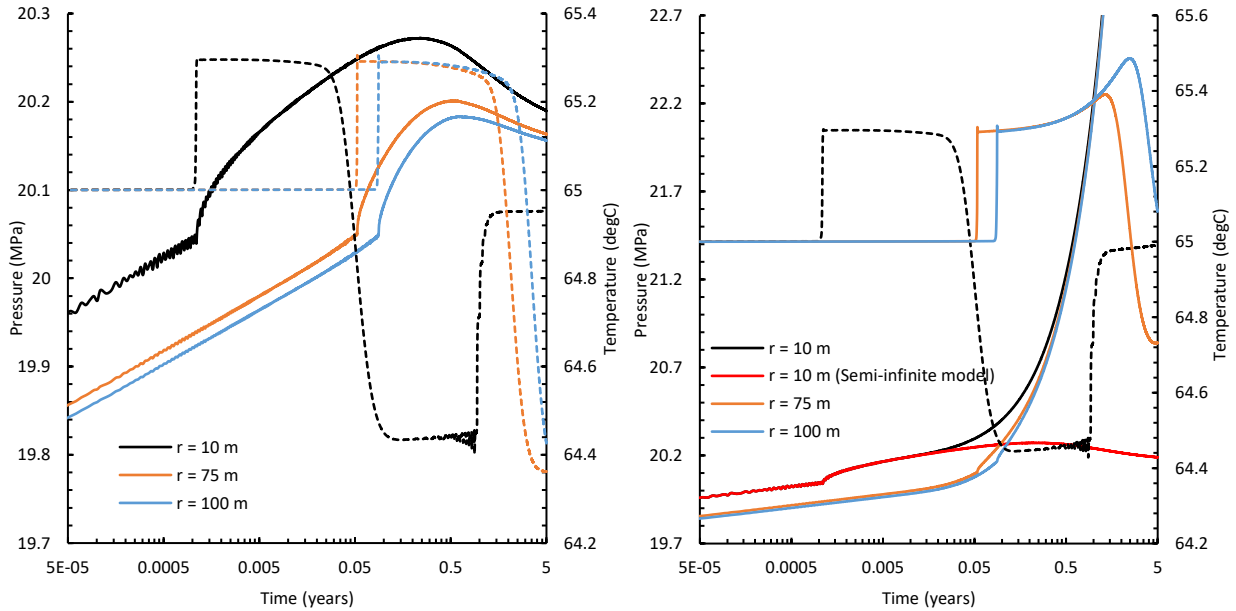


Figure 9. 3. Pressure and temperature measurements at the observation wells for an infinite-acting (left) and a closed reservoir case ($r_e = 5$ km) (right) at $z = 5$ m (solid line represents pressure and dashed line represents temperature).

The maximum temperature increase due to heat of dissolution and adiabatic compression effect is 0.5 °C at $z = 5$ m. CO_2 saturation results indicate that the effect of gravity segregation decreases during BDF conditions compared with the infinite-acting reservoir case. CO_2 saturation at $z = 45$ m for closed reservoir is 0.23 compared with 0.06 for infinite-acting reservoir case at $t = 5$ years. On the other hand, CO_2 saturation at $z = 35$ m increases monotonically for closed reservoir, while it decreases to 0.3 by the end of the injection period for semi-infinite acting reservoir case. The excessive increase of pressure during BDF period increases CO_2 density and consequently mitigates gravity segregation effect.

Figure 9.4 (e) illustrates CO_2 saturation and temperature results at OW3 ($r = 100$ m) at the different monitoring levels for infinite-acting reservoir case. At OW3, the effect of gravity segregation is more evident compared with OW2, as evidenced by the delay of CO_2 arrival at uppermost and lowermost levels (0.14 years) compared with OW2 (0.041 years). Figure 9.4 (f) illustrates the corresponding results for the closed-reservoir system. Temperature increase is more evident because of the excessive increase in reservoir pressure as well as the increased effect of gravity segregation. The maximum increase in reservoir temperature due to CO_2 dissolution and adiabatic compression effect is 0.7 °C at $z = 5$ m.

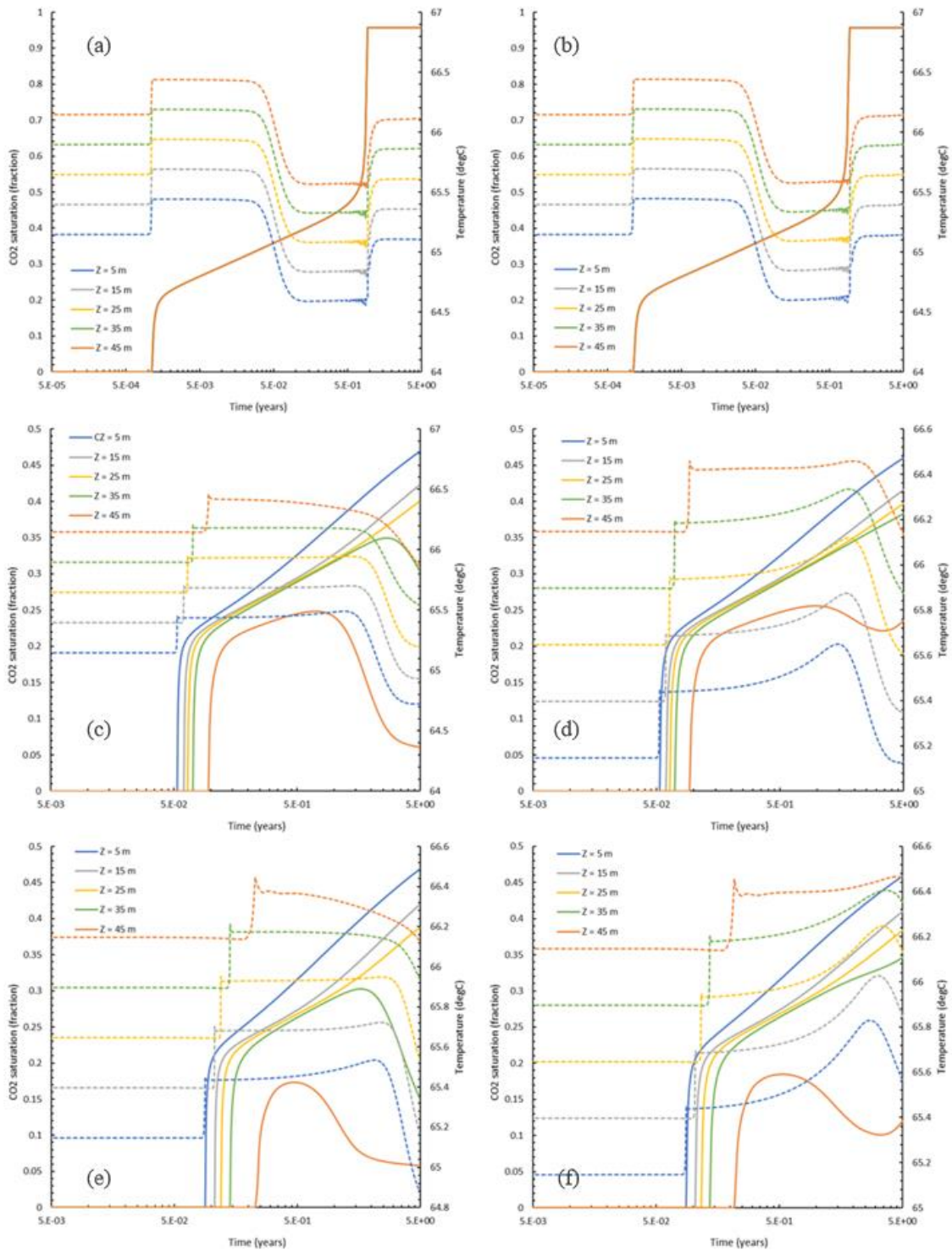


Figure 9. 4. Multilevel CO₂ saturation and temperature results for an infinite-acting (left) and a closed reservoir ($r_e = 5$ km) (right) model at OW1 (a - b), OW2 (c - d), and OW3 (e - f) (solid line represents CO₂ saturation and dashed line represents temperature) (OW = Observation well).

Fig 9.5 provides 2D illustration of CO₂ saturation evolution in the reservoir at $t = 0.5, 1, 2, 3, 4,$ and 5 years for an infinite-acting reservoir. Non-uniform CO₂ distribution over reservoir thickness is observed due to the buoyancy force that triggers upward flow of CO₂ to shallower

layers. At $t = 0.5$ years, the lateral extent of the CO₂ plume at the uppermost layer is ~300 m, while the lateral extent of the CO₂ plume at the lowermost layer is ~100 m. As CO₂ injection continues, the extent of the CO₂ plume at shallower layers increases, while it decreases at deeper layers because of upward migration of CO₂ located at deeper intervals. As CO₂ fills up the upper intervals, effective permeability of formation to gas flow at the upper regions of CO₂ plume enhances significantly (as shown in Figure 9.6) which provides preferential path for CO₂ located at the bottom of CO₂ plume to move upward rather than to migrate laterally. This explains why CO₂ saturation decreases after some time of start of injection at OW2 and OW3 at the deeper layers ($z = 35$ and 45 m), while it increases monotonically at the shallower ones (see also Figure 9.4 (left)). This behavior is especially important because it indicates that CO₂ residual trapping is not only active during the post-injection period but also during the injection period.

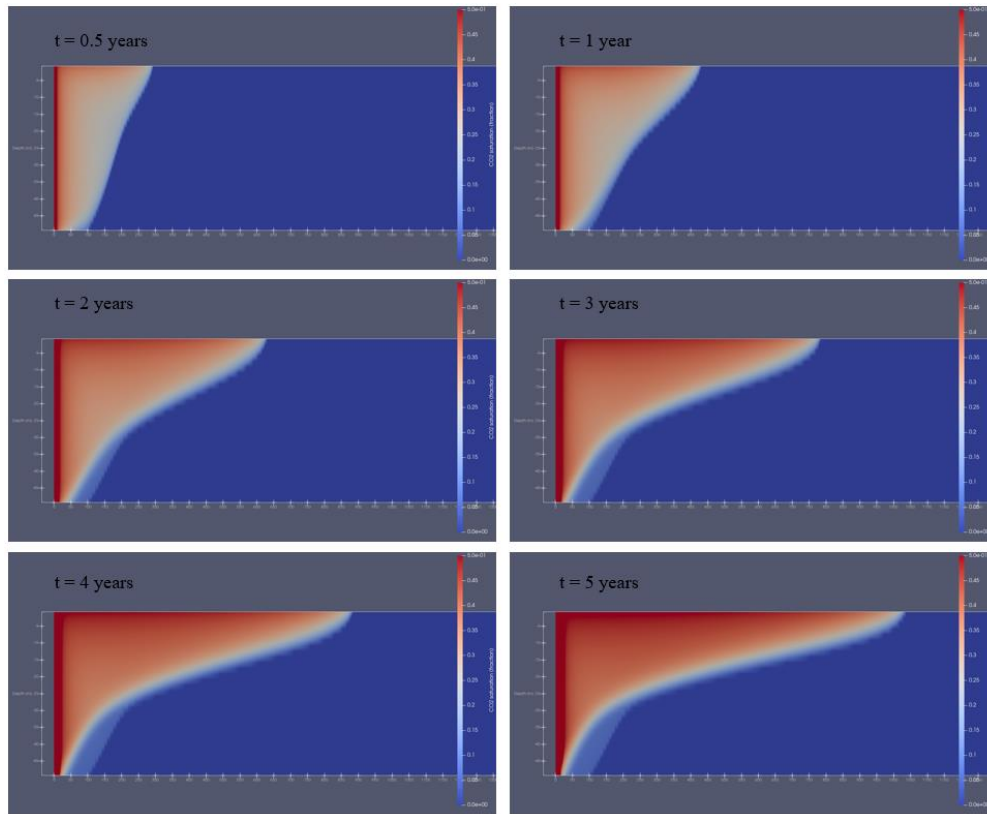


Figure 9. 5. CO₂ saturation evolution during CO₂ propagation in the reservoir (an infinite-acting reservoir).

In the following paragraphs, the effect of the injection rate on the temperature signal obtained at the observation wells during the boundary-dominated flow period and the infinite-acting flow period are investigated. Two different injection scenarios are considered in which the rate decreases stepwise in the first scenario, while it increases stepwise in the second scenario.

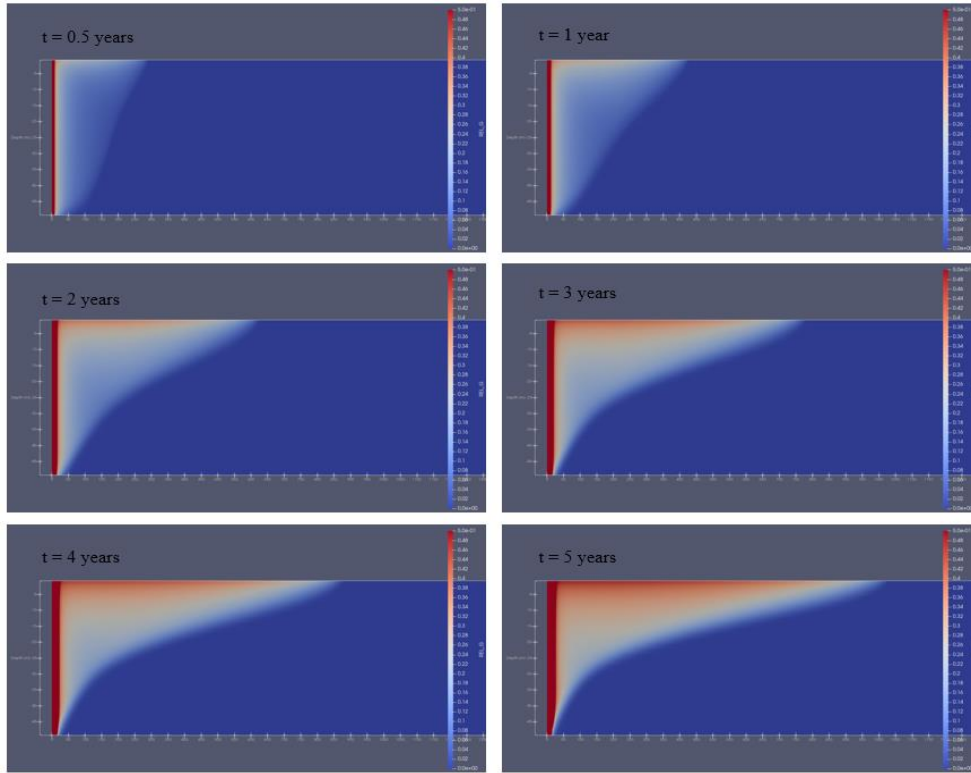


Figure 9. 6. Evolution of relative permeability to gas phase during CO₂ injection (an infinite-acting reservoir).

The cumulative volume injected after 5 years is identical for both cases and equals the cumulative injected volume for the constant rate scenario (1.576×10^6 Mt). Figure 9.7 (a) illustrates well injection rate, pressure, and temperature results at OW3 (at $r = 100$ m and $z = 5$ m) in a closed reservoir ($r_e = 5$ km) for the case of increasing injection rate scenario. The arrival time of the front is 0.06 years, which is higher than the BDF time ($= 0.03$ years). As the injection rate decreases from 16 kg/s to 4 kg/s, the pressure exhibits slight decrease at the time the rate changes. Additionally, the rate of pressure buildup decreases toward the end of injection period. The arrival time of the CO₂ front is associated with a jump in temperature by 0.4 °C at 0.06 years. The temperature results indicate that the reservoir is under boundary-dominated flow conditions due to the gradual increase in the temperature after the initial increase when the warming front arrives. As the injection rate decreases, the temperature exhibits a slight decrease at the time of rate change due to adiabatic expansion of the flowing CO₂. Additionally, it is observed that temperature shifts downward following pressure behavior after CO₂ arrival and before the ultimate reduction due to water vaporization. The maximum increase in temperature is ~ 0.7 °C and it occurs at $t = \sim 2$ years.

Figure 9.7 (b) illustrates well injection rate, pressure, and temperature results at OW3 for the increasing injection rate scenario. In this case, the arrival time is longer (0.26 years) compared with the decreasing injection rate scenario because the injection rate maintained before CO₂ arrival time is the lowest rate ($= 4$ kg/s). As the injection rate increases, the rate of the pressure buildup increases. After the arrival of the warming front, a gradual increase in temperature from 0.15 years up to 3.14 years indicates that boundary conditions dominate the

flow behavior in the aquifer. Unlike the decreasing rate scenario, temperature shifts upward following the pressure behavior after CO₂ arrival and before the ultimate reduction due to water vaporization. The maximum temperature change of ~0.7 °C occurs late at $t = 4$ years.

Figure 9.7 (c) illustrates the pressure and temperature history at OW3 for the decreasing rate scenario, assuming an infinite-acting reservoir model. The pressure behavior at the observation point follows the injection rate history. Pressure decreases in a stepwise manner as the injection rate decreases. On the other hand, the temperature behavior is not sensitive to the injection rate history because the rate of pressure buildup is small compared with the closed reservoir case. The pressure buildup by the end of the injection period is 0.45 MPa compared with 9.6 MPa for closed reservoir case. Figure 9.7 (d) illustrates the pressure and temperature history at OW3 for the increasing injection rate scenario assuming an infinite-acting reservoir model. In this case, pressure increases stepwise as the injection rate increases. The temperature behavior is not different from that depicted in Figure 9.7 (c) which indicates that temperature behavior is not sensitive to injection history for infinite-acting reservoir case compared with closed reservoir case. However, the results for both closed and infinite acting systems indicate that temperature is only slightly sensitive to rate variations. This is unlike pressure, which is strongly sensitive to rate variations and therefore its analysis requires accurate knowledge of the rate history.

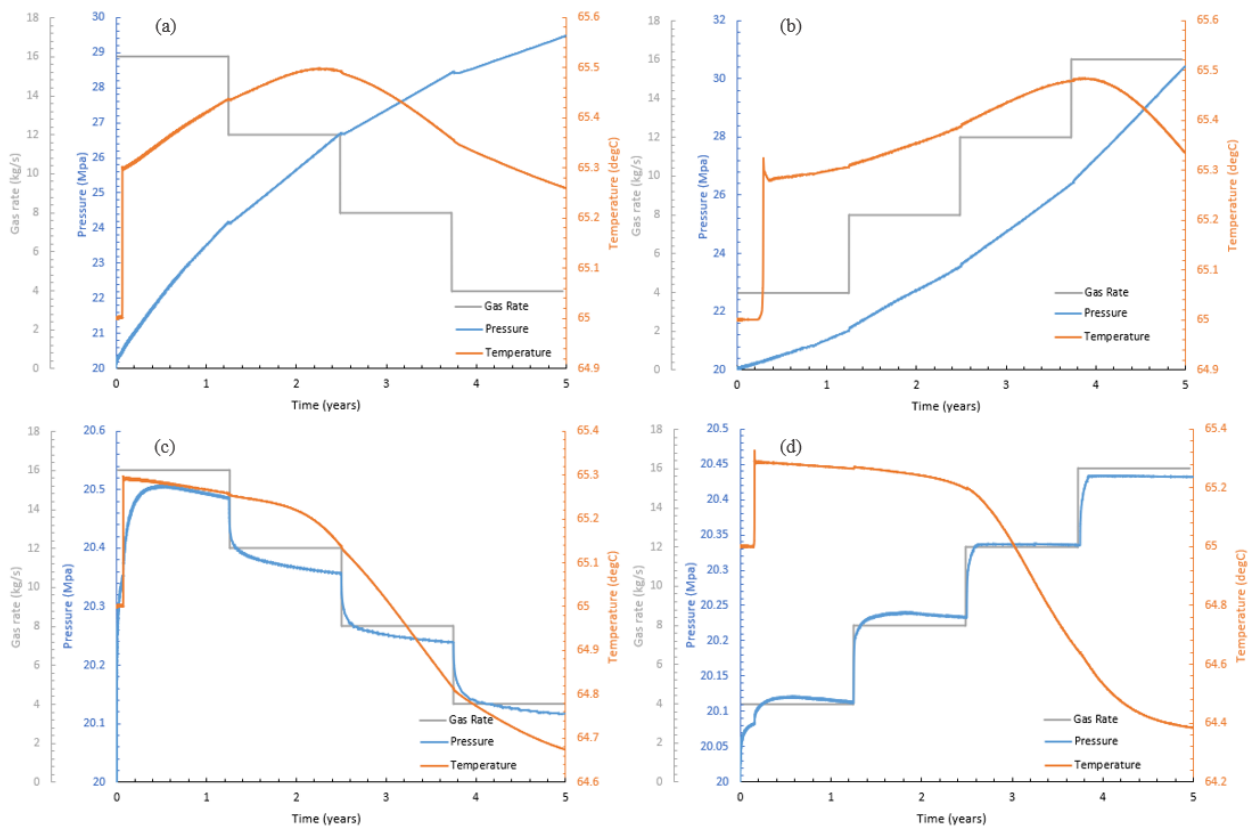


Figure 9. 7. CO₂ injection rate, pressure, and temperature at OW3 ($r = 100$ m) and $z = 5$ m for a closed reservoir (a and b) and an infinite-acting reservoir (c and d) case.

Finally, the sensitivity of the temperature signal to the location of the temperature monitoring sensor (such as a DTS cable) is investigated. Two scenarios are presented for the possible locations of the temperature monitoring tool. In the first scenario, the temperature monitoring tool is cemented behind the casing, while in the second scenario, the cable or the discrete sensors are located inside the wellbore. To model fluid flow inside the wellbore during CO₂ plume propagation, a coupled wellbore-reservoir system is modeled using T2Well/ECO2N simulation tool. The monitoring wells have a diameter of 0.2 m, and they are completed over the entire thickness of the reservoir (50 m). The upper section of the wellbore system (from caprock to the ground surface) is not considered in this case meaning that the modeled well is plugged at the bottomhole. Figure 9.8 (a) shows the temperature evolution at OW1 during CO₂ plume propagation when the temperature tool is located inside wellbore (shown in solid line) and outside wellbore (shown in dash line) at different levels ($z = 5, 15, 25, 35,$ and 45 m) for the infinite-acting reservoir case.

Figure 9.8 (a) shows a sixfold increase in the magnitude of the temperature signal due to CO₂ dissolution when temperature is obtained inside the wellbore. The observed temperatures at $z = 5, 15, 25, 35,$ and 45 m are $67, 67.2, 67.4, 67.7,$ and 67.9 °C inside the wellbore, compared with $65.5, 65.7, 65.9, 66.2,$ and 66.4 °C behind the casing.

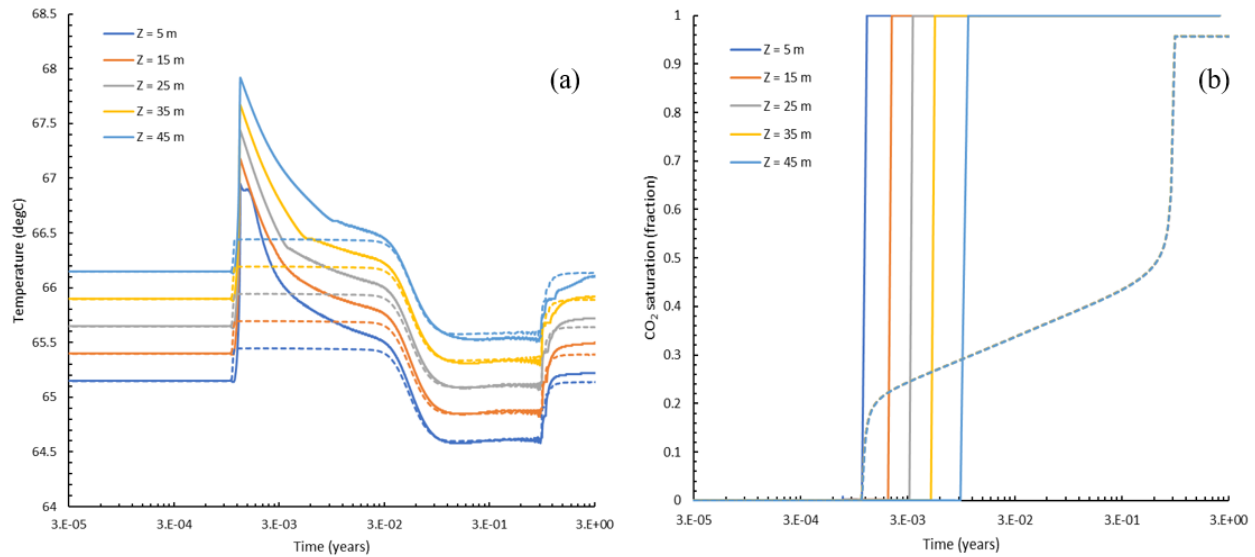


Figure 9. 8. Temperature and saturation results obtained at OW1 at different levels inside the wellbore (solid lines) and behind the casing (dash lines) using an infinite-acting reservoir model (OW = Observation well).

The excessive increase in the heat of dissolution inside the wellbore is attributed to the larger mass of the brine inside the wellbore that is available for dissolution compared with the surrounding porous media. This observation is in line with Jayne et al. (2019) study, which shows that higher dissolution heating is obtained as the porosity of the formation increases. The wellbore can be imagined as a porous media with 100 percent porosity. Consequently, larger dissolution heating is expected inside the wellbore compared with the surrounding formation, which has a porosity of 12 percent. After the initial dissolution heating, the temperature of the wellbore decreases to the temperature of the surrounding formation due to heat conduction

effect. Figure 9.8 (b) shows CO₂ saturation inside the wellbore (shown in solid line) compared with CO₂ saturation in the surrounding formation (shown in dashed line). As CO₂ gets inside the wellbore, it migrates upward due to the effect of buoyancy and fills up the shallower intervals of the wellbore. It takes 3 days for the completed interval of wellbore (50 m) to be fully saturated with CO₂.

To further support our explanation for the increase in temperature signal inside the wellbore, we investigated the effect of porosity on CO₂ dissolution heating. Three cases are presented for different formation porosity (0.1, 0.2, and 0.3) and the corresponding temperature signals are illustrated in Figure 9.9. It is evident that as the porosity increases from 0.1 to 0.3, the effect of dissolution heating increases from 0.3 °C to 0.7 °C. This indicates why a big difference in the temperature results is obtained when temperature is monitored inside the wellbore, which has a higher mass of brine compared with the pores of the surrounding formation. On the other hand, excessive delay of CO₂ plume arrival is obtained for the formation of higher porosity because it has higher storage capacity that the CO₂ has to occupy compared to those of lower porosity. Based on these findings, it is more feasible and practical to monitor the warming front that associates the CO₂ plume by measuring the temperature signal inside the wellbore rather than behind the casing.

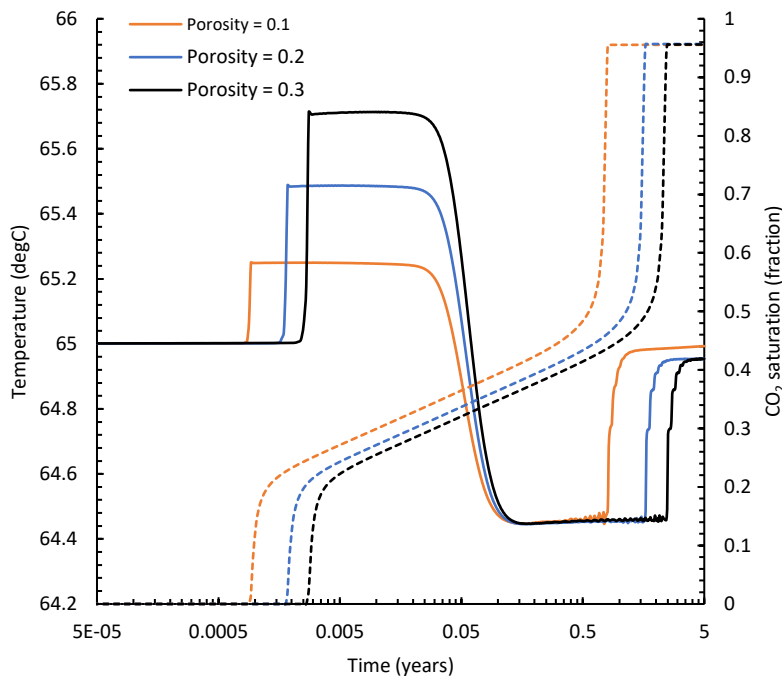


Figure 9. 9. Temperature and saturation results obtained at OW1 at $z = 5$ m in an infinite-acting reservoir with different formation porosity. Temperature results are shown in solid lines, while the saturation results are shown in dashed lines (OW = Observation well).

9.2. Monitoring CO₂ Migration Through Improperly Abandoned Wells

Improperly abandoned wells are considered a potential pathway for CO₂ leakage from storage aquifers. CO₂ leakage from storage aquifers not only decreases the effectiveness of storage efficiency but also poses human health risks associated with groundwater contamination. In this work, a fully developed wellbore-reservoir system is adopted to model pressure, temperature, and CO₂ saturation evolution inside an abandoned well during CO₂ migration. This study is presented for two scenarios: open and closed wellbore at the surface. In both cases, the wellbore is assumed to be fully communicated with the storage aquifer. The simulation tool that is used is T2Well/ECO2 which is a numerical simulator for non-isothermal, multiphase, and multicomponent fluid flow in an integrated wellbore-reservoir system (Pan and Oldenburg 2014). This model extends the numerical reservoir simulator TOUGH2, to model the fluid flow in both the wellbore and the reservoir. The fully coupled wellbore-reservoir system includes two different subdomains: wellbore and reservoir. Fluid flow inside the reservoir domain is modeled using the multiphase Darcy equation, while fluid flow in the wellbore domain is modeled using 1D two-phase momentum equation. The momentum balance equation for two-phase flow in the wellbore is solved using the Drift Flux Model (DFM) (Zuber and Findlay 1965, Wallis 2020), while the governing equations for fluid and heat flow in the porous media are solved using an integral finite difference approach. The objective of this study is to investigate the feasibility of using surface pressure and temperature measurements to detect CO₂ migration in improperly abandoned wells.

9.2.1. Conceptual Model

The conceptual model consists of a deep CO₂ storage aquifer with a thickness of 100 m which is located 1 km below the ground surface. Depth of the storage aquifer should be deeper than 800 m to ensure that the injected CO₂ is maintained at a supercritical state to increase the storage capacity of the reservoir to the injected CO₂. The storage reservoir is overlain by an impermeable stratum (cap rock) that extends from the depth of 1000 m to 900 m to ensure the containment of CO₂ in the storage reservoir. The cap rock is overlain by an overburden stratum from the depth of 900 m to the ground surface. Two wells are specified in the model; the first well is an injection well which is completed through the entire thickness of the storage aquifer, while the abandoned well is located 75 m away from the injection well.

The conceptual model is 3D Cartesian model that constitutes (40×40×11) grid cells with logarithmic discretization of the grid cells in the XY-plane and uniform discretization in the vertical direction (see Fig. 9.11). The areal extension of the model in the XY-plane (horizontal plane) is 5 km in X-direction and 5 km in Y-direction. The volume of the outermost grid cells in the storage reservoir in the lateral plane is multiplied by a large factor (1×10^{50}) to simulate Dirichlet conditions at the outer boundaries of the reservoir. For the initial reservoir conditions, initial pressure and temperature are estimated using $p = 1 + 0.1z$ and $T = 35 + 0.025z$, respectively, with p in bars, T in degrees C, and z in meters (Doughty 2008). The salinity of the brine is 0.15 weight fraction in the storage reservoir, while it is zero in the above formations. Initial CO₂ saturation is zero in all formations of the model. To account for the interfering effects of the CO₂ and the brine occupying the same pore space, Corey's model (Corey 1954) and van Genuchten's model (van Genuchten 1980) described by Eq. 9.1 – 9.3 are used to evaluate the relative

permeability and capillary pressure, respectively. The system configurations and parameters used in the simulation are summarized in Tables 9.2 and 9.3 (Pan and Oldenburg (2014)). All the layers in the model are assumed to have thermal conductivity of 2.51 W/ (m °C) and specific heat capacity of 920 J / (kg °C). CO₂ is injected at a constant injection rate of (50 kg / s – 1.578E6 Mt/y) with bottomhole temperature of 61.25 °C. Injection temperature is set equal to the initial reservoir temperature to isolate the anthropogenic contribution of the injected CO₂ to temperature evolution.

Table 9. 2. Reservoir properties of the simulation study.

Layer	Depth (m)	Porosity	Lateral permeability (m ²)	Vertical permeability (m ²)
Reservoir	1100 - 1000	0.12	10 ⁻¹³	10 ⁻¹³
Cap rock	1000 - 900	0.05	10 ⁻¹⁸	10 ⁻¹⁸
Overburden	900 - 0	0.12	10 ⁻¹³	10 ⁻¹³
Relative permeability parameters		λ	0.457	-
		S _{lr}	0.3	fraction
		S _{is}	1	fraction
		S _{gr}	0.05	fraction
Capillary pressure parameters		λ	0.457	-
		S _{lr}	0.0	fraction
		P _o	0.01961	MPa
		S _{is}	0.999	fraction

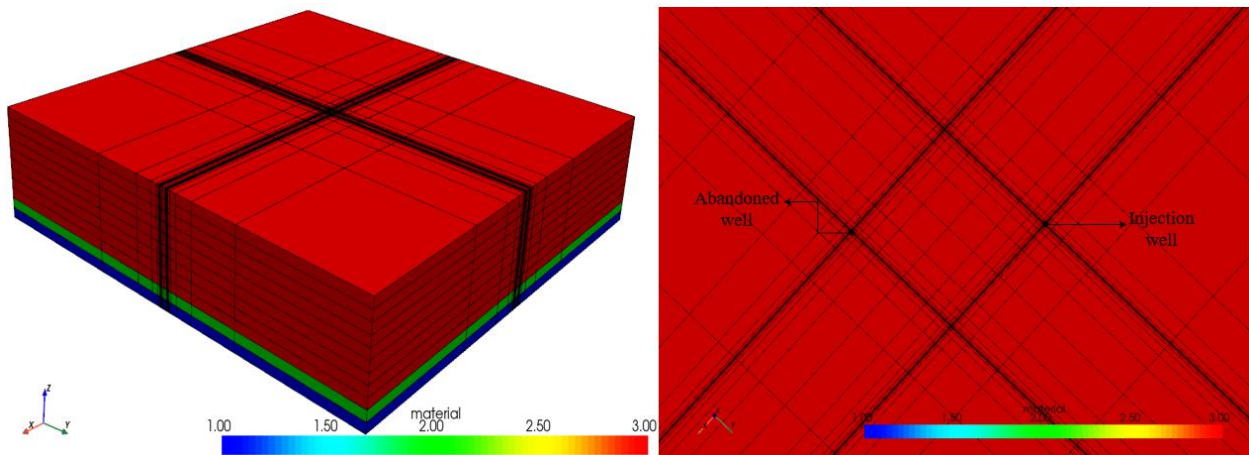


Figure 9. 10. Schematic illustration of the conceptual model showing the locations of injection and abandoned wells.

Table 9. 3. Well properties of the simulation study.

Feature	Value
Well length	1100 m (from 0 m – 1100 m)
Perforation	100 m (from 1000 m – 1100 m)
Well radius	0.1 m
Maximum C_o	1.2
Roughness	0.000046 m

9.2.2. Open Wellbore

In this case, abandoned well is open at the surface. Fig. 9.12 shows CO₂ plume propagation in the storage reservoir during CO₂ injection at $t = 1, 5, 10,$ and 20 days. As illustrated in Fig. 9.12, CO₂ distribution in the aquifer is characterized by three regions: the first region is the dry-out region which immediately surrounds the injection well and it is characterized by single phase CO₂ flow. In the dry-out region, interstitial water vaporizes into the flowing CO₂ stream and dissolved salt precipitates in the porous medium. The second region is the two-phase region, which extends from the outer radius of the dry-out region to the plume front. In this region, both CO₂ and brine are flowing at different mobilities following the saturation distribution. The third region is the single-phase brine region, which is located ahead of the CO₂ plume in which the formation is fully saturated with the in-situ brine. CO₂ plume reaches the abandoned well, which is located 75 m away from the injection well, after 10 days from the start of CO₂ injection. Fig. 9.13 shows pressure disturbance in the storage reservoir during CO₂ injection. Pressure increment is the highest at the injection well and decreases progressively away from the injection spot. The pressure increment at the injection well is 5.14 MPa after 23 days from the start of CO₂ injection. The effect of salt deposition on pressure buildup is not considered in our model because we are interested in the conditions at the abandoned well.

Fig. 9.14 shows mass flow rate and velocity of leaking fluids inside the abandoned well during CO₂ plume propagation in the reservoir. Mass flow rate of brine inside the wellbore increases progressively at early time and reaches to ~20 kg/s at $t = 10$ days before CO₂ plume reaches the abandoned well. As CO₂ propagates inside the reservoir, CO₂ displaces brine toward the abandoned well and induces a pressure increment throughout the storage reservoir, which derive brine flow through the abandoned well to the surface. At the onset of CO₂ arrival, a sharp peak of brine mass flow rate (32 kg/s) is depicted inside the wellbore due to the loss of water cap. After CO₂ arrival, CO₂ expands and pushes brine located inside the wellbore upward, which results in the sharp peak of brine mass flow rate. This observation is in line with field observations of CO₂-driven geysers at abandoned oil and gas holes at the ground surface (Han et al. 2013). Afterwards, brine mass flow rate decreases progressively to 7 kg/s at $t = 20$ days as it

is replaced by the migrating CO₂. On the other hand, CO₂ mass flow rate increase progressively throughout the abandoned well after CO₂ arrival and reaches up to 14 kg/s at $t = 20$ days.

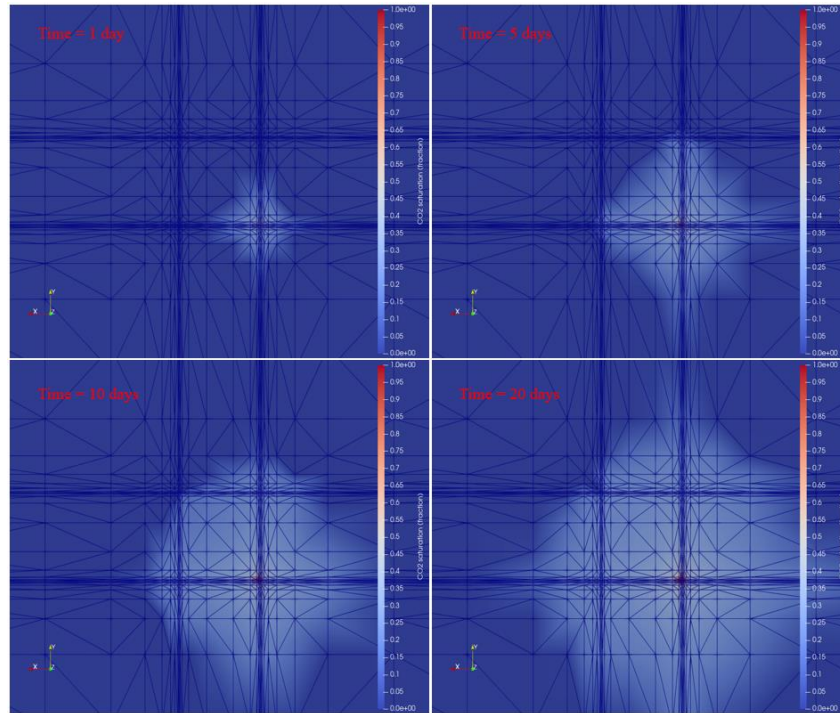


Figure 9. 11. CO₂ plume propagation in the storage aquifer at $t = 1, 5, 10,$ and 15 days.

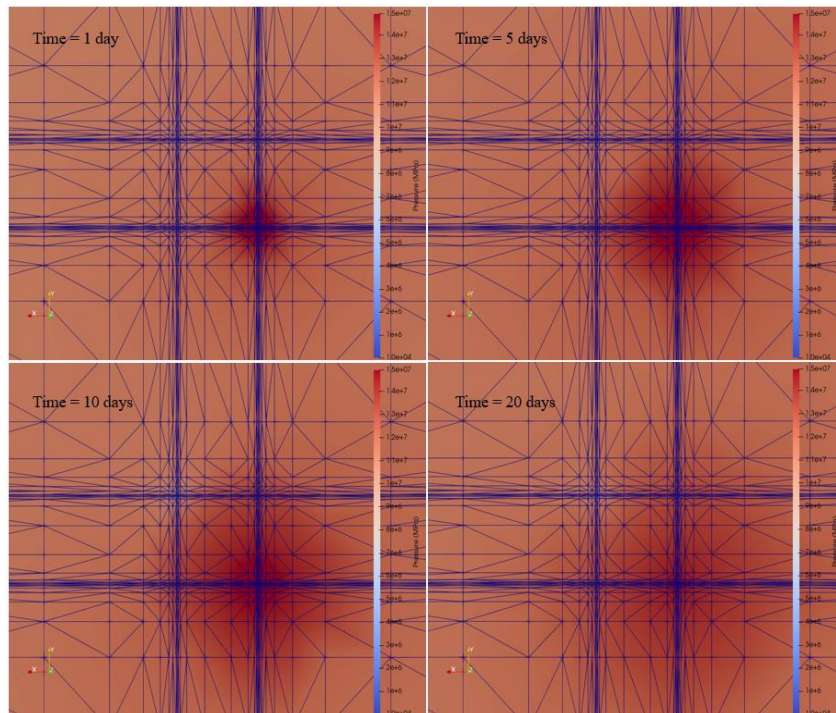


Figure 9. 12. Pressure evolution in the storage aquifer at $t = 1, 5, 10,$ and 15 days.

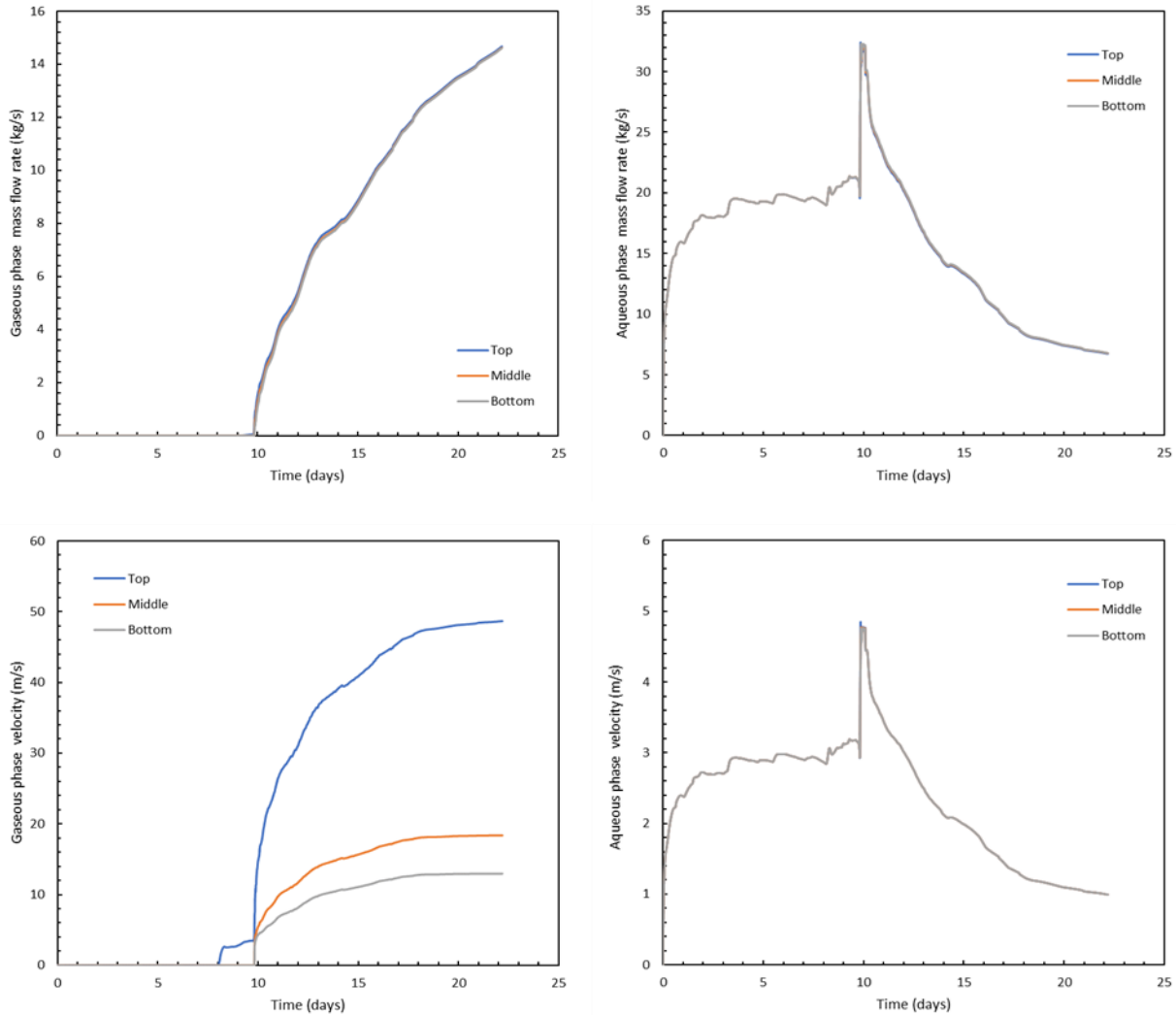


Figure 9. 13. Gas mass flow rate, liquid mass flow rate, gas velocity, and liquid velocity in the abandoned wellbore at different depths (open wellbore case).

Slight increase in the mass flow rate of CO₂ is depicted at shallower intervals because of CO₂ liberation (exsolution) from the CO₂-saturated brine as the CO₂-saturated brine migrates upward through the wellbore. CO₂ evolves and accelerates as it flows upward inside the abandoned well due to phase change of CO₂ from the supercritical state to the gaseous state as well as the expansion of gaseous CO₂ at shallower intervals. On the other hand, liquid velocity is uniform along the wellbore because the variation in liquid density is negligible through the wellbore. An early increase in CO₂ velocity at shallower intervals of the abandoned well is depicted before free phase CO₂ arrival at the bottom of the abandoned well. This is attributed to liberation of dissolved CO₂ from CO₂-saturated brine, which moves ahead of the CO₂ plume as it migrates upward in the abandoned well to the surface.

Fig. 9.15 illustrates pressure, temperature, CO₂ saturation, and CO₂ solubility in the wellbore for a longer simulation time ($t = 23$ days). Before CO₂ arrival, temperature increases

from the prevailing geothermal temperature to the reservoir temperature (61.25 °C) due to the upward flow of the brine from the aquifer to the wellbore. After CO₂ arrival, CO₂ expands significantly as it moves upward through the wellbore. As CO₂ flows upward, CO₂ saturation increases due to phase change of CO₂ from the supercritical state to the gaseous state, expansion of gaseous CO₂, and exsolution of dissolved CO₂ from CO₂ saturated brine phase. On the other hand, pressure decreases significantly at the bottom of the wellbore because of the reduction in the hydrostatic pressure inside the wellbore as brine is replaced by the migrated CO₂. The maximum reduction in wellbore pressure is located at well bottom (~ 4.73 MPa) and the magnitude of the pressure reduction decreases at shallower depths. As CO₂ moves upward through the wellbore, temperature decreases significantly due JT expansion of CO₂, phase change of CO₂ from supercritical state to gaseous state as pressure decreases below 7.4 MPa (critical pressure of CO₂), and the endothermic exsolution of CO₂ from brine. At the bottom of the well, temperature decreases from 61.25 °C before CO₂ arrival to 30 °C after CO₂ arrival.

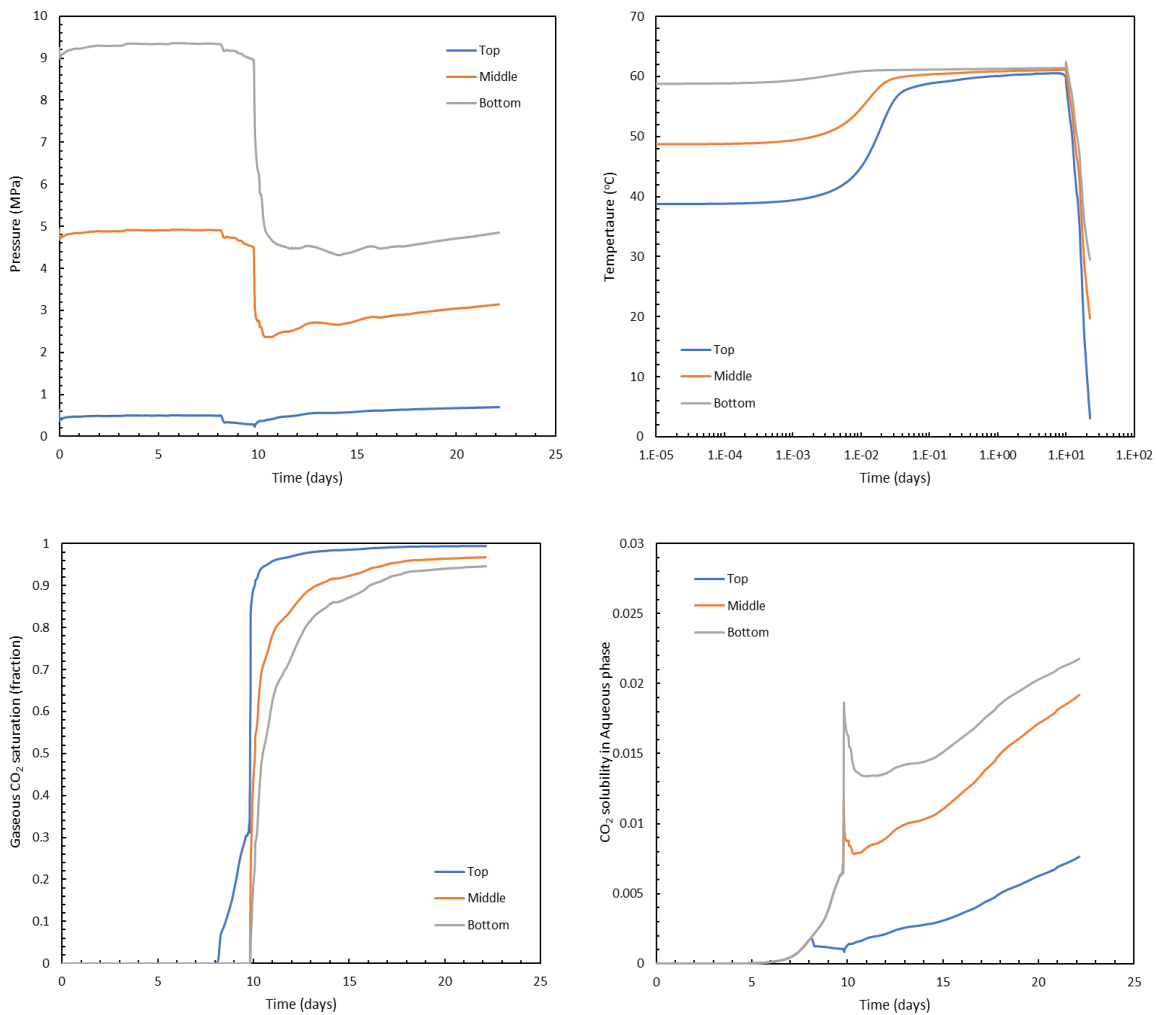


Figure 9. 14. (a) Pressure (MPa), (b) temperature (°C), (c) CO₂ saturation (fraction), and (d) CO₂ solubility in brine (mass fraction) in the wellbore for total simulation time of 28 days at different depths (open wellbore).

Temperature at the surface decreases down to very low temperature ~ 3 °C before simulation terminates. Simulation cannot run for longer time; otherwise, wellhead temperature decreases below the minimum limit of the EOS tool implemented ECO2N. The lower temperature limit of the EOS in ECO2N is 3.04 °C, so it is expected for temperature to decrease further as simulation time increases. The excessive cooling at the wellhead triggers water freezing and/or formation of gas hydrate, which agrees with field observations (Han et al. 2013). Temperature at the bottom of the wellbore shows a small but sharp spike at breakthrough time because of CO₂ dissolution. On the other hand, CO₂ solubility exhibits sharp increase after CO₂ arrival because of the intrusion of CO₂-saturated brine in the wellbore, which is located ahead of the CO₂ front. After CO₂ arrival, CO₂ solubility increases gradually with time because of the excessive cooling of temperature inside the wellbore. CO₂ solubility decreases as fluid flows upward because of exsolution of dissolved CO₂ from the aqueous phase as pressure decreases at shallower depths as indicated before.

9.2.3. Closed Wellbore

In this case, another scenario is investigated in which the abandoned well is closed at the surface and no flow out of the wellbore is allowed. To imply the new change, the top of the wellbore is overlain by an impermeable formation with properties identical to the properties of the caprock layer given in Table 9.2.

Fig. 9.16 shows the mass flow rates for the gaseous phase (CO₂) and liquid phase (brine) inside the wellbore at different depths. Since the wellhead is closed, flow rate inside the wellbore is negligible except at the instant of CO₂ arrival. As the CO₂ plume reaches the well bottom, CO₂ goes upward by the effect of buoyancy because the density of CO₂ is lower than the density of brine. Consequently, a short-time countercurrent flow prevails in which the light phase (CO₂) goes upward (positive mass flow rate), while the dense aqueous phase goes downward (negative mass flow rate). After CO₂ arrival, fluid flow inside the wellbore diminishes when the aqueous phase is displaced out of the wellbore, which occurs 2 days after the CO₂ plume reaches the abandoned well. Relatively longer time is required for CO₂ to fill-up the wellbore compared with open wellbore case because mass flow rate is smaller for closed wellbore conditions. Fig. 9.16 indicates that gas flux from the formation proceeds, and CO₂ continues to migrate upward to the top and the middle of the wellbore even after the upper section of the wellbore is completely filled with CO₂. This happens because the increase in formation pressure at the bottom of the wellbore as the CO₂ plume propagates deeper in the reservoir drives CO₂ flow to the abandoned well. The continuous flux of CO₂ increases pressure slightly at the top and middle of the wellbore which is evident as a slight increase of pressure after the initial increase at the instant of CO₂ arrival (see Fig. 9.17 (a)).

Since the magnitude of the mass flow rate inside wellbore is very small compared with the open wellbore scenario, the contribution of natural convection to heat transfer inside the wellbore is negligible. Even if the upward migrating CO₂ transfers heat from the deeper and warmer regions of the wellbore to the shallower sections, it is competed by the countercurrent flow of cold brine from the shallower and cooler regions of the wellbore to the deeper regions, as will be clarified later. Fig. 9.17 shows pressure, temperature, CO₂ saturation, and CO₂ solubility in the brine inside the wellbore during CO₂ migration. Interestingly, as CO₂ fills up the wellbore and displaces the brine outside, pressure increases significantly inside the wellbore. Additionally,

the increment in wellbore pressure is the highest at shallower depths. This phenomenon is analogous to the phenomenon of gas kick percolation inside a drilling well while the well is closed and full of drilling fluid (Grace 2017). Since the wellbore is a closed system and the CO₂ influx is not allowed to expand, the intruding CO₂ maintains the high pressure of the storage formation as it migrates upward. As the CO₂ goes upward with the high pressure, the surface pressure of the abandoned well increases because of the decrease of the column of wellbore fluid above the percolating CO₂.

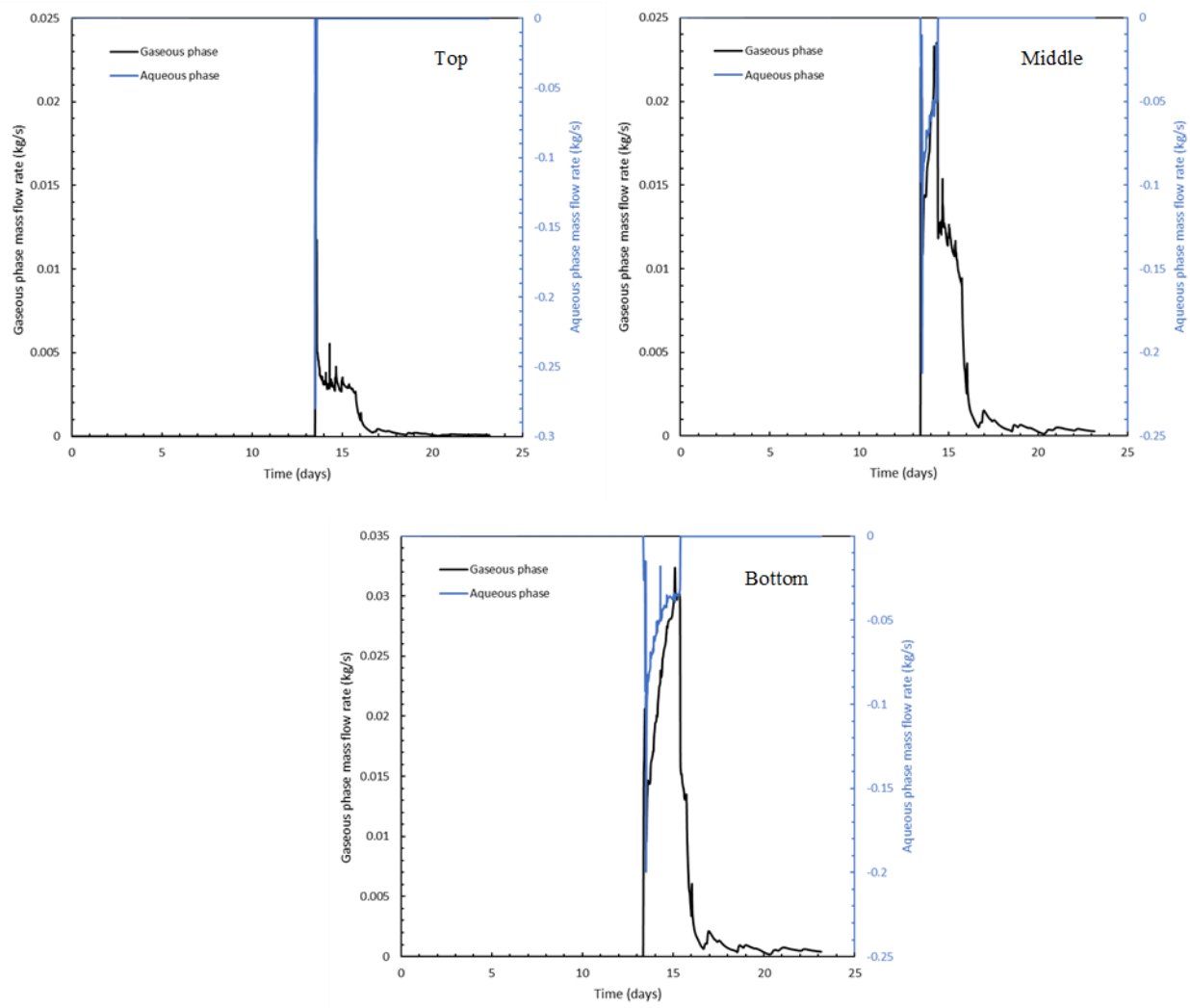


Figure 9. 15. CO₂ and brine mass flow rate in the abandoned well showing a counter flow at the CO₂ arrival time (closed wellbore case).

On the other hand, the pressure of wellbore below the migrating CO₂ increases because of the increase of wellbore fluid column below the CO₂ flux. This effect results in an excessive increase in pressure everywhere inside the wellbore. The magnitude of the pressure increase at the wellhead of the abandoned well is 5.75 MPa after CO₂ arrival. The excessive and sudden increase in wellhead pressure can easily be monitored to identify CO₂ arrival at the abandoned

well, which in turn provides a feasible technique to track CO₂ plume migration inside the storage reservoir.

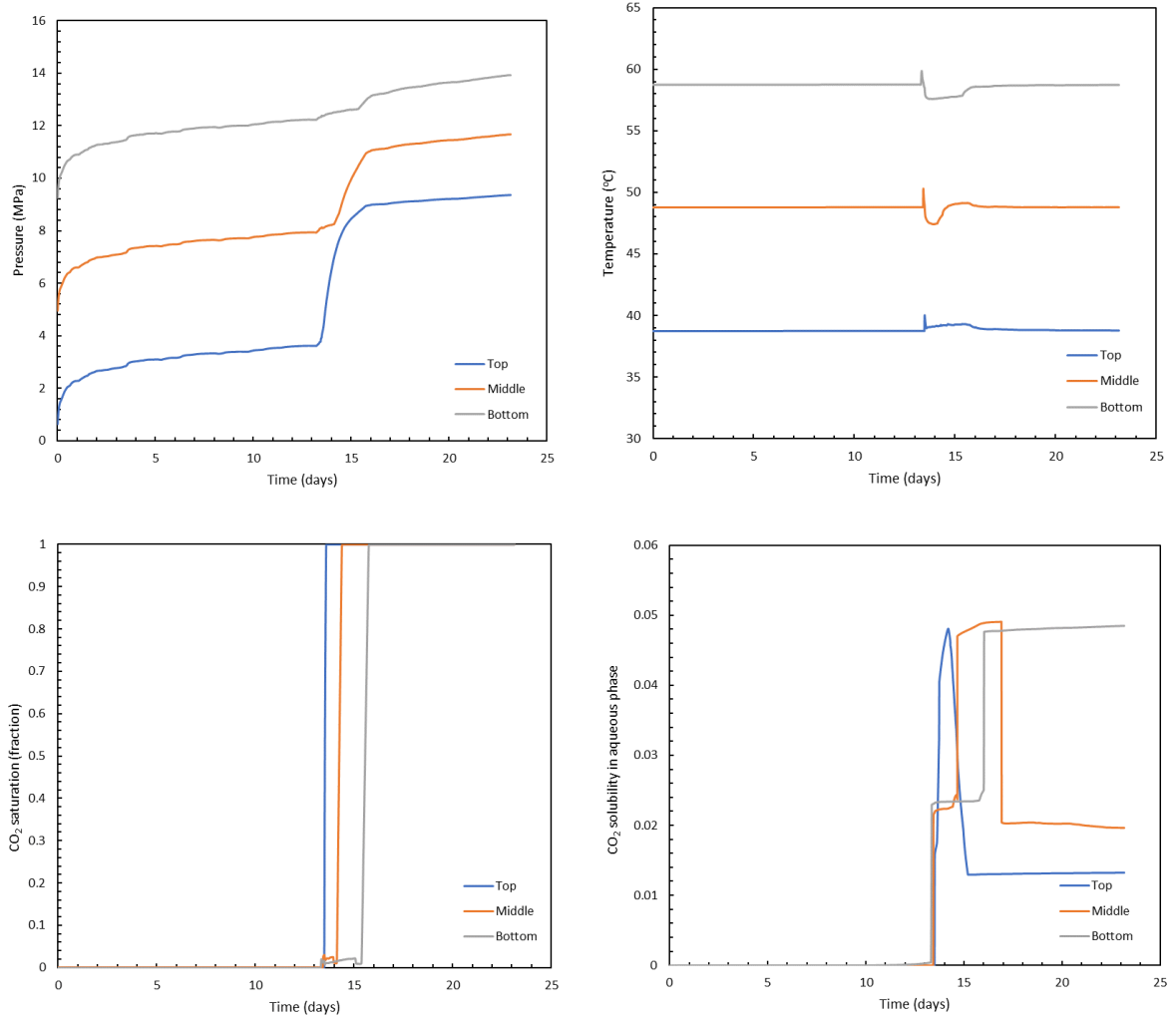


Figure 9. 16. (a) Pressure (MPa), (b) temperature (°C), (c) CO₂ saturation (fraction), and (d) CO₂ solubility in brine (mass fraction) in the abandoned well at different depths (closed wellbore).

To clarify this phenomenon further, Fig. 9.18 shows a schematic illustration of pressure evolution inside the wellbore during CO₂ migration through the abandoned well. The pressure at wellhead of the abandoned well is equivalent to the pressure at the top of CO₂ influx minus the hydrostatic pressure of fluid column above the CO₂ influx. As the CO₂ influx goes upward due to the effect of buoyancy, pressure at wellhead increases because of the reduction of the column of fluid above CO₂ influx. On the other hand, the pressure inside wellbore immediately above the formation equals the pressure at the bottom of CO₂ influx plus the hydrostatic pressure of fluid column below the CO₂ influx. As CO₂ influx goes upward, the pressure at the bottom of wellbore increases because of the increase of the fluid column below the CO₂ influx. Accordingly, excessive increase of pressure exists everywhere in wellbore after CO₂ breakthrough up to the time at which wellbore is filled with CO₂.

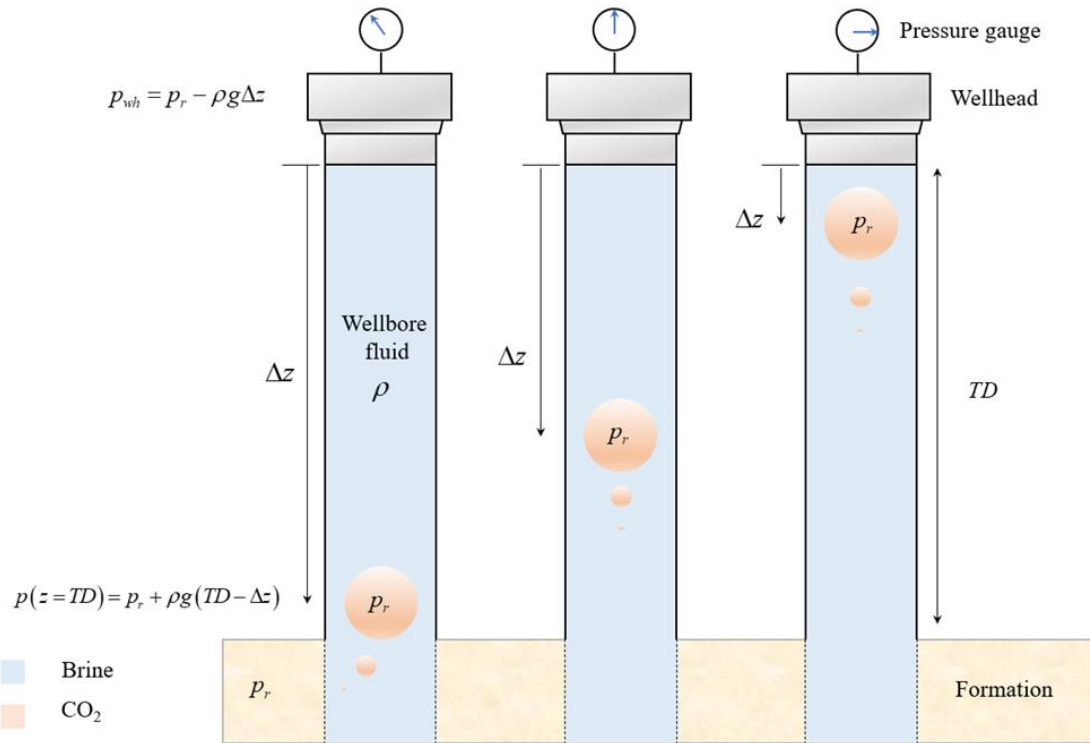


Figure 9. 17. Pressure evolution inside the wellbore during CO₂ migration in a closed abandoned well.

On the other hand, the disturbance of wellbore temperature is minor because no expansion of migrating CO₂ is allowable inside the closed wellbore. The slight disturbance of temperature at the time of CO₂ arrival is attributed to the countercurrent flow of the percolating CO₂ and the displaced brine. At the wellhead, slight increase in temperature is evident because of the upward flowing of warm CO₂ from the deeper regions. On the other hand, at the bottom of the wellbore, a slight decrease in temperature is evident, which is attributed to the downward flow of the cooled brine from the upper regions of the wellbore. At the middle of the wellbore, a combination of cooling and heating is attributed to the countercurrent flow of the cooled brine and warm CO₂. When CO₂ flux from the formation stops, the temperature disturbance created by natural convection diminishes and heat conduction with the surrounding formation dominates heat transfer in the wellbore. CO₂ solubility shows nonphysical values after CO₂ arrival, which is expected to be zero as brine is displaced out of the wellbore. This can be a pitfall of numerical simulation which, usually happens when the aqueous phase disappears or vaporizes.

Based on this study, CO₂ migration through open abandoned wells is associated with significant evolutions in pressure and temperature inside the wellbore. Accordingly, pressure and temperature monitoring at the wellhead of the abandoned well can be used to identify CO₂ migration. In the case of a closed abandoned well, an immediate and significant evolution of pressure is evident inside the wellbore during CO₂ migration. However, temperature fluctuation is negligible compared with open wellbore cases. Consequently, monitoring pressure changes at the wellhead can provide reliable indication of CO₂ migration in this case.

Chapter 10. Conclusions and Recommendations

10.1. Temperature Warmback Analysis for Estimating Injection Profile in Vertical Injection Wells

In section 3.1, an analytical solution for transient temperature in a reservoir during a warmback period that follows a cold fluid injection via vertical injection well is presented. The solution is developed through solving heat transport equation for the reservoir during the injection and shut-in periods using Hankel transformation. The obtained solution for sandface temperature is a function of shut-in time ratio ($= t_{inj} + \Delta t / \Delta t$) and Péclet number $= (q\rho_f C_f / 2\pi h\lambda_r)$. Péclet number quantifies the ratio of heat transfer via advection to heat transfer via conduction, which in turn is a function of injection rate. The obtained sandface temperature solution is casted into simple graphical techniques for estimating injection rate per zone. The first graphical technique implies plotting normalized sandface temperature at the injection zone versus shut-in time ratio on a log-log scale and identify the data to be fitted with a straight line. The slope of the fitted line is equivalent to $1/2$ of Péclet number. Consequently, injection rate for the injection zone can be estimated. The second graphical technique implies plotting the logarithmic derivative of sandface temperature with respect to shut-in time ratio versus shut-in time ratio on a log-log scale. The plotted data are fitted with a straight line with a slope magnitude of $1/2$ of Péclet number and a vertical intercept of $1/2$ of Péclet number $\times (T_{inj} - T_o)$. The latter technique can be used to estimate the initial temperature for the injection zone if the initial temperature is not known. The analytical results are verified against numerical results obtained from a thermal simulation tool. Good agreement is obtained between the analytical and numerical results during forward and inverse modeling.

In section 3.2, the effect of heat exchange with the surrounding strata is considered. Numerical simulation indicates that heat gain from the surrounding strata is significant for thin zones that are subject to large injection rates. To consider this effect, the governing equation for heat transport during the warmback period is modified to consider heat exchange with the surrounding strata. Heat exchange is well described using the convective form, $q_{ij} = UA (T_i - T_j)$. This modification results in a coupled system of heat transport equations for a given system of injection zones during the warmback period. The analytical solution is obtained using Hankel transformation technique. The sandface temperature solution is a function of shut-in time ratio, Péclet number, and Biot number ($= HU / \lambda_r$). The obtained solution is casted into graphical techniques that allow estimating injection profile using temperature data obtained during the warmback period. The analytical results are compared with numerical results obtained from a thermal simulation tool. Good agreement is obtained between the analytical and numerical results during forward and inverse modeling.

10.2. Application of Temperature Warmback Analysis under Variable Injection Rate and Variable Injection Temperature

During cold fluid injection operation, injection rate and bottomhole injection temperature can be variable over the injection duration. Bottomhole temperature decreases gradually and stabilizes through a time period that depends on the injection rate. Besides, bottomhole injection rate can be variable due to wellbore storage effect or inevitable changes in surface injection rate.

Consequently, considering bottomhole temperature and rate changes during the injection period is required for accurate warmback analysis.

To solve the problem, two approaches are followed. In the first approach, a novel semi-analytical model is presented to model temperature evolution in a reservoir during the injection and the warmback period through discretizing the injection history into small time steps such that injection rate and injection temperature can be considered constant per time step period. The solution follows a sequential procedure in which temperature obtained at the end of a time step is used as an initial condition while solving for temperature in the next time step. During the warmback period, temperature solution is obtained through solving heat transport equation considering temperature solution at the end of injection period as an initial condition. For inverse modeling, regression analysis is used to iterate on the injection profile that reproduces the observed temperature recovery. In the second approach, analytical solutions are developed for special operating conditions such as: constant q – variable T_{inj} and variable q – variable T_{inj} . The late-time asymptotic solutions are obtained which indicate that sandface temperature at late shut-in time changes as a function of $1/\Delta t$. The late-time solution is casted into a simple graphical technique to estimate the injection profile. Temperature data are plotted versus shut-in time on a log-log scale and the portion of data to be fitted with unit slope straight line is identified. The vertical intercepts of the fitted lines are used to estimate the injection profile.

The developed semi-analytical and analytical solutions consider injection well as line-source. This assumption can be violated if the temperature monitoring tool is located inside the wellbore. Simulation results indicate that neglecting the wellbore system results in an overestimated temperature recovery at early shut-in time. To consider the wellbore system, the heat transport equation of the reservoir is coupled with wellbore system while solving the warmback problem. The forward models are validated against a thermal simulation tool for different synthetic cases. Good agreement is obtained between the analytical results and those obtained numerically during inverse and forward modeling.

10.3. Applications of Temperature Warmback Analysis for Injection Profile in Horizontal Wells

Horizontal wells have been used for water injection in applications such as water flooding oil reservoirs to improve sweep efficiency through increasing contact area between injected fluid and reservoir oil. Horizontal wells are considered a good candidate for well completion through relatively thin formations that may be a few feet thick. Field observations indicate that fluid distribution along the lateral of the injection well is often biased toward heel because pressure drawdown decreases as injected fluid moves toward the toe.

In this chapter, we developed novel forward and inverse models that enable estimating the injection profile along lateral of a horizontal well using temperature data obtained during the warmback period. The forward model is developed through solving heat transport equation in the reservoir during the injection period assuming linear fluid and heat transport using Laplace transformation technique. The solution for transient temperature during the warmback period is developed accordingly using double Laplace transformation. Sandface temperature solution is presented in the form of type curves in which dimensionless temperature change is plotted versus dimensionless shut-in at different values of Péclet number. Injection profile is obtained through type curve matching the plotted temperature data, $(= T_w(\Delta t) - T_{inj})$ versus shut-in time on a log-log graph. Injection rate is estimated using Péclet number of the matched curve. The established

solution indicates that temperature recovery at intervals which accept higher injection rates is not sensitive to injection profile at early shut-in time because heat gain from the surrounding strata dominates the temperature recovery. This indicates that a relatively long shut-in time is required to obtain accurate estimation of the injection profile during the warmback period. Good agreement is obtained between the analytical results and those obtained from the numerical simulation tool during inverse and forward modeling.

10.4. Application of Temperature Warmback Analysis for Hydraulic Fracture Characterization

Horizontal wells with multistage fractures is widely used to develop complex unconventional oil and gas reservoirs. Monitoring and diagnosis of fracture treatment is required to dictate the success of the fracture treatment. Recently, temperature monitoring has been used for fracture treatment monitoring and diagnosis given the recent advances in downhole monitoring tools such as Fiber-optic DTS. Analytical forward model is developed in this work that enables modeling temperature evolution during stimulation and post-stimulation in ultra-tight formation. The analytical model is developed to enable fracture characterization using temperature data obtained during post-stimulation (warmback period). The forward model solves heat transport equations in the fracture system and the surrounding impermeable matrix during the stimulation and warmback periods. The solution neglects fluid leakoff to the surrounding matrix which render the obtained solution applicable for ultra-tight formations. The obtained solutions enable modeling temperature recovery at the perforations and cased intervals along the lateral of the horizontal well. Perforated intervals exhibit lag in temperature recovery compared with cased intervals which provide good indication for fracture initiation points. Additionally, temperature recovery at the perforation is found to be mainly dependent on fracture width as well as the thermal properties of the surrounding matrix. The negligible temperature gradient along fracture propagation compared with that perpendicular to the fracture plan results in negligible contribution of heat conduction along the fracture plane. Accordingly, temperature recovery at perforation is independent on fracture half-length.

Graphical interpretation technique is presented for fracture characterization which is developed using late-time asymptotic solution of perforation temperature. The graphical technique implies plotting perforation temperature versus shut-in time, Δt on a log-log scale. The slope and vertical intercept of the fitted line are used to estimate fracture width and unperturbed reservoir temperature, respectively. Analytical results are compared with numerical results using input data that are relevant to realistic treatment operations. A good match is obtained between the analytical based results and those obtained from the numerical simulation tool. The proposed graphical interpretation technique is used to estimate fracture width, fracture half-length and initial temperature. Good agreement is obtained between the inversion results and those provided to the simulation tool.

10.5. Application of Temperature Warmback Analysis for Allocating CO₂ Injection Rate and Plume Extent Evaluation using Temperature Warmback Analysis

Geologic Carbon Storage (GCS) has been recognized as a promising technique to cut greenhouse gas emissions into the atmosphere. Among the proposed candidates for geological CO₂ storage, deep saline aquifers are considered the prime candidate. Monitoring CO₂ distribution over the injection interval is essential to assess the heterogeneity of the target

reservoir and improve injection efficiency. Temperature warmback analysis is adopted in this chapter to estimate the injection profile and the extent of CO₂ plume propagation from the injection well. In this work, forward modeling is required to model temperature evolution considering two-phase flow conditions encountered at injection well during CO₂ injection. The forward model is developed by solving mass and heat conservation equations during the injection period using Bratvold and Horne (1989)'s procedure. Temperature solution is simply represented by step change in temperature from injection temperature to initial temperature at the thermal front because heat transfer is considered to be advection dominant. The saturation solution is represented by two saturation shocks: the main saturation shock is located at the plume front and a minor saturation shock which is located at the thermal front. One of the assumptions inherent in Bratvold and Horne (1989)'s solution is neglecting mutual solubility between aqueous brine and CO₂. Consequently, the dry-out region is neglected in their saturation solution. During the warmback period, heat transport in the reservoir is described by a heat conduction equation with variable coefficients because of the saturation dependency of effective thermal properties. To solve the problem, new forward model is developed which discretizes the aquifer into three regions: first region extends from the injection well to the thermal front, the second region extends from the thermal front to the plume front, and the third region is a head of the plume front. The heat transport equations of the discretized regions are solved simultaneously considering the boundary conditions at the interfaces using Laplace transformation technique. An early-time asymptotic solution is developed for the sandface temperature which indicates that the saturation and properties of the innermost region dominate temperature behavior at early shut-in time.

Graphical interpretation technique is presented using the early-time asymptotic solution for inverse modelling. The graphical technique implies plotting the temperature change, $(=T_w(\Delta t) - T_{inj})$ versus $1/\Delta t$ on Cartesian plot. The results from the analytical solution are produced and compared with numerical results obtained from thermal compositional reservoir simulation tool. It is obtained that the analytical solution underestimates temperature recovery at early shut-in time because the temperature solution during the injection period neglects the effect of heat conduction. The degree of mismatch decreases as injection rate increases because heat transfer tends to be advection dominant as a result. The graphical technique is applied to the numerical temperature data. Deviation of the plotted data is observed at early shut-in time (or large $1/\Delta t$) because of neglecting the contribution of heat conduction during the injection period. The inversion results are in good agreement with those obtained from the numerical simulation tool.

10.6. Application of In-well and Formation Heat Pulse Testing for CO₂ Plume Monitoring

Heat pulse testing is a thermal tracer test which is used in hydrology to estimate groundwater velocity and subsurface thermal properties. In that test, a distributed heating source is deployed within a monitoring well or embedded in direct contact with formation, and the associated temperature evolution is monitored using fiber optic DTS cable. Heat transfers from the heating source to the surrounding environment via advection due to fluid flow inside wellbore/porous medium and heat transfer by conduction through the adjacent porous medium. Through analyzing the temperature profile over the heating source, spatial estimates of subsurface fluid velocity and thermal properties of the surrounding porous media are obtainable. In this chapter, we investigated the feasibility of using in-well heat pulse testing for estimating

subsurface fluid velocity and monitoring CO₂ arrival at a monitoring well during GCS. In-well heat pulse testing involves deploying a distributed heating source through a monitoring well. Heat transfers from the heating source to the surrounding fluid in wellbore solely through advection mechanism. Because of the sensitivity of heat transport to flowing fluid velocity as well as fluid type (CO₂ versus brine), both unknowns can be estimated. Advection heat transfer is modeled using Newton's law of cooling, in which temperature difference between the heater and the surrounding fluid drives heat transfer, for which convective heat transfer coefficient controls rate of heat transfer. Consequently, estimating the convection heat transfer coefficient can provide indication of the flowing fluid type and quantification of the flowing fluid velocity. Churchill and Bernstein (1977)'s correlation is used in this work to relate convection heat transfer coefficient with flowing fluid velocity and properties of the flowing fluid. The results obtained from this technique are generated and compared with numerical results for single-phase brine flow and single-phase CO₂ flow. The results indicate that the observed temperature is sensitive to fluid velocity and fluid type. As flowing fluid velocity increases, a lower temperature signal is obtained. Additionally, the sensitivity of the temperature signal to fluid velocity decreases as velocity increases beyond 100 μm/s. Fluid type significantly affect the obtained temperature heating. The contrast between temperature signals before and after CO₂ arrival can be higher than 10 °C depending on the fluid velocity, which is attributed to poor CO₂ thermal conductivity compared with in-situ brine.

In section 8.2, we investigated the capabilities of formation heat pulse testing for monitoring CO₂ plume migration in a storage aquifer. In formation heat pulse testing, the same approach presented before is adopted however, the monitoring well should be hydraulically isolated from the monitoring zone. Heat release from the heating source is caused by heat conduction through the porous medium as well as fluid flow in the surrounding porous medium. An analytical forward model is presented to model temperature evolution surrounding the heating source considering two-phase flow conditions encountered during CO₂ storage in the storage aquifer. Temperature results obtained from the analytical solution are generated and compared with numerical results obtained from a thermal compositional simulation tool. Temperature buildup at early time is dominated by heat conduction through the surrounding porous medium, while it becomes advection dominant at late time of heating. High thermal conductivity results in a lower rate of temperature buildup and vice versa. Besides, higher flowing fluid velocities result in a lower stabilized temperature and shorter stabilization time. New graphical interpretation techniques are presented that enable estimating CO₂ saturation, individual phase velocity, and subsurface thermal properties at the monitoring well. During early heating period, temperature data are plotted versus time on a semi-log plot. The slope of the fitted line is used to estimate effective thermal conductivity of the porous medium, which in turn is used to estimate CO₂ saturation. At late-time, temperature data are fitted with a zero-slope line. The time at the intercept of the zero-slope and the early-time fitted lines is used to estimate the individual phase velocity. The proposed interpretation techniques are applied to the temperature data obtained from a compositional thermal simulation tool. Good agreement is obtained between the inversion results and those obtained from the simulation tool.

10.7. Application of Passive Temperature Monitoring for Tracking CO₂ Migration

Monitoring CO₂ migration is essential to ensure containment of stored CO₂ in geological storage reservoirs. Temperature monitoring has recently been used as a new alternative technique to track CO₂ plume migration in storage aquifers through identifying the warming wave that

migrates contemporaneously with the plume front. The warming front is established exclusively due to exothermic CO₂ dissolution into in-situ brine at the plume front. The magnitude of the temperature anomaly at the warming front is up to 1 °C depending on the hydraulic properties of the host formation. In this chapter, we presented a sensitivity study to investigate potential effects of aquifer outer boundary conditions, injection history, level, and location of the temperature monitoring tool on the established temperature signal using a thermal compositional simulation tool. Among the investigated effects, the location of the temperature monitoring tool significantly affects the established temperature signal. Temperature heating at the CO₂ front is obtained to be much higher (by six-fold) if the temperature monitoring tool is located inside the monitoring well compared with the temperature signal obtained if the monitoring cable is cemented behind the casing. This increase is attributed to the enhanced CO₂ dissolution into brine inside the wellbore because the mass of brine available for CO₂ dissolution is much higher than that located in the porous medium. Apart from pressure and saturation behaviors, temperature signal is slightly affected by the remaining effects such as boundary conditions, injection history, and level of temperature monitoring tool. Pressure exhibits excessive increase during boundary-dominated flow conditions which can result in a different CO₂ distribution compared with the case of semi-infinite aquifer system. The increase in the aquifer's pressure triggers CO₂ dissolution in the brine, which decreases free CO₂ saturation. Besides, the excessive buildup of pressure increases CO₂ density, which in turn mitigates the buoyancy effect. Consequently, late CO₂ arrival at shallower zones is depicted during boundary dominated flow conditions.

We also studied CO₂ migration from storage aquifers via improperly abandoned wells. Abandoned wells are considered a potential pathway for CO₂ migration from storage aquifers to the surface. The objective of this study is to investigate the feasibility of using surface pressure and temperature monitoring to detect CO₂ migration through improperly abandoned wells. A coupled wellbore-reservoir model is built using T2Well simulation tool to investigate pressure, temperature, and CO₂ evolutions through an improperly abandoned well for two scenarios: open and closed wellbore at the surface. In both scenarios, we assumed that the abandoned well is fully communicated with the storage aquifer. In case of open wellbore, significant reduction of pressure inside the wellbore is obtained as migrated CO₂ (less dense) replaces in-situ brine (denser). Excessive cooling of temperature is obtained as migrated CO₂ goes upward due to the adiabatic expansion driven by loss of hydrostatic pressure as well as endothermic liberation of CO₂ from brine. Temperature decreases at wellhead down to 5°C, which is the lower limit of the EOS tool implemented in T2Well. In closed wellbore scenario, an excessive increase in pressure is obtained throughout the wellbore. After CO₂ arrival, a counter-flow is established inside the wellbore in which CO₂ migrates upward due to buoyancy and brine is displaced downward. As the wellbore is a closed system, it does not allow migrated CO₂ to expand and as such it keeps formation pressure inside as it migrates upward. Consequently, pressure increases everywhere inside the wellbore during counter-flow until the wellbore becomes fully filled with CO₂. On the other hand, minor fluctuations in temperature is depicted due to advection heat transfer during counter-flow. This study shows that CO₂ migration through abandoned wells can be detected through monitoring pressure and temperature changes at the surface.

10.8. Recommendations for Future Work

Following the research topics presented in this work, several recommendations for future work are suggested below:

1. Injection wells can be a potential pathway for CO₂ leakage from storage reservoirs especially during CO₂ EOR and/or CO₂ storage in depleted hydrocarbon reservoirs. CO₂ leakage from injection wells can induce a complicated temperature signal compared with abandoned wells. In this case, the temperature signal obtained during CO₂ leakage depends not only on the hydrothermal processes that associate CO₂ leakage, but also on the temperature conditions prevailed inside the injection well. Considering injection under variable operating rates can make the observed temperature signal more complicated. Numerical modeling of CO₂ leakage can provide a better understanding of the nature of the temperature anomaly and help identify the fate of CO₂ leakage from injection wells.
2. With the recent advances in permanent downhole monitoring techniques such as Distributed Acoustic Sensing (DAS), Doppler shift effect has been used to quantify fluid flow in production wells and estimate fractions of the produced phases. Doppler shift can be used for CO₂ plume monitoring in storage reservoirs and estimate CO₂ saturation. In this technique, an acoustic source is deployed in a monitoring well which emits sound with a specific frequency in the storage formation. The received acoustic signals in the surrounding monitoring wells show a shift in wavelength, which depends on the direction of CO₂ migration and the velocity of the CO₂ plume. Additionally, the arrival time of the acoustic signals depends on CO₂ saturation in porous media. These unknowns can be obtained by analyzing the frequency and the arrival time of the received acoustic signals.

Appendix A. Numerical Investigation of Wellbore Temperature Behavior During Non-Isothermal Fluid Injection

In this appendix, we investigate the bottomhole temperature behavior during a short-term injection operation. The bottomhole temperature is modeled using CMG-STARS (2020) at different rates (250, 500, 1000, 2000 bbl/day) for a system with properties given in Table A.1 (Case 1). Water is injected for 24 hours at 60 °F surface temperature into a 200-ft thick reservoir via a 3200-ft deep vertical well. Fig. A.1 illustrates the bottomhole temperature behavior during the injection period for the specified injection rates, based on which bottomhole temperature does not stabilize over the injection duration. Rate of temperature cooling increases as the flow rate of injected fluid increases. Bottomhole temperature changes are 35, 29, 19, and 12 °F at 2000, 1000, 500, and 250 bbl/day injection rates, respectively. Accordingly, assuming constant bottomhole injection temperature during the injection period is not accurate especially for short injection durations.

Bottomhole injection rate can also be variable even for constant surface injection rate due to the wellbore storage effect at the beginning of the injection and shut-in periods. Different injection scenarios are modeled (using Kappa-Rubis, 2019) for different wellbore storage coefficients, C_s (= 0.01, 0.05, 0.1 bbl/psi) in which cold water is injected for 12 hours at 2000 bbl/day (see Table A.1 – Case 2). Fig. A.2 (a) and (b) show the bottomhole rate during the injection and the following shut-in period, respectively. The duration of the wellbore storage during the entire thermal test (injection and shut-in periods) extends up to 3 hours. Consequently, considering the variation of the bottomhole rate is required for accurate warmback analysis especially for short term injection operations.

Additionally, the thermal storage capacity of the wellbore affects the temperature recovery during the warmback period, especially at the early shut-in time. Neglecting this effect results in higher temperature recovery and accordingly overestimated injection rate. To demonstrate the importance of this effect, we model the temperature recovery for an open-hole system using CMG-STARS (2020) with properties given in Table A.1 (Case 3). Fig. A.3 illustrates the temperature recovery with/without considering the thermal storage capacity of the open hole section. The rate of temperature recovery for the case that considers the wellbore is lower than the case which assumes negligible wellbore size. This effect is more pronounced at the early shut-in time and decreases as the shut-in time increases similar to the wellbore storage effect in pressure well testing (Spivey and Lee 2013). The duration of the thermal wellbore storage effect extends up to 3 days from the start of shut in. The wellbore thermal storage is due to the thermal storage capacity of the wellbore system over the reservoir interval. It exists even if the wellbore storage is eliminated e.g., by bottomhole well shut in. To eliminate this effect, fiber-optic cable should be cemented behind the production casing to avoid wellbore fluid interventions. Otherwise, considering the thermal storage capacity of the wellbore system over the injection interval is necessary, especially for short shut-in durations to obtain accurate results during warmback analysis.

Table A. 1. Input data for the numerical investigation study.

Input data	Case 1	Case 2	Case 3
Initial reservoir temperature, F	110	110	110
Wellbore length, ft	3200	3200	3200
Casing length, ft	3000	3000	3100
Tubing size (ID, OD), in	2.992 & 3.5	2.992 & 3.5	2.992 & 3.5
Casing size (ID, OD), in	6.538 & 7	6.538 & 7	6.538 & 7
Hole size, in	6.125	6.125	6.125
Injection temperature, F	60	60	60
Injection rate, bbl/day	250,500,1000,2000	2000	100
Injection time, day	1	0.5	0.25
Wellbore storage coefficient, bbl/psi	0	0.01,0.05, 0.1	0
Thermal conductivity of tubing, Btu/ft day F	576.85	576.85	576.85
Thermal conductivity of cement, Btu/ft day	4.8	4.8	4.8
Thermal conductivity of formation, Btu/ft	44.0	44.0	40.5
Heat capacity of formation, Btu/ft ³ F	35	35	38
Heat capacity of wellbore fluid, Btu/ft ³ F	1	1	1
Geothermal gradient, F/ft	0.015	0.015	0.015
Reservoir thickness, ft	200	200	100
Reservoir permeability, md	100	100	100
Reservoir porosity, fraction	0.3	0.3	0.1

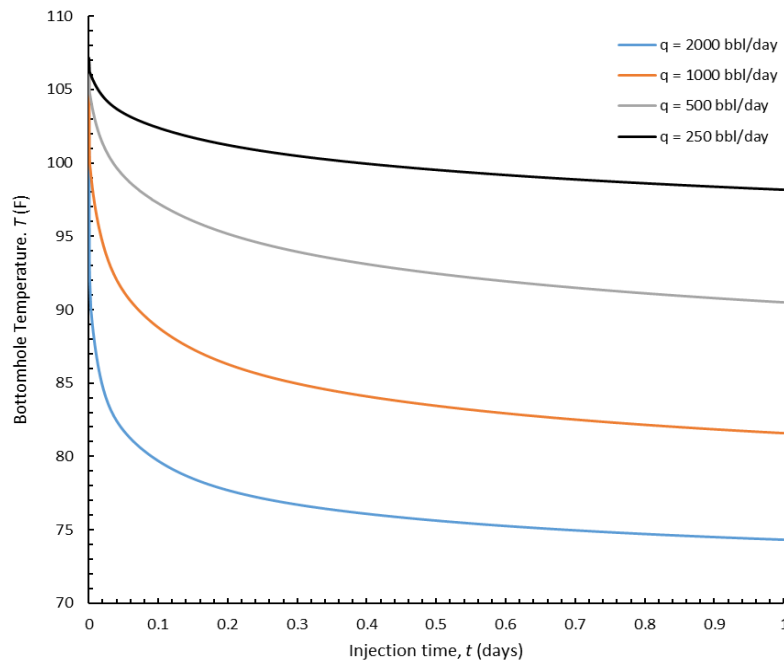


Figure A. 1. Bottomhole temperature behavior during a short-term injection at different injection rates ($q = 2000, 1000, 500,$ and 250 bbl/day).

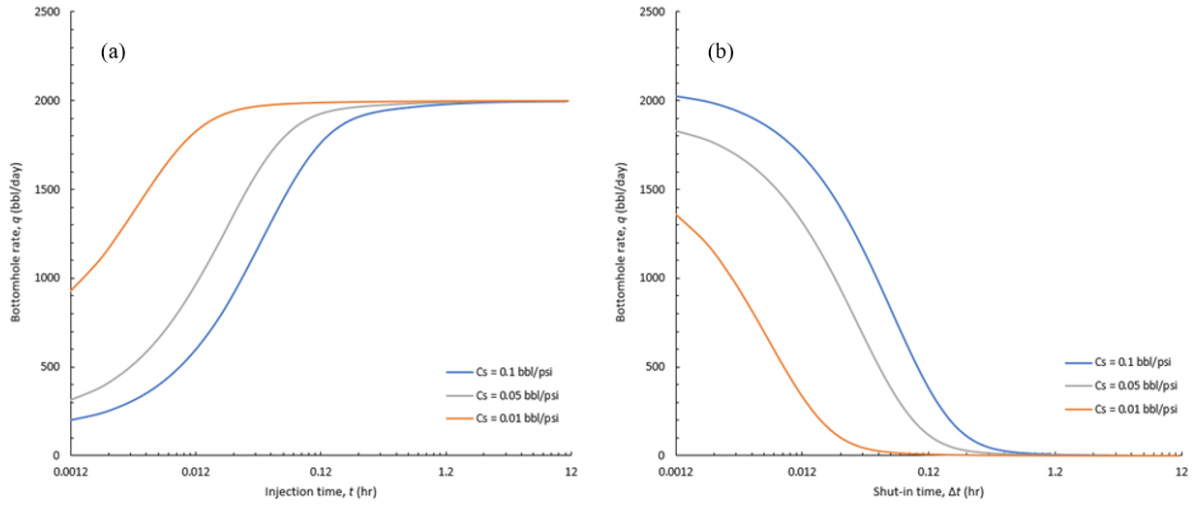


Figure A. 2. Bottomhole flow rate during/after a short-term injection for different wellbore storage coefficients: (a) injection period (b) shut in period.

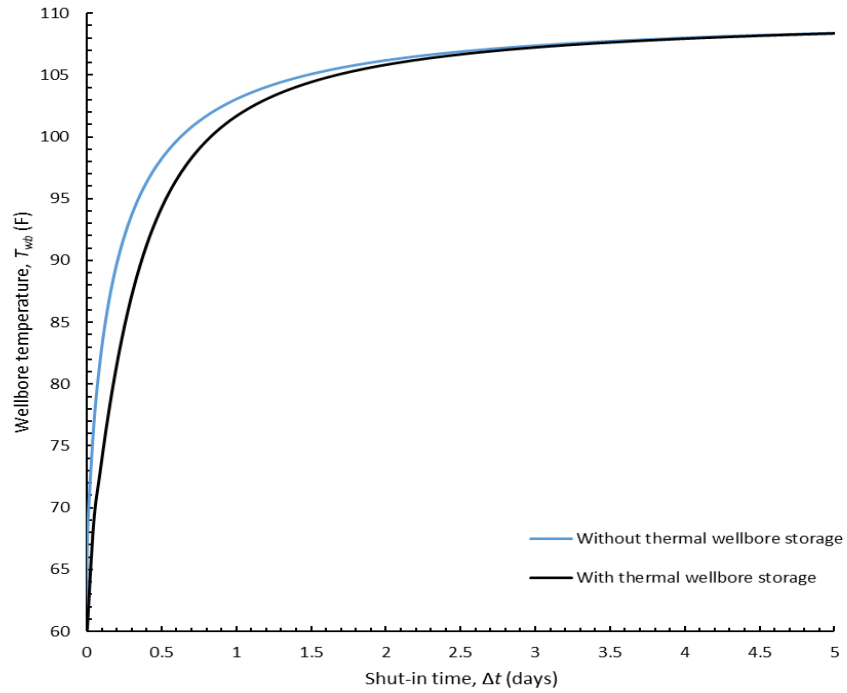


Figure A. 3. Bottomhole temperature shortly after a short-term injection with/without considering the thermal wellbore storage.

Appendix B. Derivation of the Semi-analytical Temperature Solution During the Injection Period under Variable Rate – Variable Temperature

In this appendix, the solution of the IBVP described by Eq. 4.6 – Eq. 4.9 for an arbitrary time step of size t_D is presented. During the time step period, injection rate and injection temperature are evaluated as the average values over the time step period (see Fig. 4.1). The governing equation of the problem is subject to non-homogenous initial condition and non-homogenous inner boundary condition. The solution can be formulated as a summation of two different solutions; the first one is a solution of the same problem but with homogenous initial condition. The second one is a solution of the same problem but with homogenous inner boundary condition. The first problem is formulated as follows:

$$\frac{\partial T_{D1}}{\partial t_D} = \frac{\partial^2 T_{D1}}{\partial r_D^2} + \frac{1-2\beta}{r_D} \frac{\partial T_{D1}}{\partial r_D} \quad (\text{B.1})$$

The corresponding initial and boundary conditions are as follows:

$$T_{D1}(r_D, t_D = 0) = 0 \quad (\text{B.2})$$

$$T_{D1}(r_D = 0, t_D) = 1 \quad (\text{B.3})$$

$$\lim_{r_D \rightarrow \infty} \left(\frac{\partial T_{D1}}{\partial r_D} \right) = 0 \quad (\text{B.4})$$

The solution of the IBVP has been given by Chen and Reddell (1983) which is as follows:

$$T_{D1} = \frac{1}{\Gamma(\beta)} \Gamma \left(\beta, \frac{r_D^2}{4t_D} \right) \quad (\text{B.5})$$

where $\Gamma \left(\beta, \frac{r_D^2}{4t_D} \right)$ is the incomplete Gamma function of β from $\frac{r_D^2}{4t_D}$ to infinity (Abramowitz et al. 1988). For the advection-diffusion problem that is subject to non-homogenous initial condition and homogenous inner boundary condition, the problem is described by the following equation:

$$\frac{\partial T_{D2}}{\partial t_D} = \frac{\partial^2 T_{D2}}{\partial r_D^2} + \frac{1-2\beta}{r_D} \frac{\partial T_{D2}}{\partial r_D} \quad (\text{B.6})$$

The corresponding initial and boundary conditions are as follows:

$$T_{D2}(r_D, t_D = 0) = T_D(r_D, t_D = 0) \quad (\text{B.7})$$

$$T_{D2}(r_D = 0, t_D) = 0 \quad (\text{B.8})$$

$$\lim_{r_D \rightarrow \infty} \left(\frac{\partial T_{D2}}{\partial r_D} \right) = 0 \quad (\text{B.9})$$

where $T_D(r_D, t_D = 0)$ is the temperature solution at the end of the previous time step. The following transformation is used to solve the problem:

$$T_{D2} = r_D^\beta F(r_D, t_D) \quad (\text{B.10})$$

The IBVP is simplified to the following form:

$$\frac{\partial F}{\partial t_D} = \frac{\partial^2 F}{\partial r_D^2} + \frac{1}{r_D} \frac{\partial F}{\partial r_D} - \frac{\beta^2}{r_D^2} F = \left(\nabla^2 - \frac{\beta^2}{r_D^2} \right) F \quad (\text{B.11})$$

$$F(r_D, t_D = 0) = r_D^{-\beta} T_D(r_D, t_D = 0) \quad (\text{B.12})$$

$$F(r_D = 0, t_D) = 0 \quad (\text{B.13})$$

$$\lim_{r_D \rightarrow \infty} \left(\frac{\partial F}{\partial r_D} \right) = 0 \quad (\text{B.14})$$

The solution of the problem is obtained using Hankel transformation of n^{th} -order. Hankel transformation is an integral transformation which involves Bessel function as the kernel and it arises naturally in axisymmetric problems formulated in cylindrical coordinates (Debnath and Bhatta 2006). Hankel transform of function $f(x)$ of an order n is defined by Eq. B.15. The inverse Hankel transform of function $\bar{f}(k)$ is defined by Eq. B.16. Additionally, Eq. B.17 illustrates a useful property of Hankel transformation which is used to obtain the corresponding form of Eq. B.11 in Hankel domain.

$$H_n(f(x)) = \bar{f}(k) = \int_0^\infty x J_n(kx) f(x) dx \quad (\text{B.15})$$

$$f(x) = H_n^{-1}(\bar{f}(k)) = \int_0^\infty k J_n(kx) \bar{f}(k) dk \quad (\text{B.16})$$

$$H_n \left(\left(\nabla^2 - \frac{n^2}{x^2} \right) f(x) \right) = -k^2 \bar{f}(k) \quad (\text{B.17})$$

The IBVP is simplified to an Initial Value Problem (IVP) in Hankel space domain as follows:

$$\frac{\partial \bar{F}}{\partial t_D} + k^2 \bar{F} = 0 \quad (\text{B.18})$$

$$\bar{F}(t_D = 0, k) = \int_0^{\infty} x J_n(kx) x^{-\beta} T_D(t_D = 0, x) dx \quad (\text{B.19})$$

The solution of the IVP (described by Eq B. 18 – B. 19) in Hankel domain is given by (Kreyszig 2009):

$$\bar{F} = \bar{F}(t_D = 0, k) \exp(-k^2 t_D) \quad (\text{B.20})$$

The corresponding solution in the real-space domain is obtained using inverse Hankel transformation as illustrated below:

$$F(r_D, t_D) = \int_0^{\infty} k J_n(kr_D) \bar{F}(k) dk = \int_0^{\infty} k J_n(kr_D) \bar{F}(t_D = 0, k) \exp(-k^2 t_D) dk \quad (\text{B.21})$$

$$\begin{aligned} F(r_D, t_D) &= \int_0^{\infty} \int_0^{\infty} k J_n(kr_D) \exp(-k^2 t_D) x J_n(kx) T_D(t_D = 0, x) x^{-\beta} dk dx \\ &= \int_0^{\infty} x^{1-\beta} T_D(t_D = 0, x) \left\{ \int_0^{\infty} k J_n(kx) J_n(kr_D) \exp(-k^2 t_D) dk \right\} dx \end{aligned} \quad (\text{B.22})$$

Eq B. 22 is simplified to the following form:

$$F(r_D, t_D) = \frac{1}{2t_D} \int_0^{\infty} u^{1-\beta} \exp\left(-\frac{u^2 + r_D^2}{4t_D}\right) I_{\beta}\left(\frac{ur_D}{2t_D}\right) T_D(u, t_D = 0) du \quad (\text{B.23})$$

The following integral identity is used to obtain Eq. B. 23:

$$I = \int_0^{\infty} x J_{\nu}(ax) J_{\nu}(bx) \exp(-cx^2) dx = \frac{1}{2c} \exp\left(-\frac{a^2 + b^2}{4c}\right) I_{\nu}\left(\frac{ab}{2c}\right) \quad (\text{B.24})$$

Using the transformation defined by Eq B. 10, the solution of the IBVP described by Eq B. 6 – Eq B. 9 is given by:

$$T_{D2}(r_D, t_D) = \frac{r_D^{\beta}}{2t_D} \int_0^{\infty} u^{1-\beta} \exp\left(-\frac{u^2 + r_D^2}{4t_D}\right) I_{\beta}\left(\frac{ur_D}{2t_D}\right) T_D(u, t_D = 0) du \quad (\text{B.25})$$

The summation of Eq B. 5 and Eq B. 25 results in the solution of the temperature during the time step period.

$$T_D = T_{D1} + T_{D2} = \frac{1}{\Gamma(\beta)} \Gamma\left(\beta, \frac{r_D^2}{4t_D}\right) + \frac{r_D^\beta}{2t_D} \int_0^\infty u^{1-\beta} \exp\left(-\frac{u^2 + r_D^2}{4t_D}\right) I_\beta\left(\frac{ur_D}{2t_D}\right) T_D(u, t_D = 0) du \quad (\text{B.26})$$

Eq. B. 26 can be written in a general form for an arbitrary time step i , where $i = 1:n$, and n is the number of time steps, as follows:

$$T_{D,i} = \frac{1}{\Gamma(\beta_i)} \Gamma\left(\beta_i, \frac{r_D^2}{4(t_{D,i} - t_{D,i-1})}\right) + \frac{r_D^{\beta_i}}{2(t_{D,i} - t_{D,i-1})} \int_0^\infty u^{1-\beta_i} \exp\left(-\frac{u^2 + r_D^2}{4(t_{D,i} - t_{D,i-1})}\right) I_\beta\left(\frac{ur_D}{2(t_{D,i} - t_{D,i-1})}\right) T_D(u, t_{D,i-1}) du \quad (\text{B.27})$$

where $t_{D,0} = 0$, $T_{D,i} = \left(\frac{T_o - T(t)}{T_o - T_{inj,i}}\right)$, $\beta_i = \frac{\rho_w C_w q_i}{4\pi h \lambda_r}$, and $T_D(u, t_{D,i-1})$ is the temperature solution at the end of the previous time step.

Appendix C. Derivation of the Temperature Solution During the Warmback Period Following Injection under Variable Rate - Variable Temperature

In this appendix, the solution of the IBVP described by Eq. 4.11 – 4.14 is presented. The governing equation for the transient temperature during the warmback period is a heat conduction equation that is subject to non-homogenous initial condition and homogenous boundary conditions. The solution of the problem is obtained using Hankel transformation of zeroth order as defined by Eq. B.15 – B. 17. The corresponding form of the heat diffusion equation in Hankel space domain is simplified to a first order ODE of the following form:

$$\frac{\partial \bar{T}_D}{\partial \Delta t_D} + k^2 \bar{T}_D = 0 \quad (\text{C.1})$$

The initial condition in Hankel space domain is given by:

$$\bar{T}_D(k, \Delta t_D = 0) = \int_0^{\infty} x J_0(kx) T_D(x, t_D = t_{Dinj}) dx \quad (\text{C.2})$$

The solution of the above IVP in Hankel space domain is given by:

$$\bar{T}_D(k, \Delta t_D) = \bar{T}_D(k, \Delta t_D = 0) \exp(-k^2 \Delta t_D) \quad (\text{C.3})$$

The corresponding solution in the real-space domain is obtained using inverse Hankel transformation defined by Eq. B.16 which is given by:

$$T_D(r_D, \Delta t_D) = \frac{1}{2\Delta t_D} \int_0^{\infty} u \exp\left(-\frac{u^2 + r_D^2}{4\Delta t_D}\right) I_0\left(\frac{ur_D}{2\Delta t_D}\right) T_D(u, t_D = t_{injD}) du \quad (\text{C.4})$$

The following integration identity is adopted to obtain Eq. C.4.

$$I = \int_0^{\infty} x J_0(ax) J_0(bx) \exp(-cx^2) dx = \frac{1}{2c} \exp\left(-\frac{a^2 + b^2}{4c}\right) I_0\left(\frac{ab}{2c}\right) \quad (\text{C.5})$$

The sandface temperature solution during the warmback period is obtained by assigning $r_D \rightarrow 0$ in Eq. C.4 which is given by:

$$T_{wD}(\Delta t_D) = \frac{1}{2\Delta t_D} \int_0^{\infty} u \exp\left(-\frac{u^2}{4\Delta t_D}\right) T_D(u, t_D = t_{injD}) du \quad (\text{C.6})$$

Appendix D. Derivation of the Temperature Solution During the Injection under Variable Rate - Variable Temperature Considering Advection-Dominant Heat Transfer

In the first part of this appendix, the solution of the IBVP described by Eq. 4.16 and Eq. 4.3 - Eq. 4.4 is presented. The solution of the advection problem is obtained using the superposition principle as follows:

$$T_D(r_D, t_D) = \sum_{i=0}^{n-1} \varphi(r_D, t_D - \Delta t_{D,i}) \Delta T_{injD,i} \quad (D.1)$$

where $\varphi(r_D, t_D)$ is a solution of the following auxiliary transport problem.

$$\frac{\partial \varphi}{\partial t_D} + 4\beta(t_D) \frac{\partial \varphi}{\partial r_D^2} = 0 \quad (D.2)$$

The above equation is subject to the following initial and boundary conditions:

$$\varphi(r_D, t_D = 0) = 0 \quad (D.3)$$

$$\varphi(r_D = 0, t_D) = 1 \quad (D.4)$$

To solve the IBVP described by Eq. D.2 – D.4, the moving coordinate transformation (MCT) defined by the following equation is used (Jensen and Finlayson 1980).

$$\eta = r_D^2 - 4 \int_0^{t_D} \beta(u) du \quad (D.5)$$

The solution of the auxiliary problem that satisfies Eq. D.2 – D.4 is given by:

$$\varphi = 1 - U \left(r_D^2 - 4 \int_0^{t_D} \beta(u) du \right) \quad (D.6)$$

where $U(-)$ is the unit step function. The dimensional form of the solution of the auxiliary problem is as follows:

$$\frac{T_o - T(r, t)}{T_o - T_{inj}} = 1 - U \left(\frac{r^2}{r_w^2} - \frac{1}{\pi r_w^2 h} \left(\frac{\rho_w C_w}{\rho_r C_r} \right) \int_0^t q(u) du \right) \quad (D.7)$$

Since the integration term in the unit step function represents the cumulative injected volume, Eq. D.7 can be re-written in terms of the cumulative injected volume at the time of interest. Given the discretized injection history depicted in Fig. 4.1, the following mathematical function is first used to describe the injection rate in terms of the injection time.

$$q(t) = \sum_{i=0}^{n-1} (q_{i+1} - q_i) U(t - t_i) \quad (\text{D.8})$$

Next, Eq. D.8 is substituted into Eq. D.7 to obtain the following solution in terms of the injection history.

$$\frac{T_o - T(r, t)}{T_o - T_{inj}} = 1 - U \left(\frac{1}{r_w^2} \left\{ r^2 - \frac{1}{\pi h} \left(\frac{\rho_w C_w}{\rho_r C_r} \right) \sum_{i=0}^{n-1} (q_{i+1} - q_i) (t - t_i) U(t - t_i) \right\} \right) \quad (\text{D.9})$$

The second term in Heaviside function represents the square of the thermal front radius at the time of interest. Consequently, Eq. D.6 can be re-written in the following dimensionless form:

$$\phi = 1 - U \left(r_D^2 - r_{TD} (t_D)^2 \right) \quad (\text{D.10})$$

where $r_{TD} (t_D)$ is the dimensionless radius of the thermal front which is defined by:

$$r_{TD}^2 (t_D) = \frac{1}{\pi r_w^2 h} \left(\frac{\rho_w C_w}{\rho_r C_r} \right) \sum_{i=0}^{n-1} (q_{i+1} - q_i) (t - t_i) U(t - t_i) = \frac{1}{\pi h r_w^2} \left(\frac{\rho_w C_w}{\rho_r C_r} \right) W_{inj} (t) \quad (\text{D.11})$$

Writing Eq. D.11 in dimensional form becomes as follows:

$$r_T^2 (t) = \frac{1}{\pi h} \left(\frac{\rho_w C_w}{\rho_r C_r} \right) \sum_{i=0}^{n-1} (q_{i+1} - q_i) (t - t_i) U(t - t_i) = \frac{1}{\pi h} \left(\frac{\rho_w C_w}{\rho_r C_r} \right) W_{inj} (t) \quad (\text{D.12})$$

Eq. D.12 describes the location of the thermal front for variable injection rate conditions. This form is identical to the solution provided by Platenkamp (1985) for single rate condition as illustrated below:

$$\begin{aligned} r_T^2 (t) &= \phi \left[\frac{1}{\pi h \phi} \left(\frac{\rho_w C_w}{\rho_r C_r} \right) W_{inj} (t) \right] = \phi \left(\frac{\rho_w C_w}{\rho_r C_r} \right) \left[\frac{W_{inj} (t)}{\pi h \phi} \right] = \phi \left(\frac{\rho_w C_w}{\rho_r C_r} \right) \left[\frac{\pi h \phi r_s^2 (t)}{\pi h \phi} \right] \\ &= \phi \left(\frac{\rho_w C_w}{\rho_r C_r} \right) r_s^2 (t) \end{aligned} \quad (\text{D.13})$$

where $r_s(t)$ is the radius of the flooded front. For variable injection temperature, superposition principle can be used to obtain the temperature profile in the reservoir using the following equation:

$$T_D(r_D, t_D) = \sum_{i=0}^{n-1} \left(1 - U \left(r_D^2 - \{ r_{TD}^2(t_D) - r_{TD}^2(t_{D,i}) \} \right) \right) \Delta T_{injD,i} \quad (D.14)$$

In the second part of this appendix, the equality of the first part of Eq. 4.44 is demonstrated. For sake of simplicity, we assume two-layer reservoir that is subject to the injection history depicted in Fig. D. 1.

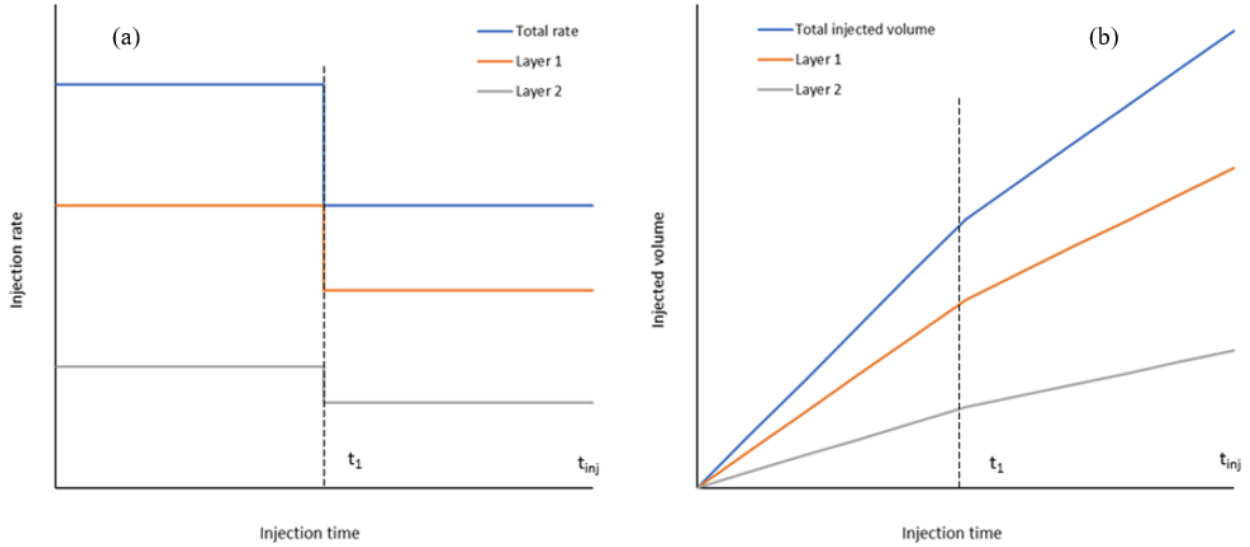


Figure D. 1. (a) Injection rate history (b) injected volume history.

The injection rate for layer 1 and 2 can be defined as follows:

$$q_1(t) = C_1 \times q(t) \quad \text{for layer 1} \quad (D.15)$$

$$q_2(t) = C_2 \times q(t) \quad \text{for layer 2}$$

where $q(t)$ is the total injection rate. Integrating the injection rates defined by Eq. D. 15 gives the corresponding cumulative injected volumes by:

$$W_{inj,1}(t) = C_1 \times W_{inj}(t) \quad \text{for layer 1} \quad (D.16)$$

$$W_{inj,2}(t) = C_2 \times W_{inj}(t) \quad \text{for layer 2}$$

where $W_{inj}(t)$ is the total injected volume. Consequently, the summation terms shown in Eq. 4.44 become:

$$\begin{aligned} \left(\sum_{i=0}^{n-1} (W_{inj}(t_{inj}) - W_{inj}(t_{inj,i})) \right)_1 &= 2W_{inj,1}(t_{inj}) - W_{inj,1}(t_1) = C_1 (2W_{inj}(t_{inj}) - W_{inj}(t_1)) \quad \text{for layer 1} \\ \left(\sum_{i=0}^{n-1} (W_{inj}(t_{inj}) - W_{inj}(t_{inj,i})) \right)_2 &= 2W_{inj,2}(t_{inj}) - W_{inj,2}(t_1) = C_2 (2W_{inj}(t_{inj}) - W_{inj}(t_1)) \quad \text{for layer 2} \end{aligned} \quad (D.17)$$

By dividing the summation term of layer 1 by that of layer 2, the injection profile is obtained by:

$$\frac{\left(\sum_{i=0}^{n-1} (W_{inj}(t_{inj}) - W_{inj}(t_{inj,i})) \right)_1}{\left(\sum_{i=0}^{n-1} (W_{inj}(t_{inj}) - W_{inj}(t_{inj,i})) \right)_2} = \frac{C_1}{C_2} = \frac{W_{inj,1}}{W_{inj,2}} \quad (D.18)$$

Appendix E. Derivation of the Temperature Solution During the Injection Period for Constant Rate – Variable Temperature

In this section, a derivation of transient temperature in a reservoir during non-isothermal fluid injection and warmback periods are presented for constant injection rate and variable injection temperature. The governing equation for heat transfer in the reservoir during the injection period is described by the following advection-diffusion equation:

$$\frac{\partial T_D}{\partial t_D} = \frac{\partial^2 T_D}{\partial r_D^2} + \frac{1-2\beta}{r_D} \frac{\partial T_D}{\partial r_D} \quad (\text{E.1})$$

The above equation is subject to the initial and boundary conditions defined by Eq. 4.7 - Eq. 4.9. Since the IBVP is homogenous, however the inner boundary condition is time dependent, superposition can be used to obtain the solution (Özışık 1980). The solution of the advection-diffusion problem is given by:

$$T_D(r_D, t_D) = \sum_{i=0}^{n-1} \varphi(r_D, t_D - t_{D,i}) \Delta T_{injD,i} \quad (\text{E.2})$$

where $\varphi(r_D, t_D)$ is the solution of an auxiliary problem which is identical to the above IBVP; however, with time-independent inner boundary condition (i.e., $\varphi(r_D = 0, t_D) = 1$) and it is given by (Chen and Reddell 1983):

$$\varphi(r_D, t_D) = \frac{1}{\Gamma(\beta)} \Gamma\left(\beta, \frac{r_D^2}{4t_D}\right) \quad (\text{E.3})$$

By applying the superposition technique, the following solution is obtained for the transient temperature in the reservoir during the injection period.

$$T_D(r_D, t_D) = \frac{1}{\Gamma(\beta)} \sum_{i=0}^{n-1} \Gamma\left(\beta, \frac{r_D^2}{4(t_D - t_{D,i})}\right) \Delta T_{injD,i} \quad (\text{E.4})$$

During the shut-in period, the advection velocity becomes negligible, and the advection-diffusion equation is simplified to the form given by Eq. 4.11. The initial and boundary conditions are defined by Eq. 4.12 – 4.14. The solution during the warmback period is obtained using Hankel transformation and is given by:

$$T_D(r_D, \Delta t_D) = \frac{1}{2\Gamma(\beta)\Delta t_D} \sum_{i=0}^{n-1} \int_0^\infty u \exp\left(-\frac{u^2 + r_D^2}{4\Delta t_D}\right) I_0\left(\frac{ur_D}{2\Delta t_D}\right) \Gamma\left(\beta, \frac{u^2}{4(t_{injD} - t_{injD,i})}\right) \Delta T_{injD,i} du \quad (\text{E.5})$$

The sandface temperature solution, obtained by assigning $r_D \rightarrow 0$ in Eq E. 5, is given by:

$$T_{wD}(\Delta t_D) = \sum_{i=0}^{n-1} \Delta T_{injD,i} \left(1 - \left(1 + \frac{t_{injD} - t_{injD,i}}{\Delta t_D} \right)^{-\beta} \right) \quad (\text{F.6})$$

For extended shut-in time, Eq E.6 is simplified to Eq E.7 using the series expansion.

$$T_o - T_w = \left(\frac{\rho_w C_w q}{4\pi\lambda_r h} \right) \frac{\sum_{i=0}^{n-1} (t_{inj} - t_{inj,i}) \Delta T_{inj,i}}{\Delta t} \quad (\text{E.7})$$

If time steps are selected such that equal temperature segments, $\Delta T_{inj,seg}$ are obtained, Eq E.7 simplifies to the following form:

$$\frac{T_o - T_w}{\Delta T_{inj,seg}} = \left(\frac{\rho_w C_w q}{4\pi\lambda_r h} \right) \frac{\sum_{i=0}^{n-1} (t_{inj} - t_{inj,i})}{\Delta t} \quad (\text{E.8})$$

Furthermore, if injection temperature is constant, Eq E. 8 simplifies to Eq. 4.24.

Appendix F. Analytical Solution for the Temperature During and Shortly after Non-isothermal Fluid Injection via Horizontal Injection Well

In this appendix, the details of the analytical solutions derivations are introduced. Starting with IBVP for injection phase (Eq 5.19 – Eq 5.26), the solution is obtained using Laplace transformation technique. The subsidiary equation of surrounding strata in Laplace domain is described as follows:

$$\frac{\partial^2 \bar{T}_{mD}}{\partial z_D^2} - s \bar{T}_{mD} = 0 \quad (\text{F.28})$$

The corresponding boundary conditions in Laplace domain are as follows:

$$\bar{T}_{mD}(x_D, z_D, s) = \bar{T}_D(x_D, s) \quad (\text{F.29})$$

$$\lim_{z_D \rightarrow \infty} \frac{\partial \bar{T}_{mD}(x_D, z_D, s)}{\partial z_D} = 0 \quad (\text{F.30})$$

The solution for the BVP described with Eq. (F.28) – Eq. (F.30) is described with the following equation (Kreyszig 2009):

$$\bar{T}_{mD}(x_D, z_D, s) = \bar{T}_D(x_D, s) e^{-\sqrt{s} z_D} \quad (\text{F.31})$$

The corresponding subsidiary equation for the reservoir in Laplace domain is described with following equation:

$$\frac{\partial^2 \bar{T}_D}{\partial x_D^2} - \beta^2 \frac{\partial \bar{T}_D}{\partial x_D} - \beta^2 (s + \sqrt{s}) \bar{T}_D = 0 \quad (\text{F.32})$$

The derivative of surrounding temperature in RHS of Eq 5.19 is obtained using Eq (F.31). Eq (F.32) is subject to the following boundary conditions in Laplace domain:

$$\bar{T}_D(x_D = 0, s) = \frac{1}{s} \quad (\text{F.33})$$

$$\lim_{x_D \rightarrow \infty} \frac{\partial \bar{T}_D(x_D, s)}{\partial x_D} = 0 \quad (\text{F.34})$$

The solution of the BVP described with Eq. (F.32) – Eq. (F.34) is described with the following equation (Kreyszig 2009):

$$\bar{T}_D = \frac{1}{s} \exp\left(\frac{x_D}{2} \left(\beta^2 - \sqrt{\beta^4 + 4\beta^2(\sqrt{s} + s)} \right)\right) \quad (\text{F.35})$$

The solution in the real-time domain is described with the following equation:

$$T_D(x_D, t_D) = \int_0^{t_D} \frac{\beta x_D}{2\sqrt{\pi\tau^3}} \operatorname{erfc}\left(\frac{\tau}{2\sqrt{t_D - \tau}}\right) e^{-\left(\frac{\beta^2(x_D - \tau)^2}{4\tau}\right)} d\tau \quad (\text{F.36})$$

The IBVP for reservoir temperature during shut-in period can be obtained using Double-Laplace transformation technique while the initial condition is described with Eq. F.35. The subsidiary equation of the surrounding strata in double Laplace domain is as follow:

$$\frac{\partial^2 \hat{T}_{mD}}{\partial z_D^2} - p \hat{T}_{mD} + \frac{1}{s} \exp\left(\frac{x_D}{2} \left(\beta^2 - \sqrt{\beta^4 + 4\beta^2(\sqrt{s} + s)} \right)\right) e^{-\sqrt{s}z_D} = 0 \quad (\text{F.37})$$

The corresponding boundary conditions in double Laplace domain are described with the following equations.

$$\hat{T}_{mD}(x_D, z_D, s, p) = \hat{T}_D(x_D, s, p) \quad (\text{F.38})$$

$$\lim_{z_D \rightarrow \infty} \frac{\partial \hat{T}_{mD}(x_D, z_D, s, p)}{\partial z_D} = 0 \quad (\text{F.39})$$

The solution of BVP described with Eq. (F.37) – Eq. (F.39) is described with the following equation (Kreyszig 2009):

$$\hat{T}_{mD} = \hat{T}_D(x_D, s, p) e^{-\sqrt{p}z_D} + \frac{(e^{-\sqrt{s}z_D} - e^{-\sqrt{p}z_D})}{s(p-s)} \exp\left(\frac{x_D}{2} \left(\beta^2 - \sqrt{\beta^4 + 4\beta^2(\sqrt{s} + s)} \right)\right) \quad (\text{F.40})$$

The governing equation of reservoir in double Laplace domain is described with the following equation:

$$\frac{\partial^2 \hat{T}_D}{\partial x_D^2} - \beta^2 (\sqrt{p} + p) \frac{\partial \hat{T}_D}{\partial x_D} + \frac{\beta^2}{s} \left(\frac{1}{(\sqrt{p} + \sqrt{s})} + 1 \right) \exp\left(\frac{x_D}{2} \left(\beta^2 - \sqrt{\beta^4 + 4\beta^2(\sqrt{s} + s)} \right)\right) = 0 \quad (\text{F.41})$$

The derivative of the temperature of surrounding in Eq 5.27 is evaluated using Eq. (F.40). Eq. (F.41) is subject to the following boundary conditions:

$$\lim_{x_D \rightarrow 0} \left(\frac{\partial \hat{T}_D(x_D, s, p)}{\partial x_D} \right) = 0 \quad (\text{F.42})$$

$$\lim_{x_D \rightarrow \infty} \frac{\partial \hat{T}_D(x_D, s, p)}{\partial x_D} = 0 \quad (\text{F.43})$$

The solution of the BVP described with Eq (F.41) – Eq (F.43) is given by (Kreyszig 2009):

$$\hat{T}_D = \frac{\frac{1}{2s} \left(\frac{1}{(\sqrt{p} + \sqrt{s})} + 1 \right) \left(\beta - \sqrt{\beta^2 + 4(\sqrt{s} + s)} \right)}{\left((\sqrt{p} + p) - \beta^2 \left(\frac{1}{2} \left(1 - \sqrt{1 + 4\beta^{-2}(\sqrt{s} + s)} \right) \right)^2 \right) \sqrt{\sqrt{p} + p}} e^{-x_D \sqrt{\beta^2(\sqrt{p} + p)}} + \frac{\frac{1}{s} \left(\frac{1}{(\sqrt{p} + \sqrt{s})} + 1 \right)}{\left((\sqrt{p} + p) - \beta^2 \left(\frac{1}{2} \left(1 - \sqrt{1 + 4\beta^{-2}(\sqrt{s} + s)} \right) \right)^2 \right)} \exp\left(\frac{x_D}{2} \left(\beta^2 - \sqrt{\beta^4 + 4\beta^2(\sqrt{s} + s)} \right) \right) \quad (\text{F.44})$$

Sandface temperature solution in double Laplace, obtained by assigning ($x_D \rightarrow 0$) in Eq. (F.44), is given by:

$$\hat{T}_{wD} = \frac{\frac{1}{s}}{\left(\sqrt{\sqrt{p} + p} - \frac{\beta}{2} \left(1 - \sqrt{1 + 4\beta^{-2}(\sqrt{s} + s)} \right) \right)} \left(\frac{1}{\sqrt{\sqrt{p} + p}} \right) \left(\frac{1}{(\sqrt{p} + \sqrt{s})} + 1 \right) \quad (\text{F.45})$$

The solution in real-time domain is obtained using inverse Laplace transformation technique. The corresponding form of Eq (F.44) and Eq (F.45) in real-time domain is described with Eq. 5.39 and Eq. 5.40, respectively. The following inverse-Laplace transformation rules are adopted to obtain the real-time solution (Bateman 1954, Spiegel 1965).

$$\mathcal{L}^{-1} \left\{ \frac{1}{s} F(a(s + \sqrt{s})) \right\} = \int_0^t \operatorname{erfc} \left(\frac{\tau}{2\sqrt{t - \tau}} \right) \frac{F\left(\frac{\tau}{a}\right)}{a} d\tau \quad (\text{F.46})$$

$$\mathcal{L}^{-1} \left\{ F(\sqrt{s}) \right\} = \frac{1}{2\sqrt{\pi t^3}} \int_0^\infty u f(u) \exp\left(-\frac{u^2}{4t}\right) du \quad (\text{F.47})$$

$$\mathcal{L}^{-1}\left\{\frac{1}{\sqrt{s}(\sqrt{s+a^2})}\right\} = e^{a^2 t} \operatorname{erfc}(a\sqrt{t}) \quad (\text{F.48})$$

$$\mathcal{L}^{-1}\left\{e^{k^2 s^2} \operatorname{erfc}(ks)\right\} = \frac{1}{k\sqrt{\pi}} \exp\left(-\frac{t^2}{4k^2}\right) \quad (\text{A.49})$$

$$\mathcal{L}^{-1}\{F(s-a)\} = e^{at} f(t) \quad (\text{F.50})$$

$$\mathcal{L}^{-1}\left\{\frac{1}{s} F(s)\right\} = \int_0^t F(\tau) d\tau \quad (\text{F.51})$$

Appendix G. Solution for the Temperature and Saturation Evolutions During CO₂ Injection in Deep Saline Aquifers

In this appendix, the solution of the advection problem - developed by Bratvold and Horne (1989) - is given for completeness. Using the dimensionless parameters given by Eq. 7.17, the hyperbolic conservation equations for gaseous CO₂ saturation and temperature are given by:

$$\frac{\partial S_g}{\partial t_D} + \frac{\partial f_g}{\partial S_g} \frac{\partial S_g}{\partial r_D^2} + \frac{\partial f_g}{\partial T_D} \frac{\partial T_D}{\partial r_D^2} = 0 \quad (\text{G.1})$$

$$\frac{\partial T_D}{\partial t_D} + g \frac{\partial T_D}{\partial r_D^2} = 0 \quad (\text{G.2})$$

The corresponding initial and boundary conditions are given by:

$$T_D(r_D, t_D = 0) = 1 \quad (\text{G.3})$$

$$T_D(r_D = 0, t_D) = 0 \quad (\text{G.4})$$

$$S_g(r_D, t_D = 0) = 0 \quad (\text{G.5})$$

$$S_g(r_D = 0, t_D) = 1 - S_{wr} \quad (\text{G.6})$$

Eq. G.1 and Eq. G.2 can be written in matrix form as follows:

$$\begin{bmatrix} S_g \\ T_D \end{bmatrix}_{t_D} + \mathbf{A} \begin{bmatrix} S_g \\ T_D \end{bmatrix}_{r_D^2} = 0 \quad \text{where } \mathbf{A} \text{ is given by } \mathbf{A} = \begin{bmatrix} \frac{\partial f_g}{\partial S_g} & \frac{\partial f_g}{\partial T_D} \\ 0 & g \end{bmatrix} \quad (\text{G.7})$$

Using the dimensionless parameters given by Eq. 7.17, the system of the hyperbolic conservation equations become:

$$\begin{bmatrix} S_g \\ T \end{bmatrix}_t + \mathbf{A} \begin{bmatrix} S_g \\ T \end{bmatrix}_{r^2} = 0 \quad \text{where } \mathbf{A} \text{ is given by } \mathbf{A} = \left(\frac{q}{\pi h \phi} \right) \begin{bmatrix} \frac{\partial f_g}{\partial S_g} & \frac{\partial f_g}{\partial T} \\ 0 & g \end{bmatrix} \quad (\text{G.8})$$

The hyperbolic conservation equations described by Eq. G.1 – G.2 with the auxiliary initial and boundary conditions given by Eq. G.3 – G.6 constitute a non-strictly hyperbolic Riemann problem which can be solved by using the Method of Characteristics. A reasonable solution of the problem is obtained by tracing the characteristic curves and introducing appropriate discontinuities to obtain a unique solution. The solution procedure presented by Bratvold and Horne (1989) is summarized below:

- Construct the f_g - S_g plots at the initial reservoir temperature, T_o and the bottomhole injection temperature, T_{inj} using Eq. 7.3 (see Fig. G.1 (a)).
- Plot the eigenvalues (ζ and g) of the system of hyperbolic conservation equations, Eq. G.7, which are defined by Eq. G.9 and Eq. G.10 versus gas saturation at both the initial aquifer temperature and the bottomhole injection temperature (see Fig G.1 (b)).

$$\zeta = \frac{r_D^2}{t_D} = \frac{\partial f_g}{\partial S_g} \quad (G.9)$$

$$g = \frac{f_g + \alpha}{S_g + \beta} \quad (G.10)$$

where α and β are given by Eq. 7.17.

- Add the characteristic curves with slopes f_s and g by plotting tangents on the f_g - S_g plot at the initial aquifer temperature starting from $(S_g, f_g) = (0,0)$ and $(S_g, f_g) = (-\beta, -\alpha)$, respectively. The tangent points identify gas saturation at the saturation front and thermal front, respectively as illustrated in Fig. G.1 (a).
- The solution is obtained by tracing the slope of the fractional flow curve and including the appropriate discontinuities represented by the tangent points obtained in the previous step in order to ensure the uniqueness of the solution. Start from $(S_g, f_g) = (1 - S_{wr}, 1)$ which is the saturation condition at the injection well and follow the slope of the fractional flow curve evaluated at the bottomhole injection temperature up to point (1) which is the gas saturation upstream of the thermal front.

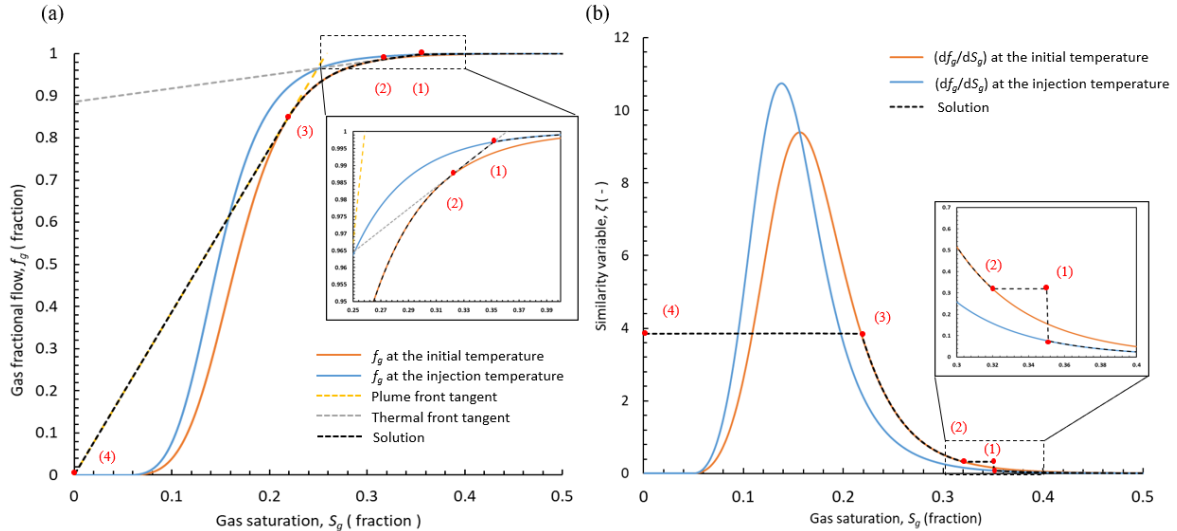


Figure G. 1. (a) f_g - S_g plots with the characteristic curves (b) derivative of the fractional flow curves along with the established solution.

Point (1) is obtained from the intercept of the characteristic curve with slope g (thermal front tangent) and the f_g - S_g plot at the injection temperature which represents the transition point from the cold to the hot fractional flow curve (see Fig. G.1 (a)). Then,

follow the $g = \text{constant}$ path up to point (2) which is the gas saturation downstream of the thermal front. This transition represents the first discontinuity in the established solution shown in Fig. G.1 (b). Point (2) is obtained from the tangent point between the characteristic curve with slope g and the f_g-S_g plot at the initial aquifer temperature. The fluid saturations obtained from point (1) to point (2) represent the saturations located at the thermal shock (i.e., they have identical thermal velocity, g).

- Next, follow the slope of the fractional flow curve evaluated at the initial aquifer temperature up to point (3) which is the gas saturation upstream of the saturation front. Point (3) is obtained from the tangent point between the characteristic curve with slope (df_g/dS_g) (saturation front tangent) and the f_g-S_g plot at the initial aquifer temperature (see Fig. G.1 (a)). The gas saturation ahead of the saturation front is equal to the initial gas saturation which is zero. The transition from point (3) to point (4) represents the second discontinuity in the established solution which is located at the saturation front. The fluid saturations obtained from point (3) to point (4) represent the saturations located at the saturation front (i.e., they have identical saturation velocity, (df_g/dS_g)).

Accordingly, the established solution constitutes a leading shock wave at the saturation front (3 – 4), followed by an expansion wave (2 – 3), followed by a trailing shock at the thermal front (1 – 2), and a zone of constant state (1 – 1). The zone of constant state reflects the difference in the speed of the propagation between the trailing shock wave and the expansion wave (Dindoruk and Dindoruk 2008). The trailing shock (1 – 2) is of a minor saturation change, and it is established due to the significant temperature contrast at the thermal front which results in different fluid mobilities. Fig. G.1 (b) shows the derivative of the f_g-S_g plots with the established saturation solution. Fig. G.2 illustrates the saturation and temperature solutions of the advection problem versus the similarity variable ζ , defined by Eq. G.9.

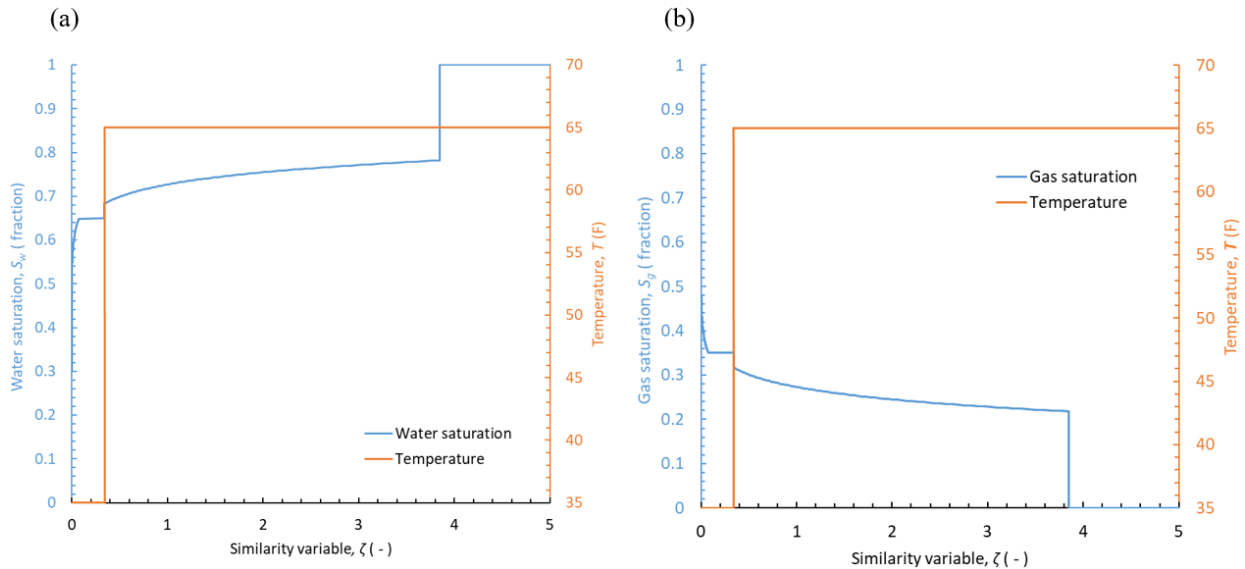


Figure G. 2. Solution of advection problem in terms of the similarity variable using Bratvold and Horne (1989)'s solution: (a) Water saturation, (b) gas saturation.

References

- Abramowitz, Milton, Stegun, Irene A, and Romer, Robert H. 1988. *Handbook of mathematical functions with formulas, graphs, and mathematical tables*, American Association of Physics Teachers (Reprint).
- Aminu, Mohammed D, Nabavi, Seyed Ali, Rochelle, Christopher A et al. 2017. A review of developments in carbon dioxide storage. *Applied Energy* **208**: 1389-1419.
- App, Jeffrey F. 2010. Nonisothermal and productivity behavior of high-pressure reservoirs. *Spe Journal* **15** (01): 50-63. <https://doi.org/10.2118/114705-PA>.
- Ashry, Islam, Mao, Yuan, Wang, Biwei et al. 2022. A Review of Distributed Fiber–Optic Sensing in the Oil and Gas Industry. *Journal of Lightwave Technology* **40** (5): 1407-1431.
- Avdonin, NA. 1964. Some formulas for calculating the temperature field of a stratum subject to thermal injection. *Neft'i Gaz* **3**: 37-41.
- Bakker, Mark, Caljé, Ruben, Schaars, Frans et al. 2015. An active heat tracer experiment to determine groundwater velocities using fiber optic cables installed with direct push equipment. *Water Resources Research* **51** (4): 2760-2772.
- Ballard, Sanford. 1996. The in situ permeable flow sensor: A ground-water flow velocity meter. *Groundwater* **34** (2): 231-240.
- Barree, Robert D, Barree, Valencia L, and Craig, David. 2009. Holistic fracture diagnostics: consistent interpretation of prefrac injection tests using multiple analysis methods. *SPE Production & Operations* **24** (03): 396-406.
- Bateman, Harry. 1954. *Tables of integral transforms [volumes I & II]*, Vol. 1: McGraw-Hill Book Company.
- Bateman, Richard M. 1985. *Cased-hole log analysis and reservoir performance monitoring*: Springer.
- Bense, VF, Read, T, Bour, Olivier et al. 2016. Distributed Temperature Sensing as a downhole tool in hydrogeology. *Water Resources Research* **52** (12): 9259-9273.
- Bielinski, Andreas, Kopp, Andreas, Schütt, Hartmut et al. 2008. Monitoring of CO₂ plumes during storage in geological formations using temperature signals: Numerical investigation. *International journal of greenhouse gas control* **2** (3): 319-328.
- Biot, Maurice A, Masse, L, and Medlin, WL. 1987. Temperature analysis in hydraulic fracturing. *Journal of petroleum technology* **39** (11): 1,389-1,397. <https://doi.org/10.2118/13228-PA>.
- Bird, R Byron, Stewart, Warren E, and Lightfoot, Edwin N. 2006. *Transport phenomena*, Vol. 1: John Wiley & Sons.

- Bratvold, Reidar Brumer and Horne, Roland N. 1989. An Analytical Solution to a Multiple-Region Moving Boundary Problem Non Isothermal Water Injection into Oil Reservoirs. *Proc.*, ECMOR I-1st European Conference on the Mathematics of Oil Recoverycp-234-00026.
- Brown, G, Carvalho, V, Wray, A et al. 2004. Monitoring alternating CO₂ and water injection and its effect on production in a carbonate reservoir using permanent fiber-optic distributed temperature systems. *Proc.*, SPE Annual Technical Conference and Exhibition.
- Brown, G, Storer, D, McAllister, K et al. 2003. Monitoring horizontal producers and injectors during cleanup and production using fiber-optic-distributed temperature measurements. *Proc.*, SPE Annual Technical Conference and Exhibition.<https://doi.org/10.2118/84379-MS>.
- Buckley, Se E and Leverett, MCI. 1942. Mechanism of fluid displacement in sands. *Transactions of the AIME* **146** (01): 107-116.
- Bui, TD and Jalali, Y. 2004. Diagnosis of horizontal Injectors with distributed Temperature Sensors. *Proc.*, SPE Annual Technical Conference and Exhibition.<https://doi.org/10.2118/89924-MS>.
- Buntebarth, G and Schopper, JR. 1998. Experimental and theoretical investigations on the influence of fluids, solids and interactions between them on thermal properties of porous rocks. *Physics and Chemistry of the Earth* **23** (9-10): 1141-1146.
- Carroll, John J, Slupsky, John D, and Mather, Alan E. 1991. The solubility of carbon dioxide in water at low pressure. *Journal of Physical and Chemical Reference Data* **20** (6): 1201-1209.
- Carslaw, HS and Jaeger, JC. 1959. Heat conduction in solids. *Oxford Univ Pr* 1st S.
- Cengel, Yunus. 2014. *Heat and mass transfer: fundamentals and applications*: McGraw-Hill Higher Education.
- Chen, Chia-Shyun and Reddell, Donald L. 1983. Temperature distribution around a well during thermal injection and a graphical technique for evaluating aquifer thermal properties. *Water Resources Research* **19** (2): 351-363.<https://doi.org/10.1029/WR019i002p00351>.
- Churchill, SW and Bernstein, M. 1977. A correlating equation for forced convection from gases and liquids to a circular cylinder in crossflow.
- CMG-STARs. 2020. *CMG-STARs User Manual*, Computer Modelling Group (CMG) Calgary, Alberta (Reprint).
- Coleman, Thomas I, Parker, Beth L, Maldaner, Carlos H et al. 2015. Groundwater flow characterization in a fractured bedrock aquifer using active DTS tests in sealed boreholes. *Journal of Hydrology* **528**: 449-462.

- COMSOL. 2018. COMSOL multiphysics reference manual, version 5.3. *COMSOL AB* **564**: 565.
- Conti, Rosaria, Gallitto, Aurelio Agliolo, and Fiordilino, Emilio. 2014. Measurement of the convective heat-transfer coefficient. *The Physics Teacher* **52** (2): 109-111.
- Corey, Arthur T. 1954. The interrelation between gas and oil relative permeabilities. *Producers monthly* **19** (1): 38-41.
- Debnath, Lokenath. 2016. The double Laplace transforms and their properties with applications to functional, integral and partial differential equations. *International Journal of Applied Computational Mathematics* **2** (2): 223-241. <https://link.springer.com/article/10.1007/s40819-015-0057-3>.
- Debnath, Lokenath and Bhatta, Dambaru. 2006. *Integral transforms and their applications*: Chapman and Hall/CRC.
- del Val, Laura, Carrera, Jesús, Pool, María et al. 2021. Heat Dissipation Test With Fiber-Optic Distributed Temperature Sensing to Estimate Groundwater Flux. *Water Resources Research* **57** (3): e2020WR027228.
- des Tombe, Bas F, Bakker, Mark, Smits, Frank et al. 2019. Estimation of the variation in specific discharge over large depth using Distributed Temperature Sensing (DTS) measurements of the heat pulse response. *Water Resources Research* **55** (1): 811-826.
- Diao, Nairen, Li, Qinyun, and Fang, Zhaohong. 2004. Heat transfer in ground heat exchangers with groundwater advection. *International Journal of Thermal Sciences* **43** (12): 1203-1211.
- Dindoruk, Deniz M and Dindoruk, Birol. 2008. Analytical solution of nonisothermal Buckley-Leverett flow including tracers. *SPE Reservoir Evaluation & Engineering* **11** (03): 555-564.
- Doughty, Christine. 2008. Estimating plume volume for geologic storage of CO₂ in saline aquifers. Report No. 0017-467X, Lawrence Berkeley National Lab.(LBNL), Berkeley, CA (United States).
- Duru, Obinna O and Horne, Roland N. 2010. Modeling reservoir temperature transients and reservoir-parameter estimation constrained to the model. *SPE Reservoir Evaluation & Engineering* **13** (06): 873-883. <https://doi.org/10.2118/115791-PA>.
- Edouard, Mvomo N, Okere, Chinedu J, Dong, Pingchuan et al. 2022. Application of fiber optics in oil and gas field development—a review. *Arabian Journal of Geosciences* **15** (6): 1-14.
- Eskilson, Per. 1987. Thermal analysis of heat extraction boreholes.
- Feng, Guan hong, Xu, Tianfu, Tian, Hailong et al. 2017. Three-phase non-isothermal flow behavior of CO₂-brine leakage from wellbores. *International Journal of Greenhouse Gas Control* **64**: 183-193.

- Foo, David Brian, Krislock, Jeremy, Meador, Trevor J et al. 2014. Horizontal Well Injection Profiling Using Distributed Temperature Sensing. *Proc., SPE/CSUR Unconventional Resources Conference–Canada*.<https://doi.org/10.2118/171586-MS>.
- Gaurina-Međimurec, Nediljka and Mavar, Karolina Novak. 2017. Depleted hydrocarbon reservoirs and CO₂ injection wells–CO₂ leakage assessment. *Rudarsko-geološko-naftni zbornik (The Mining-Geological-Petroleum Bulletin)* **32** (2): 15-27.
- Glasbergen, Gerard, Gualtieri, Dan, Van Domelen, Mary S et al. 2009. Real-time fluid distribution determination in matrix treatments using DTS. *SPE Production & Operations* **24** (01): 135-146.
- Grace, Robert D. 2017. *Blowout and well control handbook*: Gulf Professional Publishing.
- Han, Weon S, Lu, M, McPherson, BJ et al. 2013. Characteristics of CO₂-driven cold-water geyser, Crystal Geyser in Utah: experimental observation and mechanism analyses. *Geofluids* **13** (3): 283-297.
- Han, Weon Shik, Kim, Kue-Young, Park, Eungyu et al. 2012. Modeling of spatiotemporal thermal response to CO₂ injection in saline formations: interpretation for monitoring. *Transport in porous media* **93** (3): 381-399.
- Han, Weon Shik, Stillman, Greg A, Lu, Meng et al. 2010. Evaluation of potential nonisothermal processes and heat transport during CO₂ sequestration. *Journal of Geophysical Research: Solid Earth* **115** (B7).
- Hasan, AR and Kabir, CS. 2012. Wellbore heat-transfer modeling and applications. *Journal of Petroleum Science and Engineering* **86**: 127-136.
- Hashish, Refaat G and Zeidouni, Mehdi. 2019. Analysis of Warm-Back Data After Cold-Fluid Injection Into Multilayer Reservoirs. *SPE Reservoir Evaluation & Engineering* **23** (01): 212-229.
- Hashish, Refaat G and Zeidouni, Mehdi. 2021. Injection Profiling Through Temperature Warmback Analysis Under Variable Injection Rate and Variable Injection Temperature. *Transport in Porous Media*: 1-43.
- Hashish, Refaat G and Zeidouni, Mehdi. 2022. Heat Pulse Testing at Monitoring Wells to Estimate Subsurface Fluid Velocities in Geological CO₂ Storage. *Journal of Petroleum Science and Engineering* (Accepted with major revisions).
- Hoang, Hai, Mahadevan, Jagannathan, and Lopez, Henry D. 2011. Interpretation of wellbore temperatures measured using distributed temperature sensors during hydraulic fracturing. *Proc., SPE Hydraulic Fracturing Technology Conference*.<https://doi.org/10.2118/140442-MS>.
- Horner, DR. 1951. Pressure build-up in wells. *Proc., 3rd world petroleum congress*.

- Hu, Litang, Chen, Chongxi, and Chen, Xunhong. 2011. Simulation of groundwater flow within observation boreholes for confined aquifers. *Journal of hydrology* **398** (1-2): 101-108.
- Hu, Litang, Pan, Lehua, and Zhang, Keni. 2012. Modeling brine leakage to shallow aquifer through an open wellbore using T2WELL/ECO2N. *International Journal of Greenhouse Gas Control* **9**: 393-401.
- Huckabee, Paul Thomas. 2009. Optic fiber distributed temperature for fracture stimulation diagnostics and well performance evaluation. *Proc.*, SPE Hydraulic Fracturing Technology Conference.
- Hurter, Suzanne, Garnett, Andrew Alf, Bielinski, Andreas et al. 2007. Thermal signature of free-phase CO₂ in porous rocks: detectability of CO₂ by temperature logging. *Proc.*, Offshore Europe. <https://doi.org/10.2118/109007-MS>.
<https://doi.org/10.2118/109007-MS>.
- IEA. 2008a. *CO₂ capture and storage: a key carbon abatement option*: OECD/Iea.
- IEA. 2008b. Energy technology perspectives: Scenarios and strategies to 2050. *International Energy Agency and Organisation for Economic Co-operation and Development, Paris, France*.
- Jayne, Richard S, Zhang, Yingqi, and Pollyea, Ryan M. 2019. Using heat as a predictor of CO₂ breakthrough in highly heterogeneous reservoirs. *Geophysical Research Letters* **46** (11): 5879-5888.
- Jensen, Ole Krogh and Finlayson, Bruce A. 1980. Solution of the transport equations using a moving coordinate system. *Advances in Water Resources* **3** (1): 9-18.
- Jung, Yoojin, Pau, George Shu Heng, Finsterle, Stefan et al. 2018. TOUGH3 user's guide. *University of California, Berkeley*.
- KAPPA-Rubis. 2019. Multi Purpose Numerical Model.
- Kreyszig, Erwin. 2009. Advanced Engineering Mathematics 10th Edition.
- LaForce, T, Ennis-King, J, and Paterson, L. 2014. Semi-analytical solutions for nonisothermal fluid injection including heat loss from the reservoir: Part 1. Saturation and temperature. *Advances in water resources* **73**: 227-241.
- Lauwerier, HA 1955. The transport of heat in an oil layer caused by the injection of hot fluid. *Applied Scientific Research, Section A* **5** (2-3): 145-150. <https://link.springer.com/article/10.1007/BF03184614>.
- Leaf, Andrew T, Hart, David J, and Bahr, Jean M. 2012. Active thermal tracer tests for improved hydrostratigraphic characterization. *Groundwater* **50** (5): 726-735.
- Lee, John, Rollins, John B, and Spivey, John Paul. 2003. *Pressure transient testing*: Richardson, Tex.: Henry L. Doherty Memorial Fund of AIME, Society of

- Li, Min and Lai, Alvin CK. 2015. Review of analytical models for heat transfer by vertical ground heat exchangers (GHEs): A perspective of time and space scales. *Applied Energy* **151**: 178-191.
- Li, Xinyang and Zhu, Ding. 2018. Temperature behavior during multistage fracture treatments in horizontal wells. *SPE Production & Operations* **33** (03): 522-538.
- Lienhard, IV and John, H. 2005. *A heat transfer textbook*: phlogiston press.
- LING, Zong-fa, WANG, Li-juan, HU, Yong-le et al. 2008. Flood pattern optimization of horizontal well injection. *Petroleum Exploration and Development* **35** (1): 85-91.
- Liu, G, Knobbe, S, and Butler Jr, JJ. 2013. Resolving centimeter-scale flows in aquifers and their hydrostratigraphic controls. *Geophysical Research Letters* **40** (6): 1098-1103.
- Liu, Guoqing, Zhou, Tong, Li, Fengxia et al. 2020. Fracture Surface Area Estimation from Hydraulic-Fracture Treatment Pressure Falloff Data. *SPE Drilling & Completion*.<https://doi.org/10.15530/urtec-2019-40>.
- Mao, Yilin and Zeidouni, Mehdi. 2017. Analytical Solutions for Temperature Transient Analysis and Near Wellbore Damaged Zone Characterization. *Proc., SPE Reservoir Characterisation and Simulation Conference and Exhibition*.<https://doi.org/10.2118/185990-MS>.
- Mao, Yilin, Zeidouni, Mehdi, and Askari, Roohollah. 2017. Effect of leakage pathway flow properties on thermal signal associated with the leakage from CO₂ storage zone. *Greenhouse Gases: Science Technology* **7** (3): 512-529.<https://doi.org/10.1002/ghg.1658>.
- Marín, E. 2010. Characteristic dimensions for heat transfer. *Latin-American Journal of Physics Education* **4** (1): 56-60.
- Mathias, Simon A, Gluyas, Jon G, de Miguel, Gerardo J González Martínez et al. 2013. On relative permeability data uncertainty and CO₂ injectivity estimation for brine aquifers. *International Journal of Greenhouse Gas Control* **12**: 200-212.
- Mathias, Simon A, Gluyas, Jon G, Oldenburg, Curtis M et al. 2010. Analytical solution for Joule–Thomson cooling during CO₂ geo-sequestration in depleted oil and gas reservoirs. *International Journal of Greenhouse Gas Control* **4** (5): 806-810.
- Mawalkar, Sanjay, Brock, David, Burchwell, Andrew et al. 2019. Where is that CO₂ flowing? Using Distributed Temperature Sensing (DTS) technology for monitoring injection of CO₂ into a depleted oil reservoir. *International Journal of Greenhouse Gas Control* **85**: 132-142.
- McClure*, Mark, Bammidi, Vidya, Cipolla, Craig et al. 2019. A collaborative study on DFIT interpretation: Integrating modeling, field data, and analytical techniques. *Proc., Unconventional Resources Technology Conference, Denver, Colorado, 22-24 July 2019* 2020-2058.

- Meyer, Bruce R. 1989. Heat transfer in hydraulic fracturing. *SPE production engineering* **4** (04): 423-429. <https://doi.org/10.2118/17041-PA>.
- Moreira, Tiago Augusto, Colmanetti, Alex Roger Almeida, and Tibirica, Cristiano Bigonha. 2019. Heat transfer coefficient: a review of measurement techniques. *Journal of the Brazilian Society of Mechanical Sciences and Engineering* **41** (6): 1-25.
- Morgan, Vincent T. 1975. The overall convective heat transfer from smooth circular cylinders. In *Advances in heat transfer*, Vol. 11, 199-264. Elsevier.
- Nowak, TJ. 1953. The estimation of water injection profiles from temperature surveys. *Journal of Petroleum Technology* **5** (08): 203-212.
- Oldenburg, Curtis M 2007. Joule-Thomson cooling due to CO₂ injection into natural gas reservoirs. *Energy Conversion Management* **48** (6): 1808-1815. <https://doi.org/10.1016/j.enconman.2007.01.010>.
- Özişik, M Necati. 1980. *Heat conduction*: John Wiley & Sons.
- Pan, Lehua. 2011. T2Well/ECO2N version 1.0: multiphase and non-isothermal model for coupled wellbore-reservoir flow of carbon dioxide and variable salinity water.
- Pan, Lehua and Oldenburg, Curtis M. 2014. T2Well—an integrated wellbore–reservoir simulator. *Computers & Geosciences* **65**: 46-55.
- Pan, Lehua, Oldenburg, Curtis M, Wu, Y-S et al. 2011. T2Well/ECO2N version 1.0: multiphase and non-isothermal model for coupled wellbore-reservoir flow of carbon dioxide and variable salinity water, Lawrence Berkeley National Lab.(LBNL), Berkeley, CA (United States).
- Pickens, JF, Cherry, JA, Grisak, GE et al. 1978. A multilevel device for ground-water sampling and piezometric monitoring. *Groundwater* **16** (5): 322-327.
- Pimenov, Viacheslav, Brown, George Albert, Tertychnyi, Vladimir V et al. 2005. Injectivity profiling in horizontal wells via distributed temperature monitoring. *Proc.*, SPE Annual technical conference and exhibition.
- Platenkamp, RJ. 1985. Temperature distribution around water injectors: effects on injection performance. *Proc.*, Middle East Oil Technical Conference and Exhibition.
- Press, William H, Teukolsky, Saul A, and Vetterling, WT %J Cambridge, UK: Cambridge UP. Flannery 0P (1992) Numerical recipes in C: the art of scientific computing.
- Pruess, Karsten. 2005. *ECO2N: A TOUGH2 fluid property module for mixtures of water, NaCl, and CO₂*: Lawrence Berkeley National Laboratory Berkeley, CA.

- Pruess, Karsten, Garcia, Julio, Kavscek, Tony et al. 2002. Intercomparison of numerical simulation codes for geologic disposal of CO₂, Lawrence Berkeley National Lab.(LBNL), Berkeley, CA (United States).
- Ramey, Henry J. 1962. Wellbore heat transmission. *Journal of petroleum Technology* **14** (04): 427-435.
- Ranjan, Priyesh and McColpin, Glenn. 2013. Fiber-Optic Sensing: Turning the Lights on Downhole. *The Digital Oil Field*: 34-37.
- Read, T, Bense, VF, Hochreutener, R et al. 2015. Thermal-plume fibre optic tracking (T-POT) test for flow velocity measurement in groundwater boreholes. *Geoscientific Instrumentation, Methods and Data Systems* **4** (2): 197-202.
- Read, T, Bour, Olivier, Selker, JS et al. 2014. Active-distributed temperature sensing to continuously quantify vertical flow in boreholes. *Water Resources Research* **50** (5): 3706-3713.
- Read, Tom, Bour, Olivier, Bense, V et al. 2013. Characterizing groundwater flow and heat transport in fractured rock using fiber-optic distributed temperature sensing. *Geophysical Research Letters* **40** (10): 2055-2059.
- Romero, Louis A. 1995. Forced convection past a slender body in a saturated porous medium. *SIAM Journal on Applied Mathematics* **55** (4): 975-985.
- Ruan, Binglu, Xu, Ruina, Wei, Lingli et al. 2013. Flow and thermal modeling of CO₂ in injection well during geological sequestration. *International Journal of Greenhouse Gas Control* **19**: 271-280.
- Sadigov, Teymur, Cerrahoglu, Cagri, Ramsay, James et al. 2021. Real-Time Water Injection Monitoring with Distributed Fiber Optics Using Physics-Informed Machine Learning. *Proc.*, Offshore Technology Conference.
- Satman, Abdurrahman, Zolotukhin, Anatoly B, and Soliman, Mohamed Y. 1984. Application of the time-dependent overall heat-transfer coefficient concept to heat-transfer problems in porous media. *Society of Petroleum Engineers Journal* **24** (01): 107-112.
- Seabrook, Brian, Kiyouni, Ahmed, Sau, Rajes et al. 2020. First Real-Time Fiber Optic Surveillance and Analysis of a Bullhead Stimulation of an Extended-Reach Horizontal Lateral in a Giant Offshore Carbonate Oil Field. *Proc.*, Abu Dhabi International Petroleum Exhibition & Conference.
- Sellwood, Stephen M, Hart, David J, and Bahr, Jean M. 2015. An in-well heat-tracer-test method for evaluating borehole flow conditions. *Hydrogeology Journal* **23** (8): 1817-1830.
- Seth, Gaurav, Reynolds, Albert Coburn, and Mahadevan, Jagannathan. 2010. Numerical model for interpretation of distributed-temperature-sensor data during hydraulic fracturing.

- Proc.*, SPE Annual Technical Conference and Exhibition. <https://doi.org/10.2118/135603-MS>.
- Shaw-Yang, Yang and Hund-Der, Yeh. 2008. An analytical solution for modeling thermal energy transfer in a confined aquifer system. *Hydrogeology journal* **16** (8): 1507-1515. <https://doi.org/10.1007/s10040-008-0327-9>.
- Shirdel, Mahdy, Buell, Richard S, Wells, Mike J et al. 2019. Horizontal-Steam-Injection-Flow Profiling Using Fiber Optics. *J SPE Journal*. <https://doi.org/10.2118/181431-MS>.
- Simon, Nataline, Bour, Olivier, Lavenant, Nicolas et al. 2021. Numerical and experimental validation of the applicability of active-DTS experiments to estimate thermal conductivity and groundwater flux in porous media. *Water Resources Research* **57** (1): e2020WR028078.
- Sinclair, A Richard. 1971. Heat Transfer effects in deep well fracturing. *Journal of Petroleum Technology* **23** (12): 1,484-1,492.
- Smith, James T and Cobb, William M. 1997. *Waterflooding*: Midwest Office of the Petroleum Technology Transfer Council.
- Sparrow, Ephraim M, Abraham, John P, and Tong, Jimmy CK. 2004. Archival correlations for average heat transfer coefficients for non-circular and circular cylinders and for spheres in cross-flow. *International Journal of Heat and Mass Transfer* **47** (24): 5285-5296.
- Spiegel, Murray R. 1965. *Schaum's Outline of Laplace Transforms*: McGraw Hill Professional.
- Spivey, John Paul and Lee, W John. 2013. *Applied well test interpretation*: Society of Petroleum Engineers Richardson, TX.
- Stauffer, Philip H, Lewis, KC, Stein, Joshua S et al. 2014. Joule–Thomson effects on the flow of liquid water. *Transport in porous media* **105** (3): 471-485.
- Stehfest, Harald. 1970. Algorithm 368: Numerical inversion of Laplace transforms [D5]. *Communications of the ACM* **13** (1): 47-49. [10.1145/361953.361969](https://doi.org/10.1145/361953.361969).
- Strandli, Christin W and Benson, Sally M. 2013. Identifying diagnostics for reservoir structure and CO2 plume migration from multilevel pressure measurements. *Water Resources Research* **49** (6): 3462-3475.
- Tabatabaei, Mohammad, Zhu, Ding, and Hill, Alfred D. 2013. Theoretical basis for interpretation of temperature data during acidizing treatment of horizontal wells. *SPE Production & Operations* **28** (02): 168-180.
- Ugueto, C, Gustavo, A, Huckabee, Paul T et al. 2016. Perforation cluster efficiency of cemented plug and perf limited entry completions; Insights from fiber optics diagnostics. *Proc.*, SPE Hydraulic Fracturing Technology Conference. <https://doi.org/10.2118/179124-MS>.

- Ugueto, Gustavo, Huckabee, Paul, Wojtaszek, Magdalena et al. 2019. New Near-Wellbore Insights from Fiber Optics and Downhole Pressure Gauge Data. *Proc.*, SPE Hydraulic Fracturing Technology Conference and Exhibition. <https://doi.org/10.2118/194371-MS>.
- van der Horst, Juun. 2015. Recent advances in fiber optic technology for in-well production and injection profiling. *Proc.*, International Petroleum Technology Conference.
- van Genuchten, M Th. 1980. A closed-form equation for predicting the hydraulic conductivity of unsaturated soils 1. *Soil science society of America journal* **44** (5): 892-898.
- Wallis, Graham B. 2020. *One-dimensional two-phase flow*: Dover Publications.
- Wang, Jingrui, Hu, Litang, Pan, Lehua et al. 2018. Numerical studies of CO₂ and brine leakage into a shallow aquifer through an open wellbore. *Hydrogeology journal* **26** (2): 495-509.
- Wh, Press, Teukolsky, SA, Vetterling, WT et al. 1992. Numerical recipes in C: the art of Scientific Computing. In *Modeling of Data*. Cambridge University Press.
- Wheeler, JA. 1969. Analytical calculations for heat transfer from fractures. *Proc.*, SPE Improved Oil Recovery Symposium. <https://doi.org/10.2118/2494-MS>.
- Whitaker, Stephen. 2014. *Elementary Heat Transfer Analysis: Pergamon Unified Engineering Series*, Vol. 20: Elsevier.
- Whitsitt, NF and Dysart, GR. 1970. The effect of temperature on stimulation design. *Journal of Petroleum Technology* **22** (04): 493-502.
- Xu, Hui. 1990. Formation Evaluation Using Temperature Buildup Curves. https://digitalcommons.lsu.edu/gradschool_disstheses/4963/.
- Yoshida, Nozomu, Teshima, Satoshi, Yamada, Ryo et al. 2020. Pushing the Limits of Damage Identification Through the Combined Use of Coiled Tubing, Distributed Sensing, and Advanced Simulations: A Success Story from Japan. *SPE Production & Operations*.
- Zanganeh, Behnam, Clarkson, Christopher R, Hawkes, Robert R et al. 2019. A new DFIT procedure and analysis method: An integrated field and simulation study. *Journal of Natural Gas Science and Engineering* **63**: 10-17.
- Zeidouni, Mehdi. 2011. Analytical and inverse models for leakage characterization of CO₂ storage.
- Zeidouni, Mehdi, Nicot, Jean-Philippe, and Hovorka, Susan D. 2014. Monitoring above-zone temperature variations associated with CO₂ and brine leakage from a storage aquifer. *Environmental earth sciences* **72** (5): 1733-1747.
- Zhao, Ruirui and Cheng, Jianmei. 2015. Non-isothermal modeling of CO₂ injection into saline aquifers at a low temperature. *Environmental earth sciences* **73** (9): 5307-5316.

Zolotukhin, AB. 1979. Analytical definition of the overall heat transfer coefficient. *Proc.*, SPE California Regional Meeting.

Zuber, Novak and Findlay, J ASME. 1965. Average volumetric concentration in two-phase flow systems.

Žukauskas, A. 1972. Heat transfer from tubes in crossflow. In *Advances in heat transfer*, Vol. 8, 93-160. Elsevier.

Vita

Refaat Hashish is a research assistant and doctoral candidate at the Craft & Hawkins Department of Petroleum at Louisiana State University. He started his PhD study in Summer 2018, and he is expected to graduate in December 2022. Previously, he worked as a teaching and research assistant at the Department of Petroleum Engineering at Cairo University from 2013 to 2018. His research interests include analytical and numerical modeling of fluid and heat transport in porous medium and wellbores during non-isothermal fluid injection applications such as Improved Oil Recovery and Geological Carbon Storage. His research enables effective analysis of temperature data acquired using permeant downhole monitoring tools such as fiber-optic Distributed Temperature Sensing (FO-DTS) for reservoir monitoring and surveillance. Refaat got his bachelor's degree of science and master's degree of science, both in petroleum engineering, from Cairo University in 2013 and 2016, respectively.

Publications

- Hashish, Refaat G and Zeidouni, Mehdi. 2019a. Analysis of Warm-Back Data After Cold-Fluid Injection Into Multilayer Reservoirs. *SPE Reservoir Evaluation & Engineering* 23 (01): 212-229.
- Hashish, Refaat G and Zeidouni, Mehdi. 2019b. Analytical approach for injection profiling through warm-back analysis in multilayer reservoirs. *Journal of Petroleum Science and Engineering* 182: 106274.
- Hashish, Refaat G and Zeidouni, Mehdi. 2020. Warmback analysis to determine fracture geometry of a single-stage hydraulic fracturing stimulation. *International Journal of Thermal Sciences* 155: 106423.
- Hashish, Refaat G and Zeidouni, Mehdi. 2021a. Injection profiling in horizontal wells using temperature warmback analysis. *Computational Geosciences* 25 (1): 215-232.
- Hashish, Refaat G and Zeidouni, Mehdi. 2021b. Injection Profiling Through Temperature Warmback Analysis Under Variable Injection Rate and Variable Injection Temperature. *Transport in Porous Media*: 1-43.
- Hashish, Refaat G and Zeidouni, Mehdi. 2022. CO₂ zonal injection rate allocation and plume extent evaluation through wellbore temperature analysis. *Advances in Water Resources*: 104203.
- Hashish, Refaat G and Zeidouni, Mehdi. 2022. Heat pulse testing at monitoring wells to estimate subsurface fluid velocities in geological CO₂ storage. *Journal of Petroleum Science and Engineering*: 110621.